Shamim Khan

Investigation of the Hyperfine Structure of Praseodymium-Transitions using Laser Spectroscopy

DOCTORAL THESIS

For obtaining the academic degree of

Doktorin der technischen Wissenschaften

Doctoral Programme of Technical Sciences
Technical Physics

Graz University of Technology

Graz University of Technology

Supervisor:

Univ.-Prof. Dipl.-Ing. Dr.techn. Laurentius Windholz

Institute of Experimental Physics, Graz, Austria

August 2011

Deutsche Fassung:

Beschluss der Curricula-Kommission für Bachelor-, Master- und Diplomstudien vom 10.11.2008 Genehmigung des Senates am 1.12.2008

EIDESSTATTLICHE ERKLÄRUNG

Ich erkläre an Eides statt, dass ich die vorliegende Arbeit selbstständig verfasst, andere als die angegebenen Quellen/Hilfsmittel nicht benutzt, und die den benutzten Quellen wörtlich und inhaltlich entnommenen Stellen als solche kenntlich gemacht habe.

Graz, am …………………………   …………………………..
                                                                              (Unterschrift)

Englische Fassung:

STATUTORY DECLARATION

I declare that I have authored this thesis independently, that I have not used other than the declared sources/resources, and that I have explicitly marked all material which has been quoted either literally or by content from the used sources.

…………………………   …………………………
        date   (signature)

Dedicated

to

My Parents & Teachers

Thesis Advisor   Author

Prof. Dr. L. Windholz   Shamim Khan

Investigation of the Hyperfine Structure of Praseodymium-Transitions using Laser Spectroscopy

Abstract

A comprehensive knowledge of the electron levels in an atom is one of the prerequisite for understanding the electron-electron and electron-nucleus interactions inside an atom and for the classification of the atomic spectrum of an element. The spin-orbit interaction is the largest relativistic effect and is responsible for the fine structure splitting in an atom. The hyperfine structure splitting of the fine structure atomic energy levels arise as a result of the interaction between spinning and orbiting electrons and electromagnetic multipole nuclear moments. The major contributions are due to the magnetic dipole and electric quadrupole moments. The electronic ground state configuration of praseodymium $^{59}Pr_{141}$ is [Xe] $4f^3 6s^2$, with ground state level $^4I_{9/2}$. Because of its 5 outer electrons Praseodymium has a high density of energy levels which give rise to an extremely line rich emission spectrum. Due to this fact praseodymium serves as an efficient testing ground for hyperfine structure studies.

The thesis is mainly devoted to the finding of previously unknown energy levels by the investigation of spectral lines and their hyperfine structures. In a hollow cathode discharge lamp praseodymium atoms and ions in ground and excited states are excited to high lying states by laser light. The excitation source is a tunable ring-dye laser system, operated with Stilbene 3, Rhodamine 6G, Kiton Red, DCM and LD 700. A high resolution Fourier Transform spectrum is used for extracting excitation wavelengths. Then the laser wavelength is tuned to a strong hyperfine component of the spectral line to be investigated, and a search for fluorescence from excited levels is performed. From the observed hyperfine structure pattern, J-values and hyperfine interaction constants A of the combining levels are determined. This information, together with excitation and fluorescence wavelengths, allows us to find the energies of the involved levels.

During the course of this dissertation 313 new energy levels of Pr I and 4 new energy levels of Pr II were discovered. Using these newly discovered energy levels 652 spectral lines were classified via laser excitation, 836 spectral lines were classified as fluorescence lines and 178 lines were classified by their hyperfine structure and wave number.

The present work not only enhances the number of classified lines in the spectrum of Pr I but also demonstrates the advantage of laser induced fluorescence spectroscopy. The new levels might contribute also to a future theoretical analysis of the level structure of Pr I.

Betreuer der Dissertation

Autor

Prof. Dr. L. Windholz

Shamim Khan

Untersuchung der Hyperfeinstruktur von Praseodym-Übergängen mit Hilfe von Laserspektroskopie

Kurzfassung

Die umfassende Kenntnis der elektronischen Energieniveaus eines Atoms ist Voraussetzung für das Verständnis der Wechselwirkungen der Elektronen untereinander sowie ihrer Wechselwirkungen mit dem Atomkern. Die Klassifikation der Linien eines Atomspektrums kann ebenfalls nur mit Hilfe der Energieniveaus erfolgen.

Die Spin-Bahn-Wechselwirkung ist der größte relativistische Effekt und verantwortlich für die Feinstrukturaufspaltung im Atom. Die Hyperfeinstrukturaufspaltung der Feinstrukturniveaus entsteht als Resultat der Wechselwirkung der Elektronenbewegung (Bahnbewegung und Eigenrotation) und den elektrischen Multipolmomenten des Atomkerns. Abgesehen von der Coulomb-Wechselwirkung werden die Hauptbeiträge durch das magnetische Dipolmoment und das elektrische Quadrupolmoment des Kerns verursacht.

Der elektronische Grundzustand von Praseodym (^{59}Pr$_{141}$) hat die Elektronenkonfiguration [Xe] $4f^3 6s^2$, mit der spektroskopischen Bezeichnung ^{4}I$_{9/2}$. Wegen seiner 5 äußeren Elektronen hat Praseodym eine hohe Dichte der elektronischen Niveaus, was zu einem extrem linienreichen Emissionsspektrum führt. Daher ist Praseodym ein ideales Testobjekt für Hyperfein-Studien.

Die Hauptaufgabe dieser Arbeit bestand im Auffinden neuer, bislang unbekannter Energieniveaus durch Untersuchung von Spektrallinien und ihrer Hyperfeinstruktur. In einer Hohlkathodenentladung werden Praseodym-Atome und -Ionen von Grund- und angeregten Zuständen aus mit Hilfe von Laserlicht in hochliegende angeregte Zustände gebracht. Die Anregung erfolgt mit dem Licht eines durchstimmbaren Farbstoff-Ringlasers, der mit verschiedenen Farbstoffen (Stilben 3, Rhodamin 6G, Kiton Red, DCM and LD 700) betrieben wurde. Ein hochauflösendes Fourier-Spektrum wird zum Auffinden geeigneter Anregungswellenlängen benutzt. Dann wird die Wellenlänge des Farbstofflasers auf eine starke Hyperfeinstruktur-Komponente der zu untersuchenden Spektrallinie eingestellt, und es wird nach laser-induzierten Fluoreszenzlinien gesucht. Aus dem registrierten Hyperfein-Linienprofil werden die J-Werte und A-Faktoren der beteiligten Energieniveaus ermittelt. Diese Information, zusammen mit der Anregungs- und den Fluoreszenzwellenlängen, erlaubt es, die Energien der beteiligten (zum Teil bislang unbekannten) elektronischen Niveaus zu finden.

Während dieser Untersuchung wurden 313 bislang unbekannte Energieniveaus des Pr-Atoms (Pr I) und 4 neue Niveaus des Pr-Ions (Pr II) entdeckt. Mit Hilfe dieser neuen Niveaus konnten 652 Spektrallinien durch direkte Laseranregung, 836 als Fluoreszenzlinien und rund 180 weitere Linien aufgrund ihrer Lage und Hyperfeinstruktur im Fourier-Spektrum klassifiziert werden.

Die vorliegende Arbeit erweitert nicht nur die Anzahl der klassifizierten Linien im Pr-spektrum sondern demonstriert auch das Potential der laser-induzierten Fluoreszenz-Spektroskopie. Die neuen Niveaus werden auch bei zukünftigen theoretischen Untersuchungen der Energieniveaustruktur von Praseodym hilfreich sein.

Declaration

This dissertation is submitted to the Institute of Experimental Physics, Graz University of Technology, Graz Austria, in partial fulfillment of the requirement for the degree of Doctor of Technical Sciences.

The thesis is entitled:

Investigation of the Hyperfine Structure of Praseodymium-Transitions using Laser Spectroscopy

written by Shamim Khan and has been approved by the Institute of Experimental Physics, Graz University of Technology, Graz Austria.

The final copy of this thesis has been examined by the under signed authority, and find that both the content and the form meet acceptable presentation standards of scholarly work in the above mentioned discipline.

_____

Univ. Prof. Dip.-Ing. Dr. tech. Laurentius Windholz

Date _____

Acknowledgements

All appreciation to Almighty Allah, without His will and consent we can't proceed a single step. It is through His boundless and infinite mercy that I have been able to complete this research work. Respect and humble thanks to Holy Prophet Muhammad peace be upon him who is like a beacon in every aspect whether it is the purpose of education or how to work in a group of people.

I pay my heartiest gratitude to my research advisor Prof. Dr. Laurentius Windholz for supervising this research work. His guidance, valuable discussions and encouragement, lead to this research endeavor to come to an end. I am deeply thankful to him for always being so kind in addressing to my research problems affably. No matter how hectic his schedule and how insignificant my question, he always spared some time to listen my problems. During my entire stay, I never felt hesitated in communicating with him and always found him in a welcome attitude.

I am very much thankful to the Head of the Institute, Prof. W. E. Ernst for giving me this opportunity to work here as a research student. I thank all the members of the institute for their help at various occasions. I am also thankful to the people from machine workshop of the institute for providing me technical support during the years.

On this occasion, I would also like to acknowledge all my teachers that play a key role in my success throughout my education career.

It is worth to mention the role being played by Higher Education Commission (HEC) of Pakistan. The present pursuit for PhD studies was only possible with financial assistance from HEC.

This gives me pleasure to thanks my co-workers Syed Tanweer Iqbal, Betina Gamper, Imran Siddiqui and other Pakistani and Austrian colleagues in the institute for their co-operation at various occasions during my PhD studies. Special thanks are for Imran Siddiqui for his continuous support in the lab, valuable discussions and helping me in other difficult situations. Thanks are also due to all my friends in Graz. I will not forget the pleasant time which I have spent with them.

Last but not least, I wish to express my heartfelt gratitude towards my parents for their support, love and guidance in every field of life. Without their support, I would not be standing where I am now. It gives me satisfaction and pleasure to think that they are always praying for my success. I am also very much thankful to my sister Rukhsana Hafeez and brothers Arshad Iqbal and Abid Iqbal for their prayers and love.

Shamim Khan

Table of Contents

1 Introduction

1.1 Preface

The major Coulomb interaction between positively charged nucleus and electrons determines the radial distribution of electrons around the nucleus. Inside the nucleus, the distribution of charges and currents give rise to other multiple electromagnetic moments. Two major multipole electromagnetic moments are magnetic dipole moment (associated with the nuclear spin) and electric quadrupole moment (associated with a deviation from a spherical charge distribution in the nucleus). In the former case, the nuclear magnetic dipole moment interacts with the magnetic field produced by the spinning and orbiting electrons. In the latter, the interaction occurs when, at the position of a nucleus, the electronic charge distribution produces an electric field gradient with which the nuclear quadrupole moment can interact. These interactions give rise to splitting of fine structure levels into hyperfine levels which results in hyperfine structure of a spectral line. Magnetic dipole interaction leads to splitting of fine structure levels where as the electric quadrupole interaction produce a shift in the hyperfine structure levels.

Hyperfine structure investigations of an element not only give information regarding the electron structure but also provide useful information about the nucleus of an atom without probing the nucleus directly. Thus, the atomic hyperfine structure has been extensively investigated for various elements and much valuable information has been obtained.

The chemical element praseodymium belongs to the group of lanthanide series (rare earth group) where the spectroscopic properties are determined by the fact that binding energies of *4f, 5d, 6s* and *6p* electrons are of the same magnitude. These similarities give rise to overlapping complex configurations with region of high energy level density and thus, to complex rich line spectra. This motivated the investigations of spectrum of Pr.

Extensive experimental work has been done in past on the investigation of hyperfine structure of praseodymium. Nevertheless, the experimental data are not complete and it is expected that many unassigned transitions and missing levels exist. Therefore the purpose of this study is to perform systematic measurements of spectrum of Pr I using the laser induced fluorescence technique in hollow cathode discharge lamp and to deepen the understanding of atomic structure of Pr I.

1.2 Historical Background of Spectroscopy

Although Sir Isaac Newton first used a prism to generate the spectrum of the sun in 1666, spectroscopy did not emerge as a systematic empirical science until the middle of nineteenth century, when Kirchhoff clearly defined the principles of spectrum analysis. Newton in 1666 showed that the white light from the sun could be dispersed into a continuous series of colours. Newton introduced the word "spectrum" to describe this phenomenon. Newton's analysis of light was the beginning of the science of spectroscopy.

Fraunhofer extended Newton's discovery by observing that the sun's spectrum, when sufficiently dispersed, was crossed by a large number of fine dark lines, now known as Fraunhofer lines. W.H. Wollaston had earlier observed a few of these lines but failed to attach any significance to them. These were the first spectral lines ever observed, and Fraunhofer employed the most prominent of them as the first standards for comparing spectral lines obtained using prisms of different glasses. Fraunhofer also studied spectra of

the stars and planets, using a telescope objective to collect the light. This laid the foundation for the science of astrophysics.

In the early 1800's many workers, J.F.W. Herschel, W.H.F. Talbot, C. Wheatstone, A.J. Angstrom, and D. Alter among them, studied spectra from terrestrial sources such as flames, arcs and sparks. These sources were found to emit bright spectral lines, which were characteristic of the chemical elements in the flame. Foucault, the French physicist, observed in 1848 that a flame containing sodium would absorb the yellow light emitted by a strong arc placed behind it. This was the first demonstration of a laboratory absorption spectrum.

By recognizing that each atom and molecule has its own characteristic spectrum, Kirchhoff and Bunsen established spectroscopy as a scientific tool for probing atomic and molecular structure, and founded the field of spectrochemical analysis for analyzing the composition of materials. In 1868 Ångström published the first accurate tables of wavelengths of lines, which was later supplemented by those of Rowland in 1887, obtained with the aid of a concave reflection grating. Langley's invention of the bolometer in 1881 extended spectral measurements to the infrared region while Schumann in 1893 devised spectrographs for use in the vacuum ultraviolet region.

At first, spectroscopy was mainly an analytical tool. Balmer showed in 1885 that there is a simple numerical relationship between the wavelengths of the emission lines of the hydrogen atom. This work was extended by Rydberg, Ritz, Runge, and Schuster to include the lines of many other elements, but a proper theoretical basis for the subject only appeared with the development of quantum mechanics in the nineteen-twenties. Since then spectroscopy and quantum mechanics became closely interlinked, enabling modern spectroscopic theory to develop.

In the 1920s, attention turned to the spectra of diatomic molecules, the theoretical foundations for their study being laid by Hund, Mulliken, and Van Vleck, among others. Later on considerable attention has been given to spectroscopy of polyatomic molecules and ions as a means of elucidating their structures and dynamics.

Radar techniques developed in wartime opened up the new field of microwave and radio frequency spectroscopy. Microwave spectroscopy has led to an accurate determination of geometries of a large number of simple polyatomic molecules. Other important related developments are electron spin resonance and nuclear magnetic resonance spectroscopy, the latter providing valuable information concerning the neighborhood forces and interactions to which a given atom in a molecule or crystal is subjected.

1.3 The Element Praseodymium

In 1841 Mosander extracted the rare earth didymium from lanthanum; in 1879, Lecoq de Boisbaudran isolated a new earth, samaria, from didymia obtained from the mineral samarskite. Six years later, in 1885, von Welsbach separated didymium into two others, praseodymium and neodymium, which gave salts of different colors.

Praseodymium is soft, silvery, malleable, and ductile. It is somewhat more resistant to corrosion in air than europium, lanthanum, cerium, or neodymium, but it does develop a green oxide coating that falls off when exposed to air. As with other rare-earth metals, it should be kept under a light mineral oil or sealed in plastic.

Misch metal, used in making cigarette lighters, contains about 5% praseodymium metal. The rare-earth oxides, including Pr_2O_3 are among the most refractory substances known.

Along with other rare earths, it is widely used as a core material for carbon arcs used by the motion picture industry for studio lighting and projection. Salts of praseodymium are used to colour glasses and enamels; when mixed with certain other materials, praseodymium produces an intense and unusually clean yellow colour in glass. Didymium glass, of which praseodymium is a component, is a colorant for welders goggles.

The naturally occurring praseodymium is composed of one stable isotope ^{141}Pr with nuclear spin $I = 5/2$ and Z=59. Its nuclear electromagnetic moments are as follows: the magnetic dipole moment $\mu_I = 4.2754$ (5) μ_N [1], the electric quadrupole moment $Q = 0.0024$ b [2]. Two of the radioisotopes of Pr are relatively stable being ^{142}Pr with half life of about 19 hours and ^{143}Pr with half life of 13.57 hours. One of the prominent ^{141}Pr electron configuration with three valance electrons inside the 4f shell is [Xe] $4f^3\ 6s^2$. The lowest term of this configuration is ^4I, where $^4I_{9/2}$ corresponds to the electronic ground state of ^{141}Pr.

1.4 History of Spectral and Hyperfine Investigations of Pr I

In 1929, H. E. White [3] published an article devoted to the study of hyperfine spectra in ionized Pr atoms. In this study, he investigated fine-structure components of 173 spectral lines out of which, about one hundred lines were seen to consist of six hyperfine components. From this he assigned an angular momentum $i = (5/2)(h/2\pi)$ to the nucleus of Pr atom. Brix [4] in 1953 further extended the work of White and determined the magnetic hyperfine interaction constant $a_{6s} = 0.416 \pm 0.015$ for the 6s electron in the configuration $4f^3\ (^4I)\ 6s$. By the application of formula of Goudsmith and Fermi Segre, he also calculated a value $\mu(Pr^{141}) = 3.9 \pm 0.3$ nuclear magnetons for nuclear moment.

The hyperfine structure of the ground multiplet ($4f^3\ 6s^2\ ^4I_{9/2}$) was first studied in 1953 by Lew [5] using atomic beam magnetic resonance method. He determined nuclear spin, total electronic angular momentum and g_J value of ground state. J. M. Baker and B. Bleaney [6] in 1955 investigated the hyperfine structure of Pr lines and calculated the hyperfine structure constants of the level involved. K. Murakawa [7] in 1960 classified three lines in the spectrum of Pr I and measured their hyperfine structure from which he determined the interval factor of the level $4f^3\ 6s^2\ ^4I_{11/2}$. Y.C. Amado et al. [8] in 1962 studied the hyperfine structure of ^{142}Pr in the electronic ground state $^4I_{9/2}$ by atomic beam magnetic resonance method. They measured the electronic splitting factor $g_j\ (^4I_{9/2}) = - 0.7322(3)$, nuclear spin $I = 2$, magnetic dipole hyperfine constant $|A| = 67.5(5)$ Mc/Sec, electronic quadrupole hyperfine constant $|B| = 70.0(2.0)$ Mc/Sec, nuclear moment $|\mu_I| = 0.297(15)$ nm and $|Q| = 0.035(15)$ b. In 1973 R. Zalubus et al. [9] measured energy levels of Praseodymium. They observed the spectra of Pr I and Pr II in emission for the range 350 – 120 nm and in absorption for the range 200 - 870 nm. They reported three lowest levels of $4f^3\ 6s^2\ ^4I_{9/2}$ ground term. These three levels combine with 62 high even levels, accounting for 150 lines. J. Reader and J. Sugar [10] in 1964, studied the nuclear moment of Pr^{141} from the hyperfine structure of doubly ionized Pr. They calculated the probability density of the 6s electron at the nucleus and the quantum difference for the configurations $4f^2 6s$ and $4f^2 7s$. They also calculated a value 4.09 ± 0.06 nm for nuclear moment of Pr^{141}. Böklen et al. [2] in 1975 used the same technique as that of Lew et al. but with Ramsey separated field technique, to measure the ground state hyperfine structure to extremely high precision.

A first analysis of fine structure and hyperfine structure of the even configuration of Pr I was presented by Ginibre [11] in 1981 on the base of two configuration system ($4f^2 5d6s^2$ and $4f^2 5d^2 6s$) restricted to the lower energy range, where the mixing effect with other excited configurations are rather small. In 1981, Childs and Goodman [12] published their

results of precise measurements of the hyperfine structure of metastable levels obtained with the method of the laser radiofrequency double resonance on an atomic beam, which allowed more precise determination of magnetic dipole and electric quadrupole moments of the Pr nucleus. In 1982, R. M. Macfarlane et al.[1] measured the nuclear magnetic moment of ^{141}Pr to be $\mu_I = 4.2754\ (5)\mu_N$ and in 1985 K.T. Cheng and W. J. Childs [13] determined the electric quadrupole moment of Pr and found a value $Q = 0.066$ b. Reddy and Rao [14] in 1988 investigated the Pr I and Pr II spectra in the range of 576 - 625 nm and obtained the information of the hyperfine structure of four spectral lines by using optogalvanic spectroscopy. They also identified about 78 atomic transitions of Pr I and 43 transitions of Pr II. In 1988 A. Ginibre, in addition to her published work [11, 15-17], discovered lot of new lines both in Pr I and Pr II which were never published. This work is now part of her Ph.D thesis [18].

In 1996, T. Kuwamoto et al. [19] investigated the hyperfine structure of neutral praseodymium by means of the atomic beam laser spectroscopy. They reported hyperfine structure of 34 atomic transitions in the wavelength range from 544 - 596 nm and determined the hyperfine constants A and B for 57 levels. They determined the energies and electronic angular momenta of 11 fine structure for the first time. In 1997 A. Krzykowski et al. [20] determined the values of hyperfine structure of the lower levels belonging to the configuration of $4f^3 5d6s$ by using the method of laser induced fluorescence spectroscopy. In continuation to the previous experimental results, J. Ruczkowski et al. [21] in 2003 analyzed the hyperfine structure in the even configuration system $4f^2 5d6s^2 + 4f^2 5d^2 6s + 4f^3 6s6p + 4f^3 5d6p + 4f^2 5d^3$ by applying a semi-empirical method. The hyperfine structures of 546 energy levels have been interpreted.

In 1998 M. Song et al. [22] measured the lifetimes of low lying states in neutral Pr atoms and calculated the 14 new lifetimes of Pr I by monitoring the time-resolved fluorescence from the studied excited state. In 2006, Furmann et al. [23] reported 57 new electron levels of odd parity in Pr I in spectral range 560 - 590 nm. These levels have been found on the basis of an analysis of hitherto unclassified spectral line with the method of LIF.

As remarked earlier Praseodymium has five outer electrons, which gives it a high density of levels leading to an extremely line rich spectrum. Using this property of Praseodymium S. Oppel et al. in 2010 [24] performed active frequency stabilization of a diode laser on several lines between 1105 and 1123 nm. Employing the standard laser locking technique, they are able to eliminate the frequency drift of the unlocked laser of more than 30 MHz/h and achieved the laser frequency stability to within 1.4(1) MHz for averaging times > 0.2s.

In 2011, B. Gamper et al. [25] reported the recording of new highly resolved Fourier Transform (FT) spectrum of the neutal praseodymium atom. With the help of this new FT spectrum 1194 lines were classified as transitions between energy levels of Pr I atom and 19 as transitions of the Pr II. They also reported 23 new atomic energy levels of odd parity and one of even parity.

1.5 History of Spectral and Hyperfine Investigations of Pr II and Pr III

Praseodymium, like other elements in the rare earth group (Lanthanides), has a very complex energy spectrum. This is also true in all of its ionization stages. Furthermore the spectra of singly ionized atoms or of higher stages of ionization are difficult to produce as compared to neutral atomic spectrum. Also frequently the strong lines are observed in regions of spectrum where high dispersion apparatus cannot readily be used. Therefore it is not only interesting from the standpoint of atomic physics to investigate the spectra of

neutral atoms or ions of praseodymium but also the spectral lines of Pr II are being extensively investigated from the point of view of other fields in physics specially astrophysics.

H. E. White [3] in 1929 published the investigation of fine and hyperfine structure of singly ionized praseodymium atoms and determined its spin quantum number. He investigated 200 lines in the spectral region 390 - 500 nm exhibiting the complex structure and measured the component separation for 33 of those lines. At that time the insufficient resolution was the major hurdle in the measurement of the wave numbers of the involved energy levels. It could only be realized when in 1941 Rosen et al. [26] using their high resolution Zeeman Effect data for praseodymium that the wavenumbers of the levels of Pr II could be determined. They covered the spectral range from 240 - 710 nm. In addition to this, using the resolved Zeeman pattern for 141 lines, they determined the *g* and *J*-values for 74 Pr II levels.

In 1988 using the high resolution data in the range 2783-27920 cm^{-1}, A. Ginibre [16] calculated new energy levels in the odd configuration *4f²5d6p* and in the mixed even configurations *4f²5d²* + *4f²5d6s* + *4f³6p* for singly ionized praseodymium. She also corrected a number of spectral parameters such as energy, *J* and hyperfine splitting of already known 105 odd levels and 187 even levels. Extending her work [17], she further calculated new experimental even levels in the range 5854 - 31654 cm^{-1} of singly ionized praseodymium on the basis of the 3 mixed configurations *4f²5d²* + *4f²5d6s* + *4f³6p*.

In 1990 H. Iimura et al. [27] using the technique of collinear laser ion beam spectroscopy studied the hyperfine structure of Pr II and measured the magnetic dipole and electric quadrupole constants for the investigated transitions. Then in 1991, Kim [28] studied the hyperfine structure of doubly ionized Pr III. In 1994, H. Iimura et al.[29] by means of laser ion beam spectroscopy measured the magnetic dipole moment and electric quadrupole moment of a Pr isotope (Pr^{143}). In 2000, Maosheng Li et al. [30-31] using collinear laser ion beam spectroscopy investigated the atomic spectra of singly ionized praseodymium and neodymium. They measured the hyperfine structure of atomic transition in the wavelength range 560 to 590 nm.

In 2001, S. Ivarsson et al. [32] investigated singly and doubly ionized praseodymium by means of high resolution Fourier transform spectra in the region 280 - 800 nm. They improved the wavelengths of 49 lines and measured *gf*-values for 31 lines by means of branching fractions and lifetimes data. Hyperfine structure pattern of 44 levels was analyzed and magnetic hyperfine constants *A* were determined for 8 odd and 18 even levels. B. Furmann et al. [33] in 2001 discovered experimentally three new low-lying levels of Pr II by using the method of laser induced fluorescence spectroscopy in a hollow cathode discharge. This work also include the investigation of already known levels in the spectral range 562 - 602 nm with the determination of *J*-quantum numbers and *A*-values for the ionic levels.

In 2002 Ma Hong-Liang [34] by using technique of collinear fast-ion-beam laser spectroscopy measured the hyperfine structure of singly ionized lanthanum and praseodymium. Magnetic dipole and electric quadruple coupling constants were also determined for already known levels.

In 2005 B. Furmann et al. [35] investigated the hyperfine structure of singly ionized praseodymium and determined their hyperfine structure constants *A* and *B* using the method of laser induced fluorescence in a hollow cathode discharge. They discovered 42 new electron levels in singly ionized praseodymium which consist of 28 low lying odd levels with *f³* core and 14 even levels.

2 Atomic Structure

The light emitted by an atomic gas, say in a hollow cathode discharge, is due to the distribution and motion of electrons around the nucleus of an atom. The investigation of this light gives information about the electronic structure of the atom which determines the physical and chemical properties of the atom. The discrete spectrum of frequencies of any atom is the characteristic of the periodic motion of electrons, confined to specific positions. Such a motion is referred to as bound motion. Early spectroscopists interpreted the spectra of atoms in terms of models by applying classical laws of mechanics and electrodynamics to the motion of particles with suitably chosen properties. Inspite of this simple and general approach, difficulties of fundamental nature arise such as integral ratios of frequencies which is true for every classical system but is not found in atomic spectra.

In 1911 Lord Rutherford, based on his series of experiments with radioactive alpha-particles, gave revolutionary view of the structure of the atom. He suggested that the atom consisted of a small, dense core of positively charged particles in the center (or nucleus) of the atom, surrounded by a swirling ring of electrons. The nucleus is so dense that the incoming alpha particles bounce off from it, whereas the electrons are so tiny and spread out at large distances that the alpha particles pass through them. Rutherford model of atom resembled that of a solar system and the electrons under the influence of the electrostatic attraction by the nucleus, together with their mutual repulsion, perform complicated planetary motion around the nucleus. But from the laws of classical mechanics and electrodynamics it can easily be inferred that the electron would gradually lose energy by emitting light of continuously increasing frequency and would eventually fall into the nucleus. Thus laws of classical mechanics proved to be insufficient in explaining the spectra or the stability of atoms.

A completely new and more general set of laws were required which led to the development of quantum physics. Bohr and Sommerfeld took the first step in this development of the so called "old quantum theory" and were able explain to a certain extent the spectra and stability of atoms. Bohr-Sommerfeld model accounts for the allowed energies and the spectral frequencies of the atomic one-electron systems. Inspite of this, the model has serious deficiencies and is not complete. Among such deficiencies are

i)   Assignment of quantized angular momentum to atomic states is in highly arbitrary manner i.e. assignment is done merely on the basis that leads to the results which agree with the observations.

ii) No satisfactory explanation is given as to why the accelerating electrons in stable orbits does not radiate. Radiation is assumed to be emitted when the electron jumps from one stable orbit to another.

iii) The model does not explain the mechanism of electron jumps between various stable orbits. As a consequence, the model does not account for the observed intensities of the spectral emission frequency.

iv) Bohr-Sommerfeld model is incapable of giving correct results for atomic systems with more than one electron and is one of the major limitations of the model.

E. Schrödinger, W. Heisenberg and others, following the ideas of L. de Broglie removed the discrepancies in the Bohr-Sommerfeld model and explained the finer details of the internal structure of one-electron as well as many electron atoms. This laid the foundation of quantum mechanics and the development of non-relativistic and later relativistic

quantum mechanics as the theoretical framework for the structure of an atom. The literature consulted for writing chapters 2, 3 and 4 is given in 9.1.

2.1 One Electron Systems

The first quantum mechanical treatment that gave the explanation of the discrete spectra of atomic emission was based on the equation proposed by Schrödinger in 1926. For the calculations of the energy state of one-electron atoms such as H, He^+, Li^{++}, Be^{3+} etc., the time independent Schrödinger equation is written as

$$\hat{H}\psi(r,\theta,\phi) = E\psi(r,\theta,\phi) \tag{2.1}$$

$$\left[-\frac{\hbar^2}{2m}\nabla^2 + V(r)\right]\psi(r,\theta,\phi) = E\psi(r,\theta,\phi) \tag{2.2}$$

where $\hat{H} = \left[-\frac{\hbar^2}{2m}\nabla^2 + V(r)\right]$ is called the quantum mechanical Hamiltonian or total energy operator; in simple systems it is the sum of kinetic energy and potential energy operators. The nucleus of the atom is considered a point charge Ze, where Z is the atomic number of the atom. The motion of electron around the nucleus is primarily governed by the electrostatic potential around the nucleus. Therefore

$$V(r) = -\frac{Ze^2}{4\pi\varepsilon_o r}$$

Furthermore, in order to account for the motion of the nucleus, the reduced mass is used which is given by

$$m = \frac{m_e M}{m_e + M}$$

where M is the mass of the nucleus and m_e is the mass of the electron. Since the potential operator depends only on the scalar distance r of the electron from the nucleus, therefore the wave Eq. (2.2) can be separated in spherical polar co-ordinates. After substituting the Laplacian operator ∇^2 of Eq. (2.2), in spherical polar co-ordinates, the Schrödinger equation can be written as,

$$-\frac{\hbar^2}{2m}\left[\frac{1}{r^2}\frac{\partial}{\partial r}\left(r^2\frac{\partial\psi}{\partial r}\right) + \frac{1}{r^2\sin\theta}\left(\frac{\partial}{\partial\theta}\sin\theta\frac{\partial\psi}{\partial\theta}\right) + \frac{1}{r^2\sin^2\theta}\frac{\partial^2\psi}{\partial\phi^2}\right] + V(r)\psi = E\psi \tag{2.3}$$

The exact solution of the Schrödinger equation for arbitrary atoms is very difficult because of the complex nature of this second order differential equation. However, for some simple systems exact solutions are possible. Otherwise numerical solutions or some approximations are used. One such approximation is the variable separation technique; here one can assume that various motions associated with the systems can be decoupled (like in Born Openheimer approximation applied to molecules). Using this approximation to the atomic system, the eigenfunction can be written as the product of a radial part associated with the radial motion and an angular part associated with its angular

momentum, i.e.

$$\psi_{nlm}(r,\theta,\phi) = R_{nl}(r) Y_{lm}(\theta,\phi)$$

A further separation is also possible:

$$Y_{lm}(\theta,\phi) = \Theta(\theta)\Phi(\phi)$$

These separation lead to three differential equations, one each in the co-ordinates r,θ,ϕ

$$\frac{d^2\Phi}{d\varphi^2} = -m_l^2 \varphi \tag{2.4}$$

$$-\frac{1}{\sin\theta}\frac{d}{d\theta}\left(\sin\theta\frac{d\Theta}{d\theta}\right) + \frac{m_l^2}{\sin^2\theta}\Theta = l(l+1)\Theta \tag{2.5}$$

$$\frac{1}{r^2}\frac{d}{dr}r^2\frac{dR}{dr} - \frac{l(l+1)}{r^2}R - \frac{2m}{\hbar^2}V(r)R + \frac{2mE}{\hbar^2}R = 0 \tag{2.6}$$

where $-m_l^2$ and $l(l+1)$ are separation constants.

The solution of Eq. (2.4) is

$$\Phi = e^{im_l\phi} \tag{2.7}$$

where m_l can have values

$$m_l = 0, \pm1, \pm2, \pm3$$

Integer values for m_l follow from the condition

$$Y(\theta,\phi) = Y(\theta + 2\pi, \phi + 2\pi) \tag{2.8}$$

The solution of equation involving θ is given by

$$\Theta(\theta) = A P_l^{m_l}(Cos\theta) \tag{2.9}$$

where $P_l^{m_l}(\cos\theta)$ is the associated Legendre function and is defined as,

$$P_l^{m_l}(x) = (1-x^2)^{\frac{|m_l|}{2}}\left(\frac{d}{dx}\right)^{|m_l|}P_l(x) \tag{2.10}$$

and $P_l(x)$ is called the Legendre Polynomial, given by Rodrigues formula

$$P_l(x) = \frac{1}{2^l l!}\left(\frac{d}{dx}\right)^l (x^2-1)^l \tag{2.11}$$

It is clear from the Eq. (2.9) that l can only take non-negative integral values otherwise Rodrigues formula $P_l(x)$, which involves the differential operator applied "l" times, does not make sense at all. Moreover, if $|m_l| > l$, then the associated Legendre function $P_l^{m_l}(x)$ is equal to zero and hence, ultimately $\psi(r,\theta,\phi)$ is zero. Therefore no solution exists for $|m_l| > l$. The possible values of m_l are then restricted to the following range,

$$m_l = -l, -l+1, -l+2, \ldots\ldots, l-2, l-1, l$$

8

In order to find the solution for the radial function $R(r)$, the boundary condition that the probability of finding the electron should be zero at infinity, i.e. $R(r) \to 0$ as $r \to \infty$ is employed. This leads to the determination of the energy of the electrons in the nth orbit from the nucleus viz.,

$$E_n = -\frac{e^4 Z^2 m}{2(4\pi\varepsilon_o)^2 \hbar^2 n^2}$$

(2.12)

where n is an integer satisfying the relation $n \geq l + 1$. For positive energies there is no such restriction because for positive energies the electron will no longer be bound to the nucleus. The number n is called the principal quantum number.

Therefore to summarize, electron in an atom is characterized by three quantum numbers i.e. n, l, m_l. For a given value of n, the quantum number l (called the azimuthal quantum number) can take the values 0, 1, 2, …, (n-1) and to each value of l, there correspond ($2l$+1) states, differing by the values of the quantum number m_l which is often called the magnetic quantum number. The energy of an atom in the state n, l, m_l is uniquely determined by the assignment of the principal quantum number and does not depend on l or m_l. Thus, an n^2 –fold degeneracy of levels takes place for a particle in a Coulomb field. For the level n, there are $1+3+5+\ldots+2n\text{-}1 = n^2$ different states, differing in the quantum numbers l and m_l. The independence of m_l in the energy has a simple physical meaning. In a field having central symmetry all directions in space are equivalent and therefore the energy cannot depend on the spatial orientation of the angular momentum. The l degeneracy is a direct result of the Coulomb potential and is peculiar to hydrogen atom. When the spin-orbit interactions and the relativistic effects are taken into account, this degeneracy is partially removed.

2.2 Fine Structure of Atoms

For a hydrogenic atom, the gross structure energy levels only depend on the principal quantum number n. However, a more accurate model takes into account relativistic and spin effects, which break the degeneracy of the energy levels and split the spectral lines. The scale of the fine structure splitting relative to the gross structure splitting is of the order of $(Z\alpha)^2$, where Z is the atomic number and α is the fine-structure constant which gives the strength of electromagnetic interaction i.e. how strongly a charge particle interacts with electromagnetic field, viz.

$$\alpha = \frac{e^2}{\hbar c} = \frac{1}{137.035999679}$$

The fine structure can be separated into three corrective terms: the kinetic energy term, the spin-orbit term, and the Darwinian term. The full Hamiltonian is then given by

$$H = \hat{H}_0 + \hat{H}_{Kinetic} + \hat{H}_{so} + \hat{H}_{Darwinian}$$

2.2.1 Kinetic Energy Relativistic Correction

Classically, the kinetic energy term of the Hamiltonian is:

$$T = \frac{p^2}{2m}$$

However, according to special relativity, the kinetic energy (*i.e.*, the difference between the total energy and the rest mass energy) of a particle of rest mass *m* and momentum *p* is

$$T = \sqrt{p^2 c^2 + m^2 c^4} - mc^2 \qquad (2.13)$$

where the first term is the total relativistic energy, and the second term is the rest energy of the electron. Expanding this gives

$$T = \frac{p^2}{2m} - \frac{p^4}{8m^3 c^2} + \dots\dots \qquad (2.14)$$

The first term on the right-hand side of this equation is the standard non-relativistic expression for the kinetic energy. The second term is the first order relativistic correction to this energy viz.

$$H_{Kinetic} = -\frac{p^4}{8m^3 c^2} \qquad (2.15)$$

In comparison to $\frac{p^2}{2m}$, $H_{Kinetic}$ is smaller by a factor of $\frac{p^2}{m^2 c^2} = \frac{v^2}{c^2} \approx (Z\alpha)^2$. It is of the order of 0.1 cm^{-1}.

The energy corrections ΔE_1 due to relativistic effects can be calculated in first-order perturbation theory as:

$$\Delta E_1 = \left\langle nlm_l \left| -\frac{\hat{p}^4}{8m^3 c^2} \right| nlm_l \right\rangle$$

$$= -\frac{1}{8m^3 c^2} \left\langle nlm_l \left| \hat{p}^4 \right| nlm_l \right\rangle$$

$$= -\frac{1}{8m^3 c^2} \left\langle nlm_l \left| \hat{p}^2 \hat{p}^2 \right| nlm_l \right\rangle \qquad (2.16)$$

Since the unperturbed Hamiltonian $\hat{H}_0$ is

$$\hat{H}_0 = \frac{\hat{p}^2}{2m} - \frac{Ze^2}{4\pi\varepsilon_o r}$$

$$\hat{p}^2 = 2m\left(\hat{H}_0 + \frac{Ze^2}{4\pi\varepsilon_o} \frac{1}{r} \right) \qquad (2.17)$$

By using Eq. (2.17) in Eq. (2.16)

$$\Delta E_1 = -\frac{1}{8m^3 c^2} \left\langle nlm_l \left| 4m^2 \left(\hat{H}_0 + \frac{Ze^2}{4\pi\varepsilon_o} \frac{e^2}{r} \right)^2 \right| nlm_l \right\rangle$$

$$= -\frac{1}{2mc^2}\left[E_n^2 + 2E_n\left(\frac{Ze^2}{4\pi\varepsilon_o}\right)\left\langle\frac{1}{r}\right\rangle_{nlm_l} + \left(\frac{Ze^2}{4\pi\varepsilon_o}\right)^2\left\langle\frac{1}{r^2}\right\rangle_{nlm_l}\right] \qquad (2.18)$$

To complete the evaluation of ΔE_1, the expectation values of $\left\langle\frac{1}{r}\right\rangle$ and $\left\langle\frac{1}{r^2}\right\rangle$ are required viz.

$$\left\langle\frac{1}{r}\right\rangle_{nlm_l} = \frac{1}{a_0 n^2} \qquad (2.19)$$

$$\left\langle\frac{1}{r^2}\right\rangle_{nlm_l} = \frac{1}{a_0^2}\cdot\frac{1}{n^3(l+1/2)} \qquad (2.20)$$

Each of which can be expressed in terms of E_n i.e.,

$$\left\langle\frac{1}{r}\right\rangle_{nlm_l} = -2\left(\frac{4\pi\varepsilon_o}{e^2}\right)E_n \qquad (2.21)$$

$$\left\langle\frac{1}{r^2}\right\rangle_{nlm_l} = 4\frac{n}{(l+1/2)}\left(\frac{4\pi\varepsilon_o}{e^2}\right)^2 E_n^2 \qquad (2.22)$$

Inserting Eq.(2.21) and (2.22) in Eq.(2.18)

$$\Delta E_1 = -\frac{E_n^2}{2mc^2}\left[-3+\frac{4n}{(l+1/2)}\right] \qquad (2.23)$$

Because $E_n = -\frac{1}{2}mc^2\frac{(Z\alpha)^2}{n^2}$

$$\Delta E_1 = -E_n\frac{(Z\alpha)^2}{n^2}\left[\frac{3}{4}-\frac{n}{(l+1/2)}\right] \qquad (2.24)$$

2.2.2 Spin-Orbit Correction

The spin-orbit correction term arise as a result of the interaction between the spin and orbital motion of the electron. The interaction is basically between the magnetic field generated by the orbital and the spinning motions of electron.

The correction term for spin-orbit coupling in the Hamiltonian is given by

$$H_{so} = \xi(r)\vec{L}\cdot\vec{S} \qquad (2.25)$$

where

$$\xi(r) = \frac{1}{2m^2c^2}\frac{1}{r}\frac{dV}{dr}$$

In this case $V = -\frac{Ze^2}{(4\pi\varepsilon_o)r}$

11

So that

$$\xi(r) = \frac{1}{2m^2c^2} \frac{Ze^2}{4\pi\varepsilon_o} \frac{1}{r^3} \qquad (2.26)$$

Total angular momentum $\vec{J}$ can be constructed as the sum of the orbital angular momentum $\vec{L}$ and spin angular momentum $\vec{S}$, i.e.

$$\vec{J} = \vec{L} + \vec{S} \qquad (2.27)$$

squaring this vector sum gives

$$J^2 = \vec{J}.\vec{J} = (\vec{L}+\vec{S}).(\vec{L}+\vec{S}) \qquad (2.28)$$

$$J^2 = L^2 + S^2 + 2\vec{L}.\vec{S} \qquad (2.29)$$

$$\vec{L}.\vec{S} = \frac{(J^2 - L^2 - S^2)}{2} \qquad (2.30)$$

so the spin-orbit Hamiltonian becomes

$$H_{so} = \xi(r)\frac{(J^2 - L^2 - S^2)}{2} \qquad (2.31)$$

The energy shift due to spin-orbit interaction is given by

$$\Delta E_2 = \left\langle \hat{H}_{so} \right\rangle$$

$$\Delta E_2 = \left\langle jm_j ls \left| \xi(r)\frac{(J^2 - L^2 - S^2)}{2} \right| jm_j ls \right\rangle$$

$$\Delta E_2 = \left\langle \xi(r) \right\rangle \left\langle jm_j ls \left| \frac{(J^2 - L^2 - S^2)}{2} \right| jm_j ls \right\rangle$$

$$\Delta E_2 = \frac{1}{2m^2c^2} \frac{Ze^2}{4\pi\varepsilon_o} \left\langle \frac{1}{r^3} \right\rangle_{nl} \frac{\hbar^2}{2} \left[j(j+1) - l(l+1) - s(s+1) \right] \qquad (2.32)$$

The expectation value of $1/r^3$ is given by

$$\left\langle \frac{1}{r^3} \right\rangle_{nl} = \frac{Z^3}{a_0^3 n^3 l(l+1/2)(l+1)} \qquad (2.33)$$

Using Eq. (2.33) in Eq. (2.32) and after doing some mathematical manipulation, the final results is

$$\Delta E_2 = -E_n \frac{(Z\alpha)^2}{2n} \left[\frac{j(j+1) - l(l+1) - 3/4}{l(l+1/2)(l+1)} \right] \qquad (2.34)$$

12

Because j can take on the values $l \pm 1/2$, the correction in terms of l can be written as

$$\Delta E_2 = - E_n \frac{(Z\alpha)^2}{2n(l+1/2)(l+1)} \qquad \text{for} \quad j = l+1/2$$

$$\Delta E_2 = E_n \frac{(Z\alpha)^2}{2n(l+1/2)} \qquad \text{for} \quad j = l-1/2 \qquad (2.35)$$

Thus, as for the relativistic kinetic energy correction, the spin-orbit interaction produces a correction that is $(Z\alpha)^2$ times the Bohr energy.

For $l = 0$, the spin-orbit interaction vanishes and therefore $\Delta E_2 = 0$ in that case.

2.2.3 Darwin Term

The Darwin term appears for the s-orbital due to a phenomenon in Dirac theory called *Zitterbewegung*, where the electron does not move smoothly but instead undergoes extremely small-scale fluctuations, causing the electron to see a smeared-out Coulomb potential of the nucleus. The Hamiltonian for the Darwin term is given by

$$\hat{H}_D = \frac{\pi \hbar^2}{2m^2 c^2} \left(\frac{Ze^2}{4\pi \varepsilon_o} \right) \delta(r)$$

And the first-order correction to the energy due to the Darwin Hamiltonian is

$$\Delta E_3 = \left\langle nlm_l \middle| \hat{H}_D \middle| nlm_l \right\rangle$$

$$\Delta E_3 = \frac{\pi \hbar^2}{2m^2 c^2} \left(\frac{Ze^2}{4\pi \varepsilon_o} \right) \left\langle nlm_l \middle| \delta(r) \middle| nlm_l \right\rangle \qquad (2.36)$$

Because of the δ-function, the expectation value of ΔE_3 will be non-zero only for s-states because all radial wavefunctions vanish at $r = 0$ except those having $l = 0$

$$\Delta E_3 = \frac{\pi \hbar^2}{2m^2 c^2} \left(\frac{Ze^2}{4\pi \varepsilon_o} \right) \left\langle n00 \middle| \delta(r) \middle| n00 \right\rangle$$

$$\Delta E_3 = \frac{\pi \hbar^2}{2m^2 c^2} \left(\frac{Ze^2}{4\pi \varepsilon_o} \right) \cdot \frac{1}{\pi a_0^3 n^3}$$

$$\Delta E_3 = -E_n \frac{(Z\alpha)^2}{n}, \qquad \text{for } l = 0 \qquad (2.37)$$

2.2.4 The Lamb Shift (Radiative Correction)

The lamb shift or radiative correction is similar in nature as Darwin term and results due to vacuum or zero-point fluctuations of the quantized electromagnetic field. Due to these fluctuations, a shift in the position of electrons occur. The shift in the position of electron is given by

$$\left\langle (\delta x)^2 \right\rangle \approx \frac{2\alpha}{\pi} \left(\frac{\hbar}{mc} \right)^2 \log \frac{1}{\alpha Z} \tag{2.38}$$

and the Lamb shift in energy is given by

$$\Delta E_4 \approx \frac{4}{3\pi} \frac{mc^2 Z^4 \alpha^5}{n^3} \log \frac{1}{\alpha Z} \delta_{l,0} \tag{2.39}$$

For hydrogen, the Lamb shift is $\Delta \approx 660$ MHz from $2^2S_{1/2}$ towards $2^2P_{1/2}$. As compared to Darwin term, the radiative corrections are smaller by a factor of $\alpha \log (1/\alpha)$.

2.3 The Total Fine-Structure Correction

Because the Darwin correction to the Bohr energy can be included in the spin-orbit correction term, the total fine-structure correction can be written as

$$\Delta E_{FS} = \Delta E_1 + \Delta E_2 \tag{2.40}$$

If $l = 0$ then ΔE_2 in Eq. (2.36) represents the Darwin term.

$$\Delta E_{FS} = E_n \frac{(Z\alpha)^2}{n^2} \left[\frac{n}{(l+1)} - \frac{3}{4} \right] \qquad \text{For} \quad j = l+1/2$$

$$\Delta E_{FS} = E_n \frac{(Z\alpha)^2}{n^2} \left[\frac{n}{l} - \frac{3}{4} \right] \qquad \text{For} \quad j = l-1/2 \tag{2.41}$$

Because the maximum value of l is $(n-1)$, it is clear that the terms in square brackets in Eq. (2.41) can never be negative. Therefore, because E_n is intrinsically negative, the fine structure corrections will always lower the Bohr energy.

Using $j = l \pm 1/2$, Eq. (2.41) can be written in terms of j, viz.,

$$\Delta E_{FS}(n, j) = E_n \frac{(Z\alpha)^2}{n^2} \left[\frac{n}{(j+1/2)} - \frac{3}{4} \right] \qquad \text{For} \quad j = l \pm 1/2 \tag{2.42}$$

Although the three separate contributions depend on l but the total shift in energy, ΔE_{FS}, depends only on j, the total angular momentum quantum number.

2.4 Fine Structure Splitting

The non-relativistic energy levels E_n are $2n^2$ times degenerate, the factor of 2 arises due to spin of electrons. This degeneracy is partly removed by Dirac theory of relativistic treatment of electronic levels. According to Dirac theory, the non-relativistic levels E_n depending on the principal quantum number n splits into n sublevels, one for each value of total angular momentum $(j = l + s)$ quantum number $j = 1/2, 3/2, \ldots n$-1/2. This splitting is called '*fine structure splitting*', and n levels $j = 1/2, 3/2, \ldots n$-1/2 are said to form a '*fine structure multiplet*'. The dimensionless constant $\alpha \cong 1/137$ controls the scale of splitting and it is for this reason that it has been named as fine structure constant. All three

14

relativistic corrections, i.e. H_r, H_{so}, H_D, contribute to the fine structure splitting but for the most part, the dominant is the spin-orbit correction.

2.5 The Central Field Approximation

Schrödinger's equation (both relativistic and non relativistic) are single particle equations i.e. they can only model the dynamics of a single particle. In a one electron system, one only needs to take into account the interaction between the electron and the nucleus. However, in a multielectron system the interaction with other electrons within the system must also be considered.

In moving from one electron systems to N electron systems, the following interaction must be taken into account:

- The kinetic energy of the electrons and their potential energy in the electrostatic field of the nucleus.

- The electrostatic force of repulsion between electrons within the atom.

- The magnetic interactions of the electronic spin with their orbital motion.

- Small effects such as spin-spin interactions between the electrons, the relativistic effects, radiative corrections and nuclear corrections.

The Hamiltonian of an N electron system is thus given as:

$$H = \sum_{i=1}^{N}\left(-\frac{\hbar^2}{2m}\nabla_i^2 - \frac{Ze^2}{4\pi\varepsilon_o r_i}\right) + \frac{1}{2}\sum_{i\neq j}^{N}\frac{Ze^2}{4\pi\varepsilon_o r_{ij}} + \sum_i \xi(r_i)\left(\vec{l_i}.\vec{s_i}\right) \qquad (2.43)$$

where r_i denotes the relative co-ordinates of the electron i with respect to the nucleus, $r_{ij} = |r_i - r_j|$. The first sum in Eq. (2.43) is the single-particle Hamiltonian, the second is the mutual interaction between electrons, also known as the electrostatic interaction, and the last is the spin-orbit interaction.

The most important and fundamental aspect of a multielectron atom is the electron-electron non-symmetrical interactions and fermionic nature of electrons as indistinguishable particles. In this case Schrödinger equation cannot be separated into radial and angular part as is possible in one-electron atom. Calculations of energy eigenvalues and eigenfunctions become much more complicated and require intensive mathematical operations. Even for a simplest case of a multielectron atom, namely the two-electron He atom, an exact theoretical treatment is not possible.

To circumvent these difficulties either numerical methods or approximate models are used for such calculations. One such approximation is the Central Field Approximation in which all electron-electron and electron-nucleus interactions are averaged together to produce an effective field and any arbitrarily chosen electron e_i moves in this effective field, that is independent of the momentary location of the other electrons. The effective field is different for each of the electrons and the field must be computed self-consistently for all the electrons. This approximation reduces the multielectron problem into one electron problem which could be solved relatively with less complexity. In order to compute effective field V_c Hartree-Fock methods or self-consistent field approach is used. The method is based on a supposition of a trial centrally symmetric field which then could be

plugged into Schrödinger equation. The solution of Schrödinger equation results in energy eigenvalues and eigenfunctions.

2.6 Angular Momentum Coupling Schemes

In many electron atoms, for example an atom containing N electrons, there are more than two elementary angular momenta i.e. N orbital angular momenta l_i and N intrinsic spin momenta s_i. Therefore under different circumstances the order in which the momenta are coupled together can be chosen in many different ways and any specific choice is known as a *coupling scheme*. The eigenstates constructed for the total angular momentum out of the eigenstates of the separate angular momenta will correspond most closely to the various physical states of the atom if the coupling scheme used corresponds to the coupling of successive momenta in the order of decreasing strength of the various interactions.

Generally, the coupling schemes depend on many features. In central field approximation approach two broad limits can be set by considering the relative magnitudes of the last two terms in the many electrons Hamiltonian given in Eq. (2.43). These two terms describe two distinct interactions between the electrons: (i) residual electrostatic and (ii) spin–orbit. When residual electrostatic interaction between electrons is large compared with the spin orbit interaction, the electrons couple according to the *LS* or Russell-Saunders [36] coupling scheme. At the other extreme end in the central field approximation is the case in which the spin-orbit interaction is large compared with the residual electrostatic interaction. The electrons then couple according to coupling scheme known as *jj*-coupling.

The ground state is usually well represented by *LS*-coupling whereas *jj*-coupling is dominated in atoms where one electron is in highly excited, for example in a Rydberg state. When neither dominates, an intermediate coupling scheme must be employed which can occur for low-lying excited states of heavy atoms.

(i) LS-Coupling

If the physical coupling conditions existing in the atom closely approximate LS-coupling conditions i.e. when the residual electrostatic interaction is large compared to spin-orbit interaction, then the individual $\vec{l}_i$ are to be thought of as precessing rapidly in some complicated manner about the resultant $\vec{L}$, and the individual $\vec{s}_i$ similarly as precessing about their resultant $\vec{S}$. Neglecting all other interactions except the residual Coulomb interactions, then $\vec{L}$ and $\vec{S}$ are constants of the motion. The coupling of the total orbital angular momentum, $\vec{L}$ and the total spin, $\vec{S}$ give rise to the total electronic angular momentum $\vec{J}$. The maximum and minimum value of J are $\left|\vec{J}+\vec{S}\right|$ and $\left|\vec{J}-\vec{S}\right|$, respectively. The electrostatic interaction usually dominates in low-lying states of light atoms where the electron(s) in the outer shell interact strongly with electrons in the inner shells known as the core. This coupling scheme is often appropriate for the ground states of atoms as well.

The electrostatic Coulomb repulsions affect only the orbital angular momenta and not the spins. Therefore it is appropriate first to couple together all the individual orbital angular momenta and the spin momenta. This gives the total orbital angular momentum i.e.,

$$\vec{L}=\sum_{l}\vec{l}_i \quad \text{and} \quad \left|\vec{L}\right|=\sqrt{L(L+1)}\hbar \tag{2.44}$$

and the individual spins add together to give the total spin momentum i.e.

$$\vec{S} = \sum_i \vec{s}_i \quad \text{and} \quad \left|\vec{S}\right| = \sqrt{S(S+1)}\hbar \qquad (2.45)$$

of the atomic states. Therefore the total angular momentum of the electron shell is given by

$$\vec{J} = \vec{L} + \vec{S} \quad \text{and} \quad \left|\vec{J}\right| = \sqrt{J(J+1)}\hbar \qquad (2.46)$$

The wave functions and the quantum states can be decribed in terms of four good quantum numbers L, S, M_L and M_S. Physically, however, the vectors $\vec{L}$ and $\vec{S}$ are always coupled together by weak spin-orbit interactions and precess about their resultant $\vec{J}$. Precession is taking place sufficiently slowly such that the magnitudes of $\vec{L}$ and $\vec{S}$ are well-defined and sum of the z-components $(M_J = M_L + M_S)$ is defined. Now the quantum states are described in terms of four quantum numbers L, S, J and M_J.

(ii) jj Coupling

With increasing atomic number Z, the spin-orbit interactions become more dominant and in the limit in which these interactions become much stronger than the Coulomb repulsion, the coupling conditions approach the pure *jj*-coupling scheme. The reason for its being so named is that if the residual electrostatic interaction between electrons is neglected, the electrons move quite independently of each other in a central field, each electron separately being subjected to a spin-orbit interaction. For example in a situation in which the two electrons are sufficiently far from each other such that the electrostatic interaction between them is weak then only their total electronic angular momenta, *j*, are constants of the motion because there are no torques on one electron due to the others. This is most often the case when the excited electron is in a high *n* state and thus spends most of its time far from the others confined to the core near the nucleus.

Initially $\vec{l}_i$ and $\vec{s}_i$ of individual electrons couple to form the resultant angular momentum

$$\vec{j}_i = \vec{l}_i + \vec{s}_i \qquad (2.47)$$

Then the vectors $\vec{j}_i$ of different electrons couple together to give total angular momentum vector $\vec{J}$ of the atomic state, given by,

$$\vec{J} = \sum_i \vec{j}_i \qquad (2.48)$$

For example for two electron system, $\vec{j} = \vec{j}_1 + \vec{j}_2$. The possible values of *j* lie between $\left|\vec{j}_1 + \vec{j}_2\right|$ and $\left|\vec{j}_1 - \vec{j}_2\right|$.

In vector atom model each $\vec{l}_i$ and $\vec{s}_i$ process rapidly about their resultant $\vec{j}_i$ and afterwards application of the residual electrostatic interaction acting as a small perturbation causes a

slower precession of $\vec{j}_i$ about their resultant $\vec{J}$ which is a constant of motion in both *LS* and *jj*-coupling schemes. But in the *jj*-coupling scheme *L* and *S* have no meaning.

The manifold of *J* values and the total number of quantum states are the same in all coupling scheme. There are many situations for which neither *LS*- nor *jj*-coupling scheme are valid approximations. In such cases the Coulomb repulsion and the spin-orbit interaction for each value of *J* is diagonalized. The coupling is then said to be intermediate.

2.7   Electronic Configuration in an N-electrons System

For any given value of *n* (principle quantum number) there are *n* possible values of *l* (the azimuthal quantum number), for each value of *l* there are $2l + 1$ values of m_l and for each of these there are two possible values of m_s. The total number of electrons in state *n* is thus $2n^2$. Different states within an atom are denoted by the *s, p, d, f.....,* after *f* the sequence become alphabetical. The first four alphabets do not have any theoretical interpretation; they are historically named after the first series identified in the spectra of the alkali metals: **s**harp, **p**rincipal, **d**iffuse and **f**undamental.

These alphabets correspond to 0, 1, 2, 3… values of the azimuthal quantum number respectively. The principle quantum number is written as the co-efficient of the alphabetical symbol while the number of electrons in each is written as its power.

As one move from lower level states to higher lying levels (in terms of energy), the orbital start overlapping each other; a situation called configuration mixing or configuration interaction. Since the parity is a good quantum number, configuration mixing takes place only within configurations of same parity.

3 Hyperfine Structure

The term **Hyperfine structure** refers to a collection of different effects leading to small shifts and splittings in the energy levels of atoms, molecules and ions. The name is a reference to the **fine structure** which results from the interaction between the magnetic moments associated with the electron spin and the electrons orbital angular momentum. Hyperfine structure, with energy shifts typically orders of magnitude smaller than the fine structure, results from the interactions of the nucleus with the internally generated electric and magnetic fields.

In 1924, Pauli suggested that many nuclei have an angular momentum, which is characterized by quantum number I and associated with it a magnetic dipole moment μ_I which is of the order of 1000 times smaller than a Bohr magneton. The interaction of this moment with the magnetic field produced by the valance electrons causes a small splitting of the energy levels of an atom and provides the largest contribution to the observed hyperfine structures.

Anomalies in the spacing of these hyperfine structures later led to the discovery of an electrostatic interaction due to the deviations of nuclear charge distribution from spherical symmetry which can be expressed as quadrupole moment Q.

Different isotopes of an element have generally different values of I, μ_I and Q and shows different hyperfine structures. But also the centres of gravity of these hyperfine structures are often found to be displaced relative to one another. This isotopic shift is most easily observed in isotopes where the nuclei having no spin and therefore the energy levels show no hyperfine structure.

Isotopic shifts are due to two entirely different causes. The difference in the nuclear mass for different isotopes gives rise to a shift which is appreciable for the lighter elements but decreases rapidly with increasing atomic weight. The larger isotopic shifts observed in heavy elements are caused by the finite size of the nuclear charge distribution which differs for different isotopes and causes a slightly different electrostatic field to act on the electrons in the immediate vicinity of the centre of attraction (due to differences in the charge distribution of the nucleus for different isotopes). The study of these volume- or field-effects has contributed to the knowledge of the size and shape of nuclei. The quantity which governs the isotopic shift is the second radial moment of the nuclear charge distribution. This quantity is called "nuclear mean square charge radius", and can be considered as a monopole moment of the nucleus.

3.1 Nuclear Magnetic Moments

The magnetic moment of a nucleon is made up of the orbital and spin angular momenta

$$\mu = g_l l + g_s s \tag{3.1}$$

The orbital magnetic moment of a proton is defined by the formula

$$\mu = \frac{e\hbar}{2m_p c} l, \tag{3.2}$$

where m_p is the mass of the proton.

The magnetic moments of nuclei is usually express in nuclear magnetons, i.e. in the units

$$\frac{e\hbar}{2m_p c} = \left(\frac{m}{m_p}\right)\mu_o \qquad (3.3)$$

In term of these units the factor g_l for a proton equals unity and neutrons with zero electric charge has $g_l = 0$.

The intrinsic magnetic moment of a proton is directed along the spin and its experimentally measured value is $g_s = 5.58$. The intrinsic magnetic moment for a neutron is directed against the spin and $g_s = -3.82$. Thus,

$$\text{Proton:} \qquad g_s = 5.58, \qquad g_l = 1, \qquad (3.4)$$

$$\text{Neutron:} \qquad g_s = -3.82, \qquad g_l = 0$$

In the framework of the independent-particle model, the operator of the magnetic moment of the nucleus is defined by the sum of single-nucleon operators i.e.

$$\mu = \Sigma\left(g_l l + g_s s\right). \qquad (3.5)$$

The mean value of Eq. (3.5) in a state with a given value of nuclear spin I is directed along I, therefore $\langle\mu\rangle$ can be expressed in terms of I

$$\langle\mu\rangle = g_I I . \qquad (3.6)$$

The factor g_I in Eq. (3.6) is called the gyromagnetic ratio. To find g_I, it is necessary to calculate the matrix element of one of the components of μ, for example

$$\langle \gamma I m_I | \mu_z | \gamma I m_I \rangle = \langle \gamma I m_I | \Sigma\left(g_l l_z + g_s s_z\right)| \gamma I m_I \rangle \qquad (3.7)$$

The matrix element Eq. (3.7) is proportional to m_I. Therefore, taking $m_I = I$, we obtain

$$g_I = \frac{1}{I}\langle \gamma I | \Sigma\left(g_l l_z + g_s s_z\right)| \gamma I \rangle \qquad (3.8)$$

The magnitude g_I essentially depends on how the angular momenta l and s of the nucleus add up to the total angular momentum I. In the jj-coupling approximation the following scheme of addition of angular momenta occurs:

$$l_a + s_a = j_a, \qquad \Sigma_a j_a = J .$$

Just as an atom, closed shells do not contribute to the nuclear spin, and so it is sufficient to take into account only the nucleons outside the closed shells. The ground state of a nucleus is always a state for which there is the maximum possible number of closed pairs j^2 with an angular momentum equal to zero. Thus, if the nucleus contains an even numbers of protons and even number of neutrons (even-even nuclei), the spin of the nucleus I and magnetic moment μ are equal to zero. If the number of neutrons and the number of protons are both odd (odd-odd nuclei), the protons and neutrons being in the states with identical values of

20

j and the same parity, then *I = 2j*. If the number of protons is even and the number of neutrons is odd (even-odd nuclei), the spin of the nucleus is same as the angular momentum of the neutron $j_{(N)}$. On the contrary if the number of protons is odd and the number of neutrons is even (odd-even nuclei), the nuclear spin $I = j_{(P)}$. Thus, for even-odd and odd-even nuclei the spin and magnetic moment of the nucleus are determined by the last unpaired particle,

$$I = J, \quad \mu = g_I I = g_j j.$$

This shows that the magnitude of the magnetic moment of a nucleus essentially depends on the particular features of the construction of the nucleus. For this reason the measurement of magnetic moments of nuclei enables one to obtain valuable information about the nuclear structure.

3.2 Magnetic Dipole Interaction

The motion of the electrons produces a magnetic field $\vec{B}_e$ at the nucleus, which interacts with the nuclear magnetic moment $\vec{\mu}_I$. Consideration of the classical energy of orientation in the field, allows the Hamiltonian describing this interaction to be written in the form:

$$H_\mu = -\vec{\mu}_I . \vec{B}_e \qquad (3.9)$$

It is assumed that this term can be treated as a small perturbation when compared with the zeroth-order Hamiltonian, H_0, which describes the central electrostatic field of atom, the repulsion between electrons, and the spin orbit interaction. Considering only the effects of H_μ on the states labeled by the quantum numbers (γLSJ). It follows that *J* and *I* are good quantum numbers and that the nuclear magnetic moment may be written in the form

$$\vec{\mu}_I = g_I \mu_N \vec{I} \qquad (3.10)$$

where g_I is the nuclear g-factor and $\mu_N = \dfrac{e\hbar}{2M}$ is the nuclear magneton which depends on the proton mass *M*. The sign adopted in Eq. (3.10) differs from that of the corresponding equation for the electronic magnetic moments because the nucleus is positively charged.

The nuclear magnetic moment of the atom, μ_I, is defined as the largest observable component of $\vec{\mu}_I$:

$$\mu_I = \left\langle I, m_I = I \middle| \mu_z \middle| I, m_I = I \right\rangle = g_I \mu_N I \qquad (3.11)$$

Nuclear magnetic moments are typically 2000 times smaller than electronic magnetic moments since $\dfrac{\mu_N}{\mu_B} = \dfrac{m}{M} \approx \dfrac{1}{1836}$.

The nuclear g-factor, which is of the order of unity, takes account of the way the resultant nuclear moment is built up from the magnetic moments of individual nucleons. It therefore contains information about the detailed internal structure of the nucleus.

For a given atomic level characterized by the resultant electronic angular momentum quantum number $\vec{J}$ coupling with nuclear angular momentum quantum number $\vec{I}$ gives the total angular momentum quantum number $\vec{F}$ of the atom i.e.,

$$\vec{F} = \vec{I} + \vec{J} \tag{3.12}$$

$$F^2 = I^2 + J^2 + 2\vec{I}.\vec{J} \tag{3.13}$$

$$\vec{I}.\vec{J} = \frac{F^2 - I^2 - J^2}{2} \tag{3.14}$$

F remains a good quantum number under the application of the perturbation H, for hyperfine interaction does not give a torque on the atom as a whole.

Since the magnetic field at the nucleus, $\vec{B}_e$, is determined by the motion of orbital electrons, it follows that $B_e \propto J$. Thus (from the IJ coupling approximation) Eq. (3.9) becomes

$$H_\mu = A_J \vec{I}.\vec{J} \tag{3.15}$$

where A_J is called the magnetic hyperfine interaction or coupling constant and is the quantity which is determined directly from experimental measurements. For a hydrogenic atom, or an atom with just one electron outside closed shells, $\vec{B}_e$ and $\vec{J}$ are anti-parallel and the constant A_J will be positive if the nucleus has a positive value of g_I. The magnetic field at the nucleus will be zero for atoms with closed sub-shells and will be largest for those atoms with electrons in penetrating orbits. Therefore largest hyperfine splitting would be observed in atoms with unpaired s-electrons, e.g. hydrogen and the alkalis.

The interaction energy can be obtained by using the matrix elements of the operator H_μ i.e.

$$\Delta E_\mu = \left\langle \gamma IJFm_F \middle| H_\mu \middle| \gamma IJFm_F \right\rangle \tag{3.16}$$

By substituting Eq. (3.14) in Eq. (3.16) we get an expression for the hyperfine structure energies of all F levels of a hyperfine structure multiplet with respect to the atomic fine structure level J, viz.,

$$\Delta E_\mu = \frac{A_J}{2}\{F(F+1) - I(I+1) - J(J+1)\} \tag{3.17}$$

$$\Delta E_\mu = \frac{A_J C}{2} \tag{3.18}$$

where

$$C = F(F+1) - I(I+1) - J(J+1) \tag{3.19}$$

and

$$A_J = \frac{\mu_I \langle \vec{B} \rangle}{IJ}$$

$$A_J = \frac{g_I \mu_B \langle \vec{B} \rangle}{1836 J} \tag{3.20}$$

3.3 Electric Quadrupole Interaction

The quadrupole moment of a nucleus is a measure of the departure of the mean distribution of nuclear charge from spherical symmetry. It is positive for a distribution which is prolate ellipsoidal, negative for an oblate distribution, and zero for a spherically symmetric distribution. Thus a non-zero electric quadrupole moment implies that the charge distribution within nucleas is no longer spherical and the nucleus is deformed.

The electrostatic interaction between a single electron and nucleus containing Z protons is

$$W = -\sum_{p=1}^{Z} \frac{e^2}{|r_e - r_p|} \tag{3.21}$$

where the origin of co-ordinates is the centre of mass of the (infinitely heavy) nucleus, r_e is the position vector of the electron, r_p is the position vector of *pth* proton and the sum is taken over all Z protons.

In order to discuss the departure of the nuclear charge distribution from spherical symmetry, higher order electric multipole moments need to be considered. Assume that $r_e > r_p$ and expanding the factor $\dfrac{1}{|r_e - r_p|}$ in powers of r_p/r_e and in Legendre polynomials $P_l(cos\theta_{ep})$ where θ_{ep} is the angle between r_e and r_p, Eq. (3.21) becomes:

$$W = -e^2 \sum_{p=1}^{Z} \left[r_e^2 + r_p^2 - 2 r_e r_p \cos\theta_{ep} \right]^{-1/2}$$

$$W = -e^2 \sum_{p=1}^{Z} \sum_{l} \frac{r_p^l}{r_e^{l+1}} P_l(\cos\theta_{ep}) \tag{3.22}$$

Applying spherical harmonic addition theorem i.e.

$$P_l(\cos\theta_{ep}) = 4\pi \sum_{m=-l}^{l} \frac{1}{2l+1} Y_{lm}^*(\theta_p, \phi_p) Y_{lm}(\theta_e, \phi_e) \tag{3.23}$$

where Y_{lm} are spherical harmonics of rank l and projection m.

Eq. (3.22) becomes

$$W = -4\pi e^2 \sum_{p=1}^{Z} \sum_{m=-l}^{l} \frac{1}{2l+1} \frac{r_p^l}{r_e^{l+1}} Y_{lm}^*(\theta_p, \phi_p) Y_{lm}(\theta_e, \phi_e) \tag{3.24}$$

Expressing Eq. (3.24) in more compact notation viz.,

$$\sum_{m=-l}^{l} Y_{lm}^{*} Y_{lm} = \sum_{m} (-1)^{m} Y_{l,-m} Y_{lm} = Y^{(l)}(\Omega).Y^{(l)}(\Omega),$$

$$(\theta_p, \phi_p) \equiv (\Omega_p), \qquad (\theta_e, \phi_e) \equiv (\Omega_e)$$

$$Q^{(l)} \equiv e \sum_{p=1}^{Z} \sqrt{\frac{4\pi}{2l+1}} r_p^l Y^{(l)}(\Omega_p) \qquad (3.25)$$

$$U^{(l)} \equiv -e \sqrt{\frac{4\pi}{2l+1}} r_e^{l+1} Y^{(l)}(\Omega_p) \qquad (3.26)$$

Eq. (3.24) can be written as

$$W = \sum_l Q^{(l)}.U^{(l)} \qquad (3.27)$$

When $l = 0$, Eq. (3.27) becomes

$$W = Ze^2/r_e \qquad (l=0), \qquad (3.28)$$

which is just the Coulomb interaction with Z being the sum over the protons. For a nucleus of finite size, there is a correction term to be added in Eq. (3.28):

$$\frac{2}{3} \pi e^2 Z |\psi(0)|^2 \langle R^2 \rangle \qquad (3.29)$$

In which $\langle R^2 \rangle$ is the mean square charge radius of the nucleus and $e^2 |\psi(0)|^2$ is the electronic charge density at the nucleus.

The term $l = 1$ in Eq. (3.27) vanishes because it corresponds to the interaction between a nuclear electric dipole moment and the electric field established by the electrons. Nuclear states have well-defined parity so that the expectation value of nuclear electric dipole moment (which is an odd operator) vanishes. The next term, with $l = 2$, is the electric quadrupole interaction which is the Hamiltonian H_Q

$$H_Q = Q^{(2)}.U^{(2)} \qquad (3.30)$$

and is a scalar product of nuclear and electronic tensor, each of rank 2.

The matrix elements of the scalar product of two tensor operators $T^{(k)}$ and $U^{(k)}$ in the coupled representation is given by [37-38]

$$\langle \alpha j_1 j_2 jm | T^{(k)}.U^{(k)} | \alpha' j_1' j_2' j'm' \rangle = (-1)^{j_1+j_2+j_1'} \delta_{jj'} \delta_{mm'} \begin{Bmatrix} j_1' & j_2' & j \\ j_2 & j_1 & k \end{Bmatrix} \times \sum_{\alpha''} \langle \alpha j_1 \| T^{(k)} \| \alpha'' j_1' \rangle \langle \alpha'' j_2 \| U^{(k)} \| \alpha' j_2' \rangle$$

$$(3.31)$$

Suppose that the electronic state is characterized by angular momentum quantum numbers J, m_J, the nuclear state by I, m_I and when the two angular momenta are coupled the

24

quantum numbers are I, j, F, m_F. In this case, Eq. (3.31) becomes

$$\left\langle IJFm_F \left| Q^{(2)}.U^{(2)} \right| IJF'm_F' \right\rangle = (-1)^{F+J+I} \delta_{FF'} \delta_{m_F m_F'} \begin{Bmatrix} I & J & F \\ J & I & 2 \end{Bmatrix} \left\langle I \left\| Q^{(2)} \right\| I \right\rangle \left\langle J \left\| U^{(2)} \right\| J \right\rangle \tag{3.32}$$

The quantity in the curl bracket is a 6j symbol whose value is given by

$$\begin{Bmatrix} I & J & F \\ J & I & 2 \end{Bmatrix} = (-1)^{F+J+I} \times \frac{2[3X(X+1) - 4I(I+1)J(J+1)]}{\sqrt{(2I-1)2I(2I+1)(2I+2)(2I+3)(2J-1)2J(2J+1)(2J+2)(2J+3)}} \tag{3.33}$$

where

$$X = I(I+1) + J(J+1) - F(F+1)$$

In order to solve Eq. (3.32), the reduced matrix elements are evaluated. Consider the reduced matrix element for the nuclear quadrupole moment Q, viz.,

$$Q = \left\langle Im_I = I \left| \sum_p (3z_p^2 - r_p^2) \right| Im_I = I \right\rangle \tag{3.34}$$

since

$$\sum_p (3z_p^2 - r_p^2) = 2\sum_p \sqrt{\frac{4}{5}\pi} r_p^2 Y_{20}(\Omega_p) = (2/e)Q_0^{(2)} \tag{3.35}$$

where the second equality comes from Eq. (3.25), we have

$$\frac{1}{2}eQ = \left\langle Im_I = I \left| Q_o^{(2)} \right| Im_I = I \right\rangle \tag{3.36}$$

Using the Wigner-Eckart Theorem i.e.,

$$\left\langle Im_I \left| Q_o^{(2)} \right| Im_I \right\rangle = (-1)^{I-m} \begin{pmatrix} I & 2 & I \\ -m_I & 0 & m_I \end{pmatrix} \left\langle I \left\| Q^{(2)} \right\| I \right\rangle \tag{3.37}$$

Setting $m_I = I$ and evaluating the 3j symbol gives,

$$\left\langle Im_I = I \left| Q_o^{(2)} \right| Im_I = I \right\rangle = \sqrt{(2I-1)2I(2I+1)(2I+2)(2I+3)} \left\langle I \left\| Q^{(2)} \right\| I \right\rangle \tag{3.38 a}$$

$$= \frac{1}{2}eQ \tag{3.38b}$$

or

$$\left\langle I \left\| Q^{(2)} \right\| I \right\rangle = \sqrt{(2I-1)2I(2I+1)(2I+2)(2I+3)} eQ \tag{3.39}$$

It can be emphasized here from Eq. (3.38) that the nuclei with spin $I = 0$ or $\frac{1}{2}$ have no quadrupole moment.

The reduced matrix element for $U^{(2)}$ can be solved in an analogous manner.

The component of $\left\langle J \| U^{(2)} \| J \right\rangle$ proceed in analogous fashion. Now a quantity *"eq"* is defined as

$$\frac{1}{2} eq = \left\langle Jm_J = J \| U_0^{(2)} \| Jm_J = J \right\rangle \tag{3.40}$$

where, from Eq. (3.26),

$$U_0^{(2)} = \sqrt{\frac{4}{5}\pi r_e^2}\, Y_{20}(\Omega_e) = -\frac{1}{2} e \frac{3z_e^2 - r_e^2}{r_e^5} \tag{3.41}$$

Note that

$$\frac{\partial^2}{\partial z^2}\left(-\frac{e}{r}\right) = -e\frac{3z_e^2 - r_e^2}{r_e^5} \tag{3.42}$$

is the *zz* component of the electric field gradient tensor produced by an electron at a point whose co-ordinates with respect to the electron are *(x,y,z)*. Since the origin of the co-ordinate system has been positioned at the nucleus, $2U_0^{(2)}$ in Eq. (3.41) is the *zz* component of the electric field gradient tensor at the nucleus produced by an electron at a distance r_e from the nucleus, or

$$U_0^{(2)} = \frac{1}{2}\left(\frac{\partial^2 V_e}{\partial z^2}\right)_0 \equiv \frac{1}{2}V_{ZZ} \tag{3.43}$$

where *V* is the potential due to the electron and the second derivative is evaluated at the origin (nucleus). Therefore the product "eq" can be written as

$$eq = \left\langle Jm_J = J \left| V_{zz} \right| Jm_J = J \right\rangle = \left\langle V_{ZZ} \right\rangle \tag{3.44}$$

which is the average or expectation value of V_{zz} taken over the electronic state $\left| JJ \right\rangle$.

Again the use of Wigner-Eckart theorem leads to the result

$$\left\langle J \| U^{(2)} \| J \right\rangle = \frac{1}{2}\sqrt{(2J+1)(J+1)(2J+3)/(2J-1)}\, eq \tag{3.45}$$

On substituting Eq. (3.33), Eq. (3.39) and Eq. (3.45) into Eq. (3.32), we have

$$\left\langle IJFm_F \left| Q^{(2)}.U^{(2)} \right| IJF'm_F' \right\rangle = \frac{e^2 qQ}{2I(2I-1)J(2J-1)}\left[\frac{3}{4}X(X-1) - I(I-1)J(J+1)\right] \tag{3.46}$$

The quantity e^2qQ is known as the quadrupole coupling constant and *X* is the same quantity as in Eq. (3.33). The quadrupole coupling constant may be positive or negative, depending upon *Q* is positive or negative respectively. Using vector sum and scalar product of $\vec{I}$ and $\vec{J}$ i.e.

$$\vec{F} = \vec{I} + \vec{J} \qquad \text{and} \qquad -2\vec{I}.\vec{J} = I^2 + J^2 - F^2$$

Eq. (3.46) becomes

$$\left\langle IJFm_F \left| -2\vec{I}.\vec{J} \right| IJF'm'_F \right\rangle = I(I+1) + J(J+1) - F(F+1) = X \qquad (3.47)$$

Thus

$$\left\langle IJFm_F \left| 3(\vec{I}.\vec{J})^2 + \frac{3}{2}(\vec{I}.\vec{J}) - I^2J^2 \right| IJF'm'_F \right\rangle = \frac{3}{4}X(X-1) - I(I+1)J(J+1) \qquad (3.48)$$

Comparing the above equation with Eq. (3.46) gives,

$$H_Q = Q^{(2)}.U^{(2)} = \frac{e^2qQ}{2I(2I-1)J(2J-1)}\left[3(\vec{I}.\vec{J})^2 + \frac{3}{2}(\vec{I}.\vec{J}) - I^2J^2 \right] \qquad (3.49)$$

Eq. (3.49) can be written alternatively as

$$H_Q = Q^{(2)}.U^{(2)} = \frac{B_J}{2I(2I-1)J(2J-1)}\left[3(\vec{I}.\vec{J})^2 + \frac{3}{2}(\vec{I}.\vec{J}) - I^2J^2 \right] \qquad (3.50)$$

where B_J is known as the electric quadrupole interaction and can be expressed as a product of the quadrupole moment and the electric field gradient produced by the orbital electrons at the position of the nucleus i.e.

$$B_J = eQ\left\langle \frac{\partial^2 V_e}{\partial z^2} \right\rangle \qquad (3.51)$$

Hyperfine structure measurements on free atoms enable the values of B_J to be determined experimentally. However, the nuclear electric quadrupole moment can then only be calculated if theoretical estimates of the field gradient exist.

The quadrupole interaction causes a shift in hyperfine structure levels and do not produce splitting. The shift in energy is given by

$$\Delta E_Q = \left\langle IJFm_F \left| H_Q \right| IJF'm_{F'} \right\rangle$$

$$\Delta E_Q = \frac{B_J}{4} \frac{\frac{3}{2}C(C+1) - 2I(I+1)J(J+1)}{I(2I-1)J(2J-1)} \qquad (3.52)$$

where C is

$$C = F(F+1) - J(J+1) - I(I+1)$$

This interaction vanishes for S terms, because $\left\langle \frac{\partial^2 V_e}{\partial z^2} \right\rangle$ vanishes when the electron charge distribution is spherically symmetrical. The interaction also vanishes unless $I \geq 1$, $J \geq 1$.

3.4 Hyperfine (hf) Structure

In the absence of nuclear magnetic dipole or electric quadrupole interactions, the zeroth-order wavefunctions $|\gamma J I m_J m_I\rangle$ are $(2I+1)(2J+1)$-fold degenerate in the nuclear and electronic magnetic quantum numbers. To evaluate the energy shift arising from the hyperfine interaction, we take linear combinations of the functions $|\gamma J I m_J m_I\rangle$ to form new zeroth-order wavefunctions $|\gamma J I F m_F\rangle$ for which the total angular momentum F and the projection $m_F = m_J + m_I$ are good quantum numbers. The magnetic interaction $A_J \vec{I}.\vec{J}$ cause $\vec{I}$ and $\vec{J}$ to precess rapidly about the resultant total angular momentum

$$\vec{F} = \vec{I} + \vec{J} \tag{3.53}$$

The energy of a specific hyperfine level is then given by

$$E_F = \langle \gamma J I F m_F | H_0 + H_{HFS} | \gamma J I F m_F \rangle \tag{3.54}$$

$$E_F = E_J + \frac{1}{2} A_J C + \frac{B_J}{8I(2I-1)J(2J-1)} \{3C(C+1) - 4I(I+1)J(J+1)\} \tag{3.55}$$

where C is

$$C = F(F+1) - I(I+1) - J(J+1) \tag{3.56}$$

The first term in Eq. (3.55) is the energy of a fine structure multiplet level with total electronic angular momentum quantum number J, the second term is the magnetic hyperfine interaction which causes the splitting of fine structure level and the third term is the electric quadrupole interaction producing shift in energy.

Eq. (3.55) shows that the magnetic and electric interaction between a nucleus and the orbital electrons which splits a given fine structure level into hyperfine structure multiplet. The number of hyperfine structure levels depend on the number of possible orientations of the angular momentum vectors $\vec{I}$ and $\vec{J}$ i.e. a fine level splits into $2I+1$ if $J \geq I$ and $2J+1$ if $I \geq J$ hyperfine structure levels.

The total width of the splitting between levels |I-J| to /I+J/ is

$$\Delta W = A_J I(2J + 1) \text{ for } J > I$$

and

$$\Delta W = A_J J(2I + 1) \text{ for } J < I$$

The hyperfine structure splitting is in the range of 10^{-3} to 1 cm^{-1} and is smaller than the fine structure splitting. This is due to the fact that $\vec{S}$ and $\vec{L}$ are strongly coupled to each other as compared to their resultant coupling with the nuclear spin $\vec{I}$.

When $A_J > 0$ the hyperfine level having smallest possible value of F has the lowest energy value, and known as normal hyperfine multiplet. When $A_J < 0$ then the level having largest possible value of F has the lowest energy value. Such hyperfine multiplet is known as inverted multiplet. Physically it can be explained in the following manner: If the spinning

electron and nucleus are considered as small magnets which influence each other at a certain distance, then the most stable position would be one for which their magnetic moments are in opposite directions and the mechanical moments are in the same direction. This leads to normal hyperfine splitting of fine structure level such that smallest F lies deepest. In the reverse case the highest F value lays deepest i.e. inverted hyperfine structure levels.

3.5 Radiative Transitions between Hyperfine Structure Components

The electric dipole transitions between the components of the hyperfine structure of two levels γJ and $\gamma' J'$, assuming that transitions between these levels are allowed depending on selection rules, obey additional selection rules

$$\Delta F = 0, \pm 1; \quad F + F' \geq 1 \tag{3.57}$$

The electric dipole transitions between components of the hyperfine structure of the same level are forbidden by the parity selection rule. Only the magnetic dipole transitions and the electric quadrupole transitions are allowed. In the first case, the selection rules (3.57) apply and in the second

$$\Delta F = 0, \pm 1, \pm 2; \quad F + F' \geq 2 \tag{3.58}$$

3.6 Landé Interval Rule

The relative spacing of hyperfine levels obeys Landé interval rule which states that "the energy spacing between successive hyperfine levels $F - 1$ and F is proportional to F" i.e.

$$\Delta E_\mu(F, F-1) = E_\mu(F) - E_\mu(F-1)$$

$$\Delta E_\mu(F, F-1) = \frac{A_J}{2}\left[F(F+1) - (F-1)F\right] = A_J F \tag{3.59}$$

This rule is analogous to the Landé interval rule for the fine structure multiplet splitting. Just as in the case of the fine structure splitting "the centre of gravity" of the hyperfine structure of a level is not shifted.

$$\sum_F (2F+1)\Delta E_F = 0 \tag{3.60}$$

The energy of a particular hyperfine structure level is given by

$$E_F = E_J + \frac{1}{2}A_J C + \frac{B_J}{8I(2I-1)J(2J-1)}\left\{3C(C+1) - 4I(I+1)J(J+1)\right\} \tag{3.61}$$

where C is

$$C = F(F+1) - I(I+1) - J(J+1)$$

From Eq. (3.61) it is clear that the quadrupole interaction gives rise to a departure from the interval rule because its dependence on F is different from that of the magnetic dipole

interaction. Therefore interval rule for the hyperfine levels is valid only for $B_J = 0$. Also deviation from the interval rule is more prominent whenever the quadrupole constant B_J is comparable in magnitude with the magnetic constant A_J. Furthermore it is to be noted that the interval rule for a line with the hyperfine splitting is valid only if:

- The interval rule is obeyed by the individual hyperfine structure splitting of both the combining levels

- $\Delta J = 0$

For $\Delta J = \pm 1$, it does not hold with the exception of one situation where A-value of one of the combining levels is so small as compared to the A-value of the other level that it can be neglected. In such a situation the hyperfine structure pattern of the line reflects the hyperfine splitting of the level with $A \neq 0$.

3.7 Intensity Rule for Hyperfine Components

The hyperfine structure term with a given F has a statistical weight $(2F + 1)$. In hyperfine multiplets, this statistical weight is important for the determination of intensity ratios between hyperfine structure components. The relative intensities within a hyperfine multiplet is found to obey the intensity or the sum rule discovered empirically by Ornstein, Burger and Dorgelo [39-40]. It can be stated as

"within a hyperfine multiplet, the ratio of the sums of the intensities of all the transitions from two states with quantum numbers F and F' are in the ratio of their statistical weights $(2F + 1):(2F' + 1)$".

If the splitting of one of the levels is negligibly small, the intensities of the lines are simply in the ratio of the values $2F + 1$ of the level whose splitting causes the structure. This offer a means for determining the value of I.

In order to determine the value of I from a measured intensity ratio, one only has to distinguish between either different half-integral or different integral values, according to whether the mass number is odd or even. It is evident that the accuracy needed for the determination of I is greater, the higher the value of I.

If the value J of the level causing the splitting is sufficiently large, the nuclear spin I can be deduced from the number of components, provided the resolution is complete enough. The number of component is, then, simply equals to $2I + 1$.

For a dipole transition the connecting atomic states with total electronic orbital angular momentum J_o and J_u and with nuclear spin I, the line strength $S(F_o \rightarrow F_u)$ of the hyperfine components connecting F_o and F_u is given by the expression

$$S(F_o \rightarrow F_u) = \frac{(2F_o + 1)(2F_u + 1)}{2I + 1} \left\{ \begin{matrix} J_o & F_o & I \\ F_u & J_u & 1 \end{matrix} \right\}^2 \tag{3.61}$$

Above equation is applicable in cases where interactions between neighbouring levels are weak, so that J_o and J_u are good quantum numbers. The strongest components of hyperfine structure multiplet are those for which F and J change in the same direction and are called **diagonal lines or components**, i.e.

$$\Delta F = \Delta J \tag{3.62}$$

and the line strength of diagonal lines increases with increasing *F*. The other two groups of weaker lines with $\Delta F \neq \Delta J$ are called **off-diagonal lines** and usually are strongest for intermediate values of *F*. For $\Delta J \neq 0$, one group of off-diagonal lines with $\Delta F = 0$ are stronger than the other group i.e. $\Delta F = - \Delta J$. For $\Delta J = 0$, both groups of off-diagonal lines are of equal intensity. Physical interpretation of Eq. (3.62) is that since the nuclear spin is so weakly coupled to the electronic system that it does not affect the total radiation of the atom with a given *J*. But by forcing *J* into a certain orientation with regard to *F* it affects the statistical weight of the level and causes a certain distribution of radiation over the hyperfine structure components.

3.8 Experimental Determination of Hyperfine Constants

The hyperfine interaction energy has two contributions, (i) magnetic moment of the nucleus interacting with the magnetic field produced by the spinning and orbiting electrons, (ii) electrostatic interaction of electrons with asymmetric charge distribution inside the nucleus. Eq. (3.46) can be written as

$$\Delta E = \alpha \cdot h \cdot A_J + \beta \cdot h \cdot B_J \qquad (3.63)$$

where α and β are Casimir Factors and are functions of total orbital angular momentum of electrons *J* and total angular momentum *F* of atom with spin *I*, viz.

$$\alpha = \frac{1}{2}\left[F(F+1) - I(I+1) - J(J+1)\right] = \frac{C}{2} \qquad (3.64)$$

and

$$\beta = \frac{\frac{3}{4}C(C+1) - I(I+1)J(J+1)}{2I\,J(2I-1)(2J-1)} \qquad (3.65)$$

The electric dipole transition between the two different fine structure levels having hyperfine splitting *ΔE* follows selection rules *ΔJ = 0, ±1* and *ΔF = 0, ±1*. As photon carries angular momentum therefore transition between two hyperfine levels each having *F = 0* is forbidden. For electric dipole transitions parities of the combining fine structure levels must be different. Each allowed transition represents a component of the hyperfine structure pattern of a spectral line with component positions given by

$$\nu = \nu_c + \alpha_o(F_o, J_o, I)A_o + \beta_o(F_o, J_o, I)B_o - \alpha_u(F_u, J_u, I)A_u - \beta_u(F_u, J_u, I)B_u \quad (3.66)$$

ν_c is the energy difference between the fine structure levels and experimentally it is the excitation energy for the combining lower and upper fine structure levels. The upper level is labelled by the letter 'o' (German word "oben", means upper) and lower level is labelled by the letter 'u' (German word "unten", means lower). Apart from ν_c, Eq. (3.66) contains A_o, B_o, A_u and B_u as unknown quantities. Thus, for experimental determination of hyperfine constants from a given spectrum, it is necessary to identify the quantum numbers of at least 5 hyperfine components and to measure their (absolute or relative) positions. If one can identify more than 5 components, a least square method has to be used to calculate the hyperfine constants.

4 Laser Spectroscopy

The invention of the laser has brought spectacular advances in all fields of science and technology and especially in the branch of precision spectroscopy of atoms and molecules. Classical spectroscopic techniques have two major drawbacks (i) low intensity of excitation source (ii) lack of resolution of the dispersing device. The availability of widely tunable and intense highly monochromatic laser light sources has not only greatly increased the sensitivity and resolution of classical spectroscopic techniques, but also helped in rediscovering old spectroscopic techniques such as Raman spectroscopy and discovering many powerful new techniques of non-linear spectroscopy. Furthermore, laser light interaction with atoms and molecules is not just limited to their spectroscopic investigations but now the laser light is also used as a tool to manipulate atoms such as in the field of laser cooling and trapping of atoms. The high resolution and high monochromaticity of the laser beam can be used in Doppler free spectroscopy where high-resolution spectra can readily be obtained. In recent years, femtosecond (fs) lasers have been developed which are able to generate very short pulses as short as 4 femtoseconds. Commercially available femtosecond lasers can generate pulses less than 30 fs. Many processes in physics, chemistry and biology occur on a very short time scale and femtosecond laser spectroscopy has been widely used to investigate such processes. In multiphoton spectroscopy, where the high peak power of a short pulse laser allow the absorption not of one photon but two or more photons. This method has an advantage that it allows for the excitation energies not available from one photon, for instance excitation of molecules in the UV or VUV using visible light. Furthermore, multiphoton spectroscopy follows different selection rules and has different polarization dependence and therefore can be used to reach states not accessible with one photon.

In the following sections a detailed description of various line broadening mechanisms is given which is then followed by a short description of tunable lasers, with a particular emphasis on a ring dye laser system. The rest of the chapter is devoted to the discussion of different laser spectroscopic techniques.

4.1 Spectral Line Profile

The theories of atomic and molecular structure give the concepts of quantum numbers and angular momenta which provide an insight concerning the discreteness of energy levels of atoms, ions and molecules. This discrete nature of energy levels leads to discrete spectral features which are characteristic of particular atomic or molecular specie. Furthermore, selection rules provide basic criteria for the radiative transitions which occur between energy levels. From this one might infer that the spectroscopic transitions involve purely monochromatic radiations and that the associated observed spectral lines would be infinitely narrow, delta function "spikes".

Contrary to this, even the most casual inspection of any spectrum cast strong doubts on such an inference. Experimentally it is observed that the spectral lines consists of some intrinsic distribution of frequencies, $I(v)$, about the center frequency v_o. This distribution of frequencies give a characteristic shape to a spectral line and is known as spectral line profile. The characteristic shape and finite line width of spectral lines are determined by the physical conditions existing within the source of the spectrum.

Depending on the physical conditions prevailing inside an ensemble of atoms, the spectral line broadening mechanisms can be divided into two broad categories i.e.

(i) homogeneous broadening, and (ii) inhomogeneous broadening.

The spectral line profile is said to be ***homogeneously*** broadened if all of the atoms within the sample experience identical physical conditions. In other words, the spectral line profile for the transition $\Psi_k \rightarrow \Psi_i$, is homogeneously broadened if the transition probability as a function of frequency $P(\omega)$ is identical for all atoms within the ensemble that are in the initial state Ψ_k.

The spectral line profile is said to be ***inhomogeneously*** broadened if different subsets of the atoms within the sample experience different physical conditions. In other words, the spectral line profile for the transition $\Psi_k \rightarrow \Psi_i$, is inhomogeneously broadened if the transition probability $P(\omega)$ is different for different sub-ensembles of atoms that are in the initial state Ψ_k.

Natural, collisional and power broadening mechanisms are examples of homogenous broadening mechanism and are well described by normalized Lorentzian line profiles with center frequency ω_o and full width γ. Doppler broadening is a form of inhomogenous broadening and is described by a Gaussian line profile.

4.1.1 Natural Linewidth and the Lorentzian Line Profile

Consider a hypothetical two energy level atom, which is isolated and is at rest. One of the level is the stable ground level E_i and the other is the excited level E_k. Furthermore, it is assumed that each energy level is singly degenerate and excited state decay only via spontaneous radiative transition $E_i \rightarrow E_k$. The energy separation between excited and stable ground levels is given by

$$\Delta E = h\nu_o = \hbar\omega_o \tag{4.1}$$

Corresponding to such an idealized atom the spectral line profile associated with transition is examined. The system can be described by a classical damped harmonic oscillator with characteristic frequency ω_o and mass m. Radiative energy loss leads to damping of the oscillations which is characterized by the damping constant γ. The amplitude of oscillation can be obtained by solving second order differential equation, viz.

$$\ddot{x} + \gamma\dot{x} + \omega_o^2 x = 0 \tag{4.2}$$

In the limit of small damping i.e. where γ is much smaller than ω_o, the time dependent amplitude of the oscillation is given by

$$A(t) = A_o \exp\left(\frac{-\gamma t}{2}\right)\cos\omega_o t \tag{4.3}$$

where A_o is the amplitude at time $t = 0$ and the exponential term describes the time dependent damping. Using Eq. (4.3) and an expression for the energy of the oscillator, damping constant can be determined and is given as

$$\gamma = \frac{2}{3}\frac{e^2\omega_o^2}{mc^3(4\pi\varepsilon_o)} = \frac{2\pi e^2\nu_o^2}{3\varepsilon_o mc^3} \tag{4.4}$$

Now damped oscillations are of the form shown in Figure 4.1(a) with the amplitude decaying exponentially in time. The oscillations have a lifetime $\tau_{class} = 1/\gamma$. An infinite

wave train of constant amplitude is truly monochromatic. Thus the frequency of the emitted radiation is no longer monochromatic. The Fourier transformation of Eq. (4.3) from the time domain into the frequency domain gives Eq. (4.5) which describes the intensity of the line as a function of frequency, viz.

$$I(\omega - \omega_o) = I_o \left[\frac{1}{(\omega - \omega_o)^2 + (\gamma/2)^2} \right] \tag{4.5}$$

Changing from ω to ν, gives

$$I(\nu - \nu_o) = I_o \left[\frac{(\gamma/4\pi)^2}{(\nu - \nu_o)^2 + (\gamma/2)^2} \right] \tag{4.6}$$

where I_o is the central intensity. I/I_o in Eq. (4.6) gives the normalized Lorentzian line profile as shown in Figure 4.1 (b).

The Lorentzian or natural line profile is defined completely by two quantities; (i) the center frequency at which the line intensity is at its maximum and (ii) the full width at half maximum (FWHM) intensity, that is the width between the two points at which $I(\omega) = I(\omega_o)/2$. Inspection of Figure 4.1(b) clearly illustrates that the center frequency is exactly the characteristic frequency of the damped harmonic oscillator, ω_o; and that the full linewidth is exactly given by the damping coefficient γ. The linewidth can also be expressed in terms of frequency or in terms of wavelength by the following equation, i.e.

$$\gamma = \Delta\omega = 2\pi\Delta\nu = \frac{2\pi c\Delta\lambda}{\lambda_o^2} \tag{4.7}$$

and the relative width are the same and are given as;

$$\left| \frac{\Delta\omega}{\omega_o} \right| = \left| \frac{\Delta\nu}{\nu_o} \right| = \left| \frac{\Delta\lambda}{\lambda_o} \right| \tag{4.8}$$

The derivation of natural or Lorentzian line profile is based on the assumption that a single oscillator corresponds to a single isolated atom. But the result applies equally well to an ensemble of randomly phased oscillators corresponding to a collection of identical atoms under identical physical conditions that radiate at the identical center frequency, but at random times.

Heisenberg's Uncertainty Principle can also be used for an equivalent description of the natural line profile. This quantum mechanical approach is more consistent with the description of atoms and provides greater insight in physical conditions prevailing inside the atom. The uncertainty principle expressed in terms of momentum and position is given by

$$\Delta p \Delta x \geq \frac{\hbar}{2} \tag{4.9}$$

where Δp and Δx are the uncertainties in linear momentum and position, respectively. The uncertainty principle can be utilized for any pair of conjugate variables of dimension energy ×time viz.

$$\Delta E \Delta t \; \geq \; \frac{\hbar}{2} \tag{4.10}$$

where ΔE is the uncertainty in energy measurement and Δt is the uncertainty in time. Now for an excited electronic state Ψ_k, having a mean radiative lifetime τ_k, the energy can best be determined with an inherent uncertainty of

$$\Delta E \; \geq \; \frac{\hbar}{2\tau} \tag{4.11}$$
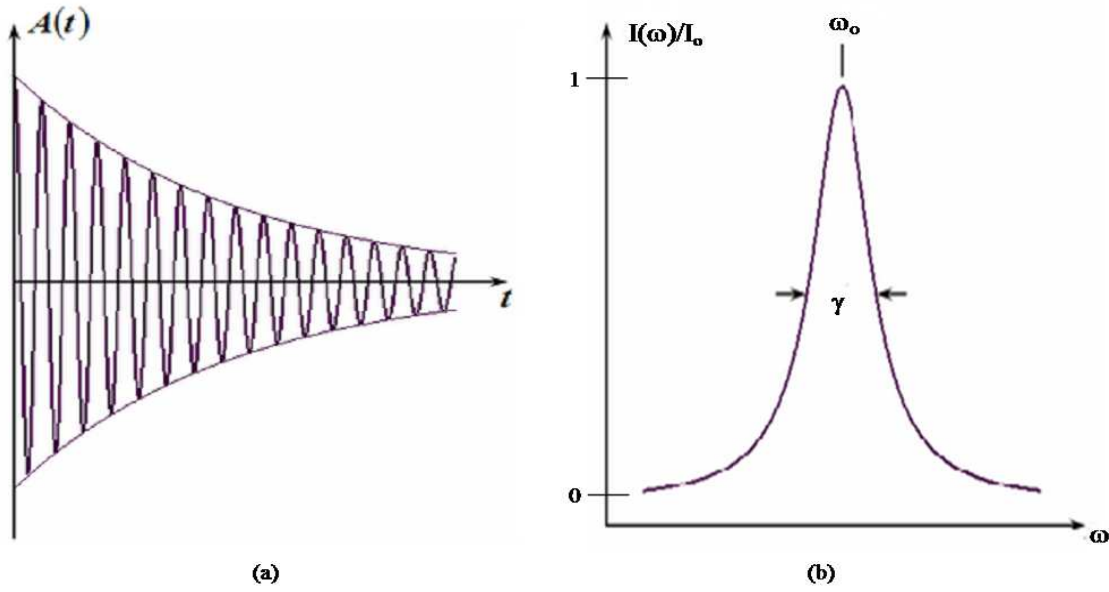
Figure 4.1: (a) Time-dependent amplitude of a classical damped harmonic oscillator. (b) Corresponding normalized Lorentzian line profile

Combining Eq. (4.1) and Eq. (4.11) gives an uncertainty in frequency $\Delta\omega$ for a transition terminating in a stable ground state, i.e.

$$\Delta\omega \; \approx \; \frac{1}{\tau_k} \tag{4.12}$$

Thus from the above equation one can conclude that for an idealized two-level atom, the natural line width is determined by the mean spontaneous radiative lifetime, τ_k, of the upper state. The transition probability A_{ki} or Einstein coefficient for spontaneous radiative decay from the upper state Ψ_k to the ground state Ψ_i in the idealized two-level atom is given by

$$A_{ki} \; = \; \frac{1}{\tau_{ki}} \tag{4.13}$$

From quantum electrodynamics the transition probability or Einstein coefficient for spontaneous radiative decay from the upper state Ψ_k to the ground state Ψ_i is proportional

35

to the matrix elements of the operator $H'(r)$ i.e.

$$A_{ki} \propto \left| \langle \psi_i(r) | H'(r) | \psi_k(r) \rangle \right|^2 \qquad (4.14)$$

where $H'(r)$ is the perturbation, or physical interaction that couples the atom and the photon thus resulting in the spontaneous radiative transition. The potential perturbations are the electric dipole *(E1)*, magnetic dipole *(M1)*, or electric quadrupole *(E2)* interactions. For the specific case of an electric dipole *(E1)* allowed, spontaneous radiative transition, Eq. (4.14) becomes:

$$A_{ki} = \left(\frac{\omega_{ki}^3}{3\pi\varepsilon_o \hbar c^3} \right) \left(\frac{1}{g_k} \right) \left| \langle \psi_i(r) | + e\vec{r}.\vec{E} | \psi_k(r) \rangle \right|^2 \qquad (4.15)$$

where

ω_{ki} is the center transition frequency in radians per second

ε_o is the vacuum permittivity

$\hbar$ is the reduced Planck's constant

c is the speed of light in vacuum

g_k is the statistical weight of level k

e is the charge of the electron

$\vec{r}$ is the position vector of the electron and

$\vec{E}$ is the electric field vector of the photon

Since the upper state is degenerate within the resolving power of the instrument, its statistical weight must be included. For example, with total angular momentum J_k, the state Ψ_k has a statistical weight given by:

$$g_k = 2J_k + 1 \qquad (4.16)$$

From the transition probability of spontaneous radiative decay, the intensity I_{ki} of the spectral emission line is determined. Assuming that the population of excited states is uniformly distributed throughout the sample volume, and that the radiation is emitted isotropically from an optically thin source such that each emitted photon escapes from the source volume rather than being reabsorbed, the line intensity is given explicitly by

$$I_{ki} = \frac{n_k V \omega_{ki} A_{ki}}{4\pi} \qquad (4.17)$$

where

n_k is the number density of excited states, and

V is the source volume

The number density of excited states, n_k, is determined by the physical conditions that excite the source. Thus if the relevant Einstein coefficients are known, direct comparison of observed line intensities for different transitions within the same atom can provide substantive information on the physical conditions within the source.

Now consider a more realistic atom with three energy levels i.e. two excited states and a stable ground state. In order to determine the natural linewidth of transitions from the higher excited to the lower excited electronic state, it is assumed that upper excited state E_i decays only via spontaneous radiative transition to the lower excited state and that the lower, or intermediate excited state E_k decays only via spontaneous radiative transition to the stable ground state. The upper and lower excited states have life times τ_i and τ_k respectively. The uncertainties of both states i.e. ΔE_i and ΔE_k contribute to the linewidth of transition. Therefore the total uncertainty

$$\Delta E = \Delta E_i + \Delta E_k$$

$$\Rightarrow \Delta\omega = \left(\frac{1}{\tau_i} + \frac{1}{\tau_k} \right) \tag{4.18}$$

Generally the decay from both the states is not only due to spontaneous emission but also has a non-radiative relaxation contribution; therefore the line profile is determined by the total decay constants γ_i and γ_k. The normalized line profile function is given by

$$g(\omega - \omega_{ik}) = \frac{\frac{1}{2\pi}(\gamma_i + \gamma_k)}{(\omega_{ik} - \omega)^2 + \left[(\gamma_i + \gamma_k)/2 \right]^2} \tag{4.19}$$

where both γ_i and γ_k have contributions from radiative and non-radiative relaxations, therefore both can be expressed as a sum. $\gamma = \gamma_R + \gamma_{NR}$

For an electric dipole *(E1)* allowed emission line occurring in the visible region of the spectrum and with a typical excited state lifetime of the order of 10^{-8} seconds, the natural linewidth is of the order of 16 MHz or 10^{-4} Å. Although the excited state lifetime appear to be exceedingly short and the natural linewidth exceedingly small but both these quantities can be measured experimentally in the laboratory.

4.1.2 Doppler Broadening

Doppler broadening belongs to the class of inhomogeneous broadening mechanisms and is due to the random thermal motions of the atoms within the gas. In gases at low pressure, Doppler broadening is one of the major contributions to the broadening of the spectral line. Doppler broadened line profile completely conceals the Lorentzian line profile with natural linewidth.

Consider an ensemble of atoms in gas phase at low pressure which are in an effective state of thermal equilibrium within the laboratory rest frame and moving with a velocity $\vec{v} = \{v_x, v_y, v_z\}$ relative to this rest frame. For such an ensemble the distribution of atomic speeds, $f(v)dv$, is well described by a Maxwell-Boltzmann distribution such that

$$f(v)dv = 4\pi v^2 \left(\frac{m}{2\pi k_B T} \right)^{3/2} exp\left(\frac{-mv^2}{2k_B T} \right) dv \tag{4.20}$$

where v is the speed, m is the mass of the atom, T is the temperature of the ensemble and

k_B is the Boltzmann constant. For such an ensemble the most probable speed of any atom within the sample, $\langle v \rangle$, is a simple function of the temperature and the mass of the atom i.e.,

$$\langle v \rangle = \left(\frac{2k_B T}{m} \right)^{1/2} \qquad (4.21)$$

Consider an atom in an excited state ψ_k which undergoes a spontaneous radiative decay to a lower state ψ_i with a characteristic central frequency ω_o in the rest frame of the atom. Now let the atom moving with velocity $\vec{v}$ with respect to the laboratory rest frame, then the observed frequency of the emitted photon ω' is shifted by the Doppler effect and is given by:

$$\omega' = \omega_o + \vec{k} \cdot \vec{v} \qquad (4.22)$$

where $\vec{k}$ is the wave vector of the photon. For an atom moving towards the observer, $\vec{k}.\vec{v} > 0$ and the apparent frequency is shifted to the blue of ω_o. For an atom moving away from the observer, then $\vec{k}.\vec{v} < 0$ and the apparent frequency is shifted to the red of ω_o. Assuming that the observations are made along the z-direction, then $\vec{k} = \{0, 0, k_z\}$ and only the z-component of the velocity is of significance. Eq (4.22) with $|k| = 2\pi / \lambda$ becomes

$$\omega' = \omega_o \left(1 + \frac{v_z}{c} \right) \qquad (4.23)$$

At thermal equilibrium, the number of atoms $n_k(v_z)dv_z$ in the excited ψ_k per unit volume within the speed interval v_z to $v_z + dv_z$ is given by

$$n_k(v_z)dv_z = \frac{N_k c}{\langle v \rangle \sqrt{\pi}} \, exp\left\{ -\left(\frac{v_z}{\langle v \rangle} \right)^2 \right\} dv_z \qquad (4.24)$$

where N_k is the total density of atoms in state ψ_k, and $\langle v \rangle$ is the most probable speed as given by Eq. (4.21). Substituting the value of v_z from Eq. (4.23) in Eq. (4.24) gives the number of atoms in state ψ_k which are observed to emit a photon of frequency ω' that is shifted from ω_o within the frequency interval ω and $\omega + d\omega$:

$$n_k(\omega)d\omega = \frac{N_k c}{\omega_o \langle v \rangle \sqrt{\pi}} \, exp\left\{ -\left(\frac{c(\omega - \omega_o)}{\omega_o \langle v \rangle} \right)^2 \right\} d\omega \qquad (4.25)$$

Since the emitted radiant power $P(\omega)d\omega$ is directly proportional to the number density $n_k(\omega)d\omega$ as given in Eq. (4.25), this leads to the intensity profile of a Doppler broadened spectral line, viz.

$$I(\omega) = I_o\, exp\left\{-\left(\frac{c(\omega - \omega_o)^2}{\omega_o\langle v\rangle}\right)\right\} \tag{4.26}$$

This describes the Gaussian line profile characterized by full linewidth Γ_D, where the FWHM is given by

$$\Gamma_D = 2\sqrt{\ln 2}\,\frac{\omega_o\langle v\rangle}{c} \tag{4.27}$$

Substituting the value of $\langle v\rangle$ from Eq. (4.21) in Eq. (4.27) yields

$$\Gamma_D = \frac{\omega_o}{c}\left(\frac{8k_B T \ln 2}{m}\right)^{1/2} \tag{4.28}$$

This quantity is known Doppler width and therefore Eq. (4.26) written in terms of Doppler width

$$I(\omega) = I_o\, exp\left\{-\left(\frac{(\omega - \omega_o)^2}{0.36\Gamma_D^2}\right)\right\} \tag{4.29}$$

From Eq. (4.28) it is clear that Doppler width is directly proportional to the transition frequency and to the square root of the temperature, and inversely proportional to the square root of the mass of the atom. Thus the largest Doppler widths are observed for high frequency spectral lines; high temperature sources; and light atoms, especially hydrogen and helium.

A comparison between Lorentzian and Gaussian line profiles is given in Figure 4.2. The line profiles have been normalized to the identical center frequency, identical maximum amplitude, and identical linewidth, thus facilitating comparison of their individual characteristics. It can be noted that the line kernels, that area of the line profile falling between the half-maximum points, are virtually indistinguishable. However, the properties of the wings are fundamentally different. Therefore at the wings the Lorentzian profile clearly has much larger amplitudes for large values of $(\omega - \omega_o)$ than does the Gaussian profile, this means that the intensity I approaches zero for large argument $(\omega - \omega_o)$ much faster for a Gaussian line profile than for a Lorentzian profile. Although the Gaussian linewidth is much larger than natural or Lorentzian linewidth of a spectral line even then the information about the Lorentzian line profile can be obtained from the extreme line wings. Furthermore the Doppler broadened line profile cannot be strictly represented by a pure Gaussian line profile. This is due to the fact that not all atoms with definite velocity component v_z emit or absorb radiation at the same frequency ω'. Due to the finite lifetimes of the energy levels, the frequency response of these atoms is represented by Lorentzian line profile. In our investigation of hyperfine structure of Praseodymium atoms and ions using laser spectroscopy the observed Doppler width is around 800 MHz, while the natural width is approximately 20 MHz.
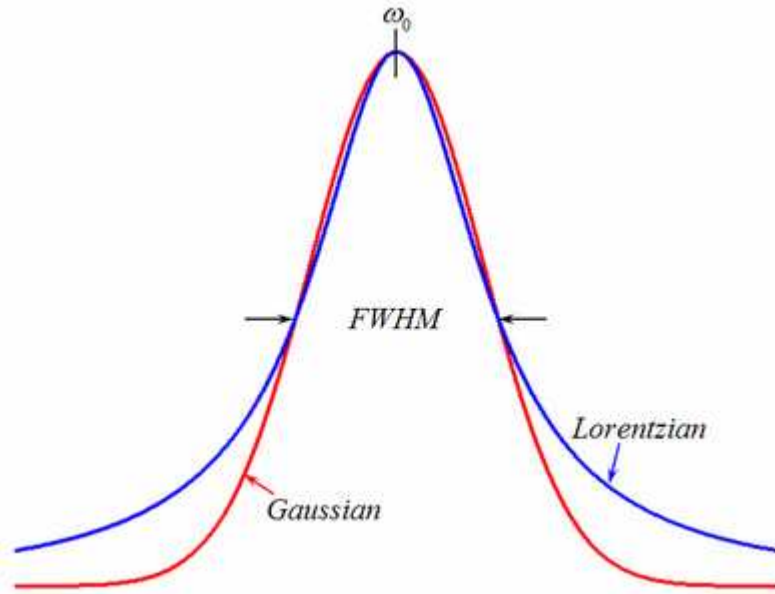
Figure 4.2: Comparison between Lorentzian and Gaussian line profile of equal halfwidth and equal height. The area below the curves is different.

4.1.3 Collisional or Pressure Broadening

An isolated atom will emit a spectral line of finite width. Contrary to this in any real source the atoms are subjected to the interaction forces of the neighbouring atoms, ions and electrons. This shifts the energy levels of the radiating atom and will lead to the broadening of the spectral line which is often greater than natural linewidth. The increase in linewidth depends on the density of the perturbing species and the broadening of the spectral line is known as collisional or pressure broadening.

Consider an ensemble of atoms at low pressure that is in an effective state of thermal equilibrium within the laboratory rest frame. Before addressing the effects of collisions on the spectral line profile, it is advantageous to discuss fundamentally two different kinds of collisions that occur between atoms within the ensemble. These can be distinguished as reactive or non-reactive in nature.

Chemical reactions between neutral atoms, ions or free electrons constitute reactive collisions. Such collisions change the chemical composition of the ensemble resulting in changes in the number densities of the various species present in the ensemble. This changes the intensities of the observed spectral features. Although such processes are important for excitation mechanisms leading to emission spectrum but have little relevance to the discussion of the effects of collisions on the spectral line profile. The reactive collisions are excluded as a consequence of the assumption that the atoms in the ensemble are chemically inert.

Non-reactive collision between two atoms or particles is the case in which the respective atoms or particles come into a finite separation such that the potential energies of one or both of the atoms changes which leads to changes in the energy level structure of the atoms.

Non-reactive collision is a complicated phenomenon which involves the electrostatic Coulomb interactions between each electron with both nuclei, the nuclear-nuclear Coulomb repulsion, and all electron-electron Coulomb repulsions. These interactions affect the electronic energy levels of the atoms of interest and thereby have an effect on the

40

observed spectrum of that atom. There are two general categories of non-reactive collisions i.e., elastic collisions and inelastic collisions. In an elastic collision only a change in the momentum and kinetic energy of the collision partners takes place and there is no change in the populations of the internal quantum states. An elastic collision between atom A in quantum state i and atom B is represented by the following stoichiometric equation:

$$A(v_1, i) + B(v_2) \rightarrow A(v_1', i) + B(v_2')$$ (4.30)
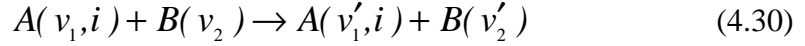
where v_1, v_2 are velocities before collision and v_1', v_2' velocities after collision of the colliding partners. The quantum state, *i*, of atom *A* is not changed in the elastic collision.

In an inelastic collision the internal quantum state populations of one or both of the collision partners change. Such an inelastic collision between atoms *A* and *B* with atom *A* in an initial quantum state *k* is also represented by a stoichiometric equation:

$$A(v_1, i) + B(v_2) \rightarrow A(v_1', k) + B(v_2') \quad i \neq k$$ (4.31)
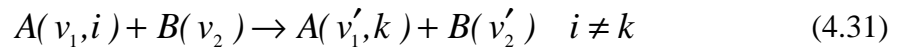
the atom *A* ends up in a different quantum state *k*. In an inelastic collision the internal energy of an atom can either increase or decrease, but the total energy of the system must be conserved such that:

$$E_i + \frac{\mu v^2}{2} = E_k + \frac{\mu v'^2}{2}$$ (4.32)

where E_i and E_k are the initial and final internal energies of the atom, μ is the reduced mass of the system. Inelastic collisions are often called quenching collisions when they decrease the number of excited level atoms and therefore quench the fluorescence intensity.

Now let the two atoms, *A* and *B*, separated by time-dependent distance $R_t(A,B)$. Further assume the energy levels of atom *A*, ψ_i and ψ_k, are influenced as the atoms first approach and then recede from one another. As the atoms approach and then separate from each other, the two energy levels of atom *A* can be differentially shifted in energy as a direct result of the varying Coulomb interactions which are functions of $R_t(A,B)$. Depending upon the internal structures of the respective collision partners, the electronic energy levels of atom *A* can be shifted either to higher or to lower energy during the time interval of the collisional interaction. An energy level will be shifted to higher energy if the interaction between atoms *A* and *B* is repulsive and it will be shifted to lower energy if the interaction is attractive.

Both elastic and inelastic collisions cause spectral line broadening. The elastic collisions may additionally cause a line shift which depends on the potential energy curves $E_i(R)$ and $E_k(R)$. The collisional broadening produces a Lorentzian line profile, the same as that of natural broadening. But it is of increased width. In order to avoid collisional or pressure broadening, the pressure in the spectral source should be kept low. By changing the pressure and observing the corresponding change in line width the information about the collisions occurring in the gas can also be obtained. The collisions which have large impact parameter cause noticeable line broadening but can also shift the line center.

4.1.4 Stark Broadening

The levels of atoms or molecules in the presence of electric field split into *(2J + 1)* stark components where *J* is the total angular momentum quantum number. This splitting of

levels and corresponding splitting of spectral lines is called Stark effect named after *J.* Stark who first studied this effect in 1913 for hydrogen atom. In gas discharges due to strong electrical fields experienced by atoms colliding with electrons and ions can also occur. This also contributes to total line broadening and is known as Stark Broadening.

4.1.5 Saturation Broadening

A laser of sufficiently high intensity operating at near resonant frequency can significantly change the population densities N_1 and N_2 of an atomic system by induced absorption and emission. This saturation of population densities also causes additional line broadening and is known as Saturation Broadening. Saturation broadening is also called power broadening. The spectral line profiles for saturation broadening are different for homogeneously and for inhomogenously broadened lines. For a homogeneously broadened spectral line, the line profile is Lorentzian and for inhomogeneouly broadened spectral line, the line shape is Gaussian.

4.1.6 Self-Absorption Broadening

Photons emitted in one region of a source may partly be absorbed when they pass other regions, of the source. These photons may be lost as a contribution to the original spectrum line either as a result of radiative decay to a different lower level or through collisional de-excitation of the absorbing atom. This process of re-absorption is known as self-absorption. Since the absorption profile is of the same shape as the emission profile, therefore energy is selectively absorbed from the emission line, i.e., the absorption coefficient is a maximum at the centre of the line or central wavelength. This means that the intensity of spectral line is reduced proportionately more in the center then elsewhere altering the line shape and making the line appear broader. This is termed as self- absorption broadening.

4.1.7 Combined Line Profile or Voigt Profile

In any experiment the different line broadening mechanisms contribute to the total line width of the emitted or absorbed spectral line. One can reduce a specific line width contribution by modifying experimental parameters, e.g. Doppler broadening can be reduced by cooling the ensemble of atoms by using liquid Nitrogen or water, pressure or collisional broadening is reduced by reducing pressure, by reducing the intensity of laser light saturation broadening can be minimized. Ultimately it comes down to natural line width which is limited by the finite lifetime of the energy state.

A spectral line profile $I(\omega)$ can be obtained which include contributions from all the broadening mechanisms i.e.,

$$I(\omega) = I_N(\omega) * I_D(\omega) * I_P(\omega) * I_S(\omega) \qquad (4.33)$$

Where

$I_N(\omega) \equiv$ Natural line profile

$I_D(\omega) \equiv$ Doppler line profile

$I_P(\omega) \equiv$ Pressure or Collisional line profile

$I_S(\omega) \equiv$ Saturation line profile

Natural and Collisional line broadening mechanisms have Lorentzian line shape, Doppler broadening has Gaussian Line shape, whereas Saturation broadening depending on homogeneous or inhomogeneous class give Lorentzian or Gaussian line shape. Therefore depending on line shape all the broadening mechanisms can be grouped into two classes i.e. Lorentzian and Gaussian types. So the combined line profile of a spectral line is a convolution of Lorentzian and Gaussian line profiles and is known as Voigt Profile, $I_V(\omega)$ i.e.

$$I_V(\omega) = I_L(\omega) * I_G(\omega) \tag{4.34}$$

where $I_L(\omega)$ is the Lorentzian line profile due to broadening mechanisms which give Lorentzian line shape, $I_G(\omega)$ is the Gaussian line profile due to broadening mechanisms which give Gaussian line shape. In our investigations of hyperfine structure of atoms and ions we mainly observe Gaussian line profile and rarely saturation broadening is observed as excitation probability is less then what is needed for saturation effect. However, in cases where excitation probability is high, saturation effects leads to saturation broadening and we observe Voigt line profiles.

4.2 Laser Light Source for Spectroscopic Investigations

Lasers as coherent and monochromatic light sources for excitation, have significant advantage over the conventional light sources. Some of the characteristics are listed below:

- High spectral power density, significantly improve the signal-to-noise ratio and by using this characteristic nonlinear spectroscopic techniques can be explored.

- Due to small divergence of the collimated laser beam, long path length through the absorbing sample can be obtained.

- Extremely narrow spectral linewidth of lasers is particularly advantageous for high resolution spectroscopy. In laser spectroscopy usually the spectral linewidth of the absorbing or emitting atoms or molecules determines the resolution of the spectroscopic technique.

- Continuous tunability over wide range of frequencies has made lasers an alternative to conventional intense light sources and ultrahigh resolution spectrometers.

Laser basically consists of three components (a) active medium, where population inversion takes place, (b) energy pump (for example flash lamp or electrical discharges) that generates population inversion, (c) optical resonator which stores the light emitted by active medium in few modes of the radiation field. Different frequencies at which the laser resonator oscillates are determined by two factors:

- the gain profile of the amplifying medium
- eigenfrequency spectrum of the resonator

Without any wavelength selective elements inside the laser cavity, laser oscillation on all resonator modes are possible with wavelengths within the gain profile above threshold because for all modes gain exceeds the total losses. This is true for resonators which have completely inhomogeneous gain profile such that no gain competition occurs between different modes. On the basis of the width of the gain profile, lasers can be classified as:

(i) ***Fixed wavelength or fixed frequency lasers*** where laser wavelength is restricted to a narrow gain region such as in gas lasers, for example He-Ne lasers, or in solid-state lasers, for example Nd:YAG lasers.

(ii) ***Multiline fixed wavelength lasers***. In this case the active medium shows gain on several transitions and the laser can oscillate simultaneously on many lines. In this case also the wavelength of each line is restricted to its narrow gain range. For example Argon-ion laser or Krypton-ion laser with multiline operation.

(iii) ***Tunable lasers***. Here the gain profile extends over a broad spectral range of laser wavelength that can be tuned continuously over a wide range. For example dye-lasers, where stimulated emission from the excited state to many vibronic levels of the electronic ground state is possible.

The difference between fixed wavelength lasers and tunable lasers lies in the width of the tuning range which is narrow for the "fixed wavelength" lasers and broader for the so called "tunable" lasers.

4.2.1 Energy Level Diagram of a Dye Molecule

In the visible part of electromagnetic spectrum dye lasers are by far most widely used excitation sources for doing laser spectroscopy. The main advantage is their continuous tunability over a wide range of frequencies.

Active media in dye lasers are organic dye molecules dissolved in liquid solvents and, upon irradiation by visible or UV light, show a strong broad-band fluorescence spectrum. Figure 4.3 is an energy level scheme of an organic dye molecule showing rovibronic singlet *(S)* and triplet *(T)* states.

Dye molecules are pumped from rovibronic levels of the ground singlet state S_o to higher rovibronic levels of excited singlet state S_1. Collisions with the solvent molecules induce a fast radiationless transition to the lowest rovibronic level of S_1 state with relaxation times of 10^{-11} to 10^{-12} s. This level is depopulated either by spontaneous emission into different rovibronic levels of ground state S_o or by radiationless transition into the lower triplet state T_1. Transition to the ground state S_o determines the laser frequency. Due to strong interaction of dye molecules with the solvent the fluorescence spectrum of dye molecules is continuous rather than discrete, in essence this gives a continuous tunability over the wide range of frequencies.

High pump intensity ensures a population inversion between the rovibronic level v_o of S_1 and higher rovibronic levels v_k of S_o which have negligible population at room temperature, due to its small Boltzmann factor $exp[-E(v_k)/kT]$. As soon as the gain on the transition $v_o(S_1) \rightarrow v_k(S_o)$ exceeds the total losses, laser oscillation starts. The lower level $v_k(S_o)$ which now is populated by stimulated emission, is depleted rapidly by collisions with the solvent molecules to the lowest vibrational level v_o of the ground singlet state S_o.

The population inversion between S_o and S_1 is strongly affected by transitions from S_1 into the long-living triplet state T_1. Furthermore, transitions from lower triplet state T_1 into higher triplet states can also take place. To minimize these effects, molecules with populated state T_1 should be removed from the laser active zone in a time scale much shorter than the life-time of T_1. One way of doing this is by forming a flat stream of dye solution (dye jet) in a nozzle and inserting this free jet in the cavity, where the path inside the cavity and the focused pump beam overlap. At high enough pressure, the time of flight of the dye through the active region satisfies the above condition.
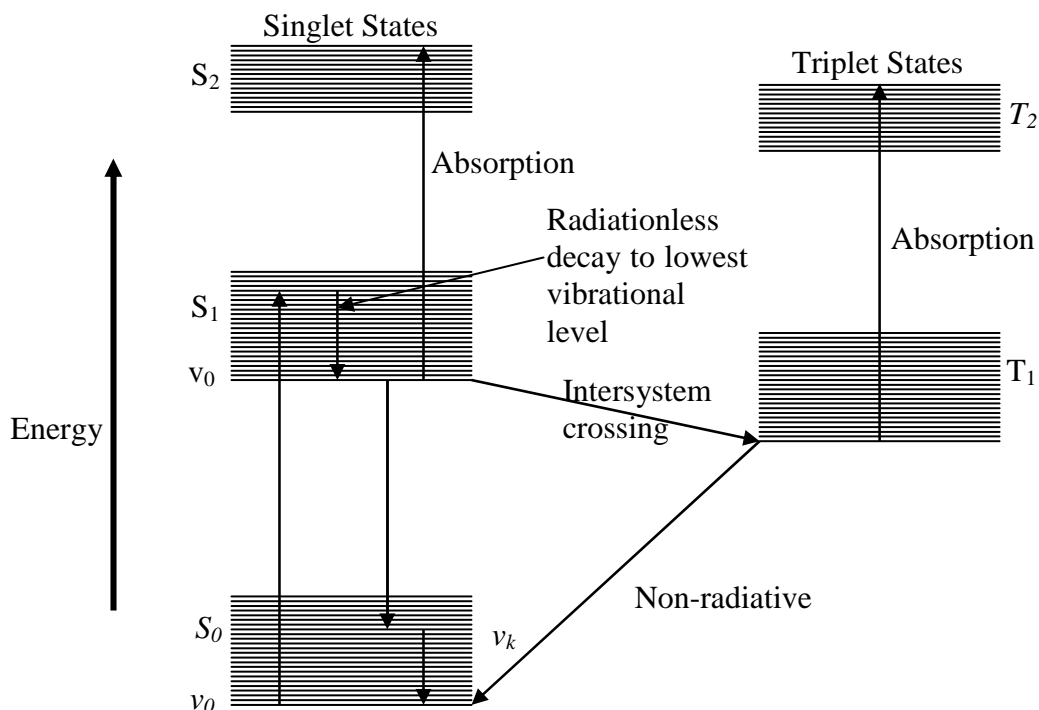
Figure 4.3: Energy level diagram of an organic dye molecule

4.2.2 Ring Dye Laser

Active medium in a ring-dye laser system (see Figure 4.4) is a thin liquid jet of the dye solution oriented at Brewster angle for avoiding reflection losses. A pump beam which is focused by a spherical mirror onto the dye jet excites the dye molecules in the jet. Four mirrors *M1*, *M2*, *M3* and *M4* are used which closes the laser beam path on to itself forming a ring resonator arrangement with a running laser wave only in one direction. Transmissivity of *M4*, which is the output coupler, depends on the dye being used. In contrast in a linear dye laser system a standing wave is established in the cavity. The advantage of ring-cavity scheme over linear scheme is that no nodes of the electromagnetic field within the jet are present and whole inversion of the active medium can contribute to the laser amplification. Unidirectional propagation of laser wave is achieved by inducing more losses for one direction as compared to the other. This can be achieved by a unidirectional device known as optical diode. An optical diode consists of a Faraday glass in a longitudinal magnetic field and a polarization rotator, which turns the birefringent rotation back to the input polarization for the wave incident in one direction, but increases the rotation for the other direction. Waves with incorrect polarization direction suffers large losses at the many Brewster surfaces in the resonator cavity and therefore do not reach the threshold. Mirror *M2* is mounted on a Piezo-Electric Transducer *(PZT)* also known as tweeter mirror and a Galvo or Brewster Plate is inserted in front of the output coupler *M4* inside the laser cavity. Both these elements work in conjunction with each other for tuning the laser wavelength. To select one of the modes of laser cavity, a number of mode selection elements with different finesse and free spectral range (FSR) are inserted. These include birefringent filter and two Fabry-Perot etalons, i.e. a thick etalon and a thin etalon.

A Birefringent filter is a Lyot type filter consisting of more than one quartz plate each plate being four times the thickness of the previous one and inserted at Brewster angle in the

cavity. The Birefringent filter has low finesse and an FSR of the order of THz. Due to its low finesse the birefringent filter alone cannot select a single mode of the laser cavity. Therefore thin and thick Fabry-Perot etalons are also placed inside the cavity. Thin etalon is a glass plate of 0.5 mm thickness with a reflectivity of $R \approx 20$ % and is inserted at close-to-normal incidence. Last of the mode selection elements is the thick etalon which is a 10 mm solid prism etalon and is divided into two parts. It is piezo driven and is also inserted at nearly normal incidence. Thick etalon also has a reflectivity of $R \approx 20$ % and is most effective in selecting one mode of laser cavity. The FSR of both thin (200 GHz) and thick (10 GHz) etalons is in GHz.
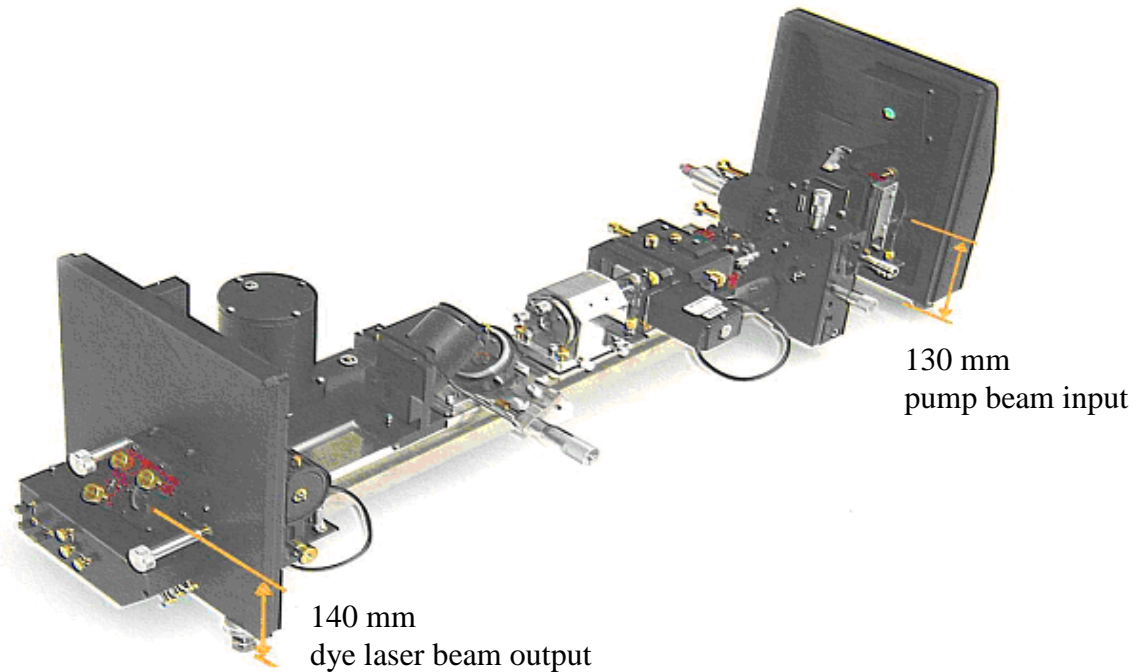
Figure 4.4: Ring Dye laser system

        Optical layout   : Coherent Inc.

        Mechanical Layout: Institute of Experimental Physics, TU Graz

Proper alignment of etalons and laser cavity avoids any sudden jumps in laser frequency. This sudden jump in laser frequency is known as "mode hopping". In addition to misaligned etalons and laser cavity, mode hopping may also be due to thermal fluctuations, turbulence in the dye jet, presence of microbubbles in the dye jet etc. In order to avoid mode hopping and to perform frequency stabilization, thick etalon and laser cavity each need an electronic feedback loop. This feedback signal or the "error signal" is generated by a temperature stabilized confocal external reference cavity. With the help of a beam splitter mounted outside the laser cavity, a fraction of the linearly polarized laser beam is passing through the reference cavity and detected by a photodiode known as reference diode. Another fraction of the main laser beam is directly reflected to a second photodiode known as power diode which is used to detect the total power level. A side-locking technique is used in which laser wavelength is directly locked to one side of a transmission peak of the confocal reference cavity. Therefore the signal from reference photodiode acts as an error signal for the feedback loop. To avoid intensity fluctuations the signal from the reference photodiode is divided by the total power level using the signal from the power diode. The error signal generated is then divided into a low frequency and high-frequency parts. The high-frequency part is feedback to the tweeter mirror *M2* whereas low-frequency part is

used to drive the Galvo plate. Both these tuning elements allow changing the length of the cavity for stabilizing the frequency of laser.

If the transmission peaks of all these elements are tuned to same wavelength λ, the laser will oscillate at this wavelength as a single mode laser. Laser wavelength can be scanned continuously without mode hopping if all the elements are synchronously tuned using this electronic feedback control system.
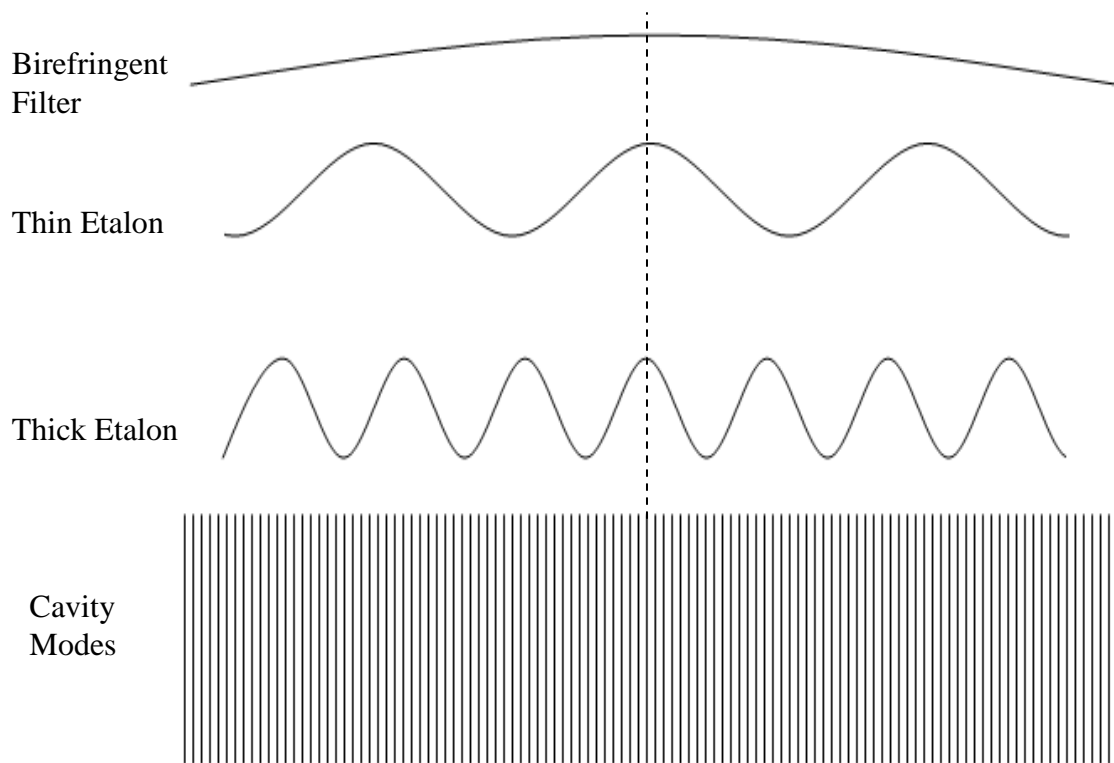
Figure 4.5: Transmission curves for Birefringent filter, thin etalon and thick etalon

4.3 Laser Spectroscopy

Classical absorption spectroscopic techniques utilizing conventional radiation sources with broad emission continuum (for example high pressure Hg arcs or Xe flash lamps etc.) are mainly limited by detection sensitivity and in spectral resolution which in turn is limited by the resolving power of the apparatus profile. The detection sensitivity defined as minimum detectable absorbed power is limited by the detector noise and intensity fluctuations in radiation source. In classical absorption spectroscopy a collimated beam of light is passed through an absorption cell containing the sample to be investigated. Absorption of light at specific frequencies occurs inside the absorption cell. Using a dispersing device the intensity of the transmitted light $I_T(\lambda)$ is measured as a function of wavelength. By comparing the intensity of the transmitted light beam with the intensity of the reference beam $I_R(\lambda)$, the absorption spectrum of the sample is obtained.

Contrary to absorption spectroscopy in laser spectroscopy the radiation sources with broad emission continuum are replaced by tunable laser sources with extremely narrow line width. Tunable lasers offer a wide spectral region extending from UV to IR with extremely

narrow bandwidths and with power densities much greater than conventional incoherent light sources. Therefore due to high power densities and extremely narrow line width of lasers, high detection sensitivity and high spectral resolution are achievable in laser spectroscopy. Some of the main features of laser spectroscopy are listed below:

The absorption coefficient $\alpha(\omega)$ and its frequency dependence can be measured directly from the difference $I(\omega) = aI_R(\omega) - I_T(\omega)$ ('a' represent reflection losses) between the intensities of the reference beam and transmitted beam. A monochromator is not required. With the use of tunable single-mode lasers the spectral resolution is much higher than in conventional spectroscopy and is only limited by the line width of the absorbing transition.

i. Due to high power density achievable with lasers, the detector noise is generally negligible. This increases the signal-to-noise ratio and enhances sensitivity.

ii. Because of low divergence long absorption paths are possible by multiple reflections back and forth through the absorption cell. Such long absorption paths facilitate the measurements of transitions with small absorption coefficients.

iii. By allowing a small fraction of main laser beam to pass through a Fabry-Perot interferometer with a separation d of the mirrors, a photodetector receives intensity peaks each time the laser frequency v_L is tuned to a transmission maximum of interferometer at $v = mc/2d$. These equal spaced intensity peaks serves as accurate wavelength markers which allow measurement of adjacent absorption lines. The separation between two adjacent transmission maxima or this wavelength interval is called free spectral range of interferometer (FSR).

iv. The laser frequency may be stabilized onto the center of an absorption line. The need for frequency stabilization can be relaxed if the frequency jitter is small compared to absorption line width.

v. It is possible to tune the laser frequency over the spectral region of interest. For example the transitions between hyperfine levels of two fine structure levels can be observed in a single scan of laser.

vi. With high intensity and small laser line width appreciable population in selectively excited states can be achieved. This is advantageous for doing absorption and fluorescence spectroscopy of excited states.

Despite of all the above advantages the achievable resolution is finally limited by finite line width of the absorption line. This could be due to the natural line width of the atomic or molecular levels, as energy levels have an energy uncertainty related to their finite life time, or it may be due to the Doppler broadening of the absorption line which is caused by the thermal motion of atoms or molecules, usually $\Delta v_D \approx 100\Delta v_N$ for gases. Spectroscopic techniques in which Doppler broadening limits the achievable resolution are known as Doppler limited techniques. In these techniques primarily the level structures are determined without any regard to their finer details such as their hyperfine structure. Two photon absorption spectroscopy, optogalvanic spectroscopy, optical double resonance and level crossing spectroscopy are few examples of Doppler limited laser absorption spectroscopy.

In Doppler free high resolution spectroscopy extremely narrow band single mode lasers are utilized. The collimated atomic beam spectroscopy and saturation spectroscopy are the examples of the Doppler free absorption spectroscopy. The saturation spectroscopy is based on nonlinear spectroscopic techniques.

4.3.1 Two-Photon Spectroscopy

In 1929, Maria Göppert-Mayer predicted theoretically that an atom might absorb two or more photons simultaneously. She subsequently first published the concept in her doctoral dissertation [41] in 1931. The prediction allows an electron to make a transition to states unreachable by single photon absorption. Because the effect could only be observed with a very intense beam of radiation so her prediction could not be investigated experimentally until the construction of the first laser in 1960.

Two-photon excitation can be described as two successive one-photon excitations. Excited levels with same parity can be reached via two-photon excitation. The probability that two photons are absorbed simultaneously is extremely low. Therefore a very high density of photons is required usually using a pulsed laser. In a simple case of single photon transitions, the selection rules for such transitions are such that the change in angular momentum $\Delta J = \pm 1$. When an atom absorbs two photons simultaneously, the electron will change angular momentum by $\Delta J = 0$ or ± 2, this is due to the fact that each photon has an angular momentum of +1 or -1.

Two-photon excitation can be distinguished either as a step-wise excitation with intermediate eigenstate where two photons are in resonance with the successive excitations, or it is a simultaneous absorption of two photons with an intermediate virtual state, undergoing a transition from $E_i \rightarrow E_f$. Two photons may either come from a single laser beam passing through the absorbing sample or they may come from two separate lasers. These virtual states are not eigenstates and do not correspond to specific n or l state. Instead, they are merely superpositions of waves. No population of electrons accumulates in virtual state. The lifetime of a virtual state is short, relative to eigenstates. Actually, the closer the virtual state is to an actual eigenstate, the longer the lifetime of the virtual state. Nevertheless, the above mentioned transition rules hold also for virtual levels.

In an atom or molecule at rest, two photons with energy $\hbar\omega_1$ and $\hbar\omega_2$ either coming from two laser beams, or two photons with energy $\hbar\omega$ from the same laser, induce a transition from an initial level $\langle i |$ to the final level $\langle f |$, using conservation of energy; viz.

$$E_f - E_i = \hbar(\omega_1 + \omega_2) \tag{4.35}$$

For an atom or molecule moving with velocity v, the frequency ω of the light wave is shifted in the atomic or molecular frame to

$$\omega = \omega' - \vec{k} . \vec{v} \tag{4.36}$$

Therefore the resonance condition given in Eq. (4.35) becomes

$$\left| E_i - E_f \right| = \hbar(\omega_1 + \omega_2) - \hbar\vec{v}(\vec{k}_2 + \vec{k}_2) \tag{4.37}$$

Now if the two photons come from the two beams of the same laser but traveling in opposite direction, i.e. $\omega_1 = \omega_2$ and $\vec{k}_1 = -\vec{k}_2$ then as a consequence the last term in Eq. (4.37) vanishes. This implies that the absorption of two photons becomes independent of the velocity of atoms or molecules. This means that all atoms or molecules independent of their velocity group contribute to the two photon absorption, making two-photon absorption Doppler-free. Experimentally the two-photon absorption is monitored by laser-

induced fluorescence emitted from the upper level E_f by an allowed one-photon dipole transition into a lower level E_m.

As the laser frequency ω is tuned over the two-photon resonance, the resulting signal consists of a narrow peak produced by two photons with opposite $\vec{k}$ vectors and a Doppler-broadened background produced by two photons coming from the same beam with parallel $\vec{k}$ vectors. The main characteristics of two photon spectroscopy:

- Optical transitions which are parity forbidden by a single photon excitation can be excited via a two photon transitions.

- The final state may have an excitation energy in the far UV, while the incident light beam has a frequency in the near UV or visible region,

- By proper combination of participating photons, it is possible to eliminate momentum transfer between electromagnetic fields and atoms or molecules, this allows one to get Doppler free spectrum. However the cross section of two photon absorption is usually very small compared to that of a direct transition, this make this process not of general use.

4.3.2 Saturation Spectroscopy

Saturated absorption spectroscopy is a precision spectroscopic technique and is one of the frequently used techniques for measuring narrow-line atomic spectral features, limited by saturation broadening and by the natural linewidth Γ of the transition. In all the labs involved with laser cooling and trapping of atoms, the technique of Doppler-free saturated absorption spectroscopy is frequently used as a tool for locking the lasers to particular atomic lines. The first saturation spectroscopy experiments using a tunable narrow-band laser were performed by Hänsch, Schawlow [42-43] and co-workers and by Borde [44].

A monochromatic laser beam with frequency ω propagating in x direction passes through a vapor cell containing an ensemble of atoms or molecules. Since the atoms are in thermal motion with velocity distribution given by Maxwell-Boltzmann statistics, so the Doppler-broadened absorption profile is of Gaussian line shape with center frequency ω_o. Atoms which are Doppler-shifted into resonance with the laser frequency can absorb the laser photons with Doppler shifted frequency given by $\omega = kv_x$ and inducing a transition from an initial level i to the final level f. The population N_i of these atoms in the absorbing level decreases whereas population N_f in the final level increases accordingly. Therefore a narrow dip is burnt in the velocity distribution $N_i(v_x)$ of these atoms in initial level and correspondingly a narrow peak appears in the distribution $N_f(v_x)$ of atoms in the upper level.

In saturation spectroscopy instead of a single laser beam two counter propagating laser beams derived from the same laser with frequency ω_L are sent through the vapor cell. The experimental setup is as shown in Figure 4.6. The laser beam from a tunable laser source is split by a beam splitter BS into a strong pump beam and a weak probe beam that passes through the absorption cell in opposite direction. The probe and pump beams must have a good overlap inside the absorption cell. The pump beam is intensity modulated by a mechanical chopper and the modulation frequency is fed into the lock-in amplifier as reference frequency. A detector sees the transmitted probe beam intensity as a function of the laser frequency ω_L whose output goes to the lock-in amplifier as second input.

Laser frequency is tuned over the Doppler-broadened absorption profile of the ensemble of atoms moving with different velocities. When the laser frequency ω_L coincides with the

center of absorption line ω_o, only one velocity class in the interval dv_x around $v_x=0$ interacts with the laser beam.
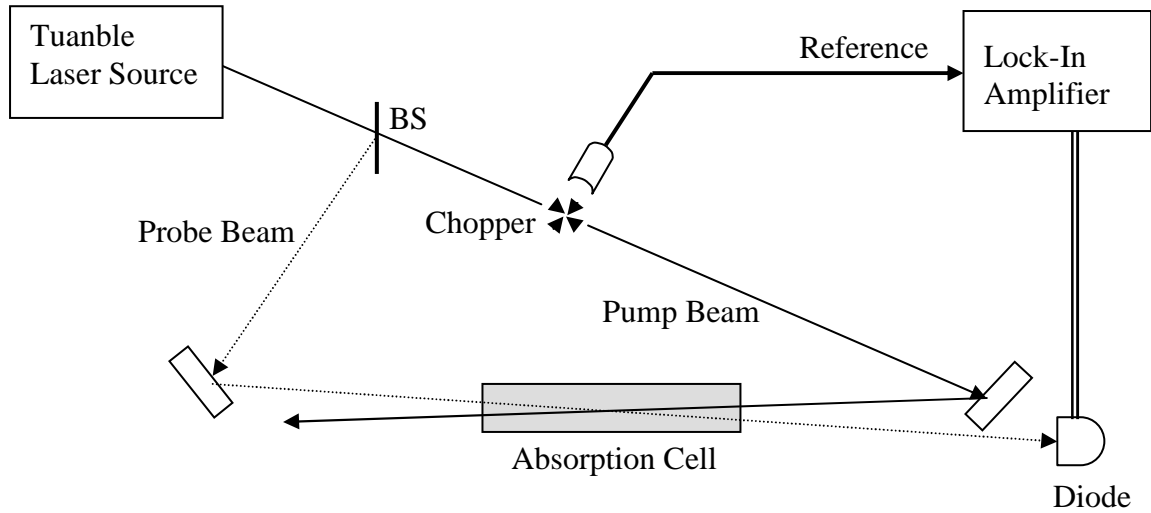
Figure 4.6: Experimental setup for saturation spectroscopy

The pump beam is strongly absorbed, depleting the population in the initial level *i* with corresponding increase in the population of the final level *f*. A narrow hole or dip is burnt in the velocity distribution $N_i(v_x)$ of the initial level and a corresponding narrow peak appears in the distribution $N_f(v_x)$ of atoms in final level. The absorption coefficient $\alpha(\omega)$ with a Doppler-broadened profile has a dip around the center frequency ω_o. The counter propagating weak probe beam interacts with atoms whose absorption is saturated by the strong pump beam, resulting in a sharp decrease of absorption of the weak probe beam at the center of the line. The intensity of the probe beam is modulated only when the probe beam is responsive to the hole burnt in the Doppler profile by the strong modulated pump beam. The modulated part of the probe beam intensity recorded by a phase sensitive lock-in amplifier depends only on the saturated absorption and is not sensitive to the unsaturated part of the Doppler profile. The dip at the center of Doppler-broadened absorption profile caused by the saturation of the population, which is probed by the second weak probe beam is called Lamb Dip named after Willis Lamb who first explained this effect quantitatively. Since the detector measure the intensity of the transmitted probe beam so each time Laser frequency coincides with the center frequency of atomic transition, a Lamb peak appears in the transmitted intensity, because the absorption exhibits a dip at this frequency.

For monitoring laser induced fluorescence (LIF) signal two counter propagating laser beams must be of equal intensity and the Lamp dips can seen easily. The total LIF intensity is proportional to

- Laser intensity

- Number density in the initial sate

- Einstein coefficient for absorption, and

- Quantum yield (ratio of the number of photons to the number of photons absorbed

Obviously the Lamb dip is much narrower than the Doppler width. If the intrinsic frequency width or linewidth of the laser used in the experiment is small enough, the

observed width of the Lamb dip is always limited by saturation broadening. The Doppler-broadened background can be eliminated when the pump beam is periodically chopped. A lock-in detector measures the difference of the transmitted probe intensity with the pump beam on and off. The result is a Doppler-free spectrum with a better signal-to-noise ratio.

4.3.3 Collimated Atomic Beam Spectroscopy

In 1936, long before the invention of lasers, D. A. Jackson and H. Kuhn [45] experimentally investigated the absorption in atomic beams. In their work the absorption was analyzed by means of a high resolution Fabry Perot interferometer. The first application of atomic or molecular beams in laser spectroscopy was described S. Ezekiel and R. Weiss [46].

In high resolution spectroscopy a typical atomic beam experiment is performed by irradiating a well collimated atomic beam at right angles with a narrow-band, single-mode laser. The advantage of this method comes from the fact that the atoms in the collimated beam do not have velocity components in the direction of laser beam. Doppler width is reduced by the collimation ratio C (Figure 4.7) and very small absorption width of atoms is formed.

The main characteristics of atomic beam spectroscopy are:

- An atomic beam can be produced easily for any element.

- The Doppler width is reduced by a factor of *sin(ε)* which is equal to the collimation ratio.

- The number of collisions are small subsequently collisional broadening is reduced. This is because all atoms have almost same velocity so fewer collisions occur as compared to a gas at equivalent pressure.

- Fluorescence light radiates in 4π steradians and very few of them reach the photodetector.
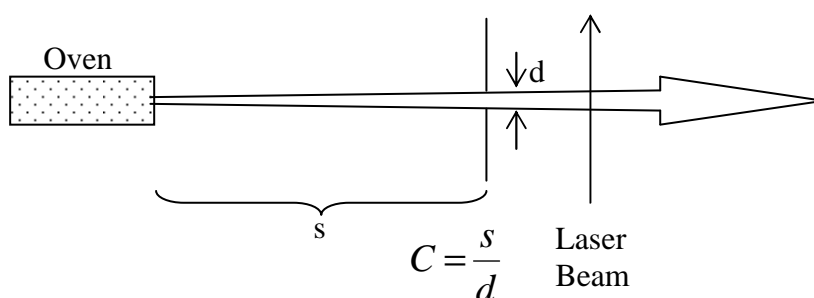
Figure 4.7: Collimation Ratio C

Detection techniques:

> *Detection by fluorescence:* The most direct way to study the optical resonance is to observe fluorescence light, released after excitation.

> *Detection by photoionization:* Here the atomic beam interacts simultaneously with a narrow band laser and an intense laser. The narrow band laser brings the atoms to an excited state and an intense laser, having sufficient energy, ionizes the atoms in excited states. The photoelectrons or the ions are detected in an electron detector [47]. This process has also been demonstrated for isotopes separation [48].

Detection of recoil atoms: When an atom absorbs a photon, the momentum of the photon is transferred to the atom. As a result the atom is deflected from the beam. In the de-excitation process the recoil momentum transferred either is cancelled (stimulated emission) or is transferred to the atomic beam (spontaneous emission). The latter result in a spreading and broadening of the atomic beam. The deflection of an atomic beam was first demonstrated by R. Frish in 1933 [49]. A. Ashkin [50] proposed to use this technique for isotope separation. P. Jacquinet et al. [51] first time recorded the hyperfine structure by beam deflection for the sodium D lines.

Detection of change in magnetic sublevels in an atomic beam deflected by an inhomogenous magnetic field: The first application of the magnetic resonance principle was made with the introduction of atomic beam magnetic resonance technique by I. I. Rabi, J. R. Zacharias, S. Millman, and P. Kusch in 1938 [52]. They discovered that any change in magnetic sub levels of an atom in the atomic beam can be detected by a change in the deflection of the beam in an inhomogeneous magnetic field. In 1952 I. I. Rabi [53] suggested that this technique could be used in the study excited states if atoms are illuminated resonantly in the interaction region. He also suggested that this method could be used to study isotope shifts. In 1965 Marrus [54] used Rabi's arrangement and by using the change in magnetic sub levels of ground state he detected and measured optical transitions.

4.3.4 Laser Induced Fluorescence (LIF) Spectroscopy

Laser induced fluorescence (LIF) is one of the powerful spectroscopic techniques for investigating the spectra of neutral atoms and ions. LIF technique offers the advantage of selective excitation not only from the excited states but also from the ground states and provides high resolution only limited by the linewidths of the absorbing transition. The principle is very simple and is as follows: Laser beam is allowed to pass through an absorption chamber containing atoms or molecules to be investigated. One or several photons from the laser beam are absorbed, provided that the laser frequency is in resonance with the atomic or molecular transition. The probed atoms or molecules are pumped from an initial state *(i)* to an excited state *(f)* and the atoms or molecules thus excited can relax or de-excite in a number of ways for example by spontaneously emitting light or by collisional de-excitation. Thus a transition takes place from the excited state *(f)* to final state *(k)* and in the process the spontaneously emitted light constitutes a fluorescence signal. Employing good collection geometry, part of the emitted radiation is detected. By means of a dispersing device such as a monochromator, it is possible that the light is detected at a wavelength different from the laser wavelength meaning that the states *(i)* and *(k)* are different. This eliminates any spurious signal due to scattered laser light. The dispersing device also serves to reduce the background radiation. Since the fluorescence signal is laser induced so such a spectroscopic investigation of atoms and molecules is known as **laser induced fluorescence spectroscopy**.

Dye lasers have narrow linewidths and are easily tunable over large wavelength domains, LIF measurements can be made by tuning the laser frequency across the atomic or molecular resonances and capturing the resulting fluorescence signals. The fluorescence intensity recorded as a function of the laser wavelength is usually called an excitation spectrum. The observed fluorescence intensity reflects the change of population of the upper excited state *(f)*. The strength of the signal depends on a number of factors such as laser intensity, number of atoms or molecules, temperature of ensemble of atoms or

molecules and also on the collisional environment of the investigated atoms or molecules.

When exciting sufficiently higher lying states, a number of fluorescence wavelengths are observed due to the decay to lower states according to allowed dipole transitions as shown in Figure 4.8. The strength of a LIF signal is determined by the branching ratio of the upper excited level. The hyperfine transition of the LIF lines does not play any role, since the monochromator selecting one LIF line does not resolve the hyperfine structure of this line, but acts only as a filter to suppress other lines of the discharge.

This dissertation is mainly dedicated to the investigation of the hyperfine structure of the fine structure energy levels characterized by a number of parameters such as level energy, parity, total electronic orbital angular momentum J and nuclear spin I. Besides these other parameters of interest are the hyperfine constants and Lande 'g' factor. These parameters characterize a specific energy level.

4.3.4.1 Detection of LIF Signal and Decay Mechanisms

LIF signal is monitored by a technique called phase-sensitive detection. The lock-in amplifier is tuned to the modulation frequency (reference frequency) which is the chopping frequency of the incoming excitation light beam. The detail of this electronic detection of LIF signal is as follows:

Laser frequency is tuned across hyperfine components of a line and those atoms which are in resonance with the laser light are excited. This modulates the population of the levels involved in the transition which results in the modulation of fluorescence intensity of only those fluorescence lines originating from the levels involved in the excited transition. These modulated fluorescence lines are selected by tuning the transmission wavelength of a monochromator across the spectrum. The optical signal is detected by a Photomultipler tube mounted at the exit slit of the monchromator. Finally phase sensitive detection is carried out by a phase sensitive lock-in amplifier which has two input signals (i) modulated fluorescence intensity (ii) modulation or chopping frequency of the laser beam. These two signals are combined; this has an advantage that only those fluorescence lines which are in-phase with the modulation frequency of the laser beam are detected. As a result the modulated and non-modulated fluorescence lines are distinguished. The other advantage of phase sensitive detection by lock-in amplifier is the distinction between fluorescence lines originating from the upper or from the lower transition levels. Accordingly as the modulation phases of the fluorescence lines are in phase or out of phase with respect to intensity modulation phase of the laser beam. This can be understood as follows. The intensity of a fluorescence line is proportional to the population of the upper level of the fluorescence line. Laser induced absorption increases the population of the upper level of the excited transition in phase with the modulation frequency of the laser beam therefore the fluorescence lines originating from the upper level are also in phase. At the same time laser induced absorption also diminishes the population of the lower level of the excited transition and thus the corresponding fluorescence lines originating from lower level are antiphase modulated i.e. are 180 degrees out of phase compared with the intensity modulation phase of the laser beam. According to experimental terminology the fluorescence lines originating from the upper level of an excited transition are termed as **positive fluorescence** and the fluorescence lines originating from the lower level are termed as **negative fluorescence**.

Figure 4.8 shows a simple scheme of transitions between various levels. The observed fluorescence lines can be categorized in the following manner:

(i)   ***Fluorescence with positive LIF Signal:*** Due to the resonant transition from lower

level E_2 to the upper level E_3, the population of excited level E_3 increases and at the same time population of lower level E_2 decreases. A subsequent decay occurs to more than one lower levels i.e. E_4 and E_5 by emitting fluorescence light of wavelengths λ_{34} and λ_{35}. Laser frequency is modulated at a chopping frequency 'f' which acts as a reference frequency for phase-sensitive detection (Lock-in amplifier). If LIF signal and reference frequency are in phase, maximum LIF signal is observed. Since the LIF signal intensity increases with laser light on, this type of fluorescence is called a **positive phase** or a **positive fluorescence**. This type of fluorescence which is observed as a result of decay from the upper level of excited transition is also termed as direct fluorescence.

(ii) ***Impact or Collisional Coupling:*** If other level energies lie close to a level populated or depopulated by laser light, the probability of impact or collisional transfer of population is high. In such a situation through impact or collision an excited state atom transfers its energy to another atom whose excited level energy happens to lie close by which subsequently decays to lower level by emitting fluorescence light. This type of fluorescence is also positive phase fluorescence. As shown in Figure 4.8 due to an impact a population transfer occurs from E_3 to E_6 which decays to E_7 by emitting a fluorescence wavelength λ_{67}. This is an indirect fluorescence as it is observed due to decay from an upper level which is not directly excited in original transition. Population transfer between lower levels, E_2, E_8 is also possible.

(iii) ***Negative Fluorescence:*** In situations where the lower level of a certain transition is high lying as compared to very low lying levels, this lower level decays to the further low lying levels by emitting fluorescence light. Such LIF signal is negative in phase and is known as **negative fluorescence**. In Figure 4.8 for the resonance excitation from E_2 to E_3 some of the atoms in lower level E_2 decay to level E_1 by emitting a fluorescence wavelength λ_{12}. The population of level E_2 decreases when the laser light is on and the fluorescence observed has 180° phase shift as compared to a positive fluorescence. Negative fluorescence wavelengths are useful in identifying the lower level of an excitation transition. Furthermore if exact fluorescence wavelengths are determined the lower level of fluorescence decay can also be identified.

(iv) ***Self-absorption:*** Usually in optically thin light sources the photon emitted by the spontaneous emission has a little chance of being re-absorbed. For spectral lines involving ground state of the atom this assumption in most cases breaks down. Especially true for spectral lines arising due to combination between the ground state and the lower excited states. These are very strong lines and are called resonance lines. For such lines it may happen that a photon emitted by an atom at one point in a light source may be re-absorbed by a different atom before it has a chance to escape from the source. This phenomenon is known as self-absorption. It can happen if the photon which is being re-absorbed has an energy coincidence with the energy difference of the two levels involved in the re-absorption excitation. Due to self-absorption line shape changes, making it appear broader. Since the probability of emission is greatest at the center of the line, the probability of absorption is also greatest at the center. Thus as a result of re-absorption within the light source, the intensity of the spectral line decreases proportionately more in the center of the line than elsewhere. If the self-absorption is strong, then an intensity minimum develops in the center of the spectral line and the line is said to be self-reversed.
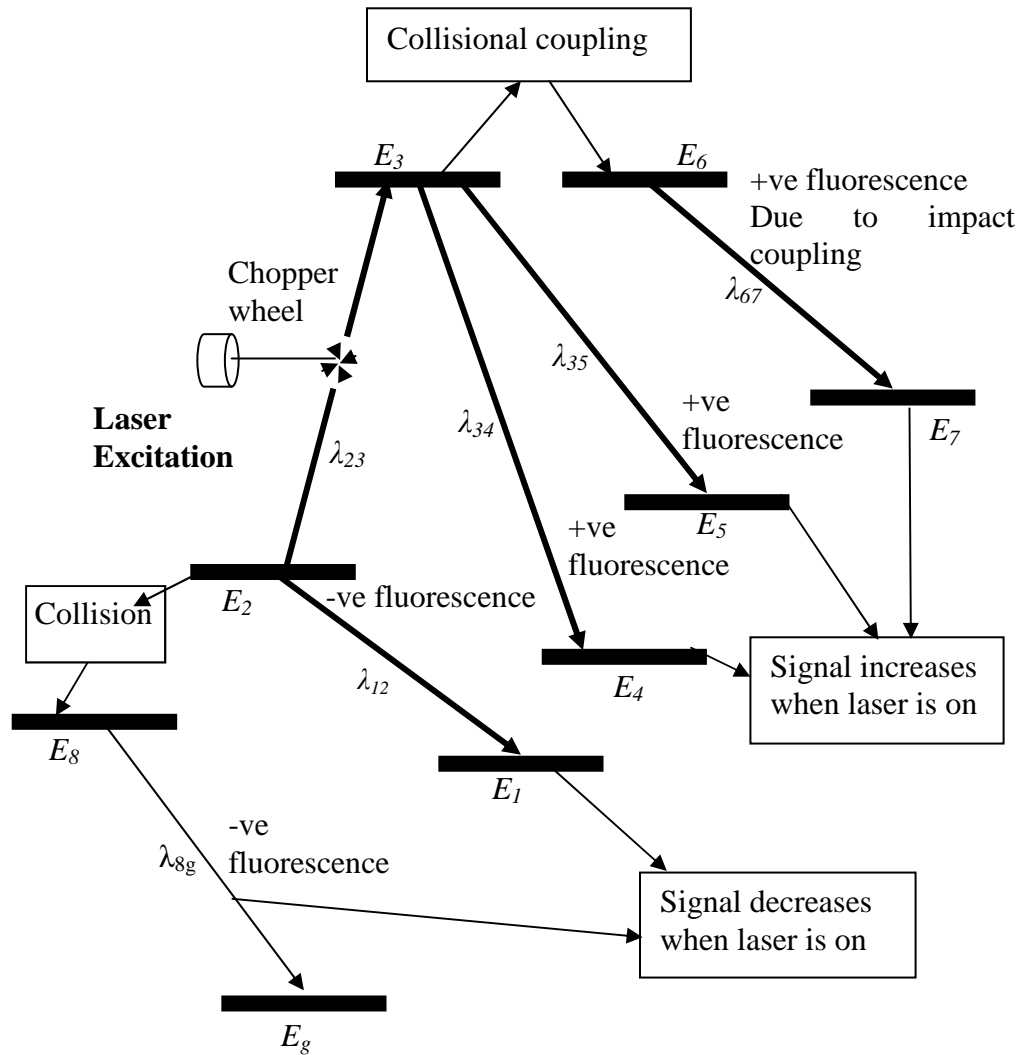
Figure 4.8: Direct and collisionally coupled LIF signals

4.3.4.2 Advantages of LIF Spectroscopy

- *Blend situation:* In elements like praseodymium where there are regions of high energy level density, more than one level is excited simultaneously in a single range of laser. So the observed LIF patterns corresponding to all excited levels show a complex structure caused by this blend situation. LIF spectroscopy has the advantage that individual transition lines can be separated by searching for fluorescence decay channels corresponding to a specific upper level. In this way the hyperfine structure of each line can be recorded and the level energy is determined by using the information from the recorded structure, wave number of the excitation line and the energy of lower level.

- *LIF signal of free atoms:* In a hollow cathode discharge it is easier to produce free atoms than free ions, therefore LIF signal of an atomic line of comparable intensity should be stronger than that of an ionic line.

- *Large laser intensity:* Availability of lasers with high intensities makes it possible to achieve of large population densities in the excited states, yielding high intensities of the fluorescence lines even for transitions with low transition probabilities.

- **_Higher sensitivity for Fluorescence Signal:_** Using Lock-in techniques higher sensitivity is achievable for the fluorescence signals as compared to absorption measurements.

4.3.5 Optogalvanic Spectroscopy

In 1928, F. M. Penning [55] discovered the light induce changes in the electrical properties of plasma. He observed a perturbation of a gas discharge caused by the light of a second discharge. This effect as a spectroscopic tool had to await till the invention of tunable dye laser. In 1976 Green et al. [56] gave the first spectroscopic investigation of this effect, named it as an 'optogalvanic effect'. They used a commercially available hollow cathode lamp as a gas discharge tube. Laser light is tuned to the transition frequency of one of the species present in the discharge. The effect was apparent as a change in the tube voltage. The use of this effect opened a new branch of spectroscopy know as Optogalvanic Spectroscopy which is a very sensitive and simple technique of performing laser spectroscopy in a hollow cathode gas discharge. The standard experimental setup is shown in Figure 4.9.
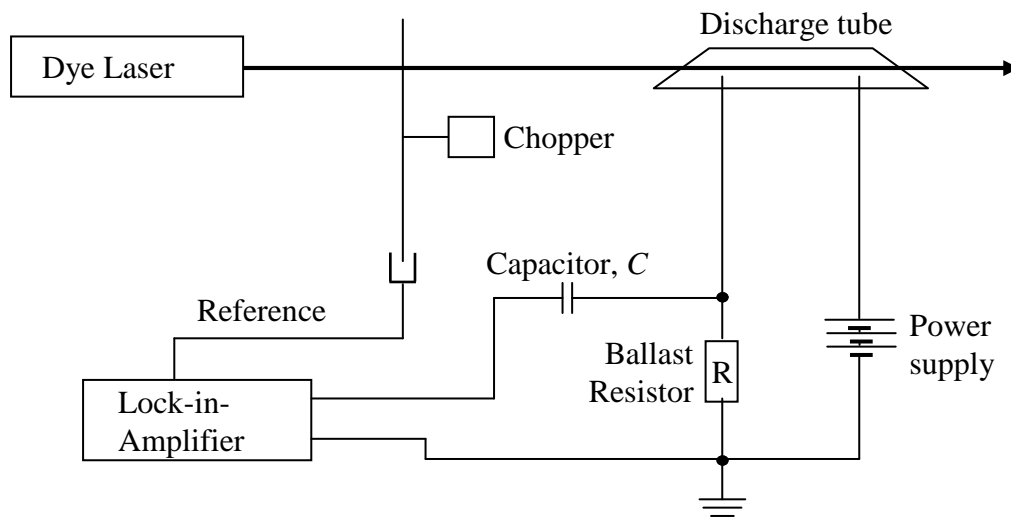
Figure 4.9: Experimental setup for Optogalvanic Spectroscopy

Laser frequency is tuned to a resonance transition $E_i \rightarrow E_f$ between levels of atoms or ions in a hollow cathode discharge. Due to excitation a change in the population densities $n_i(E_i)$ and $n_f(E_f)$ of the combing levels occurs. Since atoms in different stationary states E_i and E_f have different ionization probabilities this change in population results in a change of discharge current ΔI which could be detected as a voltage change $\Delta V = R\Delta I$ across the ballast resistor R. In order to have a good signal-to-noise ratio, the excitation is done by mechanically chopping the laser beam and a lock-in amplifier is used for phase-sensitive detection. Periodic changes in tube voltage can be detected by connecting one of the electrodes via a capacitor C to the input of the lock-in amplifier. The effect is more pronounced for high lying levels as they have a reasonable probability of collisions and ionization compared to low lying levels. Both positive and negative signals are observed, depending on the levels E_i and E_f involved in the laser-induced transition $E_i \rightarrow E_f$. Since the absorbed laser photons are detected by optically induced current change of discharge, therefore this sensitive technique for doing spectroscopy is so named as Optogalvanic Spectroscopy.

Several competing processes may contribute to ionization of an atom in level E_i. Some of them are discussed below:

(i)   Direct ionization by electron impact

$$A + e^- \rightarrow A^+ + 2e^- \tag{4.38}$$

This process dominates at low pressure.

(ii)   Two step ionization or multi step ionization:

$$A + e^- \rightarrow A^* + e^-, \; A^* + e^- \rightarrow A^+ + 2e \tag{4.39}$$
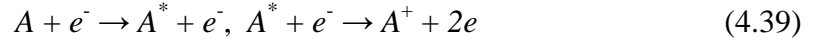
In noble gases this process is particularly important if excited states are metastable states.

(iii)   Collisional ionization by metastable atoms:

Two atoms in metastable states collide with one another; one of the atoms absorbs sufficient energy and becomes ionized

$$A^* + B^* \rightarrow A^+ + B + e^. \tag{4.40}$$

4.3.5.1   Advantages/Disadvantages of Optogalvanic Spectroscopy

(i)   The experimental setup is very simple since it does not require a monochromator and a detector such as photomultiplier tube or photodiode detector to obtain the investigated spectra. This is because the discharge itself acts as a detector.

(ii)   Only excitation wavelength is required no need to monitor fluorescence signal.

(iii)   The substantial disadvantage of this type of spectroscopy is unstable discharge condition. For recording optogalvanic signal the discharge must be burning very calmly.

(iv)   The optogalvanic signal has nothing to do with the fluorescence light, hence nothing can be said about the levels involved in the transition. Of course the excitation probability and thus the hyperfine structure of the excited transition are mirrored in the OG signal.

4.3.5.2   Application of Optogalvanic effect

(i)   Determination of the hyperfine constants by exciting classified lines.

(ii)   When exciting an unclassified line, OG signal can help in recording the hyperfine structure of the line, and to place the laser frequency when later searching for LIF lines.

(iii)   To study the collision process and ionization probabilities in a gas discharge.

(iv)   This technique can be used for wavelength calibration in laser spectroscopy [57].

(v)   The study of Rydberg states is also possible by optogalvanic spectroscopy [58].

(vi)   It is very efficient for the investigation of Autoionizing levels [59].

(vii)   The optogalvanic signals may be used for laser frequency stabilization [60-61].

5 Experimental Setup

Invention of intense, highly monochromatic, tunable lasers with good frequency and intensity stabilization covering UV, visible and infrared regions have revolutionalized the field of experimental atomic spectroscopy in an unprecedented way. This results in a transition from classical spectroscopy to laser spectroscopy which is far more superior in terms of sensitivity, resolution and measurement accuracy. The present work is based on the investigation of spectral lines of praseodymium using laser induced fluorescence spectroscopy in a hollow cathode discharge lamp, where free Pr atoms and ions are produced in ground and excited states. These excited atoms and ions decay to lower states by emitting light which is recorded as a fluorescence signal. Excitation by direct absorption of electromagnetic radiation is only possible if the resonance condition $\Delta E = h\nu$ is fulfilled. Apart from the metastable states the lifetime of excited states is of the order of 10^{-8} sec. so the excited states decay spontaneously by emitting electromagnetic radiation at discrete frequencies. A dispersing device resolves the emitted radiation into components or discrete lines. The observed spectrum (distribution of intensity as a function of frequency or wavelength) is characteristic for a specific element. Using high resolution techniques, the hyperfine structure of the spectral lines can be investigated, provided that the spectral lines have sufficiently high intensity. A large number of spectral lines must be experimentally investigated to have a complete and reliable knowledge of the electron structure of the emitting atom. This requires a high resolution spectrum from UV to far infrared. Such a high resolution spectrum is a Fourier Transform (FT) spectrum which is being used in our research group for the investigation of spectral lines of praseodymium, tantalum, lanthanum, and neodymium.

5.1 Experimental Layout

Laser Induced Fluoerescnce (LIF) spectroscopy in combination with a hollow cathode lamp (HCL) is a sensitive and widely used technique for hyperfine structure investigations of various elements. This method of investigation is useful since, in addition to the information about the hyperfine structure of the spectral line under investigation, one also obtains information on the fluorescence wavelengths which mark the excited upper level. Naturally occurring praseodymium has only one stable isotope and in most cases hyperfine splitting of a fine structure level is large enough, therefore LIF spectroscopy in a HCL is particularly efficient and even with large Doppler width the hyperfine structure spectrum of Pr is quite legible.

The experimental setup for LIF spectroscopy in HCL is shown in Figure 5.1 which can be divided into three major sections.

i. Excitation source
ii. Sample whose spectrum has to be investigated
iii. Detection system

Ar-ion laser operating at 7.5 watts was used to pump the dye laser. The lasing action in dye laser produces laser light which has a certain range of wavelengths depending on the type of dye used for lasing. By adjusting different optical elements, the laser can be set to any wavelength or frequency within this spectral range.

The single mode laser light from a tunable dye laser is splitted into two parts by beam splitter B1. The minor portion of the beam falls on beam splitter B2 which further divide it into two parts. One part of the beam after reflection from mirror M1 goes into wavemeter

for reading wavelength and the other part is again splitted into two parts by beam splitter B3. One portion goes to the spectrum analyzer to monitor the mode structure of laser and the other portion after reflection from M2 goes to marker etalon.
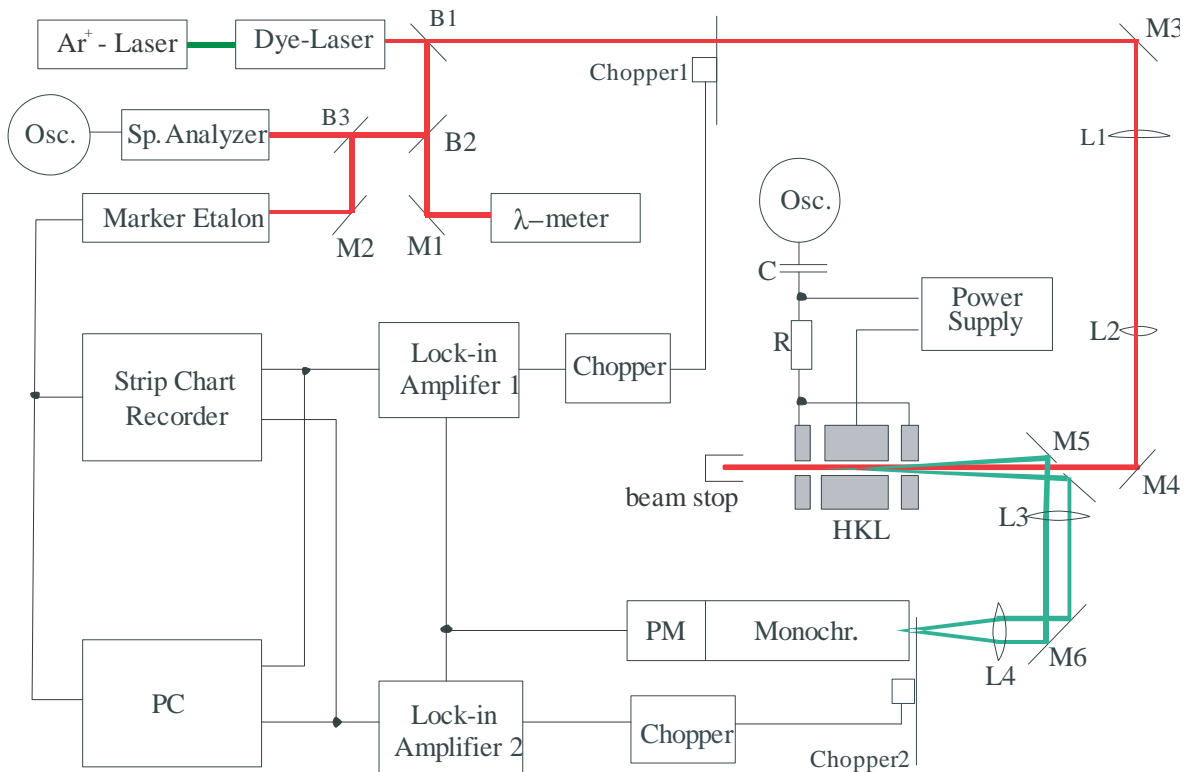
Figure 5.1: Schematic representation of experimental setup

HKL...Hollow Cathode Lamp, M1-M4, M6-M7...Mirrors, M5...Mirror with central hole, L1-L4 lenses, B1-B2...Beam splitters, Ar$^+$-Laser...Pump Laser, Dye-Laser...Ring Dye Laser, Osz...Oscilloscope, Sp. Analyzer...Spectrum-Analyzer, Marker Et…Marker etalon for measuring frequency markers, λ–meter...Wavemeter, Monochr...Monochromator, R...Ohmic resistance, C...Capacitive reactance

The major portion of the laser beam passes through a mechanical chopper 1 which modulates the intensity of the laser beam. The intensity modulated laser light after reflection from mirror M3 passes through a telescope arrangement of lenses L1 and L2 and goes through a hole in mirror M5 to the hollow cathode lamp. Inside the hollow cathode the sputtered Pr atoms and ions are excited by laser light at resonance.

The fluorescence light that leaves the HCL is collected by mirror M5 and directed to the entrance slit of a monochromator by a set of mirrors and lenses. A tunable monochromator (Jobin Yvon HRS 2) with tuning range from 300-750 nm is used to filter single LIF wavelength out of a total florescence spectrum. A photomultiplier tube (Hamamatsu R955) with high sensitivity for the visible spectrum is mounted at the exit slit of monochromator which allows the detection of extremely low fluorescence signal changes. A mechanical chopper 2 placed in front of the entrance slit of monochromator is used to chop the fluorescence light intensity coming from the hollow cathode lamp. This is used in case, if we need a more accurate measure of the fluorescence wavelengths.

The frequency spacing between various hyperfine components of the recorded hyperfine structure must be measured exactly. For this a small portion of the laser beam is given to a temperature stabilized confocal Fabry-Perot interferometer which gives equidistant frequency marks along with the hyperfine structure of the spectral line. Conventionally such a device is known as a marker etalon. The difference between the adjacent transmission peaks of the marker etalon is known as Free Spectral Range (FSR) and its magnitude is dependent on a specific interferometer. The interferometers available in our laboratory for blue, red and yellow regions have FSRs 150.2976 MHz, 149.7 MHz and 367.33 MHz, respectively. The LIF signal together with the signal from marker etalon is recorded simultaneously on a computer as well as on a strip chart recorder for further analysis.

5.2 Excitation Source

The source of exciting radiation for the investigations of the hyperfine structure of Pr-spectral lines is cw (continuous wave) single mode tunable ring dye laser optically pumped by Ar^+-Laser, Kr^+-Laser or by diode pumped, frequency doubled Nd:Vanadate (Nd:YVO$_4$) Verdi V-18 laser system. Noble gas ion lasers such as Ar^+-Laser or Kr^+-Laser are not very efficient due to high energy requirement. This is due to the fact that the atoms are first ionized and only after ionization, a population inversion can be established in the ion population. Despite of high energy requirements, the ion lasers are advantageous mainly because

   i.   The optical gain of plasmas is very high. This makes laser oscillation easy to achieve.

   ii.   Ion lasers provide numerous lines in the visible and UV part of the spectrum.

For Ar^+-Laser, a number of different wavelengths are emitted simultaneously but the strongest are at 488 and 514.5 nm. Kr^+-Laser as pumping laser produces about nine lines in the range 476-800 nm, with the 647.1 nm being the most intense. The Verdi laser produces single frequency light at 532 nm. For pumping the ring-dye laser system, the power of pump laser range from 4 to 7.5 watts.

Single mode cw tunable laser frequency operation can be achieved by using various laser dyes. The lasing action in dye laser produces a broad frequency spectrum and to obtain a stable single mode laser light within the spectral range of dye, various mode selective elements in ring-dye laser cavity are tuned synchronously. Frequency stabilization is achieved by locking the laser wavelength to a very stable external reference cavity.

The wavelength regions of different laser dyes which were used for the investigation of spectral lines of Pr are:

Laser dyes	range / nm
Stilbene 3	420 – 460
Rhodamine 6G	560 - 620
Sulforhodamine B	598 – 650
DCM	630 - 690
LD 700	690 – 780

5.3 Hollow Cathode Lamp

A hollow cathode lamp (HCL) is a kind of glow discharge lamp and is an efficient light source producing comparatively narrow spectral lines. The width of emission lines from HCL is usually limited only by Doppler Broadening.

HCL was first used by Paschen [62] for the investigation of spectral lines of helium. Hollow cathode made by Paschen consists of central cathode with two anodes. Schüler [63-64] also used a HCL however it had one anode. Feldmann [65] was the first who introduced a discharge with clear path through the electrodes. Later on Miyazaki et al. [66] modified Feldmann design by placing the hollow cathode between two hollow anodes. Behrens and Guthöhrlein [67-68] also developed modified Schüler-type hollow cathode for generating atoms of the various elements under investigation.

Hollow cathode lamps are used in a variety of applications, for example in ion etching, thin film deposition, surface treatment, ion gas lasers and in spectroscopic analysis. In spectroscopy, HCL can be used as emission source, allowing direct excitation and analysis of a sample or as light source in absorption spectroscopy because of its sharp and intense spectral lines.

In case of metallic samples, the whole cathode is made up of the material to be investigated. On the other hand, for non metallic sample, a hollow cylindrical piece of the material is well fitted into a copper or aluminum hollow cylinder. In this case the cathode itself does not or very little contribute to the discharge. An advantage of hollow cathode is that the plasma is more localized inside the cathode which increases the efficiency of excitation. Furthermore, the metal concentration obtained by sputtering is far enough sufficient for spectroscopic purposes.

The home made HCL especially designed for the spectroscopic investigations of the hyperfine structure of spectral lines of praseodymium consist of several parts. The central element of the HCL is a copper tube into which an axially hollowed cathode is screwed which is filled on the inner wall with praseodymium. The typical length of the cathode is approx. 20 mm with optimum inner bore diameter of 3 mm. Two axially hollow anodes made of aluminum are placed on both sides of the hollow cathode. The anodes are electrically insulated from the metal tube and also from the cathode using ceramic holders. The separation between anode and cathode is approximately 0.75 mm. The anodes, the cathode and the ceramic parts had coaxial hole of almost same diameter which serve as a path for laser beam.

The copper tube together with the cathode and anodes is enclosed in a glass tube which extends symmetrically at both ends forming the actual discharge container. The anodes are provided with conducting pins, led to the outside of the device through a feedthrough. The ends of glass tube are sealed by the two circular quartz glass plates acting as windows of hollow cathode lamp. The complete hollow cathode lamp is shown in the Figure 5.2.

Before the discharge is switched on, the device is normally evacuated for 10-12 hours by a rotary vane pump to create a good vacuum. Hollow cathode lamp is then filled with argon as a carrier gas at a pressure ranging from 0.3-0.8 mbar depending on the type of specie to be investigated i.e. neutral atoms and ions, region of investigation and discharge conditions. Discharge current is typically 60 mA and DC voltage varies from 350 to 650V. HCL with vacuum system is shown in Figure 5.3.
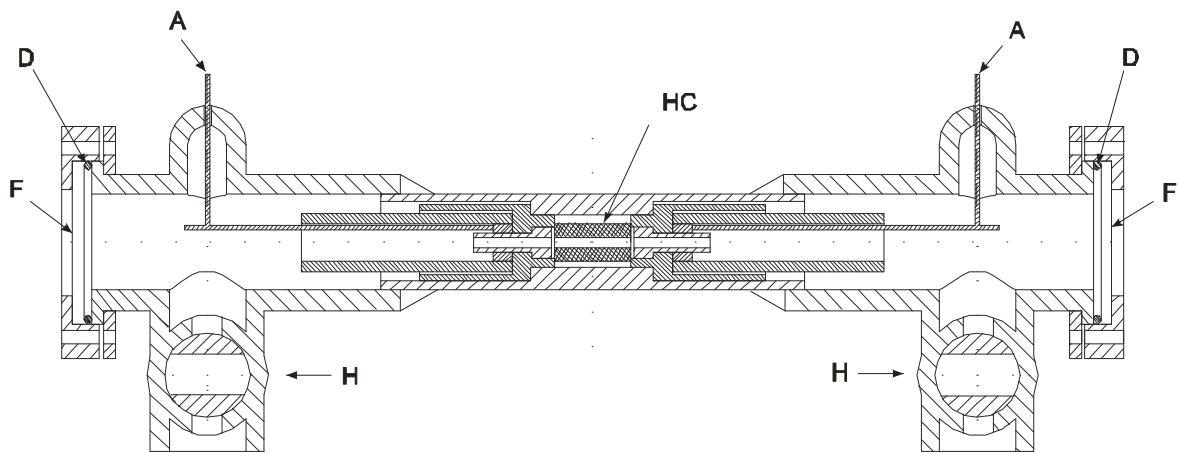
Figure 5.2: Hollow cathode lamp HC...Hollow Cathode, A…Anode current feedthrough F…Quartz windows, D…O rings, H…Glass stop cocks
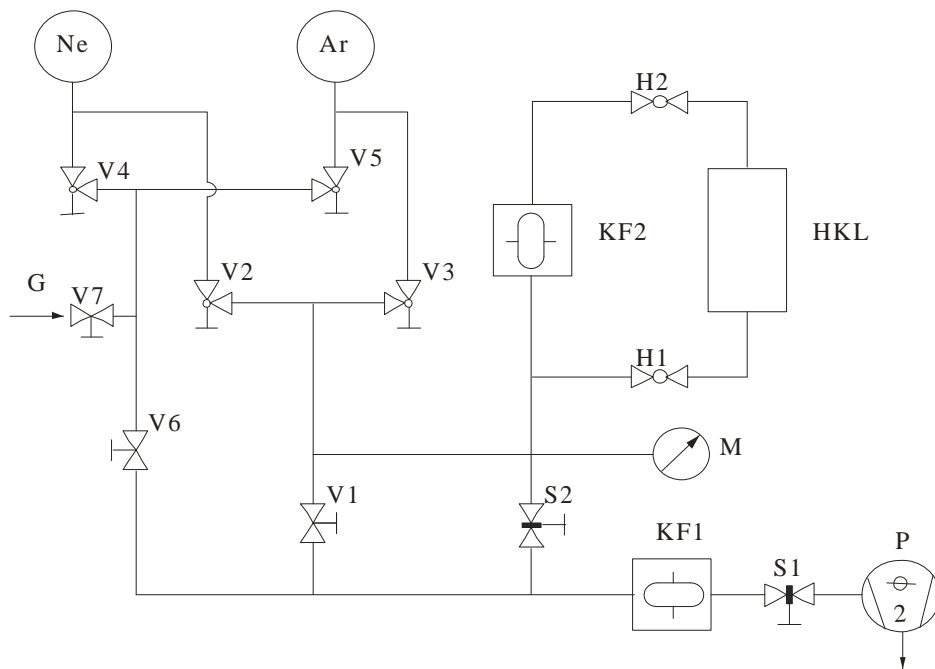
Figure 5.3: Schematic design of the vacuum system

HKL...hollow cathode lamp, H1 H2…Glass stop cocks, S1-S2...Slide valves, V1-V7...Shut-off and gauge valves, KF1, KF2...Cold traps, M...Manometer, P...Two-stage rotary vacuum pump, G...Gas inlet, Ne...Reservoir for Neon, Ar...Reservoir for argon.

A DC voltage applied across the discharge lamp ionizes the buffer gas into positive ions and electrons. The field distribution around the co-axial hole is such that the discharge burns down into the hole. The carrier gas ions are accelerated and hit the inner wall of the cathode material which in our case is praseodymium. If the bombarding ions have sufficient energy which is in excess of the binding energy of the atoms of the cathode material then the atoms can be ejected from the surface. This process is called cathode sputtering. The probability that an atom or an ion is ejected from the cathode surface is

defined by sputtering yield. Sputtering yield is "the number of sputtered particles per incident particle as a function of the energy and the identity of the incident particle". Both mass and energy of the incident particle are important factors which govern the sputtering yield. For example an incident Ar ion has a higher sputtering yield with lower energy threshold as compared to the Ne ion which has a lower sputtering yield with higher energy threshold for the same kind of sputtered material.

The sputtered species consists predominantly of ground state neutral atoms, and a small fraction of excited atoms and ions. The ejected atoms may be excited or ionized due to collisions with the energetic ions and electrons of the discharge with broad range of energies.

This broad-band collision induced excitation mechanism in the hollow cathode discharge give rise to a highly excited plasma having a population distribution predominantly among various atomic energy states. This makes HCL particularly useful to investigate the level schemes of high lying states using LIF technique. For example in case of Pr levels up to 35000 cm^{-1} above the ground state can be investigated. The cloud of free atoms and ions both in ground and excited states gives an intense light emission with a color which is characteristic of the sputtered material. For a stable discharge, the HCL is cooled by liquid nitrogen. The nitrogen cooling results in a reduction in the thermal velocities of the sputtered species which greatly reduces the Doppler width of the spectra. For Pr the typical Doppler width is around 800 MHz.

5.4 Measurement and Fluorescence Detection

The laser induced fluorescence signal is detected and measured by means of a lock-in amplifier using phase sensitive detection technique. A lock-in amplifier is a very sensitive instrument and is able to detect very weak AC signals as low as a few nanovolts. DC signal such as photomultiplier tube dark current are not amplified. This is done by a technique known as phase sensitive detection which filters out the component of the signal at a specific reference frequency and phase. In fluorescence signal measurements, the phase of the signal is tuned such that lock-in amplifier output is maximum. This would correspond to a signal that is in phase with the intensity modulated laser excitation wavelength. In this way, even very low intensity LIF signal in an extremely noisy environment can be observed and recorded.

In our experimental setup (Figure 5.1) the intensity of the incoming laser beam is modulated by a mechanically chopper 1 and the modulation frequency is given as reference frequency to the lock-in amplifier. Initially the phase of the lock-in amplifier is set by means of a known LIF signal. This is done by first tuning the laser frequency to the strongest hyperfine component of a spectral line and setting the transmission wavelength of the monochromator to a detection line having a strong LIF signal.

The experimental investigations of the hyperfine structure of the spectral line is performed in two steps. In first step the laser frequency is set to one of the hyperfine components of the line, usually to the strongest hyperfine component and the transmission profile of the monochromator is varied to search the fluorescence lines originating from the levels that are involved in the excitation of line (Figure 5.4).
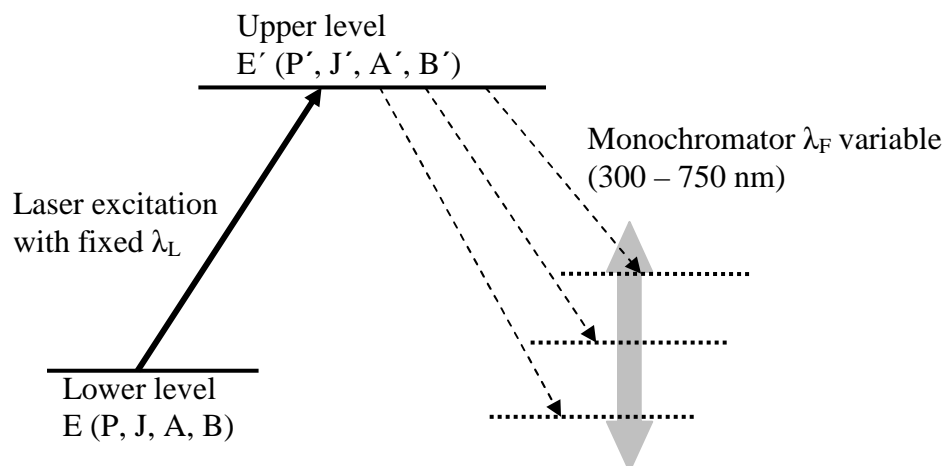
Figure 5.4: Searching for fluorescence lines

In the second step, the hyperfine structure of the spectral line is recorded using the observed fluorescence wavelengths. For this purpose the monochromator is set to a pre-selected transmission wavelength, which were observed previously in the first step, and laser frequency is scanned (~ 45 GHz) across the hypefine components of the spectral line (Figure 5.5). In order to avoid laser stray light a detection line for laser induced fluorescence is chosen which is different from the excitation line. In this way, the hyperfine structure of the excitation line together with the information of fluorescence wavelengths is studied.
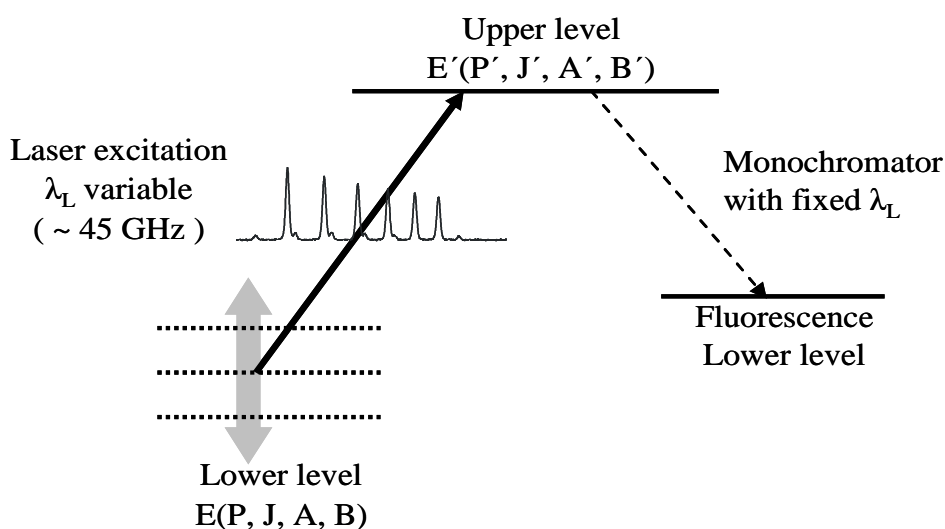
Figure 5.5: Recording the hyperfine structure of a spectral line.

The nominal reading precision of the monochromator used is about 1 Å, but sometimes it is necessary to determine the fluorescence line wavelength more accurately. This is done by placing a second chopper wheel in front of the entrance slit of the monochromator. This modulates the intensity of fluorescence light coming from HCL. The output signal of the photomultiplier is given to a second lock-in-amplifier, with the modulation frequency of second chopper as a reference. Laser frequency is tuned to the strongest hyperfine component of the excited transition, and the grating monochromator is automatically scanned over a certain spectral range.

The output signals of both lock-in-amplifiers are recorded simultaneously on separate traces. In this way the spectrum of HCL can also be used to calibrate the monochromator wavelength scale. Comparison of the recorded hollow cathode spectrum with the corresponding part of FT-spectrum gives the wavelength of LIF line with an accuracy of ±0.05 Å despite the relatively low resolution of the monochromator. Accurate measure of fluorescence wavelengths is also beneficial in situations where the excited transition could not be identified meaning in the involved transition both lower and upper level could be unknown. In such cases fluorescence wavelength information provides a clue to identification of the upper level.

5.5 Fourier Transform Spectrum

The progress of Fourier transform (FT) spectroscopy has made it possible to record spectra with resolutions down to 0.01 cm^{-1}, over spectral ranges from the ultraviolet (~ 2000 Å) to the infrared (~ 5μm). Such spectra are characterized by a very high accuracy of wavenumbers assignable to the observed lines and by a wide dynamic range of intensities. A further advantage is that the spectrum is available in electronic form, which makes it easy to handle the data and to fit the hyperfine patterns using shape functions for the individual hyperfine components.

The FT-spectrum of praseodymium was recorded in the Institute of Quantum Optics at the Leibniz University in Hanover Germany as a part of a diploma thesis [25]. This was done by continuously scanning high resolution FT-IR spectrometer model number IFS 120 HR. A hollow cathode discharge lamp was used as an emission source and the emitted light is focused on to an entrance slit of the FT spectrometer. The recorded Fourier-transformed emission spectrum covers a very wide region ranging from 2380 Å to 12500 Å. The resolution of the recorded spectrum is a convolution of the instrumental profile and the Doppler width of the spectral lines. Multiple scans were taken and were then averaged to improve the signal-to-noise ratio and to get a typical resolution of 0.03 cm^{-1}. A small portion of a spectrum is shown in Figure 5.6.
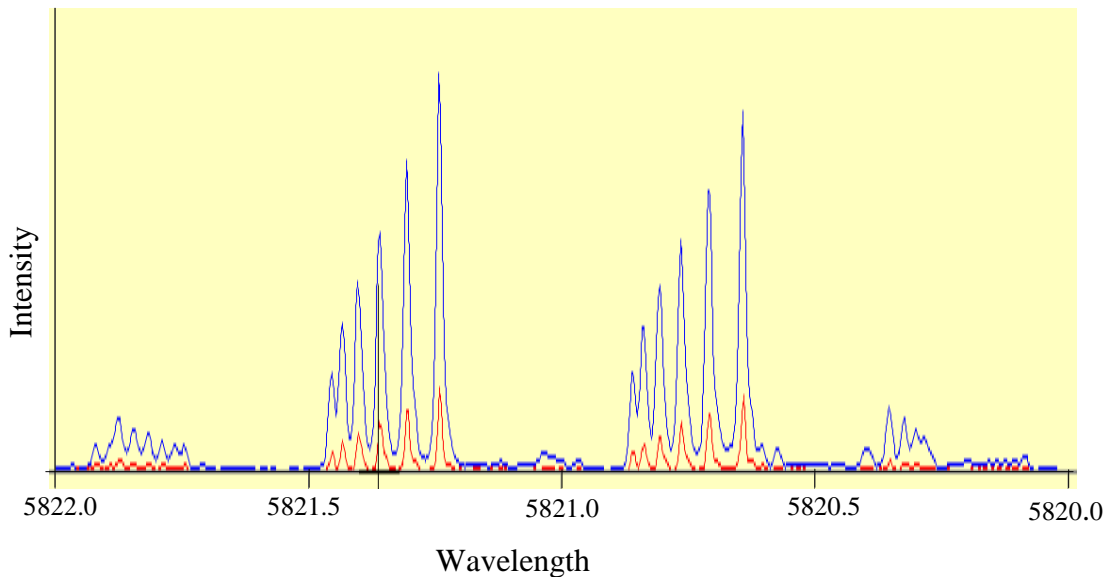
Figure 5.6: Fourier Transform spectrum in the region 5822.0 Å to 5820.0 Å

The recorded data files were in the form of intensity versus wave numbers. The files were

then converted by employing the dispersion formula given by Peck and Reader [69] into a spectrum with intensity versus air wavelength.

Wave number of a line is equal to the difference between the term values of the levels involved in its formation. For those spectral lines in FT-spectrum whose hyperfine structure is fully resolved, the hyperfine structure constants can be determined by fitting the line profile obtained from FT-spectrum to a mathematical function. In the FT-spectrum the majority of spectral lines have only partially resolved hyperfine structure for such lines, LIF signal need to be recorded for the determination of the hyperfine structure constants of the involved levels.

6 Computer Programs for Data Analysis

Various computer programs are used for the analysis of the experimentally recorded data. Two main programs are

(i) **Classification Program 'Elemente'** is used to manage the huge number of spectral lines found in an element such as praseodymium.

(ii) **Fitter Program** is used to fit the experimentally recorded hyperfine structure of a spectral line or a line profile extracted from FT-spectrum to a mathematical function which then gives a best estimate of the spectroscopic parameters of the levels involved in the formation of the line.

6.1 Classification Program 'Elemente'

One of the most difficult tasks in investigating the spectrum of an element is to manage and classify the huge number of spectral lines belonging to that element. This can be done in a conveniently manner by a specially designed computer program known as 'Elemente'. The program not only manages the large number of spectral lines but also allows the classification of known and unknown lines via their center-of-gravity wave number and expected hyperfine structure. The program was developed by L. Windholz [70] and its viewer version is available on the internet. The program is designed in such a way that it can be used for any element. Our research group is using this program to study spectral lines belonging to various elements such as Praseodymium, Tantalum, Lanthanum, and Neodymium. It can simultaneously handle both atomic and ionic lines. The program also includes several search strategies for finding unknown energy levels from unclassified lines. The program needs three data files to work:

(i) The wavelength file or table, containing all the known spectral lines whether classified or unclassified. The Pr wavelength table has presently more than 29000 entries in the following format:

5699.305, nl 4, , , , 30576.861,4.5 ,o, 770.47, ,*Sm080, 13035.73 ,5.5 ,e, 795.9v, -, Helmri,(Pr I) in Pr5003 vorh. #Sm080809 pr214055 a5699.305 f4787 f+4656 f5155 f5180 f5255

The first entry is line wavelength in Å in air, next four entries are intensities from different sources. If the line is classified the next entries are the energy, angular momentum, parity, *A* and *B* values and comment about the upper level. Then the next entries are for lower levels in the same order as for the upper level. Finally, it is possible to comment the lines, for example to give excitation wavelengths, fluorescence wavelengths and so on.

(ii) A data file containing all the known neutral atom levels, e.g. in case of praseodymium this file is named Level_pr.dat, for example,

0.5, o, 30400.042, 1890(10), , *Sm080318 pr127038 a5756.53 pr350039 a5141.70 f5141.703 f5251.114, f5448.51

(iii) A data file containing all known ionic levels, e.g. lev_prii.dat, for example,

3, o, 33850.957, 937, , *Sm110201 pr641010 a4275.15 pr641013 a4385.45 f+3841 f3757 f4077 f4243 f4446

The newest version of the classification program has two main frames, an upper main window and a lower graphic window displaying the FT-spectrum. The program has an

option to show or hide the FT-spectrum. The main window is divided into three sections. The middle section lists all the suggestions for the selected spectral line. For each listed suggestion the spectroscopic parameters such as energy, angular momentum *J*, parity and hyperfine interaction constants *A* and *B* for the combining levels are displayed. Wavenumber of the line from wavelength file, center-of-gravity wavenumber of the spectral line, the difference between the energies of the combining levels and center-of-gravity wavelength of the spectral line are also displayed. The leftmost section on the main window displays the classification of the spectral line as contained in wpr and the rightmost graphical section gives the graphical representation of all the list suggestions for a quick overview.

Spectral line is selected by the option **"GoTo Lambda"** for already known classified line or by the option **"Insert Line"** for an unknown unclassified line. The program calculates and searches for all possible transitions (number of possible suggestions depends on the selectable bandwidth) by comparing the wave number of the line with the difference of energies of the pairs of levels which fulfill selection rules. The classification suggestions are then displayed in the middle section of the main window. Atomic suggestions are listed in the beginning and the ionic at the end, anyone can be suppressed by using an option in the menu bar. The listed suggestions are sorted by energy and parity of the upper level with low energy and odd parity having higher priority. The program calculates the graphical hyperfine structure for each suggestion based on *J*, *A* and *B* values of the combining levels. This graphical representation is displayed in the bottom frame of the middle section.
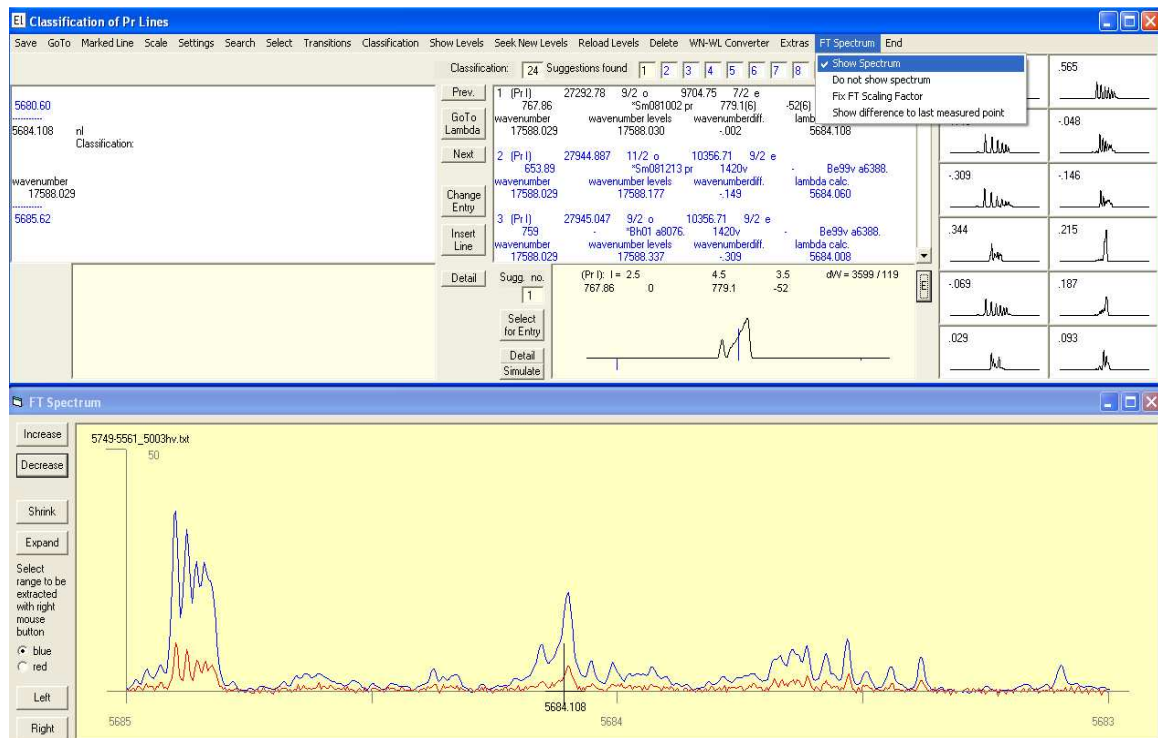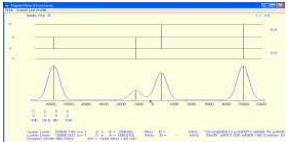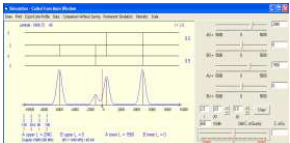
Figure 6.1: Main window of classification program

The program reads the data from wPr for the selected line and if the selected line is already classified, it is displayed in the leftmost section of the main window of the program. Some of the main features of the classification program are:

- Navigation from one spectral line to another can be done using *Prev*. and *Next* options.

- **GoTo Lambda** is used to move to a selected wavelength.

- **Insert Line** is used to insert a new spectral line to a wavelength table and placed it in a properly position.

- **Select for Entry** selects a specific suggestion for a possible classification of the current spectral line. A dialog box appears which display specific information regarding the line such as wavelength, relative intensity, comment window, etc.

- **Detail** displays the hyperfine pattern of the current suggestion for the spectral line along with its level scheme.

- **Simulate** show the hyperfine pattern like using "**Detail"** option but also allows to simulate a hyperfine pattern by changing all hyperfine constants. It is usually used if the classification suggestion contains levels for which the hyperfine constants are not known.

- **Save** permanently store the information about the classified line in the wpr.dat file without ending the program.

- **GoTo** moves to a selected spectral line if it is already contained in the wavelength table, to the lowest and the highest wavelength or to the start wavelength (beginning of work).

- **Marked Line.** The current wavelength can be marked by using this menu option which can be visited later on.

- **Scale** is used to select the width of the graphic fields. This is needed when comparing the calculated hyperfine structure pattern with the FT-spectrum.

- **Settings** set certain parameters for the classification program. It has various options. Some of them are the *wave number difference* used for finding classification suggestions, the *wavelength difference* used later on in transition list frame of a specific level, the *Doppler width* to set the width of the hyperfine components.

- **Search** is used to select either atomic or ionic levels schemes or both. Arbitrary selections rules for *J* can also be selected independently.

- **Transitions** show all the transitions having the upper or the lower level of the current line as their upper level. A specific line can be selected which then displays selected suggestion with its hyperfine structure pattern.

- **Classification** facilitates a faster movement from one spectral line to another by suppressing the *Classification Routine*. In this option, suggestions for the line are not displayed.

- **Show Levels** displays atomic or ionic levels from the respective database.

- **Seek New Levels.** It has four menu options

    o *Based on Current Line:* It calculates the possible odd or even levels using the wavelength table (wpr.dat in case of praseodymium). Calculations are performed for atomic or ionic or for both levels using selection rules.

- o *Based on Fluorescence line:* It has two options **"Seek New Levels"** and **"Seek Known levels"**. In each case, the experimentally observed fluorescence wavelengths are given to the search routine, the routine then selects all the lines from the wavelength table (wpr.dat) within a specified interval of wavelength of fluorescence lines. It then uses these lines to calculate new level or known level.
- o *Based on A and J:* A new upper or lower level is searched based on the spectroscopic parameters as obtained from the analysis of the experimentally recorded hyperfine structure.

- **Reload Levels** allows reloading of the atomic and ionic levels from the respective data bases.

- **Delete** is used either to delete a classification entry by *"Delete Classification"* or entirely delete the line by using *"Delete Current Line"*. This is beneficial when a wrong line has been inserted.

- **WN-WL Converter** is a small program which converts the wavelength in air to vacuum or vice versa or from wavenumber to wavelength. It also displays the difference between two wavelengths in wavenumber or difference between two wave numbers in terms of wavelength.

- **Extra** is used to calculate all possible levels just by adding the wave number of the lines contained in the wavelength table to all known levels.

- **FT Spectrum** displays a separate frame for Fourier transform spectrum. It also has option to calculate wavelength/wave number difference between two points in FT spectrum.

- **End** ends the program.

6.2 Hyperfine Structure Simulation Program

A simulation program is used to have an approximate estimate of the spectroscopic parameters such as angular momentum values for the upper and lower levels, the magnetic hyperfine interaction constant *A* and the electric quadrupole interaction constant *B*.
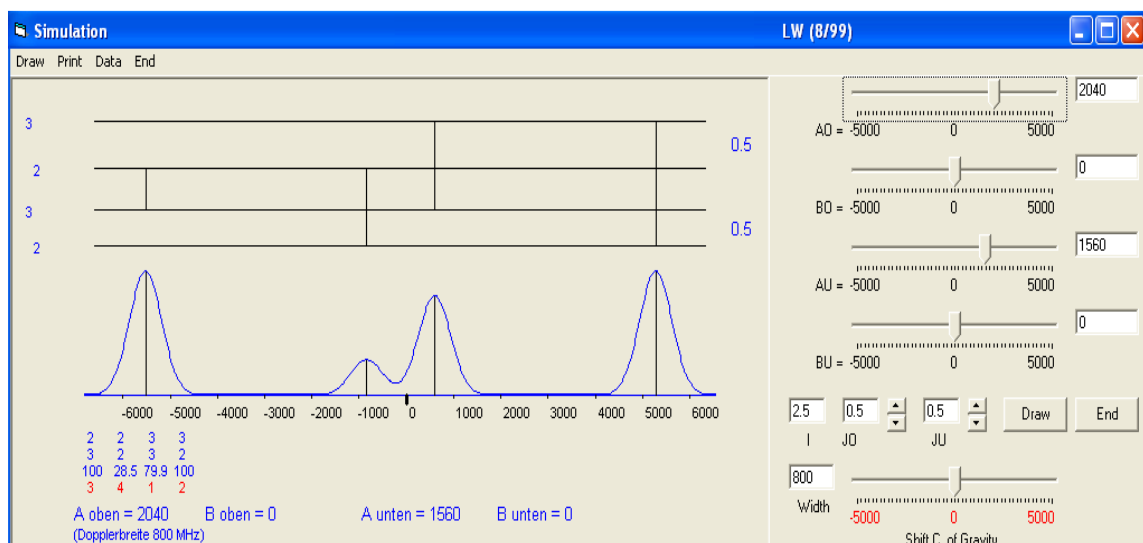
Figure 6.2: Hyperfine structure simulation program

The inspection of the recorded hyperfine structure of the line gives some idea about the spectroscopic parameters of the combining levels involved in the formation of the hyperfine structure. Using some initial guesses about the angular momentum values, the recorded hyperfine structure is simulated by varying the *A* and *B* values in the simulation program for the lower and upper levels. In this way, using these estimated *J*, *A* and *B* values, further analysis of the recorded hyperfine structure is performed. The Doppler width and nuclear spin can also be changed in the simulation program, if needed.

In situations where either the linearized recorded hyperfine structure or the line profile from the FT-spectrum is to be simulated, the simulation program which is the part of classification program is used to estimate the spectroscopic parameters related to the line profile. Using these estimated parameters as the starting point give best fit spectroscopic parameters of the experimentally recorded hyperfine structure or of a line profile from FT-spectrum. This helps in the identification of the levels forming the spectral line. The program can also be used in situations where one of the listed suggestions in the classification program can be classified by simulating the hyperfine structure line profile from FT-spectrum
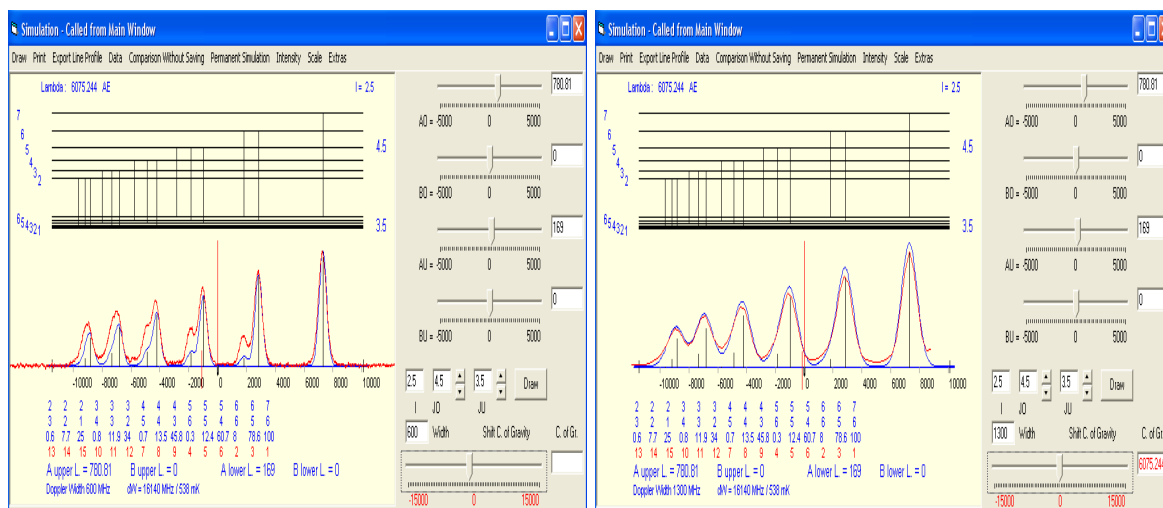
Figure 6.3: Simulation program. Left is the simulation of the recorded hyperfine structure line profile (red curve). Right is the simulation with line profile from FT-spectrum (red curve)

6.3 Data Viewer Program

A data viewer program is used to display the unlinearized recorded hyperfine structure of various investigated spectral lines (see Figure 6.4). The program consists of two frames. The smaller frame or window is used to convert wavelength in air to wavelength in vacuum or vice versa or to convert wave numbers to wavelengths. In addition, it can also calculate the differences in terms of wavelength in air, wave numbers in cm^{-1} and frequency MHz. The large window has three sections: a dialog box for displaying names of the recorded data files, a text window for the comments and a graphic window for displaying the recorded hyperfine structure of the line. The program has the facility to calculate roughly the position of any hyperfine component provided the free spectral range (FSR) and starting wavelength of the recorded hyperfine structure are known. The program also has the facility to convert the recorded data file in to a format suitable for the fitter program.
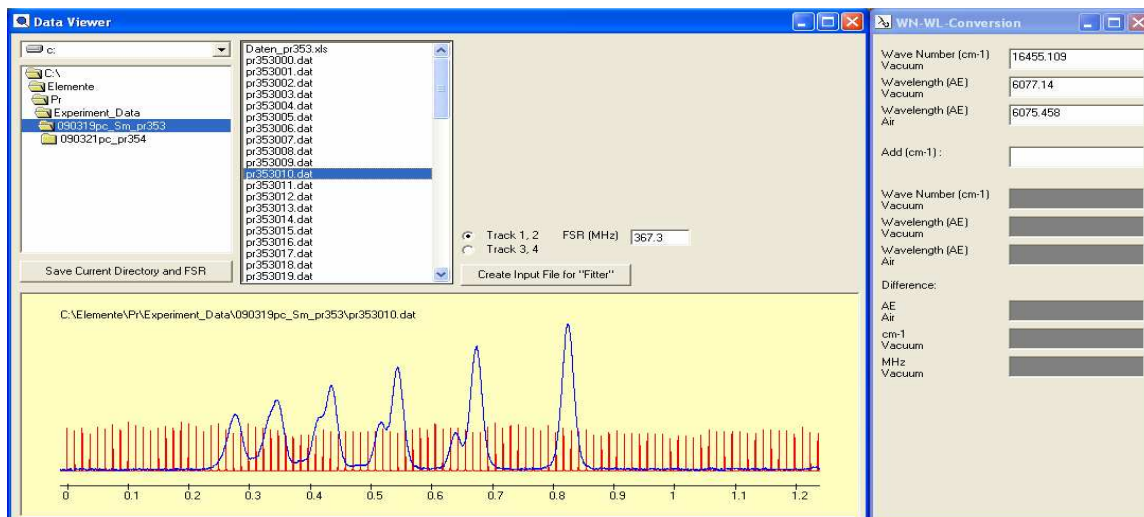
Figure 6.4: Data viewer program

6.4 Classification of a Line

Praseodymium with its five outer electrons has a large number of electron levels and this leads to an exceptionally high density of lines. This is evident from the FT-spectrum of praseodymium where one can observes large number of classified and unclassified spectral lines formed by the combination of energy levels which are yet to be discovered. In the classification program a spectral line is inserted, the program first calculates the wave number of the line and then lists only those transitions for which difference of levels energies fit (within some specified limit) with the wavenumber of the line. These listed transitions are called suggestions. The classification program generates the hyperfine structure pattern for each suggestion provided the hyperfine structure constants for combining levels are known. The hyperfine structure pattern is then compared with the hfs of the line in FT-spectrum or with the recorded hyperfine structure of the line. If the calculated hyperfine structure is in a good agreement both in terms of the shape and position of hyperfine components then the line can be classified as a transition between known lower and upper levels as shown in Figure 6.5.
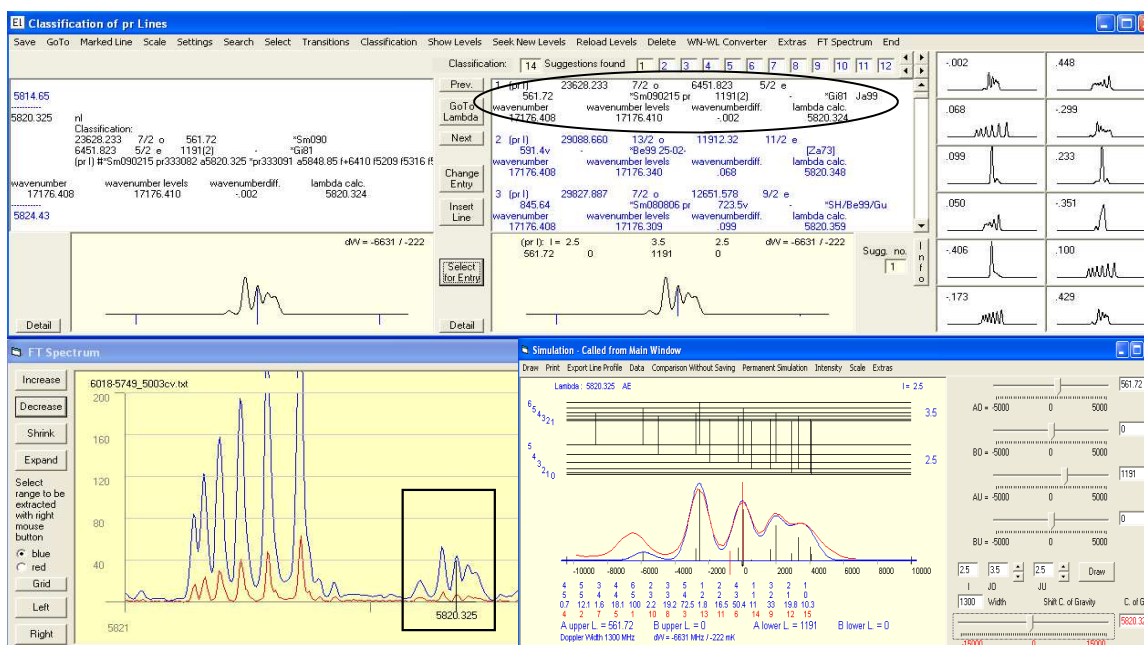
Figure 6.5: Classification of the line 5820.325 Å

73

In case, if the hyperfine structure profile in FT spectrum or the recorded hyperfine structure does not match with any of the listed suggestions then at least one of the combining levels is not known. There are a number of search strategies present in the classification program for finding new energy levels, some of them are discussed below.

6.4.1 Determination of New Levels by the Combination of Wave Numbers

Ritz combination principle [71] together with the wavenumber of an unclassified line can be used to determine a new level. The line then can be classified with the help of the new level and its hyperfine structure parameters. The method can be understood in following steps.

1. The first step in the search for a new level is to assume certain parity for the new level, for instance taking the parity of the new level to be odd. Now all the even levels are sorted with respect to their energy in ascending order. The energy of the new odd level is determined by adding the wave number of the unclassified line to the energy of the lowest energy even level.

2. In the second step, the energy of this new odd level is compared with the energies which are obtained by adding the wave numbers of all the lines in our line list to other even level energies. The energies obtained in this manner which is coincident with the energy of the predicted new odd level, the wavelength and the even lower levels are listed.

3. In the third step, the steps 1 and 2 are repeated but now taking the next higher even level from the sorted list as the basis of the calculation.

4. Completing the process for all even parity levels give a number of possible lower even parity levels.

5. The *J*-value for the possible new odd level is determined by employing the selection rules for the combining new odd level and one of possible lower even level in the list.

6. For each of the calculated transition, the hyperfine structure is simulated by varying the *A* and *B* values for the new odd level and using the known *A* and *B* values of the lower even levels. If the simulation for this combination is not possible then this suggestion is excluded.

7. In case the simulation is possible the *A* and *B* values for the new odd level are obtained. The new level is introduced and the hyperfine structure pattern of other lines can be calculated and compared with their hyperfine structure appearing in FT spectrum.

8. If after executing above step no new odd level is suggested then the whole process from step 1 is repeated but now assuming a new even parity level.

The strategy enumerated above is used for investigating the spectrum with not too many spectral lines such as the spectrum of Ta, but is not useful for Pr since it has a very high density of lines and this may lead to many coincidences appearing just by an accident.

6.4.2 Finding of a New Level by Fluorescence Lines

If an unclassified line is excited by laser light and some fluorescence lines are observed, then a possible new energy level involved in the excitation can also be determined by using fluorescence information. This method is again based on the Ritz combination principle with the difference that this time it only uses the current line and lines from the database in a certain wavelength range around the observed fluorescence lines. For the method to work

at least three fluorescence lines with accurate measure of fluorescence wavelengths must be observed which decay to known lower levels.

To seek a new level, the center-of-gravity wavelength (in air) of the excitation line is inserted in the classification program as the current line. The observed fluorescence wavelengths $\lambda_{fl,n}$ are given to the search routine of the classification program using the option "**Search for New Levels based on Fluorescence Lines**" as shown in Figure 6.6.
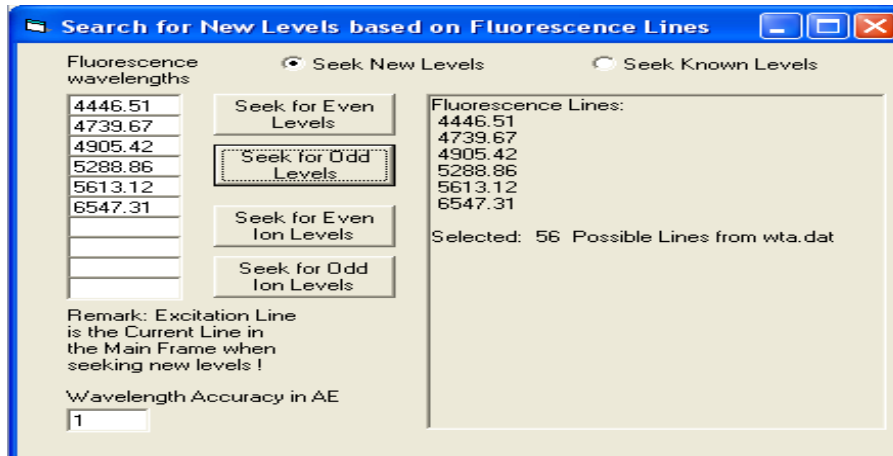
Figure 6.6: Window for seeking a level based on fluorescence lines

We assume a certain parity of the new level for example odd parity and seek for the new level. Program calculates the wave number of the line, takes the lower even levels from the list of known levels and add the wave number of the line. This gives the wave number of the hypothetical new upper level. Program then calculates the transition wavelengths from the new hypothetical upper level and displays possible suggestions for the lower and upper energy levels with fluorescence wavelengths within a certain specified limit as shown in Figure 6.7
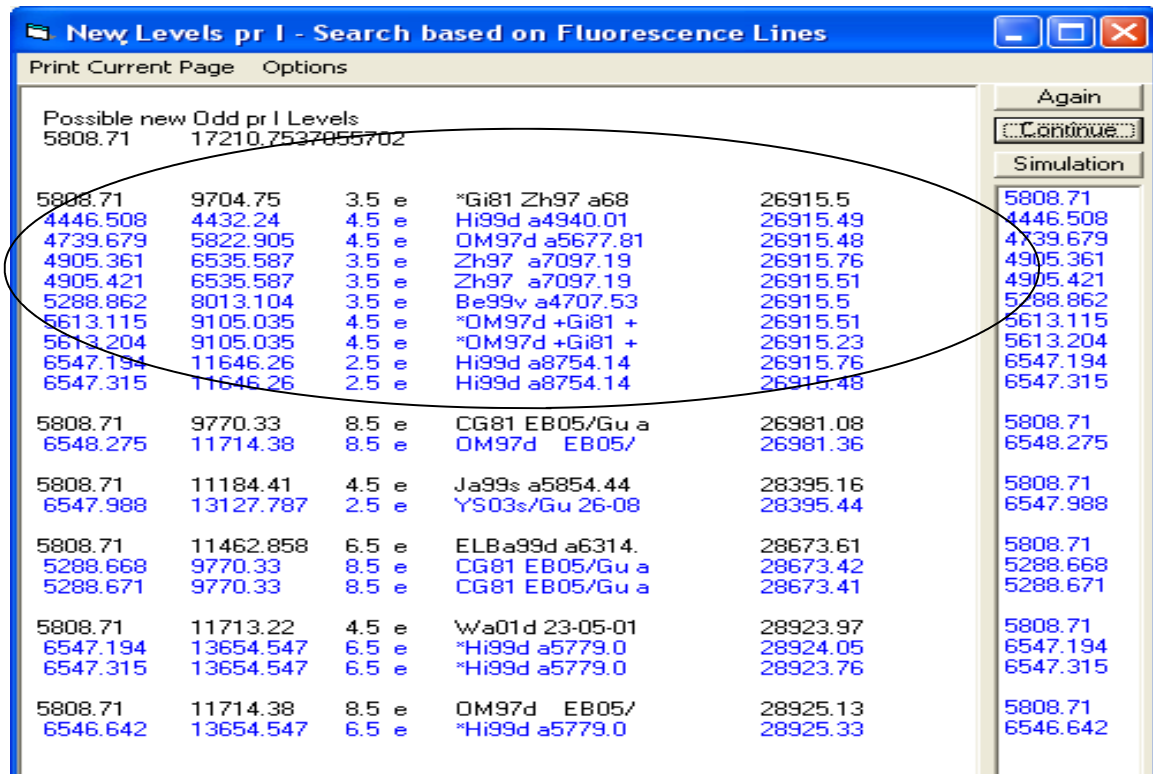
Figure 6.7: An unclassified line at 5808.71 $\mathring{A}$, with a new level $26915.499^{o}_{7/2}\ cm^{-1}$

The hypothetical level which explains most of the observed fluorescence lines $\lambda_{fl,n}$ can be treated as the level which is being searched. If none of the suggestion explains the observed fluorescence lines, then the process is repeated but this time searching for new even parity level. This method is especially suitable in cases where both lower and upper levels in an excited transition are unknown but then one of the fluorescence lines has to be chosen as the current line.

6.4.3 Finding a New Level by Analysis of the Hyperfine Patterns of Unclassified Lines

Knowledge of the pair of hyperfine interaction constants and *J*-values in most cases is sufficient to identify a level involved in the formation of a spectral line. The angular momentum values and hyperfine interaction constants for the combining levels i.e. *Jo, Ju, Ao, Bo, Au, Bu* are estimated by fitter program. Assuming that one of the levels involved in the transition is known, the level is searched in the database of known levels. This is done by using the search routine in the classification program called "***Seek New Levels Based on A and J***".

As an example consider the excitation of spectral line at $\lambda = 5966.38$ Å. A hyperfine structure with well splitted components was recorded on fluorescence wavelengths 4304 Å, 4385 Å, 4683 Å, 5257 Å, and 5568 Å. Fitting the recorded hyperfine structure of the line by "Fitter program" gave the best fit values as *Jo* = 9/2, *Ju* = 11/2, *Ao* = 919 MHz, *Au* = 295 MHz. Assuming an unknown upper level is involved in the excited transition, best fit *A*-value of the lower level and the *J*- values of both upper and lower levels are given to the search routine. The program searches the database for a known lower level of specified *J*-value and *A*-value (within specified interval). It then displays number of suggestions for possible upper level along with its transition list both in even and odd parity as shown in Figure 6.8
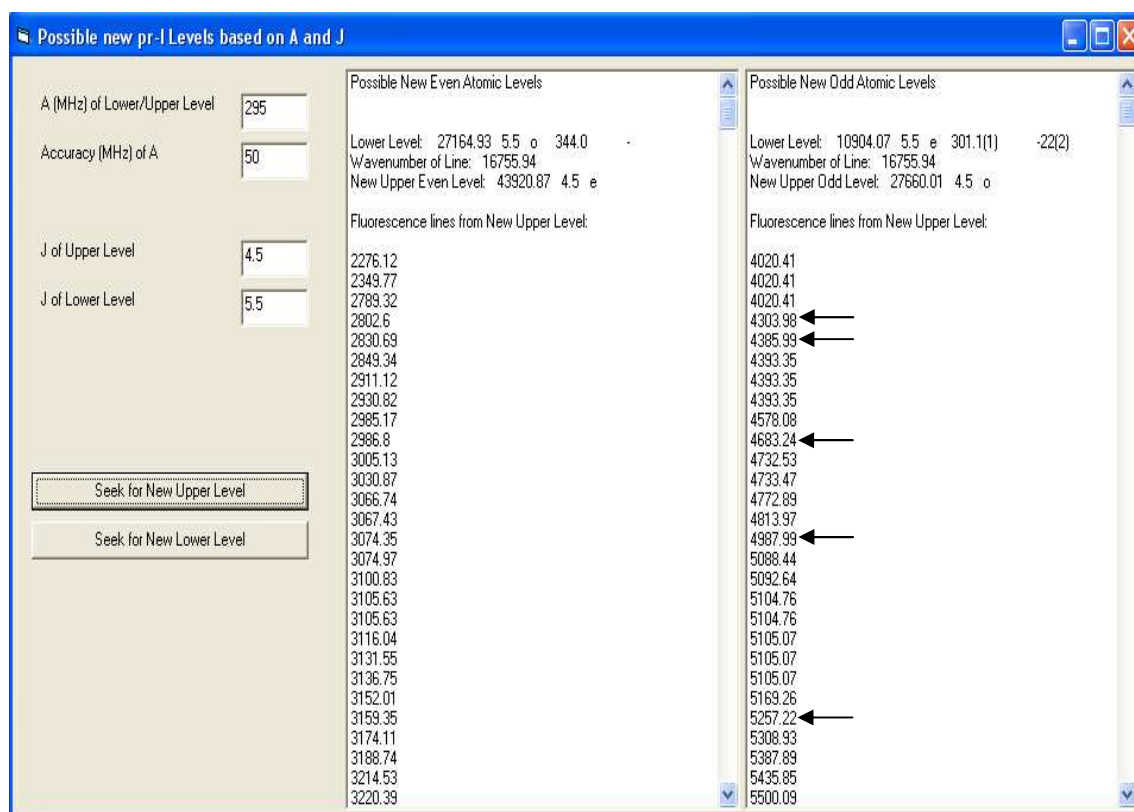
Figure 6.8: Possible new upper levels for the excitation of line at 5966.38 Å

The observed fluorescence wavelengths are then searched in the transition list of each suggestion. In this example, first listed suggestion in odd parity explains all the observed fluorescence wavelengths. The next step is to assume that this lower level is involved in the observed transition, and to fit the recorded hyperfine structure again with $A_u = 295$ MHz and $B_u = -22$ MHz being fixed. The energy of the new level is calculated by adding the wavenumber of the line, 16755.991 cm^{-1} to the enrgy of lower level, 11904.07 cm^{-1}. Finally one gets for the new upper level 27660.001 cm^{-1}, $J = 9/2$ $A = 925$ MHz. The new level explains the observed fluorescence lines which confirm the energy and existence of level.

6.4.4 Determination of Both New Lower and Upper Levels

In some cases, it is observed that J-value and hyperfine constants determined from the recorded hyperfine structure cannot be associated with the values of a known level. This implies that both lower and upper involved in the formation of the spectral line might be unknown. The identification of such levels is based on the observed fluorescence wavelengths provided that the number of observed fluorescence wavelengths is three or more and fluorescence lower levels are known. The basic idea behind this procedure is to look for known lower levels to which fluorescence lines from the unknown upper level decay. The procedure is as follows:

1. The exact fluorescence wavelengths are measured and converted in to wave numbers. For each pair of fluorescence lines the wave number differences i.e. $\Delta_{ij} = | \sigma_i - \sigma_j |$ are calculated.

2. The data base of known levels is search for known lower levels with same parity, based on the criteria that the differences between the wave numbers of these searched lower levels are within some margin of error equal to the wave number differences Δ_{ij} of fluorescence lines.

3. Once such a set of lower levels are found which fulfills the criteria listed in step 2, then by using the energy of the any of lower level in the set and the wave number of fluorescence line the energy of the unknown upper level is calculated.

4. Parity of the estimated upper can be set opposite to that of the set of lower levels.

5. Now the energy of the excitation lower level is determined using the energy of the proposed upper level and the wave number of the excitation line.

Hyperfine structure constants and *J*-values of the unknown lower and upper levels are determined using the mathematical fit of the recorded hyperfine structure.

This procedure can be performed by the classification program (see 6.4.2) if a fluorescence line decaying to a known level is used as a current line (fictitive excitation of the fluorescence line).

6.5 Mathematical Fitting of Hyperfine Structure Pattern

In order to determine the spectroscopic parameters (such as angular momentum J values and the hyperfine interaction constants *A* and *B*) for combining levels from the experimentally recorded hyperfine structure of the spectral line, it is necessary to fit the recorded hyperfine structure profile to an appropriate mathematical function using the **"method of least squares"**. It is an iterative process in which a curve is fitted to a set of data points so as to minimize the sum of the squares of the deviation of the points from the curve. Usually a pre-fit analysis of the recorded hyperfine structure profile is helpful in

evaluating best fit spectroscopic parameters. The spectroscopic parameters such as nuclear spin quantum number I, angular momentum J values of upper and lower levels and hyperfine interaction constants A, B characterizes a particular hyperfine splitting of a fine structure level.

A rough estimate of the magnitudes of the hyperfine interaction constants A and B can be given by inspecting the amount of splitting of a fine structure level in to the hyperfine structure levels. Assuming that the hyperfine interaction constants for both upper *(A_o)* and lower *(A_u)* levels are positive (which is mostly the case with praseodymium), then from relative intensities of diagonal *($\Delta F = \Delta J$)* components it can be decided whether $A_o > A_u$ or $A_o < A_u$ accordingly if the relative intensities of diagonal components are decreasing towards shorter or longer wavelength. The relative intensities and spacing between the diagonal components give a suggestion about the *J*-values of the combining levels with an error of *±1*. It is also possible to suggest a change in J values of fine structure levels for a transition from lower to upper level. If the off-diagonal *($\Delta F \neq \Delta J$)* components appear on both sides of diagonal components then there is no change in J value in going from lower to upper level i.e. *$\Delta J = 0$*. If the off-diagonal components appear either on the longer or on the shorter wavelength side then the *J*-value changes by *+1* or *-1* respectively. One can also use the rough estimate of the recorded hyperfine structure profile by using the simulation program (see section 6.2).

These roughly estimated spectroscopic parameters together with the center of gravity excitation wavelength are used to fit the recorded hfs patterns to an appropriate mathematical profile function. The mathematical profile function can be chosen between **Gaussian** or **Lorentzian,** depending on the intensity profile of the recorded hyperfine structure. If both Gaussian and Lorentzian profiles are observed in the recorded hyperfine pattern then a convolution or mixture of both functions is used. Such a function is known as the **Voigt** function.

In order to determine the hyperfine interaction constants and the center-of-gravity wavelength, a especially designed computer program known as **Fitter** is used. The program fits the recorded hyperfine structure to a mathematical function. The program can also fit the hyperfine structure profile of a line extracted from FT spectrum.

6.5.1 Fitter

This program was developed in University of Bundeswehr Hamburg, Germany as a part of diploma thesis [72]. The program calculates the spectral intensity distributions associated with various hyperfine structures of spectral lines recorded experimentally. These hyperfine structures are electronically recorded in a digital form as a function of changing laser frequency. The recorded file containing the data points must be converted in a form acceptable to the fitter program. The fitter program fits the recorded hyperfine structure of an excited line or a hyperfine structure of the line profile from FT-spectrum to a mathematical function using the method of least squares. The program determines the hyperfine constants and center of gravity wavelength. In this way, the physical information embedded in the recorded hyperfine structure of an excited line or a profile from FT-spectrum is extracted.

In an experiment, the intensity distribution of an excited transition is recorded in time domain i.e. as a function of equidistant time intervals. The data points representing the intensity distribution are not equally spaced in frequency. This is due to the non-uniform scanning behavior of the laser. Therefore a process known as linearization of the recorded data is adopted. The process converts the recorded spectrum which is in time domain *I(t)*

into frequency domain $I(v)$ using the marker etalon signal which is simultaneously recorded with the LIF spectrum. The process of linearization works only if the start wavelength of the laser scan and the free-spectral range (FSR) of the marker etalon are given to the electronically recorded data file.

The mathematical least square routine has a rapid convergence towards the best fit situation for the data points if the data points are equally spaced. Program calculates the position of individual hyperfine components and the hyperfine constants by the following relation

$$ \nu = \nu_c + \alpha_o \cdot A_o + \beta_o \cdot B_o - \alpha_u \cdot A_u - \beta_u \cdot B_u \qquad 6.1 $$

where $\alpha_o, \beta_o, \alpha_u, \beta_u$ are the Casimir factors for upper and lower energy levels respectively (see section 3.9). Intensity of each component is taken from the theoretical intensity formula using 6*j* symbols (see section 3.8). A suitable mathematical model (Gaussian or Lorentzian or Voigt model depending on the shape of the recorded hyperfine structure profile) is used with physical boundary conditions as input parameters. The program gradually varies the values of these parameters, and the model progressively evolves and adjust according to the method of least squares or Gauss-Newton method to the series of experimentally recorded data points, i.e. minimizing squared error sum given by the function *ESS*,

$$ ESS = \sum_{k=1}^{n} [I_v(k) - I_v(\nu_k, \vec{a})]^2 \qquad 6.2 $$

where $I_v(k)$ is the measured intensity at a given frequency point v_k, $I_v(\nu_k, \vec{a})$ is the calculated intensity at the corresponding position and $\vec{a}$ is a set of fit parameters. Using Tayler series the expansion of the above equation gives a system of nonlinear, inhomogeneous equations. The number of such equations in the system equals the number of parameters in $\vec{a}$. The method of least square is an iterative process so a solution of these equations is obtained in such a way that the deviation from the measured intensity becomes less and less and a new set of parameters values are obtained for the next iteration. The procedure is repeated until termination criterion is reached. Important input parameters are hyperfine constants of lower and upper levels, the frequency of a certain hyperfine component, the half width of the components, the underground intensity and center of gravity wavelength.

The program is based on a complicated iterative procedure and runs only in a pure mathematical sense with only objective of minimizing the squared error sum. This pure mathematical evaluation sometimes leads to unreasonable values of the physical parameters such as negative intensities or negative frequencies. One way of avoiding this is to reduce the number of input parameters. This can be done by fixing certain parameters according to a specific situation. For example if one of the levels involved in a transition is known then by fixing the hyperfine constants of this level the number of parameters are reduced by 2. If half-width is known then the number of parameters is reduced by 1. Furthermore this can also be done by coupling the relative intensities of various components together. So by coupling, the intensity coupling parameters are reduced by 1. Coupling of components can also be done in situations where saturation effects change the relative intensity of hyperfine components.

In addition to the single line fit, fitter program can also be used for multi-line fitting. In cases where simultaneously more than one hyperfine structure patterns are overlapped such as in a blend situation or more than one isotopes are involved in a transition, multi-line

fitting procedure is adopted. Figures 6.9 and 6.10 show a single line and two line best fit situations respectively.
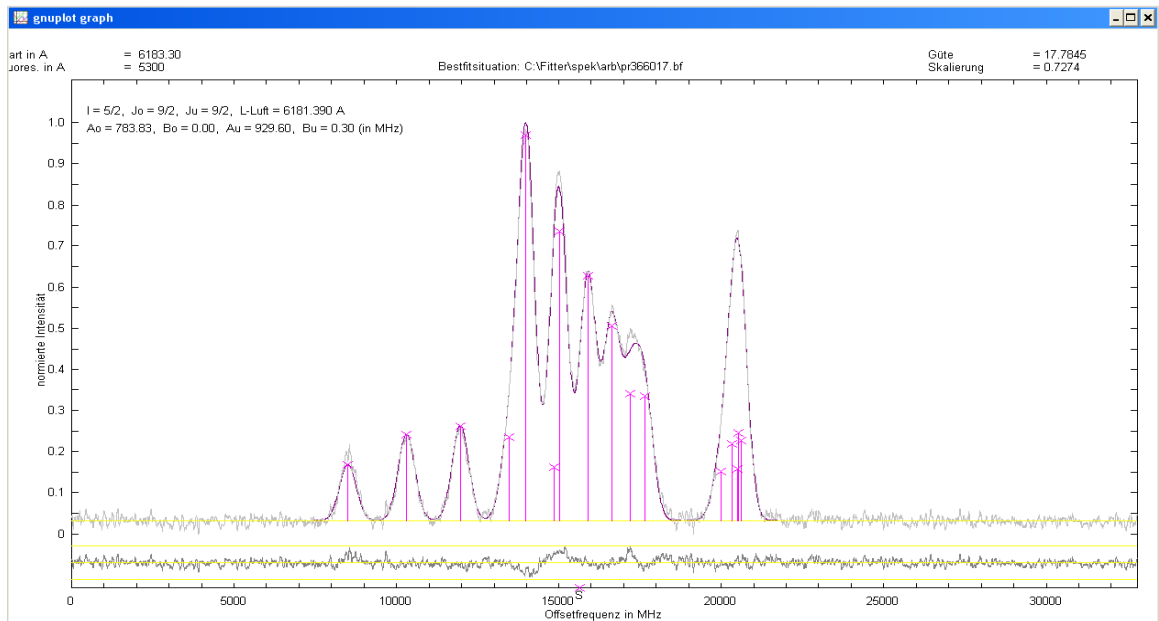
Figure 6.9: Fitting of single Pr I line at 6181.39 $\mathring{A}$
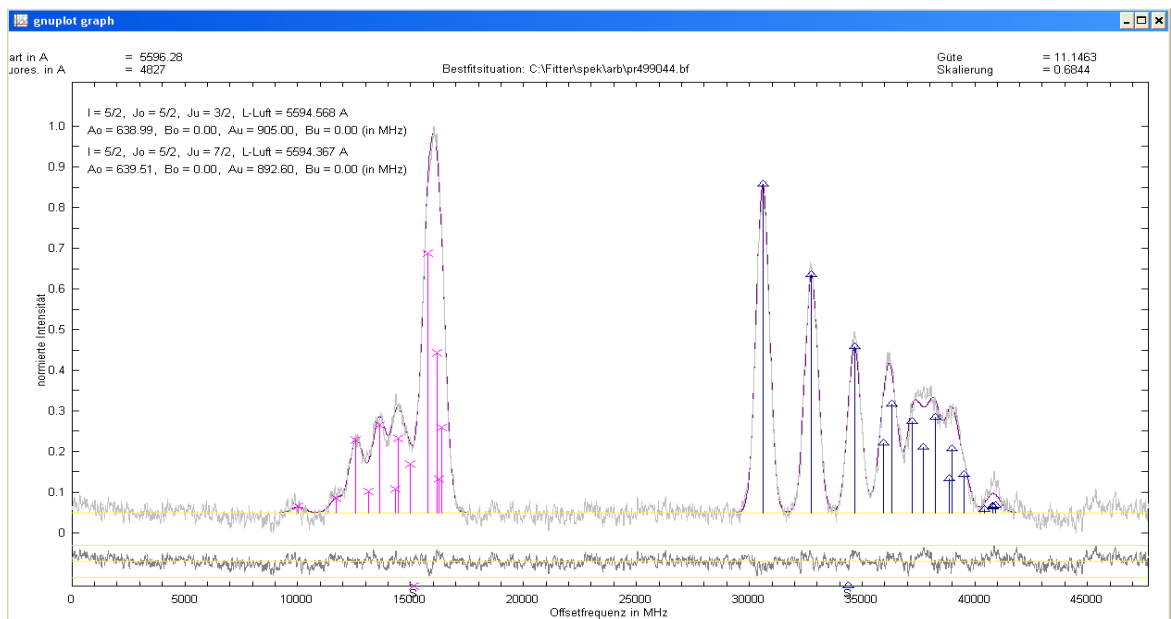
Figure 6.10: Fitting of two Pr I lines at 5594.57$\mathring{A}$ and 5594.36 $\mathring{A}$

7 Results and Discussion

The spectrum of praseodymium due to the open f-shell electrons has a very complex structure and high line density, because of this its spectrum is referred to as 'quasi-continuous'. Consequently on the average 5 to 10 lines per $\mathring{A}$ are frequently observed in the spectrum of praseodymium. The spectrum of praseodymium has been investigated thoroughly over the past few decades. These investigations are performed not only by our group but also by several other groups[11, 16, 20, 23, 73]. So far we have in our level database more than 2500 energy levels of even and odd parity belonging to Pr I and around 300 energy levels belonging to Pr II. Around 29000 lines are known to us in the spectral range from 320 *nm* to 3.5 μm and more than half of them have been classified.

During the course of this dissertation large numbers of unclassified and classified spectral lines were experimentally investigated using laser induced fluorescence spectroscopy. The hyperfine structure of these lines is used for the identification of energy levels involved in the transition. The investigations not only led to a proper identification of already known levels but also, in large number of cases, resulted in the discovery of new energy levels. The experimental investigations are organized as follows:

- New Pr-I and Pr-II energy levels in even and odd configurations by laser excitation.
- Classification of lines using known or unknown levels via laser excitation.
- Classification of lines by position and shape of the hyperfine pattern as shown in our FT spectrum.

A high resolution FT-spectrum of praseodymium, extending from UV to far infrared is helpful for our investigations. Excitation wavelengths of the lines are extracted from FT-spectrum and laser excitation is performed. In case the recorded hyperfine structure of the line could not be explained using known levels, then either the upper level or the lower level is unknown, or it may happen in an extreme case that both the combining levels are not known. The level energy is then calculated and the line is classified. Spectral lines appearing in the FT-spectrum with good signal-to-noise ratio and fully resolved hyperfine components can be classified without laser excitation, provided the combining levels are known. Conversely, if the line could not be explained by any of the known levels, then the estimated hyperfine structure constants from the simulation can be used to determine the possible unknown involved levels.

It is observed in certain cases that some lines in FT-spectrum are very weak, this may be due to the fact that the upper level is less populated, or the transition probability to the lower level involved in the formation of such a line is low. For such lines laser excitation spectroscopy is far more advantageous than emission spectroscopy. Also, if a line in FT-spectrum whose hyperfine splitting is not quite legible or line profile appears as a convolution of more than one lines, i.e. a blend of lines, then it is useful to study their hyperfine structure by laser induced fluorescence technique. Each line in the convolution can then be separated with help of the fluorescence information. In case of praseodymium, which has a very dense population of lines, blend situations are quite common and most of the investigations in this dissertation are performed by laser excitation. The spectral lines in praseodymium are so numerous that one frequently observes a LIF signal from two or more distinct levels at a specific excitation wavelength. This means that in the same scan range of laser either two very closely spaced lines involving different pairs of levels are excited simultaneously or a single upper level is excited from two very closely lying lower levels.

7.1 Hyperfine Structure of Praseodymium

The hyperfine multiplet is one of the characteristic features of any element. For praseodymium with nuclear spin quantum number $I = 5/2$, mostly a well resolved hyperfine structure is observed having six main or diagonal hyperfine components. As is common with the hyperfine spectra of other elements, a regular decrease of spacing and intensities of hyperfine components is seen. This can be explained in terms of the fact that one of the combining levels has a larger width of hyperfine splitting and this in turn means that the magnitudes of the hyperfine interaction A constants of the combining levels differ appreciably. Conversely, in situations where the magnitudes of the hyperfine interaction constants of the upper and lower levels are comparable, a hyperfine structure with closely spaced hyperfine diagonal components, forming a single peak, is observed. The spacing between the hf components of a level is governed by Lande's interval rule i.e. "in a multiplet, the differences between adjacent levels are in the ratio of the two F-values, where for each interval the higher of the two F-values is to be taken". The intensities within the hyperfine multiplets are governed by intensity rule i.e. "within a hf multiplet, the ratio of the sums of the intensities of all transitions from two states with quantum numbers F and F' are in the ratio of their statistical weights $(2F +1) : (2F' + 1)$". If one of the combining levels has a negligible splitting, the intensities of the lines are simply in the ratio of the values $(2F + 1)$ of the level whose splitting caused the structure.

The interaction between the electronic and nuclear moments leads to the splitting of fine structure level in to $(2I + 1)$ or $(2J + 1)$ hyperfine levels accordingly as $J > I$ or $J < I$. The transition between different hyperfine levels of two fine structure levels give rise to 6 $(J > I)$ main or diagonal hyperfine components. Beside these main components two additional groups of weaker off-diagonal hyperfine components can also be observed. The number of off-diagonal hyperfine components depends upon the change in J (ΔJ). If $\Delta J = 0$ then one can find 10 0ff-diagonal components

Figure 7.1 : A sketch showing diagonal and off-diagonal compnents.

whereas if $\Delta J = \pm 1$ only 9 off-diagonal components can be observed (Figure 7.1). Each hyperfine component has a Doppler profile which arises from the plasma conditions within the hollow cathode lamp.

This research work is based on hyperfine structure investigations of more than 1500 spectral lines in Praseodymium using laser induced fluorescence spectroscopy. These investigations are performed in very wide spectral region ranging from 4300 Å to 7500 Å. The major part of the investigations belongs to atomic transitions but few singly ionized levels have also been discovered. In most of the investigated transitions an upper level is unknown and only in few cases lower or both lower and upper levels were found to be unknown. These investigations led to the discovery of more than 300 new previously unknown energy levels, both in even and odd configurations. Angular momentum quantum number of these newly discovered atomic energy levels range from 1/2 to 21/2. Level energies are corrected at various observed fluorescence lines using the FT-Spectrum. Furthermore, the existence of the new level and its energy is confirmed by more than one

excitation. In general, the magnetic hyperfine interaction constant "*A*" can be positive or negative, which give rise to normal or inverted hyperfine multiplets, respectively. In case of praseodymium, the value of constant *A* is mostly positive. The quadrupole moment *Q* for praseodymium is very small therefore the magnitude of quadrupole interaction constant "*B*" in most cases is taken as zero. All wavelengths, excitation and fluorescence, are measured in air. In the following sections some of the newly discovered energy levels of Pr-I and Pr-II are discussed.

7.1.1 Discovery of New Pr-I level via Laser Excitation of Line 7573.761 Å

In an attempt to classify systematically lines in FT-spectrum, a line at 7573.761 Å (Figure 7.2) was observed. The line in FT-spectrum shows a well separated and resolved hyperfine structure with S/N ratio of 78. The suggestions listed in the classification program were compared with hyperfine structure of the line, but none of the listed suggestion had any agreement neither in terms of the shape nor in terms of position of hyperfine components. Therefore, it was concluded that either both or at least one of the levels involved in the formation of the line with the observed hyperfine structure in FT-spectrum is not known so far and yet to be discovered.
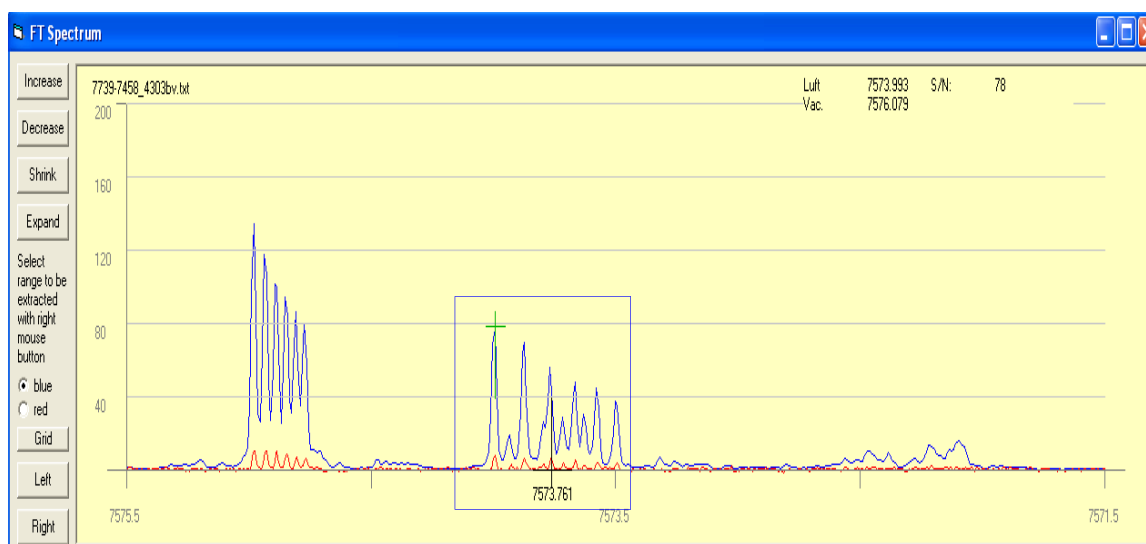
Figure 7.2: FT-spectrum for the line 7573.761 Å

The first step in the investigation is to search for LIF signals. This is done by setting the laser frequency to the strongest hyperfine component of the line i.e. 7574.00 Å and then searching for fluorescence wavelengths by tuning the transmission wavelength of the monochromator. In such a way, LIF signals were observed at fluorescence wavelengths 5861 Å, 6136 Å, 6157 Å, 6214 Å, 6376 Å, 6615 Å, 6640 Å, 6791 Å, 7059 Å, 7095 Å. The hyperfine structure of the line is then recorded on all observed fluorescence wavelengths by scanning the laser frequency across the hyperfine components of the line. Since the hyperfine structure of the line is larger than the scanning range of the laser (30 GHz), the scan is done in three parts and then using a program, the recorded parts were merged to form a single data file containing the entire hyperfine structure of the line. Two different hyperfine structures were recorded at these fluorescence wavelengths. The hyperfine structure recorded at 6157 Å, 6214 Å, 6640 Å, 6791 Å can be explained as a transition between the known levels $\mathbf{27999.623^e_{19/2}}$ **cm^{-1}** to $\mathbf{14799.842^o_{19/2}}$ **cm^{-1}**. On all other remaining observed fluorescence wavelengths, a widely splitted hyperfine structure was recorded as shown in Figure 7.3
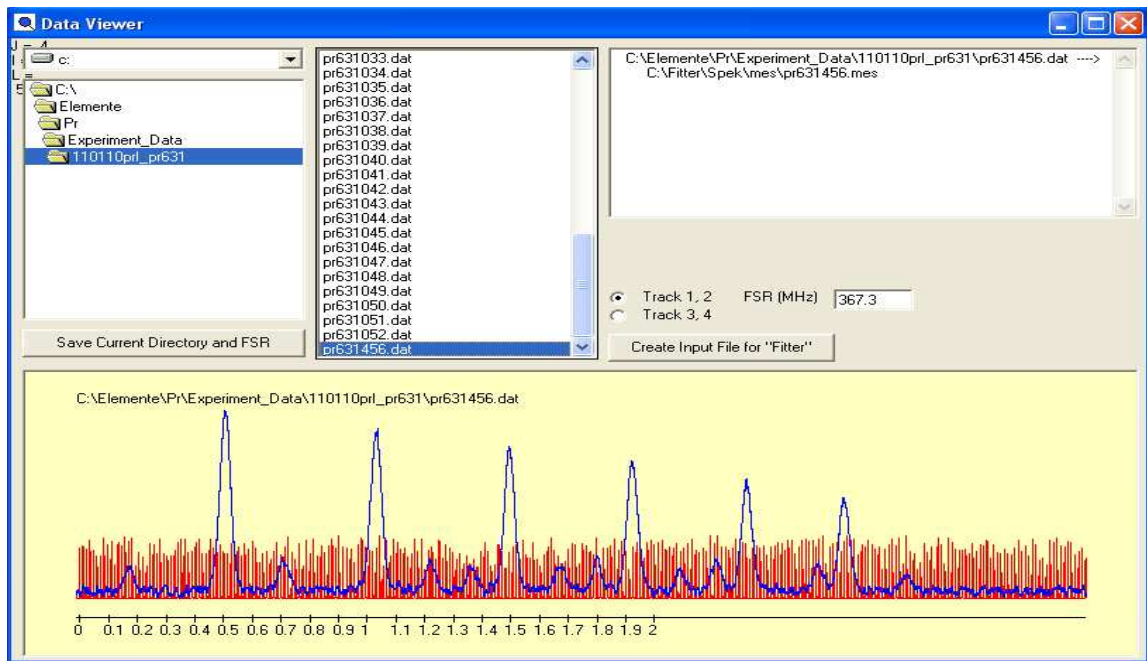
Figure 7.3: Laser excitation of the line 7573.761 Å showing a widely splitted hyperfine structure

A gradual decrease in the intensity of the diagonal components and the separation between them suggest high angular momentum values of the combining lower and upper fine structure energy levels of the excited transition. The intensity of the diagonal components decreases towards high frequency indicating that $A_u > A_o$ (valid in case of praseodymium where the A values are mostly positive). Also the off-diagonal components appear on both sides of diagonal components which shows that $\Delta J = 0$. In the next step, the recorded LIF spectrum is fitted to a theoretical curve using "Fitter Program". The evaluation gave the following results with a quality factor of 6.35 (Figure 7.4).

Center of gravity wavelength = 7573.761 Å

$J_o = 19/2$, $A_o = 337$ MHz and $J_u = 19/2$, $A_u = 847$ MHz,
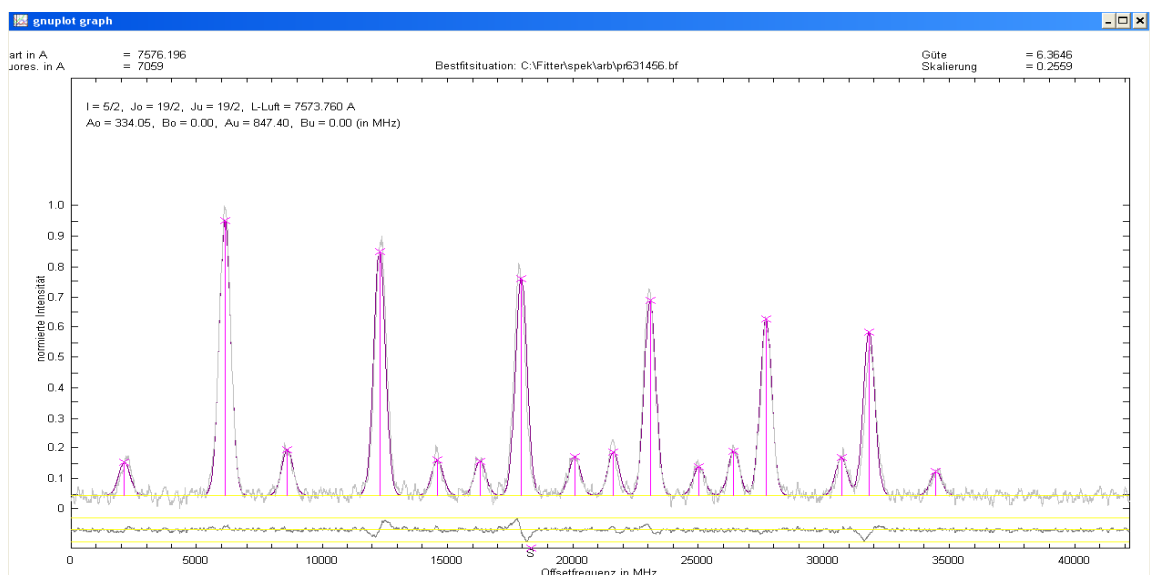
Figure 7.4: Best fit situation of the recorded hyperfine structure of the line 7573.761 Å

Using these best fit spectroscopic parameters as a finger print for a fine structure level, the combining levels are then search in the database of known levels. Assuming an unknown upper level is involved in the excited transition, a known lower level is searched in the database by using the search routine *'seek new level based on A and J'.* A number of suggestions for possible new upper levels along with its fluorescence lines are displayed.

One of the suggestions for a possible new upper level explains all the observed fluorescence lines. The lower combining level of the said suggestion is 13626.672 cm^{-1}, $J = 19/2$ even parity, $A = 865$ MHz. The recorded hyperfine structure is again fitted with the A-value of the lower level being fixed. The energy of the upper level is then determined by adding the wave number of the excitation line, 13199.845 cm^{-1}, to the energy of the lower level, 13626.672 cm^{-1}. The new upper level with spectroscopic parameters **26826.517 cm^{-1}, $J = 19/2$, odd parity, $A = 341(5)$ MHz** is obtained. The level is introduced in the classification program and explains all the observed fluorescence lines from upper level in accordance with FT-spectrum. The comparison of the hyperfine patterns of observed fluorescence lines in FT-spectrum at 7059.326 Å and 7095.327 Å with the predicted hyperfine patterns calculated using A_u and A_o, confirmed the existence and reliability of newly measured upper level (Figure 7.5 & 7.6).
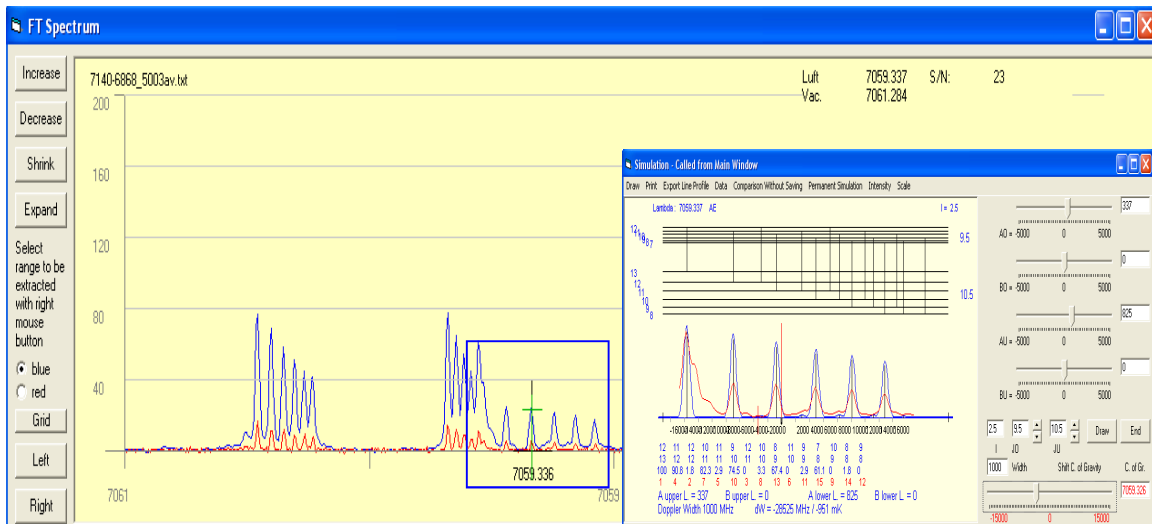
Figure 7.5: Comparison of the observed and predicted hyperfine pattern of the fluorescence line 7059.33 Å
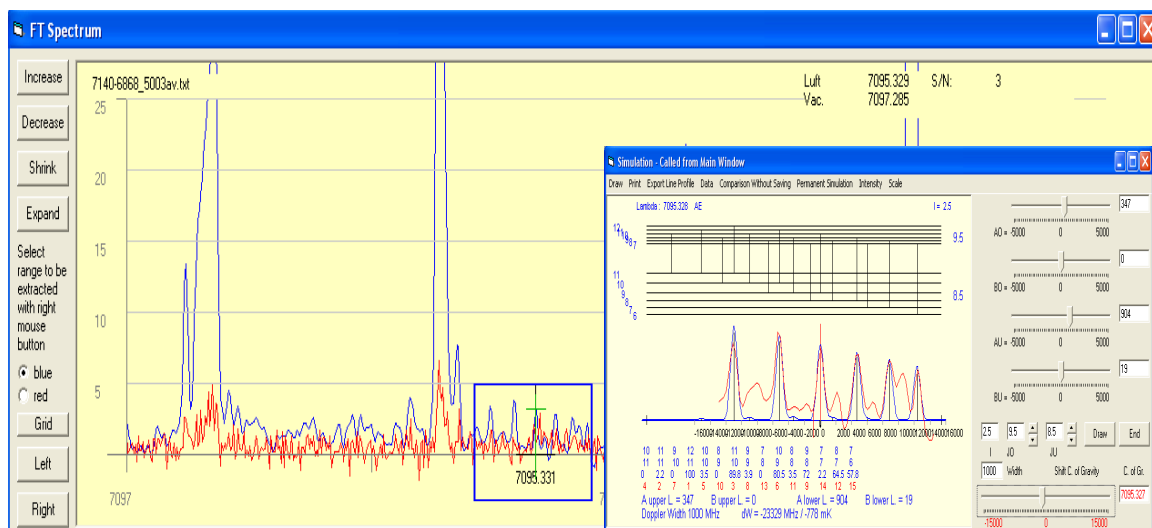
Figure 7.6: Comparison of the observed and predicted hyperfine pattern of the fluorescence line 7095.33 Å

Laser excitation was also performed at 7059.327 $\mathring{A}$ (Figure 7.7) to further consolidate the newly found upper level.
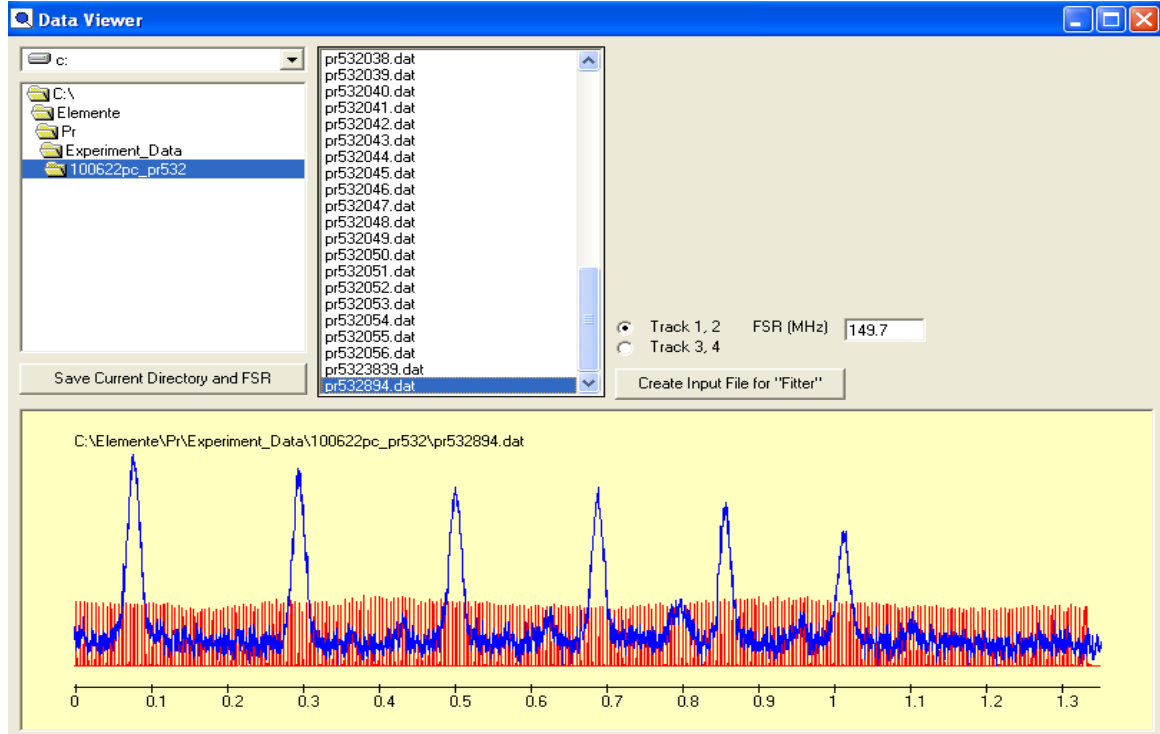
Figure 7.7: Recorded hyperfine structure of the line 7059.327 $\mathring{A}$

Table 7.1: Lines classified by the new Pr I level 26826.517 cm^{-1}, $J = 19/2$, odd parity, $A = 347(5)$ MHz

Wavelength ($\mathring{A}$, *air*)	Lower levels			
	Energy (cm^{-1})	J	A (MHz)	B (MHz)
5861.328	9770.273	17/2	905.498	-40.819
6377.79	11151.433	19/2	876.1	-31
7059.326	12664.774	21/2	825.3(12)	-
7095.327	12736.621	19/2	904.1	19
7573.761	13626.672	19/2	865	-

7.1.2 Discovery of Pr-I Level $25788.548^{o}_{7/2}$ cm^{-1} via Laser Excitation

In FT-spectrum a blend of two or more lines is clearly visible in the vicinity of 5624.172 $Å$, see Figure 7.8. A well resolved six peak hyperfine structure can be seen, the intensity of the second and last diagonal hyperfine components of the line show a blend situations. This suggested that possibly two other lines with their hyperfine structure are present at these positions. At center-of-gravity wavelength 5624.067 $Å$, the widely splitted six peak hyperfine structure is explained as a known transition between $24668.723^{o}_{13/2}$ - $6892.934^{e}_{11/2}$. At 5624.006 $Å$ laser excitation was performed and a single peak hyperfine structure at fluorescence wavelength 5194 $Å$ was recorded. This line could be explained as already known transition between $\mathbf{20622.677^{e}_{13/2} - 2846.741^{o}_{13/2}}$.

Now the laser wavelength is fixed at 5624.172 $Å$ and the transmission wavelength of the monochromator is varied to search for LIF signals. Since the last diagonal hyperfine structure component of the already known transition is coincident at 5624.172 $Å$, a number of fluorescence lines were observed belonging to the upper levels of both lines. By excluding those fluorescence lines appearing in the transition list of the already known upper level, the remaining observed lines 5007 $Å$, 5192 $Å$, 5501 $Å$, 5863 $Å$, 5831 $Å$, 6215 $Å$ could not be explained by any of listed suggestions in the classification program. Now the laser wavelength is scanned across the hyperfine pattern of the line in FT-spectrum and successively on each of the observed fluorescence wavelengths, a hyperfine structure is recorded.
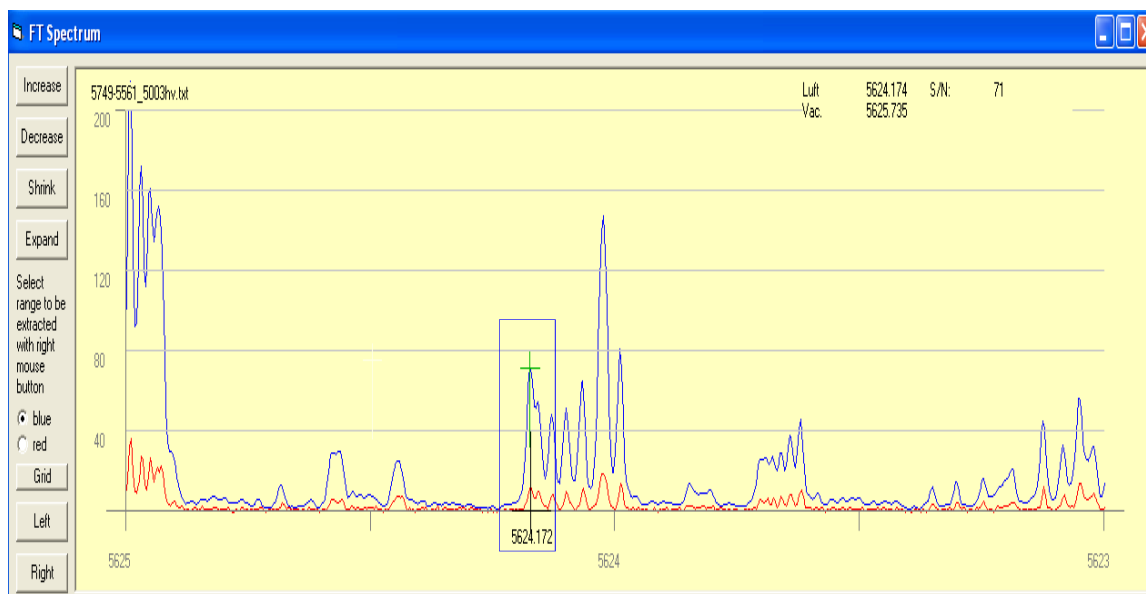
Figure 7.8-: FT-spectrum for the line 5624.172 $Å$

A narrowly spaced single peak hyperfine structure was recorded on all observed fluorescence wavelengths, see Figure 7.9. Apparently all the diagonal and off-diagonal hyperfine components are bunched together, suggesting that the hyperfine splitting of the levels involved is small, which in turn means small values of the hyperfine interaction A constant. The recorded hyperfine structure for the line is compared with listed suggestions in the classification program but none of the suggestion explained the observed pattern. This implies that at least one or both of the combining levels for the line are unknown and yet to be discovered. A pre-fit analysis of the recorded structure by using simulation

program suggests small angular momentum values of upper and lower levels having small values of hyperfine interaction A constants.
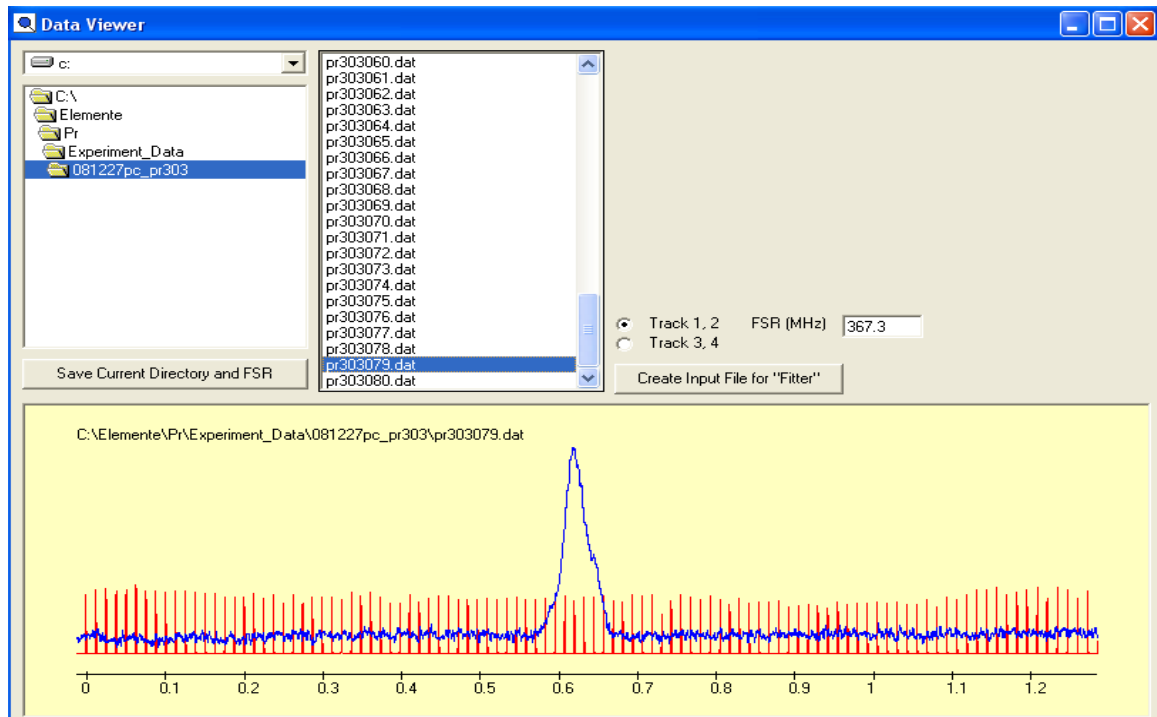
Figure 7.9: Recorded hyperfine structure of the line 5624.172 Å

Taking the simulated J- and A-values for the combining levels as the start values, the recorded hyperfine structure was mathematically fitted using the fitter program. A best fit situation of the recorded structure was obtained for $\Delta J = 0$ at $J_o = 7/2$, $J_u = 7/2$, $A_o = 125$ MHz and $A_u = 162$ MHz, see Figure 7.10. B_o and B_u are assumed to be zero which is usual for praseodymium.
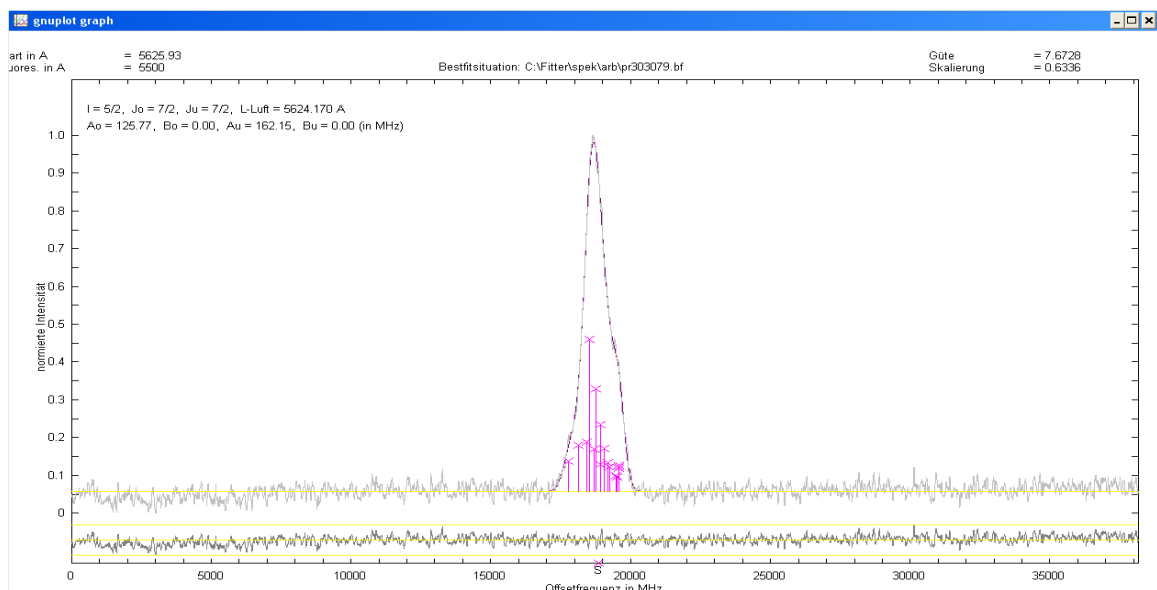
Figure 7.10: Best fit situation of the recorded hyperfine structure of the line 5624.172 Å

With an assumption that the upper level in the excited transition is unknown, the best fitted J-values for the combining levels and the best fit A value of the lower level are used for

searching a known lower level in the data base of known levels. A lower level with parameters 8013.089 cm^{-1}, even parity, $J = 7/2$ and $A_u = 165$ MHz combining with a possible new upper level was found. This possible new upper level explained all the observed fluorescence lines. Assuming this to be a correct combination of involved levels, the recorded structure was again fitted but now keeping fix the A value of the lower level. The energy of the assumed newly found upper level was calculated by the center-of-gravity wave number of the excited line and the energy of the lower level. The spectroscopic parameters of the upper level are **25788.548 cm^{-1}**, **odd parity**, **$J = 7/2$** and **$A_o = 131.14$ MHz**. The level is introduced in the database of known levels and after reloading the levels from the data base the classification program generates a transition list for the newly found upper level. All the observed fluorescence wavelengths are present in the transition list of the newly computed upper level and as seen in the FT-spectrum fluorescence lines were fully explained. As an example the simulation of line at 5501.713 $Å$ is shown in Figure 7.11. The simulation shows an agreement of the predicted hyperfine pattern of the line with the line profile in FT-spectrum. At the first approximation the existence and the assignment of the newly found upper energy level is confirmed.
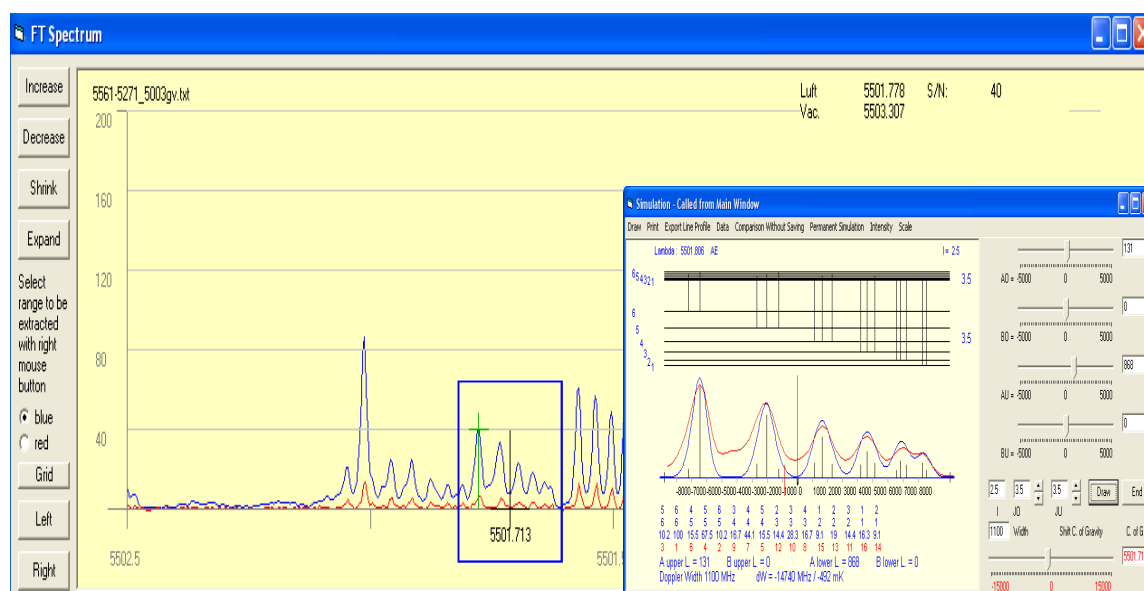
Figure 7.11: Comparison of the observed and predicted hyperfine structure pattern of the fluorescence line 5501.713 $Å$

A second laser excitation was performed at one of the observed fluorescence wavelengths i.e. at center-of-gravity wavelength 5831.080 $Å$. The LIF signal at all previously recorded fluorescence wavelengths was observed and the hyperfine structure of the line at center-of-gravity wavelength 5831.080 $Å$ was recorded, see Figure 7.12. The recorded hyperfine structure of the excited line at 5831.080 $Å$ is in full agreement with the hyperfine pattern calculated with the now already known hf constants. To further substantiate the agreement the recorded structure of line at 5831.080 $Å$ was fitted keeping fix the A value of the newly discovered upper level (Figure 7.13), the fitting process reproduce the A value of the lower level at this line. This confirmed beyond doubt the existence of the newly discovered upper energy level. As a final step in the analysis, the level energy is corrected at various spectral lines whose hyperfine structure is clearly visible in FT-spectrum. Provided the energy of the lower level is correct, the energy of the upper level can be corrected with an accuracy governed by the recorded resolution limit of the FT-spectrum of praseodymium which is typically 0.03 cm^{-1}
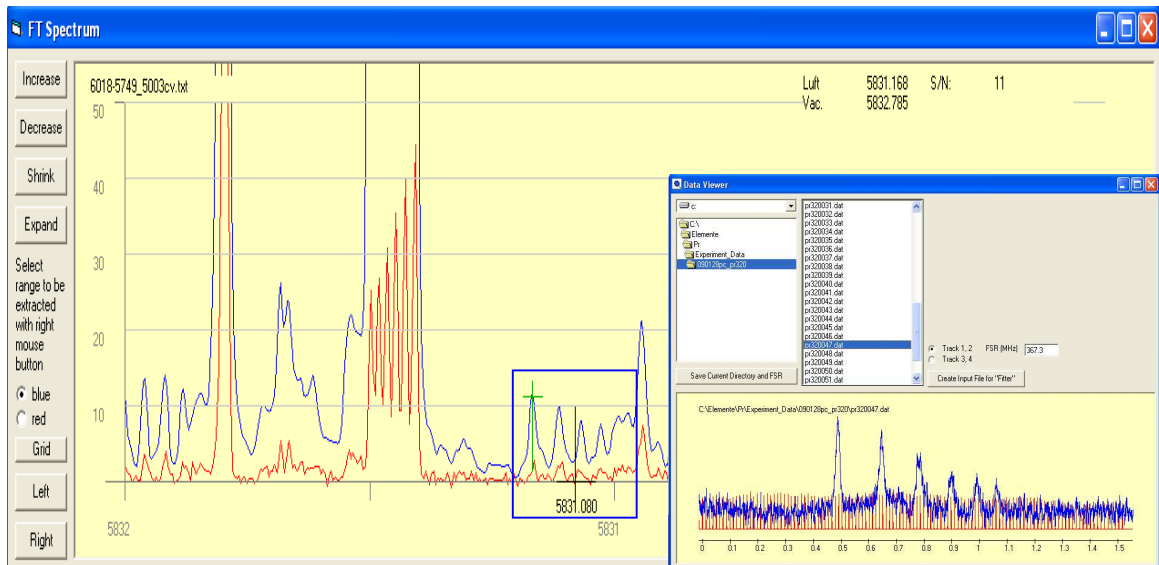
Figure 7.12: Confirmation of the newly found upper level 25788.548 *cm^{-1}* at 5831.080Å
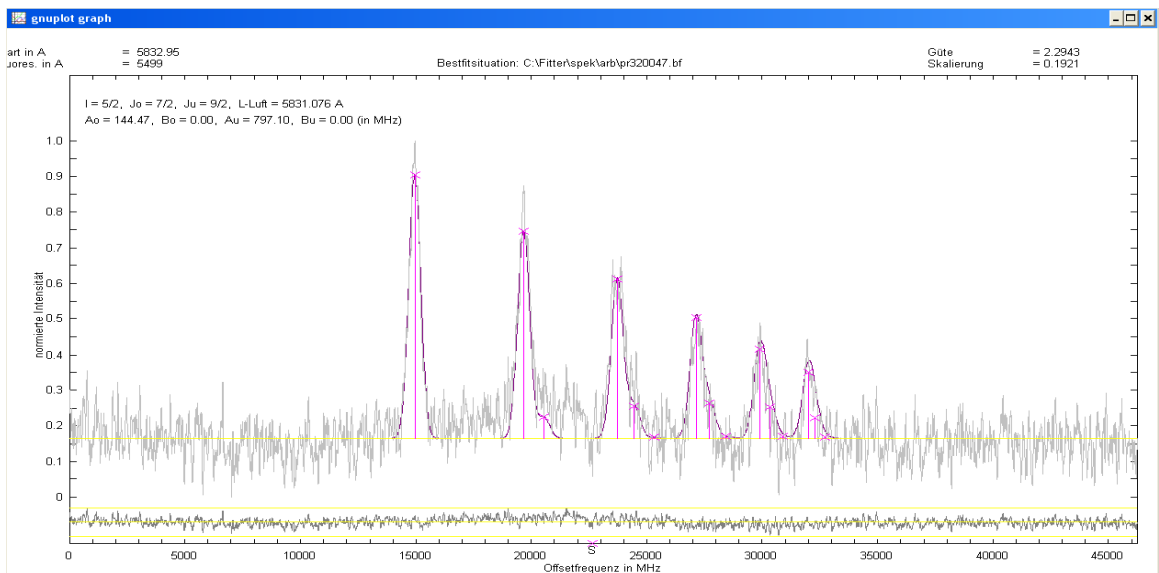
Figure 7.13: Best fit situation of the recorded hyperfine structure of the line 5831.080 *Å*

Table 7.2: Lines classified by the level 25788.548 *cm^{-1}*, *J* = 7/2, odd parity, *A* = 138(6) MHz

Wavelength (Å, air)	Lower levels			
	Energy (cm^{-1})	J	A (MHz)	B (MHz)
5007.20	5822.890	9/2	861.3(5)	-
5192.56	6535.572	7/2	979.0(8)	26(16)
5501.713	7617.440	7/2	868	-
5624.172	8013.089	7/2	165	-
5831.080	8643.824	9/2	797.1(11)	-
5863.14	8737.556	5/2	1149(5)	-
6215.714	9704.744	7/2	779.1(6)	-52(6)
7590.434	12617.701	7/2	883(2)	-

7.1.3 New Pair of Pr-I Energy levels via Laser Excitation

In the vicinity of 5700.92 Å, the structure in the FT-spectrum apparently suggests a blend of more than one lines with weak signal-to-noise ratio having a relative intensity of 13, see Figure 7.14. The classification program suggests only few transitions with a small wave number difference. Furthermore for these few transitions the predicted hyperfine pattern is in poor agreement with line profile in FT-spectrum. So the line or lines in the neighborhood of 5700.92 Å cannot be classified without laser excitation.
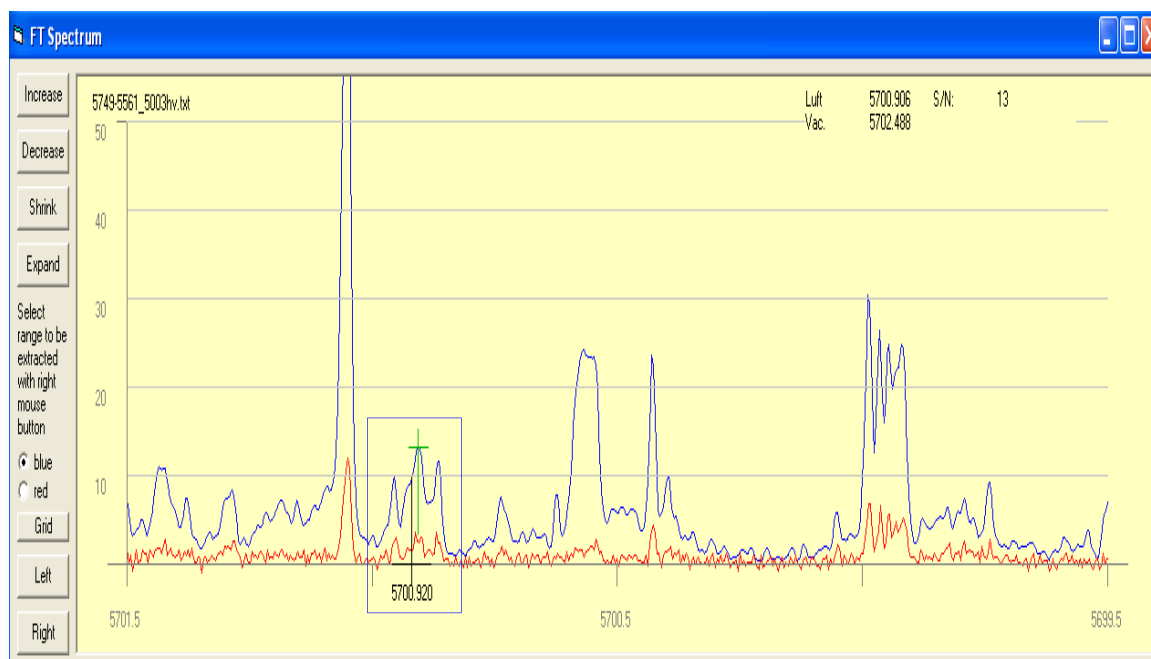
Figure 7.14: FT spectrum for the line 5700.92 Å

Laser excitation wavelength was set to 5700.92 Å and LIF signal was observed on a number of fluorescence lines at wavelengths 4928 Å, 4978 Å, 5293 Å, 5340 Å, 5363 Å, 5446 Å, 5578 Å. Now the hyperfine structure was recorded on all observed fluorescence wavelengths and two different hyperfine structure patterns with good signal-to-noise ratio were recorded. One of the hyperfine structure is recorded at fluorescence wavelengths 4928 Å, 5363 Å (Figure 7.15) and the other on 4978 Å, 5293 Å, 5340 Å, 5578 Å (Figure 7.16). At fluorescence wavelength 5446 Å, a mixture of both hyperfine structures were recorded suggesting a possible fluorescence blend situation. A blend situation occurs in case the laser may have excited two or three transitions to two or three different levels which by chance have almost the same wave number difference. The recorded structure would then be a convolution of two or three hyperfine structures apparently depicting an excitation and fluorescence blend situation. From the experimentally recorded hyperfine structures center-of-gravity wavelengths were estimated as 5700.92 Å and 5700.94 Å. Once again the suggestion list in the classification program for both lines was inspected but none of the listed suggestions explained the recorded hyperfine structure patterns. It was concluded that either the upper or lower level or all involved levels for both lines are not yet known. Pre-fit analysis using a simulation program give an approximate estimate of *J*- and *A*-values of the combining levels for both recorded structures. Taking these estimated values as start values, the recorded hyperfine structures were mathematically fitted by using the fitter program.

91
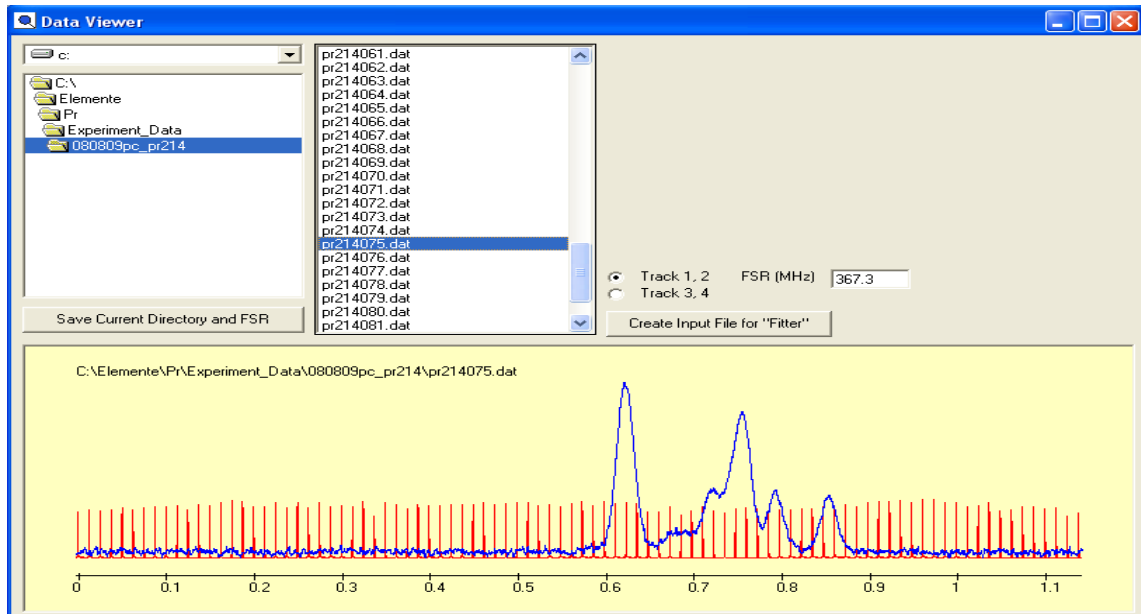
Figure 7.15: Recorded hyperfine structure of the line 5700.92 Å
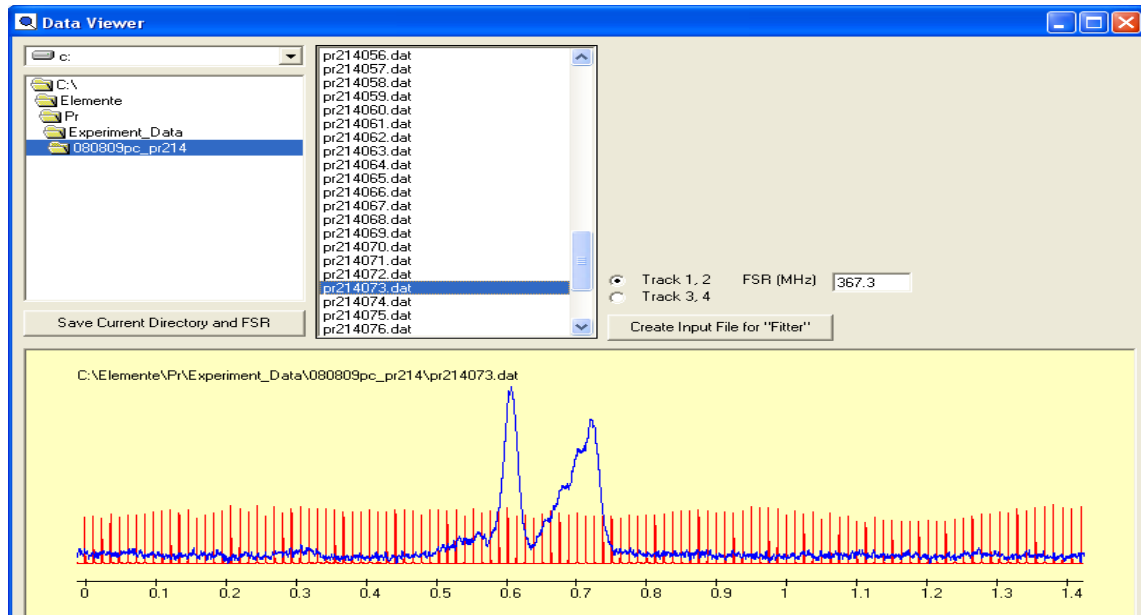
Figure 7.16: Recorded hyperfine structure of the line 5700.94 Å

The best fit situation for the hyperfine structure recorded at center-of-gravity wavelength 5700.90 Å is shown in Figure 7.17 with fitted parameters $J_o = 3/2$, $J_u = 3/2$, $A_o = 985.08$ MHz and $A_u = 712$ MHz. For the hyperfine structure recorded at center-of-gravity wavelength 5700.94 Å the fit result is shown in Figure 7.18 with fitted parameters $J_o = 5/2$, $J_u = 3/2$, $A_o = 704.55$ MHz and $A_u = 712$ MHz. It is noticeable that for both structures the fitter program gave the same J and A values for the lower level. Center-of-gravity wavelengths were inserted in the classification program and it was assumed that for both lines the upper levels are unknown. Taking the best fit J values and A value of lower level the data base of known levels is searched for a lower level using the searching routine in classification program. This was done separately for both lines. In each case the classification program generated a number of suggestions for possible new upper levels. Two possible new upper levels explained all the observed respective fluorescence wavelengths.
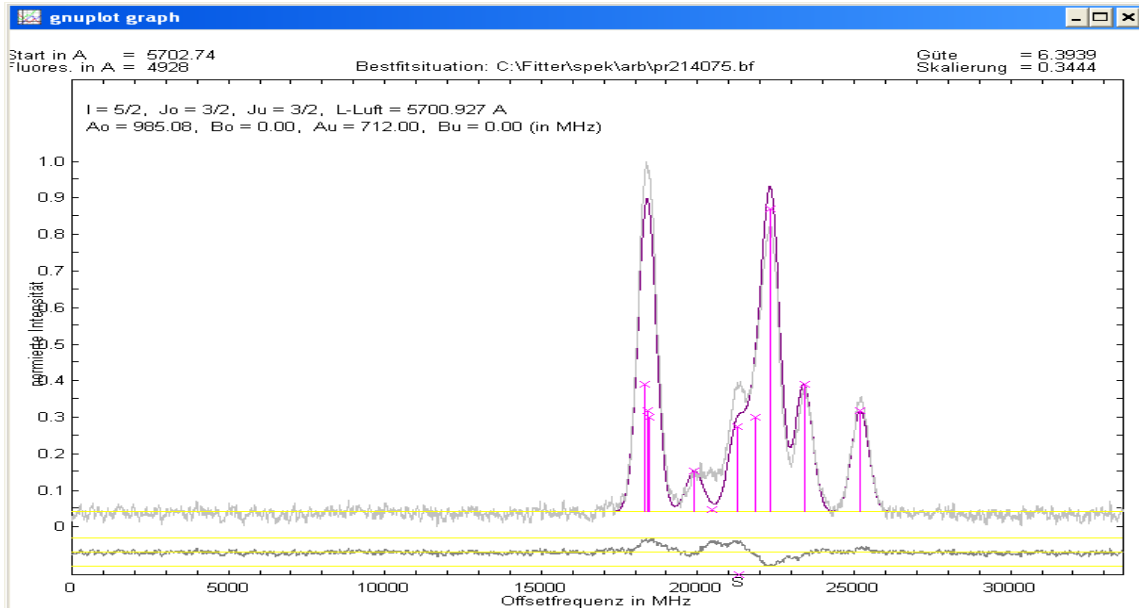
Figure 7.17: Best fit situation for the line 5700.92 Å
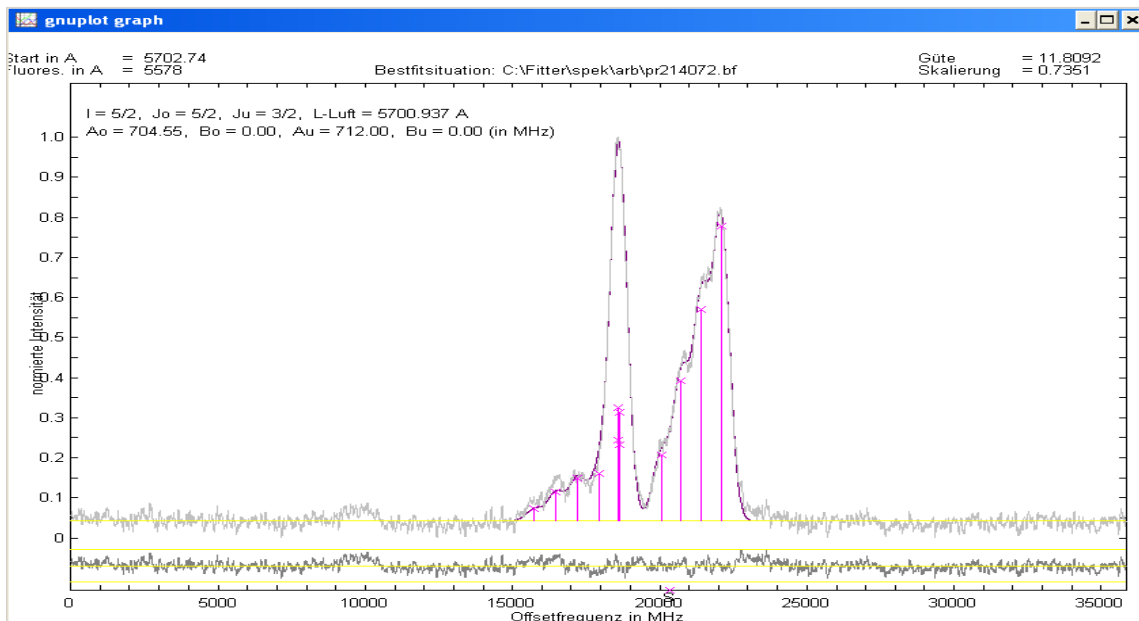
Figure 7.18: Best fit situation for the line 5700.94 Å

Interestingly, the same lower level at each excited transition combines with the two different upper levels. The parameters for this lower level are 12464.369 cm^{-1}, even parity, $J_u = 3/2$ and $A_u = 712(4)$ MHz. The energy of the two upper levels at center –of-gravity excitation wavelengths 5700.92 Å and 5700.94 Å were calculated by using center-of-gravity wave numbers for each line and the energy of the common lower level. The spectroscopic parameters for the upper level with center-of-gravity excitation wavelength 5700.92 Å are 30000.532(20) cm^{-1}, odd parity, $J_o = 3/2$ and $A_o = 1000(15)$ MHz and for the upper level at center-of-gravity excitation wavelength 5700.94 Å are 30000.493(20) cm^{-1}, odd parity, $J_o = 5/2$ and $A_o = 708(8)$ MHz. Both newly discovered upper levels were then introduced in the database of known levels and after reloading, the classification program generates a transition list for both newly found upper levels. Both upper levels were then

93

confirmed separately at other excitation wavelengths, i.e. 30000.532(20) cm^{-1} was confirmed by a second excitation at 6121.87 Å and 30000.493(20) cm^{-1} was confirmed at 6121.88 Å. Interestingly here again at second excitation wavelengths for both closely lying upper levels, a common lower level combines. The predicted hyperfine structures for both lines are in complete agreement with the recorded hyperfine structures, see Figures 7.19 and 7.20. This confirms the existence and energy of the newly discovered upper levels beyond any doubt.

Figure 7.19: Comparison of the recorded hyperfine structure (Red curve) of the line 6121.87 Å with the predicted hyperfine structure (Blue curve).
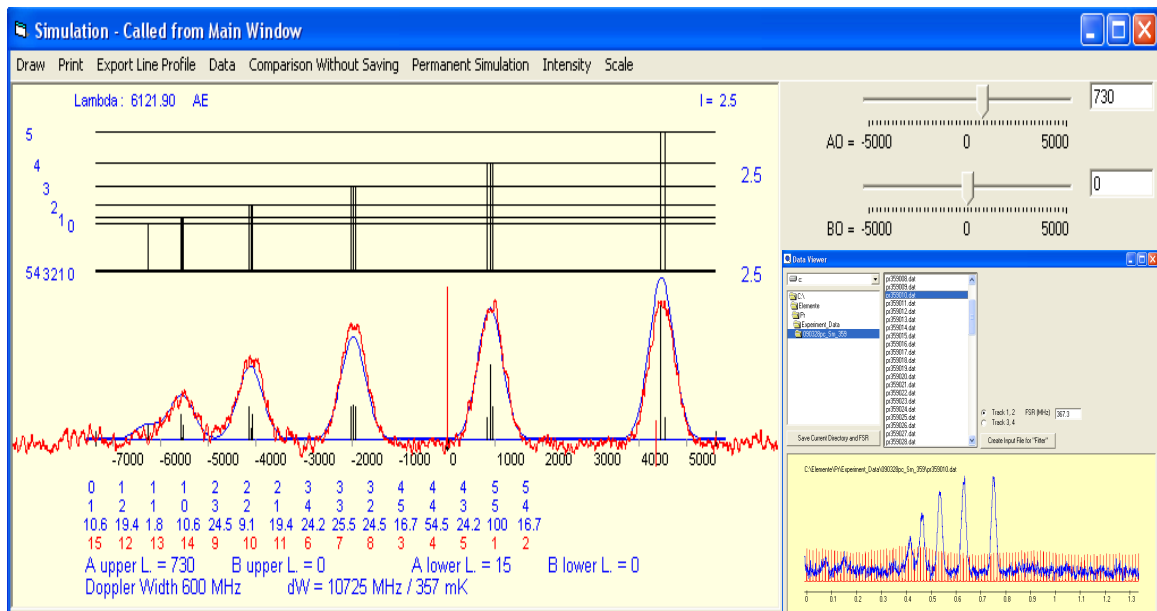
Figure 7.20: Comparison of the recorded hyperfine structure (Red curve) of the line 6121.88 Å with the predicted hyperfine structure (Blue curve).

The level scheme for both spectral lines is shown in Figure 7.21. A fluorescence blend is observed in the original excitation at fluorescence wavelength 5446 Å where both level decay to a common fluorescence lower level.

94
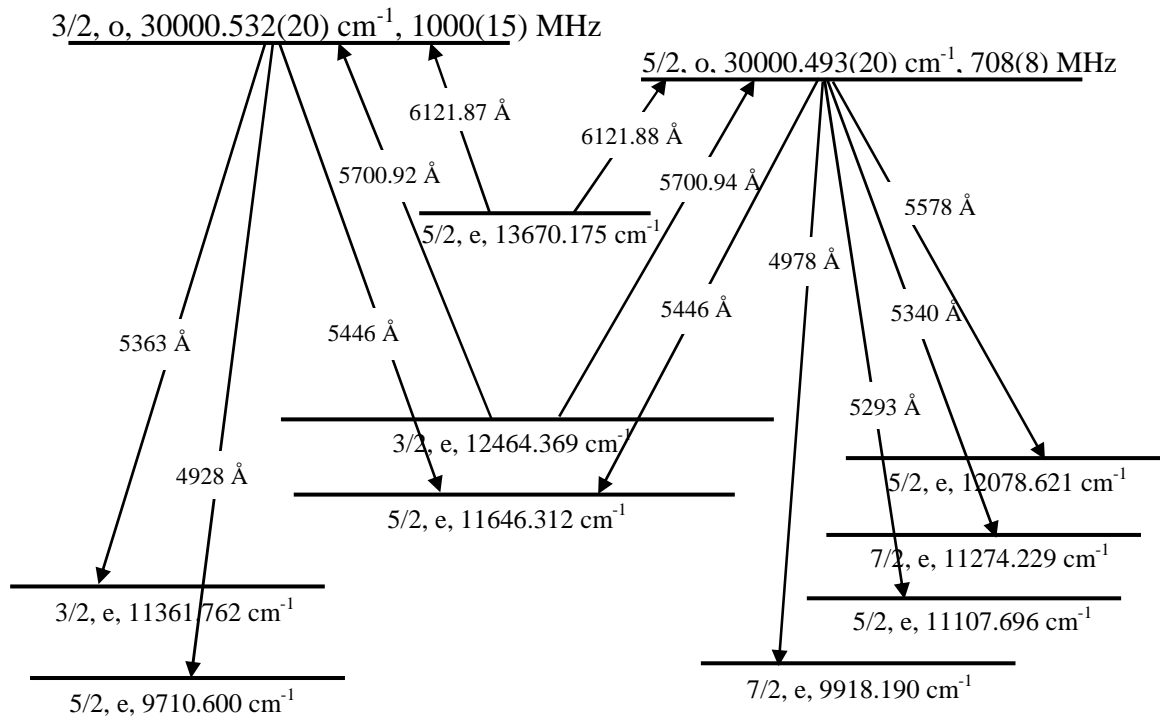
Figure 7.21: Level scheme for the excitation of 30000.532(20) *cm⁻¹* and 30000.493(20) *cm⁻¹*

It is important to note that although the two newly discovered upper levels are in a close proximity with each other i.e. with an energy separation of only 0.039 *cm⁻¹*, the intensity distribution of hyperfine components for both structure show a normal behavior. Furthermore, at the initial center-of-gravity excitation wavelengths 5700.92 Å and 5700.94 Å a hyperfine structure was recorded at the fluorescence line 5446 Å. The recorded structure show a mixture of both lines which is due to the fact that 5446 Å is appearing in the transition list of both the newly discovered upper levels 30000.532(20) cm⁻¹ and 30000.493(20) cm⁻¹. A center-of-gravity wave number difference of 0.040 cm⁻¹ was obtained from a two line fit of the recorded structure (Figure 7.22). This is in agreement with the difference, calculated from level energies of the newly discovered levels.
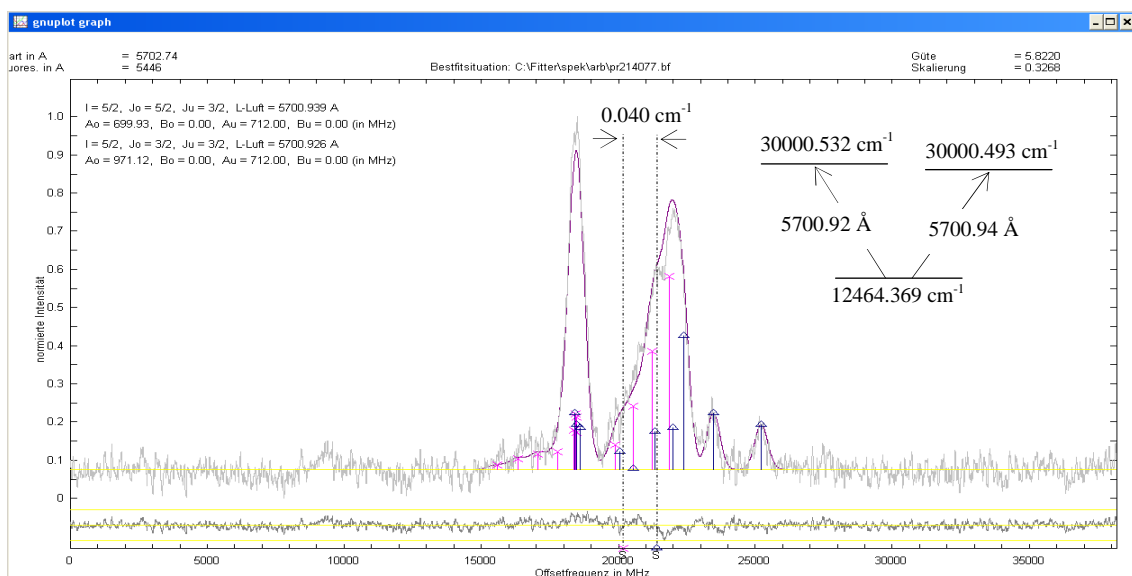
Figure 7.22: Best fit situation for multiline fit for the lines 5700.92 *Å* and 5700.94 *Å*

7.1.4 Discovery of Pr-I Levels $33264.21^{e}_{17/2}\,\mathrm{cm}^{-1}$, $16180.200^{o}_{15/2}\,\mathrm{cm}^{-1}$ and $16865.034^{o}_{15/2}\,\mathrm{cm}^{-1}$ via Laser Excitation

The laser excitation of the spectral line 5851.80 Å was performed. In the FT -spectrum, the line has a weak signal-to-noise ratio with a relative intensity of 6, see Figure 7.23. The listed suggestions for the line in the classification were inspected for a possible match. Since none of the suggestions has any coincidence with the hyperfine structure of the line, so possibly one or both the combining levels are not known and yet to be discovered.

The laser excitation wavelength was set to 5851.80 Å and LIF signals were searched. A number of fluorescence lines with good signal-to-noise ratio at wavelengths 3460 Å, 5001 Å, 5414 Å, 6096 Å, 6153 Å were observed. Now the hyperfine structure of the line was recorded by setting the monochormator at 3460 Å which has the best signal-to-noise ratio and scanning the laser frequency across the hyperfine components of the line (Figure 7.24).
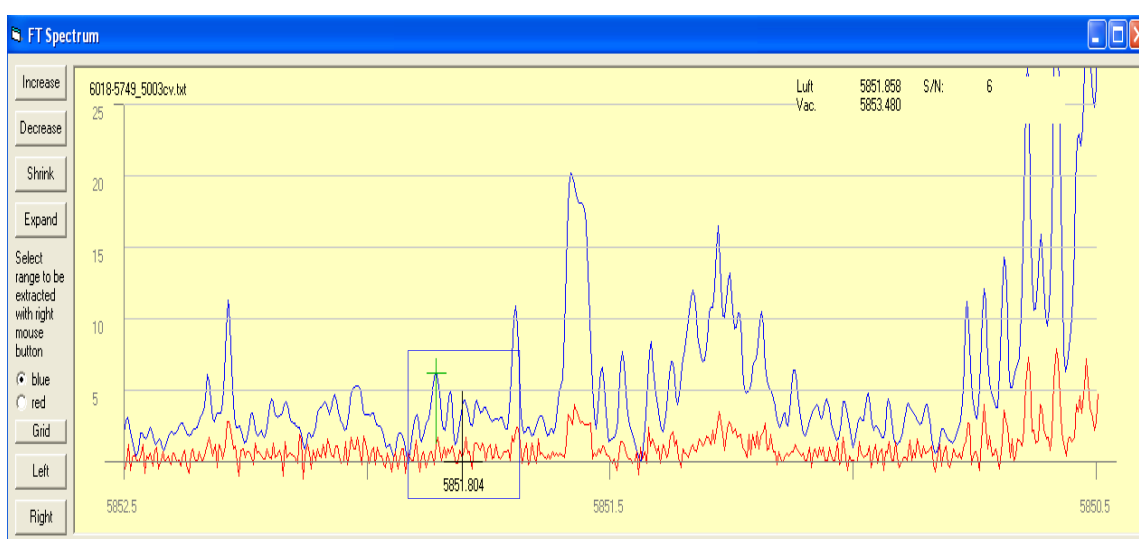
Figure 7.23: FT-spectrum of the line 5851.80 Å
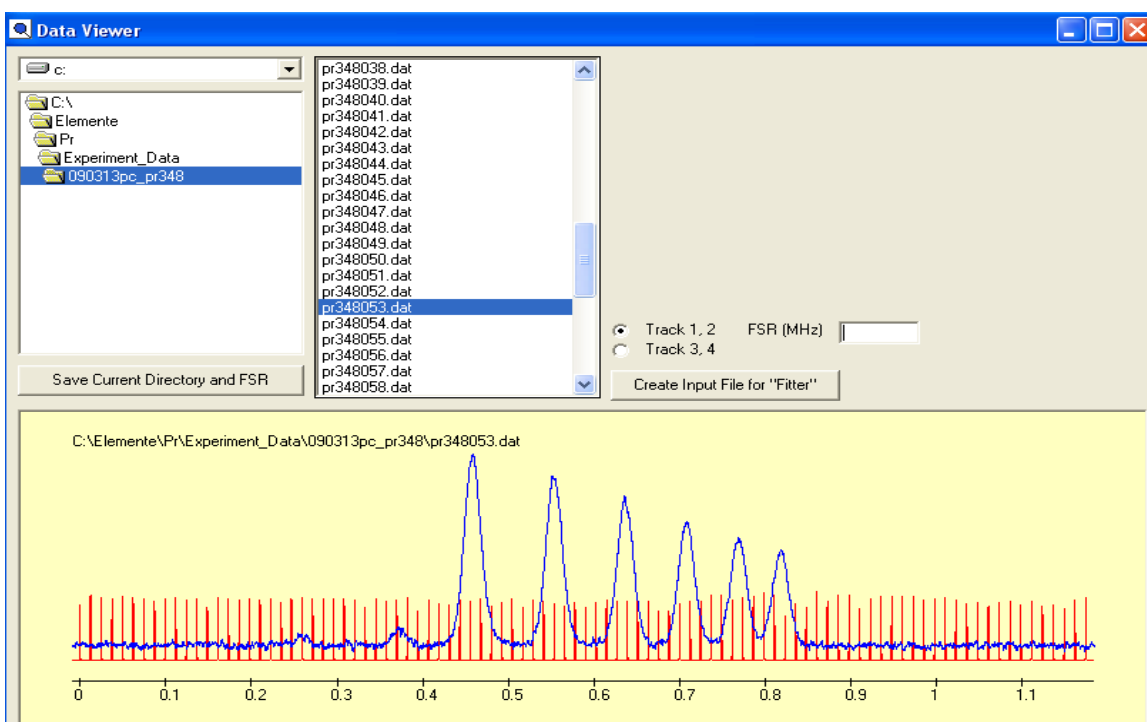
Figure 7.24: Recorded hyperfine structure of the line 5851.80 Å.

The recorded LIF spectrum shows a widely splitted hyperfine structure with appreciable separation between diagonal components. The suggestion list was again inspected for a possible match but proved unsuccessful. Using the simulation program, the spectroscopic parameters for the lower and upper combining levels in the formation of the spectral line were estimated. Taking these parameters as an initial guess, the recorded hyperfine structure was fitted to a mathematical function using the fitter program. A best fit situation is obtained (Figure 7.25) which gave the following spectroscopic parameters for the combining levels:

$$J_o = 17/2 \qquad\qquad J_u = 15/2$$

$$A_o = 546.92 \text{ MHz} \qquad\qquad A_u = 885.47 \text{ MHz}$$
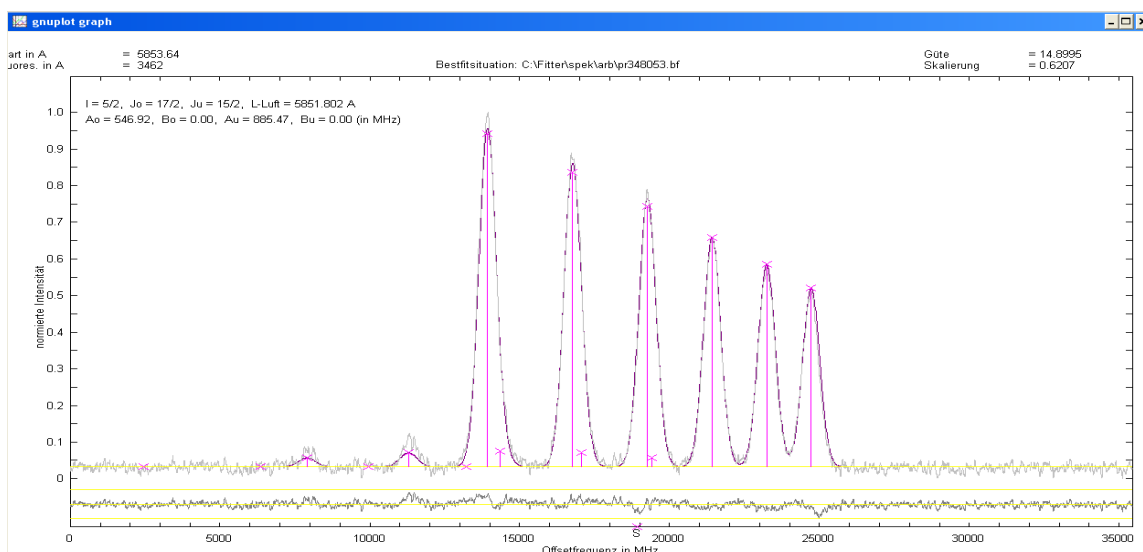
Figure 7.25: Best fit situation of the recorded hyperfine structure of the line 5851.80 Å

As is usual, initially assuming that the upper combining level is unknown, a known lower level is searched in the database of known levels based on best fitted *J*-values for upper and lower levels and *A*-value of the lower level. The search routine in the classification program computes a number of suggestions both in even and odd parity but none of the suggested upper levels explain the observed fluorescence lines. The procedure was again repeated but this time assuming an unknown lower level and searching for a known upper combining level. In searching for an unknown lower level, best fit *A*-value of the assumed upper level is given to the searching routine. But once again the computed suggestions for a possible new lower level combining with a known upper level do not explain the observed fluorescence lines. It was thus concluded that both the lower and upper levels in the formation of the excited line were yet to be discovered.

Two of the observed fluorescence lines i.e. 6096 Å and 6151 Å lie in the wavelength range of our dye laser, if the same upper level combines with the known lower levels at these lines then the unknown upper level can be identified. The exact fluorescence wavelengths were measured for the excitation of these lines. This is done by setting the laser frequency to the highest hyperfine component of the original excitation line and chopping the fluorescence light intensity coming from the hollow cathode lamp. The monochromator is automatically scanned across the fluorescence wavelength and discharge emission spectrum along with laser induced signal is recorded. A computer program called 'Comparison' is used to determine the exact fluorescence wavelengths which takes as input the wavelength range containing the fluorescence wavelength, the recorded file and the FT

spectrum file corresponding to the specified wavelength range. The exact values determined with the help of the program were 6096.21 Å and 6151.54 Å (Figures 7.26 & 7.27).
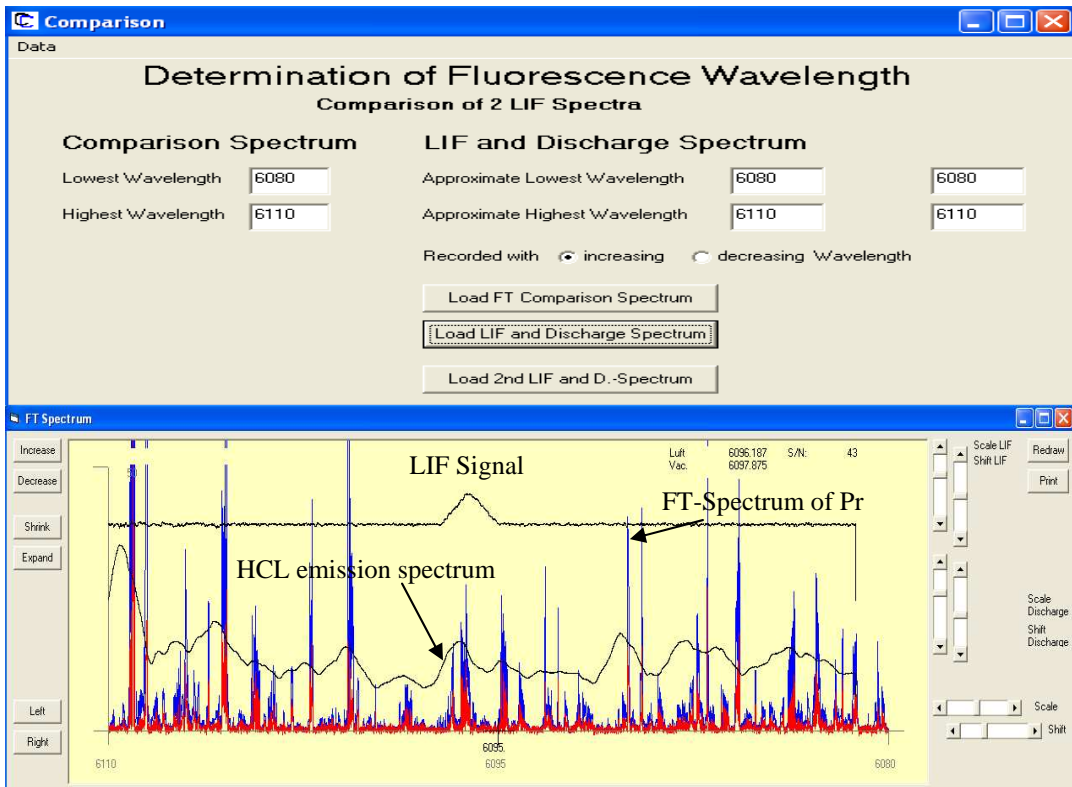
Figure 7.26: Exact measure of fluorescence wavelength 6096.19 Å
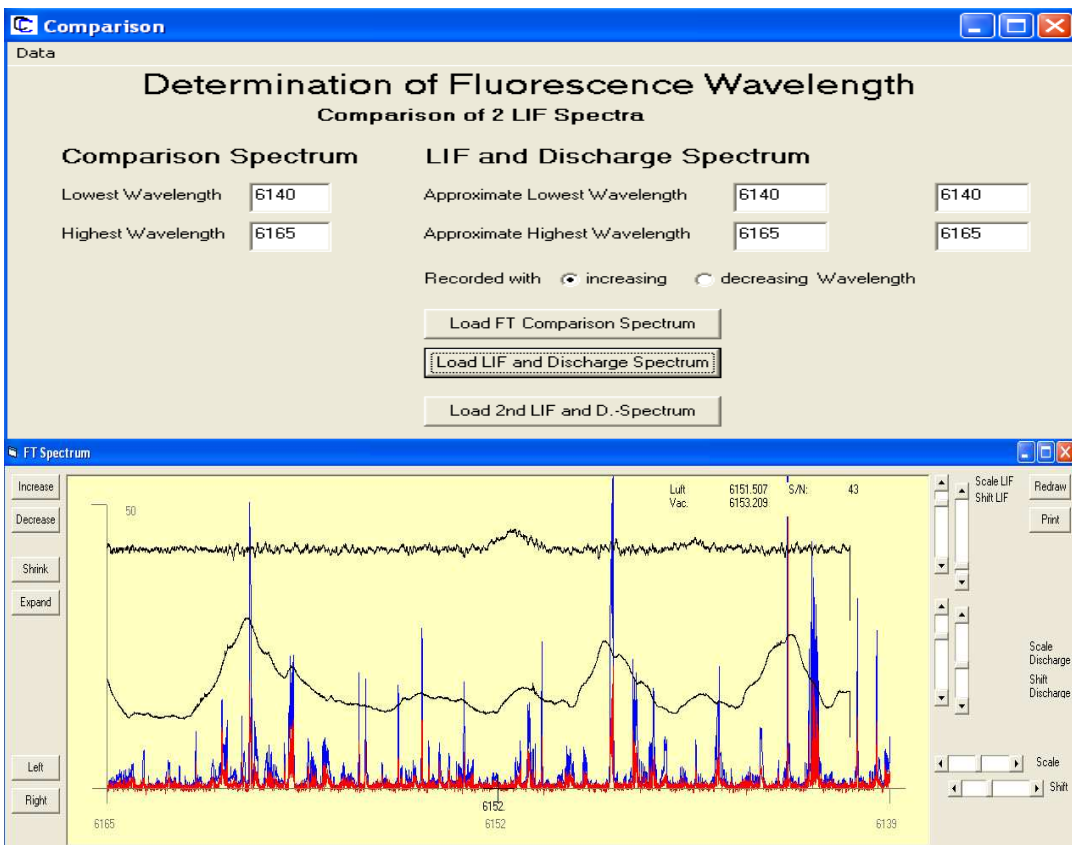
Figure 7.27: Exact measure of fluorescence wavelength 6151.50 Å

In the FT spectrum the spectral line profile in the vicinity of 6096.21 $Å$ appears to be a mixture of more than one line with a good signal-to-noise ratio having a relative intensity of ~ 65, see Figure 7.28. The line at center-of-gravity wavelength 6096.32 $Å$ belongs to a transition with known combining lower and upper levels, i.e. $27721.206^{e}_{13/2} - 11322.443^{o}_{11/2}$.
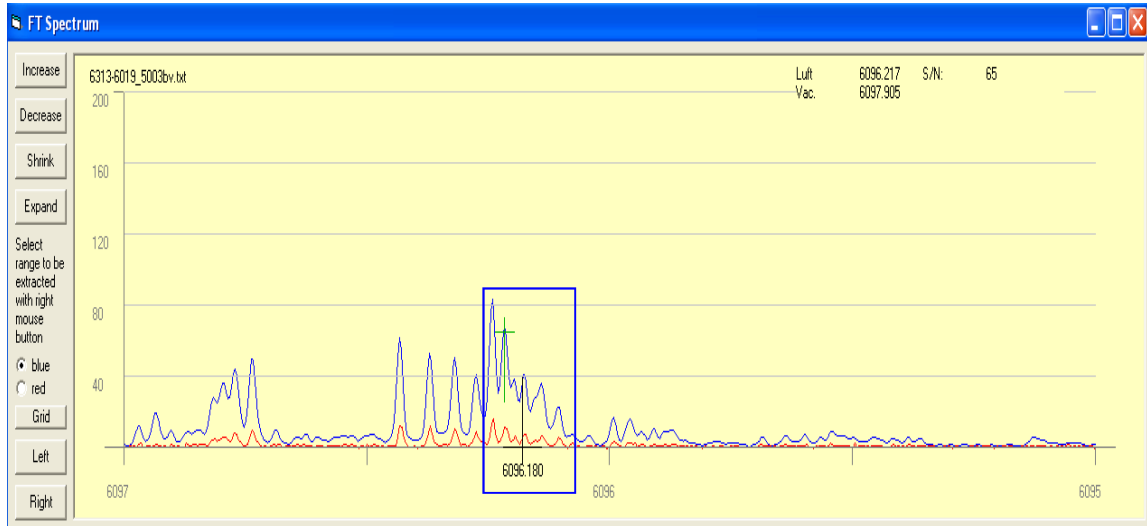
Figure 7.28: FT-spectrum for the line 6096.18 $Å$

To investigate the line at 6096.21 $Å$, the monochromator was set to 3460 $Å$ which has the strongest LIF signal. Now by scanning the laser frequency around 6096.21 $Å$. LIF signal at this wavelength was observed. The intensity of the LIF signal increases to maximum at 6096.11 $Å$ corresponding to the largest hyperfine diagonal component of line. The fluorescence signal was also observed on all other previously recorded fluorescence wavelengths as well as on the original excitation wavelength i.e. 5851 $Å$. This indicates to some extent that the same upper level is excited in the excitation of this line. The hyperfine structure of the line was then recorded by scanning the laser wavelength across the hyperfine components of the line. A hyperfine structure with good signal-to-noise ratio and well resolved diagonal components was recorded on all previously observed fluorescence wavelengths, see Figure 7.29. The suggestions listed for the line in the classification program were inspected but none show any coincidence neither in terms of shape nor in terms of positions of hyperfine components.
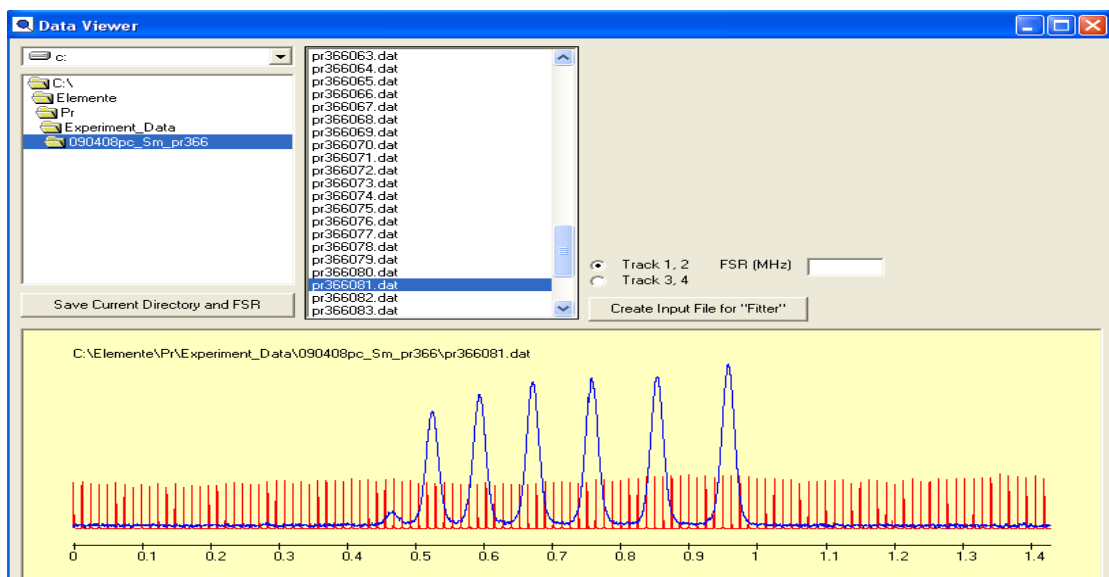
Figure 7.29: Recorded hyperfine structure of the line 6096.18 $Å$.

99

The recorded hyperfine structure for this line with best signal-to-noise ratio was fitted using fitter program and a best fit situation was obtained on the same *J*- and *A*-values of the upper level as obtained for the fitting of hyperfine structure of the line at 5851.80 Å, see Figure 7.30.
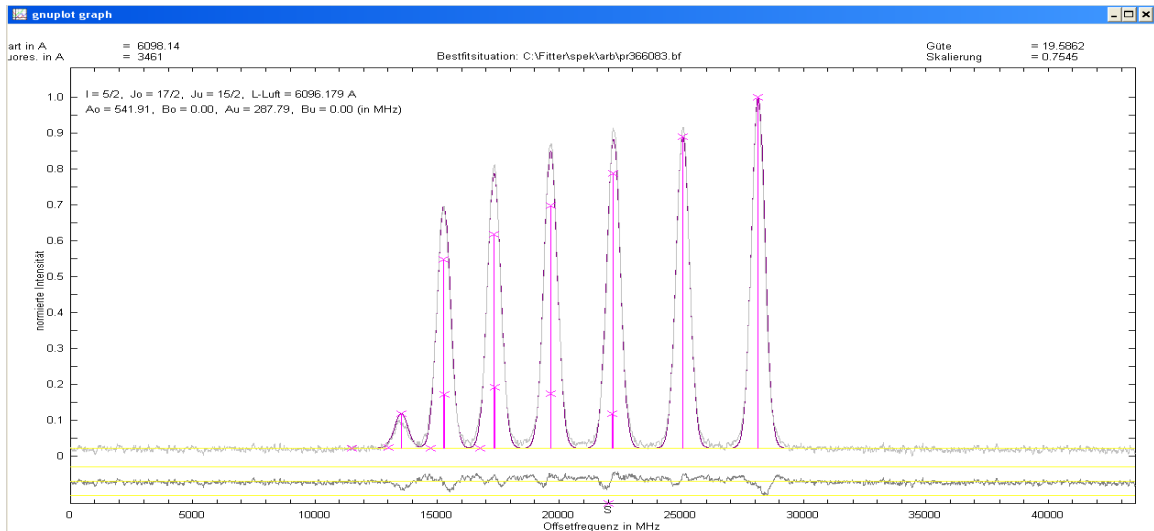
Figure 7.30: Best fit situation of the recorded hyperfine structure of the line 6096.18 Å

The best fit situation gave the center-of-gravity wavelength as 6096.18 Å and the spectroscopic parameters of the combining lower and upper level as $J_o = 17/2$, $J_u = 15/2$, $A_o = 541.91$ MHz and $A_u = 287.79$ MHz. Using the same procedure, the combining levels for the line were searched independently by first assuming an unknown upper level and a known lower level and vice versa. For this line, again neither of the combining levels can be identified. It is then again concluded that both the lower and upper levels combining at this line are unknown. If the same upper level is combining with different lower levels at lines 5851.80 Å and 6096.18 Å then all together three levels are unknown.

In FT-spectrum the line profile in the vicinity of 6151.54 Å again appears to be a blend of more than one line. Here the signal-to-noise ratio is weak with a relative intensity of only 1 (Figure 7.31).
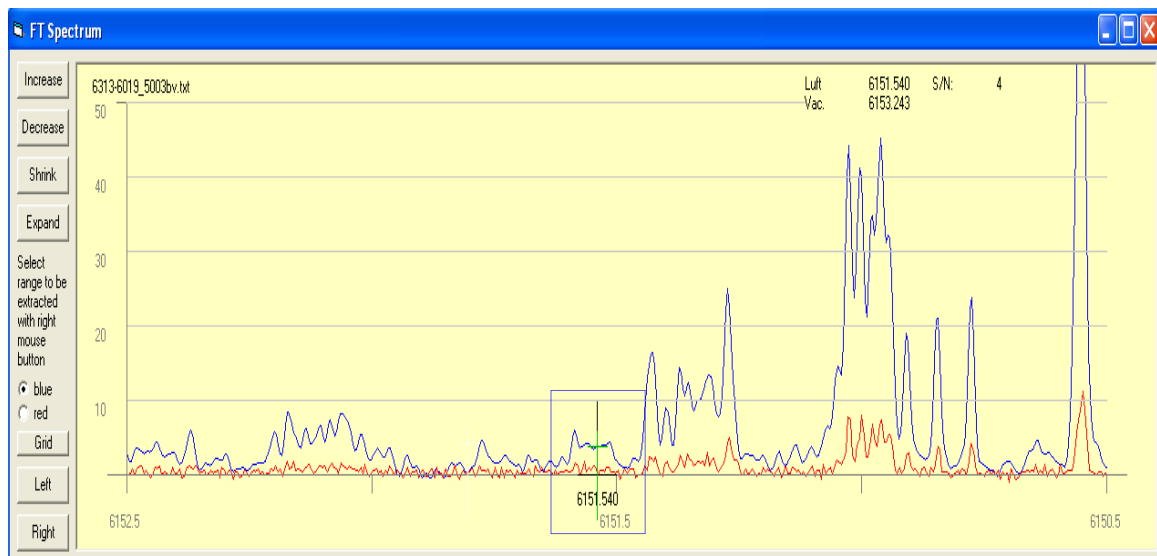
Figure 7.31: FT-spectrum for the line 6151.54 Å

The laser excitation wavelength was set at 6151.54 Å and again the monochromator was set at 3460 Å. A strong LIF signal was observed when the laser wavelength was set to 6151.52 Å on all previously observed fluorescence wavelengths, implying that possibly the same upper level has been excited but now from a third different lower level at this line. The hyperfine structure of the line was recorded by setting the monochromator to the strongest fluorescence wavelength which in this case is 3460 Å and scanning the laser frequency across the hyperfine components of the line. Again the recorded LIF spectrum has a good signal-to-noise ratio, see Figure 7.32.
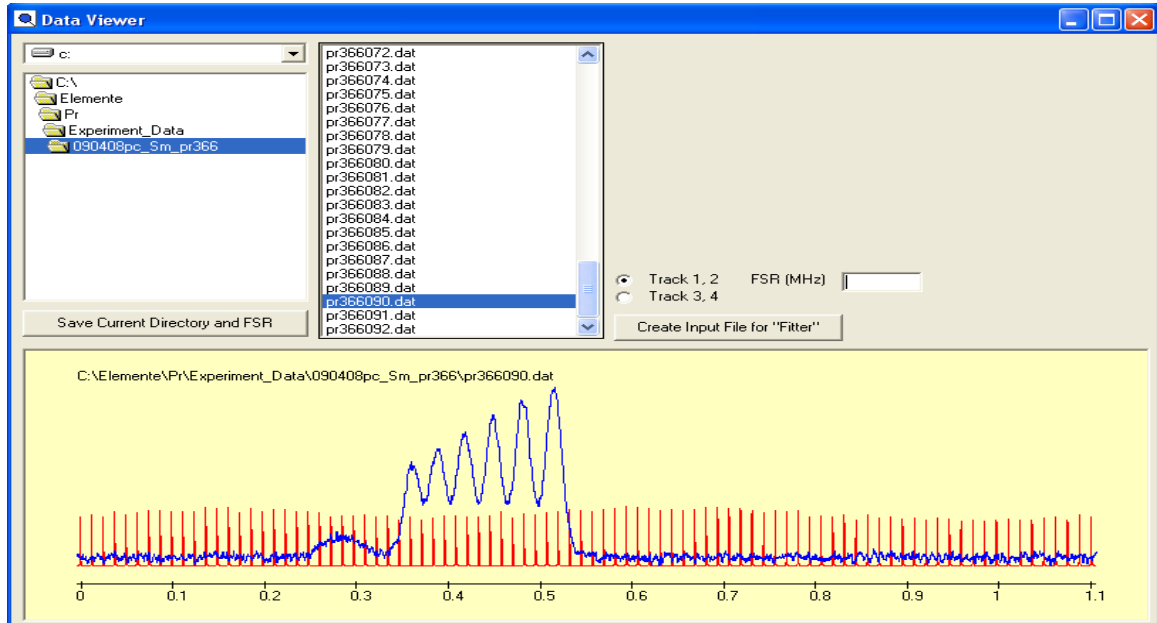
Figure 7.32: Recorded hyperfine structure of the line 6151.53 Å.

The same hyperfine structure was recorded on all other observed fluorescence wavelengths. The suggestions for the spectral line in the classification program was inspected for a possible match with the recorded hyperfine structure but again none of the suggestions show any coincidence with the recorded hyperfine structure.

The recorded hyperfine structure with best signal-to-noise ratio was independently fitted using fitter program. Best fit situation was obtained (Figure 7.33) giving a center-of-gravity wavelength at 6151.54 Å with spectroscopic parameters $J_o = 17/2$, $J_u = 15/2$, $A_o = 539.09$ **MHz** and $A_u = 492.06$ **MHz.**
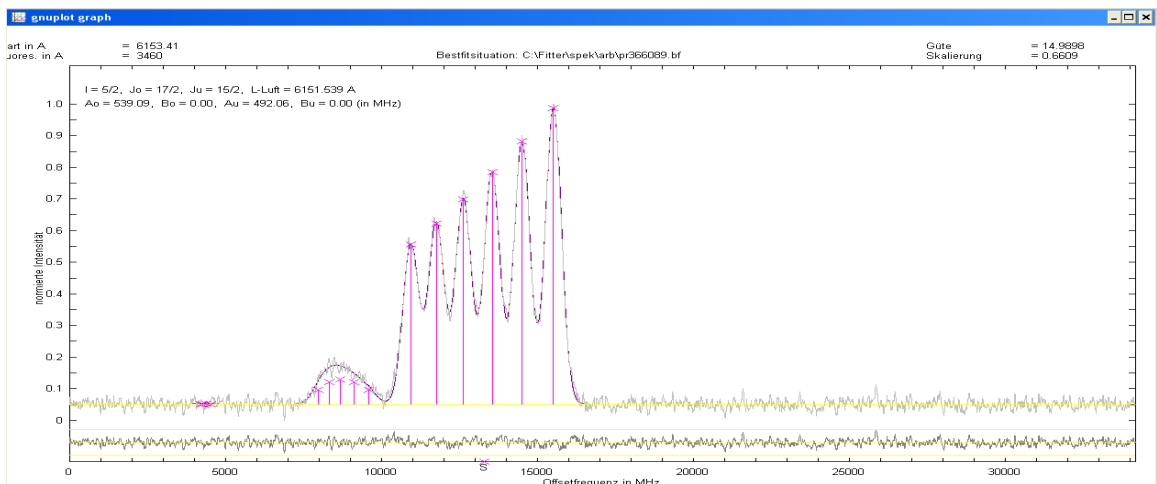
Figure 7.33: Best fit situation of the recorded hyperfine structure of the line 6151.53 Å

Based on the fluorescence information obtained in the excitation of this line and previous two lines (5851.80 Å and 6096.18 Å), it was assumed that this same newly found upper level is involved in the excitation of lines at 5851.80 Å and 6096.18 Å and further assuming that lower combining levels at both these lines are unknown, the energy of these unknown lower levels were determined using the energy of the newly discovered upper level 33264.21 cm^{-1} and the respective wave numbers of the lines at 5851.80 Å and 6096.18 Å.

The group of these three newly calculated levels is:

16180.200 cm^{-1}, odd parity, $J_u = 15/2$ and $A_u = 883.26$ MHz

16865.034 cm^{-1}, odd parity, $J_u = 15/2$ and $A_u = 290.96$ MHz

33264.21 cm^{-1}, even parity, $J_o = 17/2$ and $A_o = 544.65$ MHz

In order to confirm the energies and existence of the newly found levels, the levels must be confirmed at some other lines from FT-spectrum with their hyperfine structure profile in agreement with the hyperfine structure predicted by the classification program. It would further consolidate if laser excitation at these or other lines could be performed where the newly discovered levels combine with known lower and upper levels and the resulting hyperfine structure is in agreement both in terms of shape and hyperfine component positions with the predicted hyperfine structure by the classification program.

7.1.4a Confirmation of 33264.21 cm^{-1}:

The upper level in the group is confirmed from FT-spectrum at lines 3461.236 Å and 5414.331 Å. The hyperfine structures of the lines as predicted by classification program are in good agreement with the hyperfine structure line profile in FT-spectrum (Figure 7.34 and 7.35). Experimentally, the level was confirmed by a laser excitation at line 6066.498 Å where it combines with a known lower level $16784.800^o_{15/2}$. Figure 7.36 shows the experimentally recorded hyperfine structure of the line and the simulation with the predicted hyperfine structure as given by classification program. This confirms the level energy and existence of the level beyond doubt. The level energy was corrected and the lines were then classified.
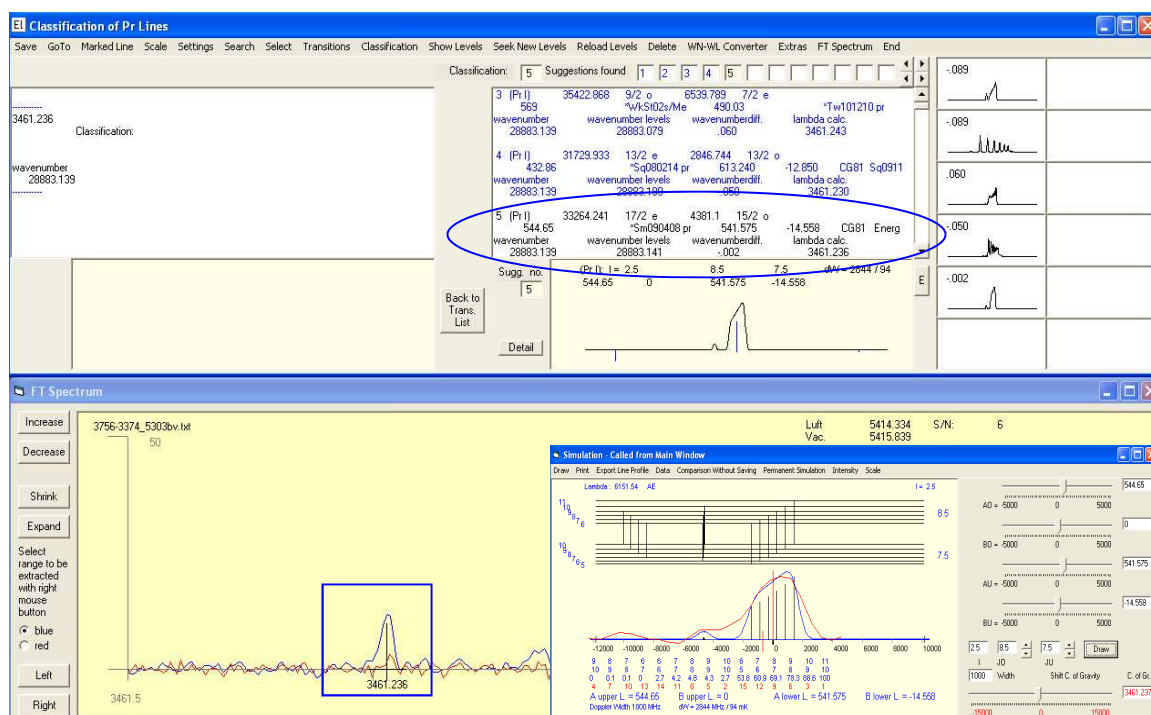
Figure 7.34: Confirmation of 33264.21 cm^{-1} at 3461.236 Å
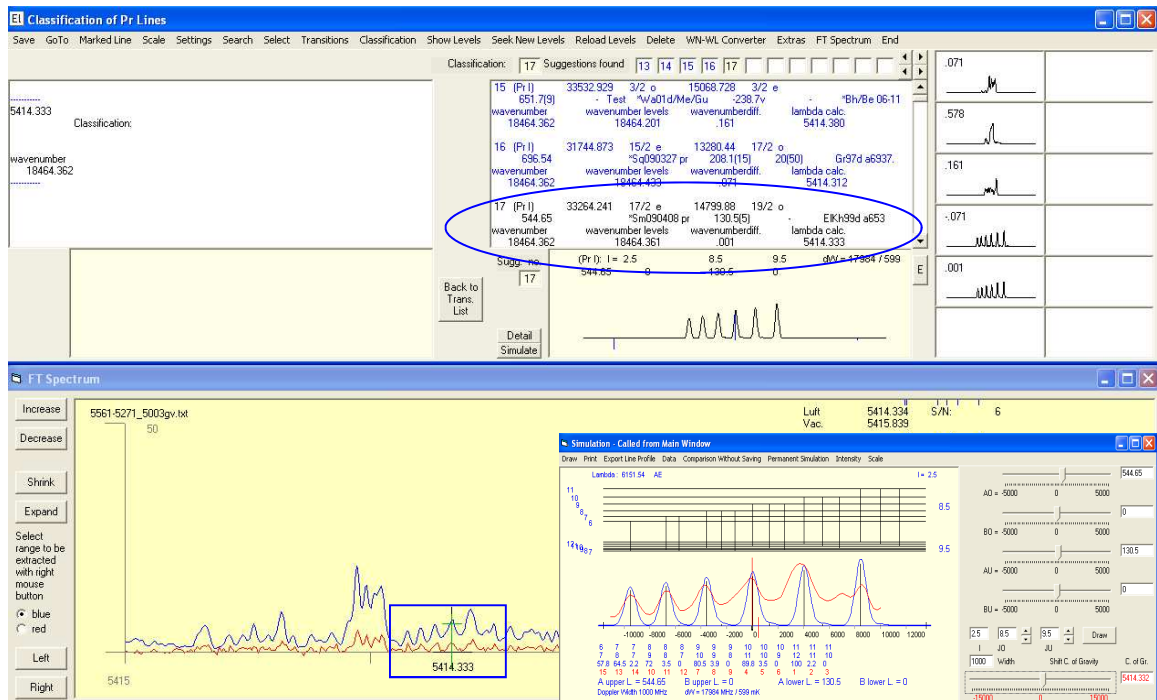
Figure 7.35: Confirmation of 33264.21 cm^{-1} at 5414.332 $\mathring{A}$
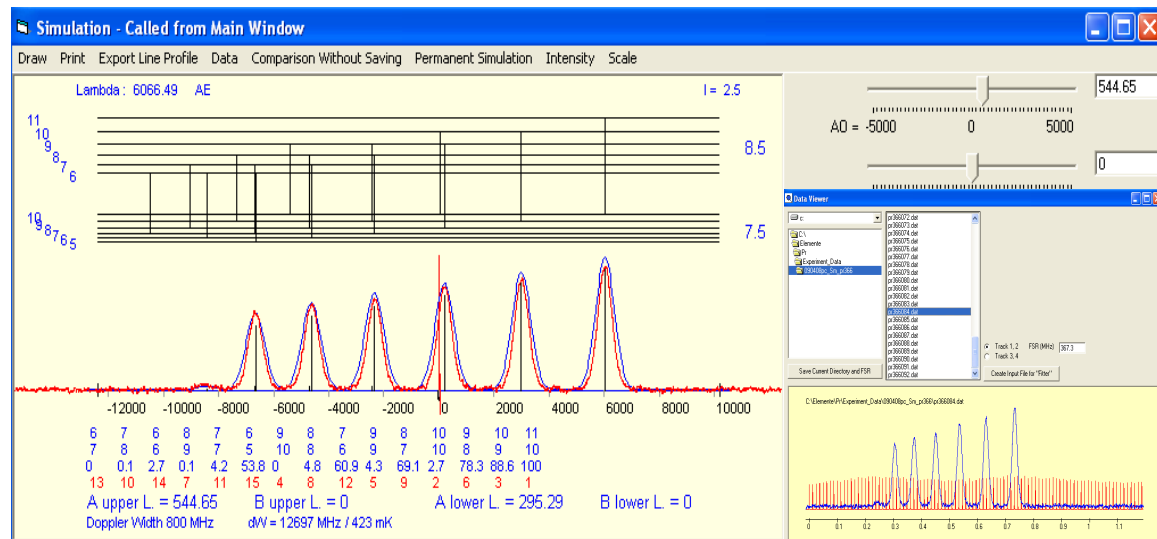
Figure 7.36: Comparison of the recorded hyperfine structure (Red curve) of the line 6066.498 $\mathring{A}$ with the predicted hyperfine structure (Blue curve).

7.1.4b Confirmation of 16180.200 cm^{-1}:

In order to confirm the lower level 16180.200 cm^{-1}, laser excitations were performed at lines 5651.35 $\mathring{A}$, 6399.562 $\mathring{A}$ and 6429.226 $\mathring{A}$. The lines at 5651.35 $\mathring{A}$ and 6429.23 $\mathring{A}$ in FT-Spectrum appear in a mixture of more than one line with partially resolved hyperfine components whereas line at 6399.562 $\mathring{A}$ in FT-spectrum has good signal-to-noise ratio with resolved hyperfine components. The level 16180.200 cm^{-1} combines with different already known upper levels at the respective lines (Figure 7.37, 7.38 & 7.39) i.e.

$$cog \; \lambda = 5651.35 \; \mathring{A} \rightarrow 33870.186^e_{13/2} - 16180.200^o_{15/2}$$

$$cog \; \lambda = 6399.562 \; \mathring{A} \rightarrow 31801.951^e_{17/2} - 16180.200^o_{15/2}$$

$$cog \; \lambda = 6429.23 \; \mathring{A} \rightarrow 31729.874^{e}_{13/2} - 16180.200^{o}_{15/2}$$
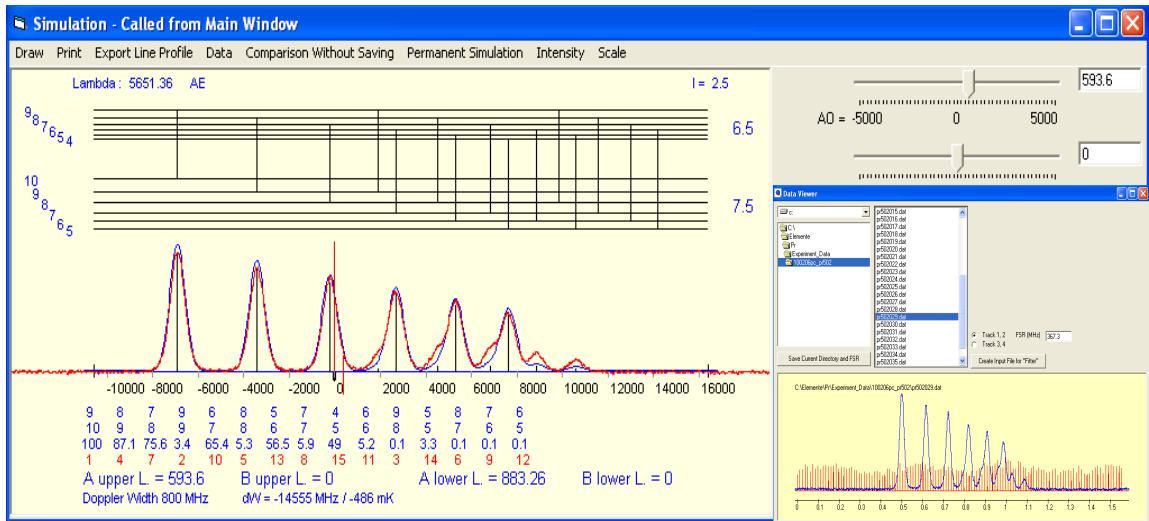
Figure 7.37: Comparison of the recorded hyperfine structure (Red curve) of the line 5651.35 Å with the predicted hyperfine structure (Blue curve).
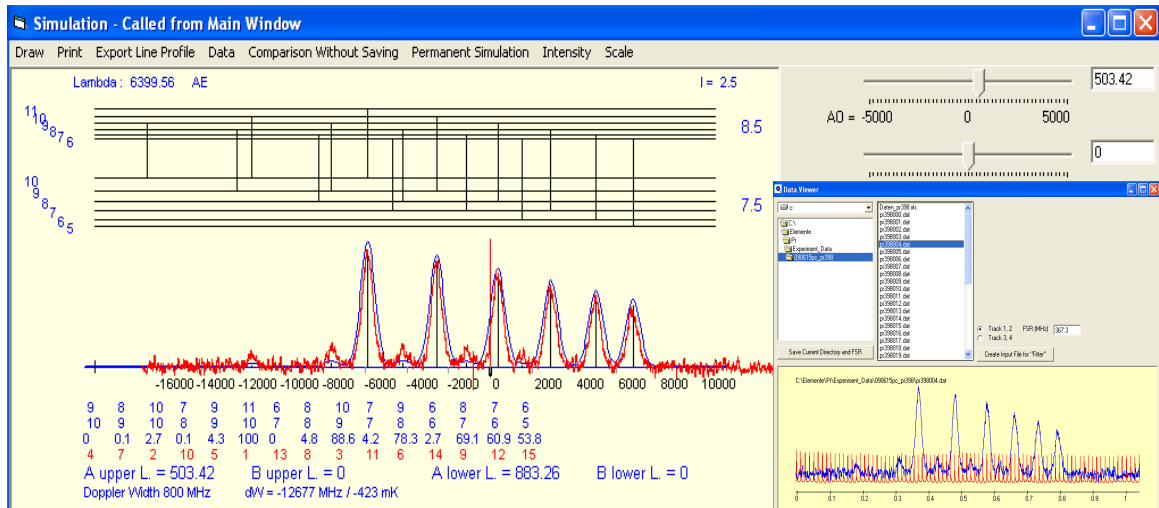
Figure 7.38: Comparison of the recorded hyperfine structure (Red curve) of the line 6399.562 Å with the predicted hyperfine structure (Blue curve).
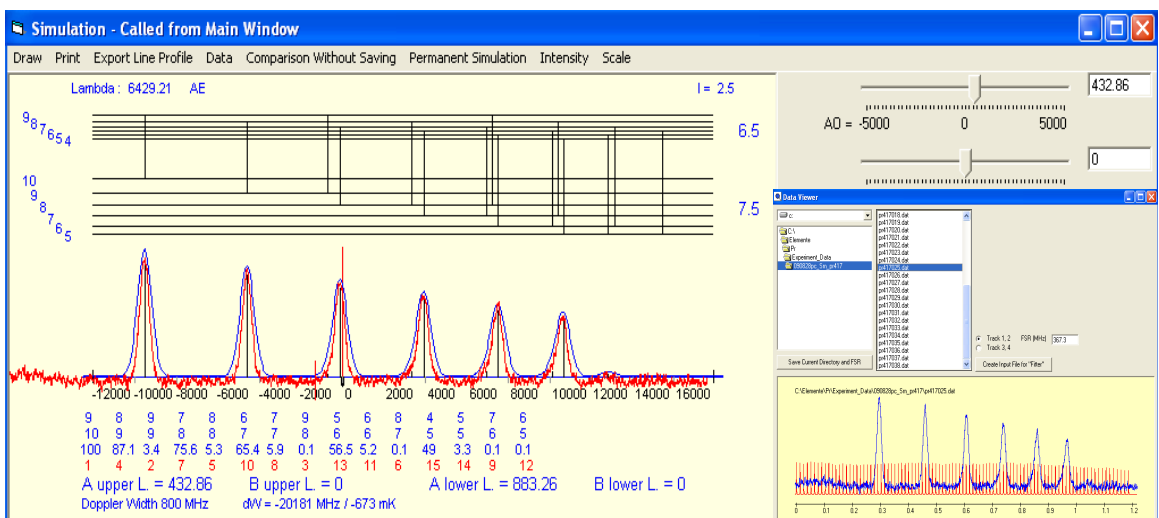
Figure 7.39 Comparison of the recorded hyperfine structure (Red curve) of the line 6429.23 Å with the predicted hyperfine structure (Blue curve).

7.1.4c Confirmation of 16865.034 cm^{-1}:

The level 16865.034 cm^{-1} was also confirmed experimentally at three other positions i.e. 5953.48 Å, 6546.12 Å and 6583.66 Å as a lower level for the respective transitions. The lines in FT-Spectrum appear with a very weak signal-to-noise ratio but contrary to this, recorded LIF spectrum for all three lines show a good signal-to-noise ratio. At the respective lines, the level combines with already known upper levels (Figure 7.40, 7.41 & 7.42) i.e.

$$cog\ \lambda = 5953.48\ \AA \rightarrow 33657.265^e_{17/2} - 16865.034^o_{15/2}$$

$$cog\ \lambda = 6546.12\ \AA \rightarrow 32137.040^e_{17/2} - 16865.034^o_{15/2}$$

$$cog\ \lambda = 6583.65\ \AA \rightarrow 32049.984^e_{13/2} - 16865.034^o_{15/2}$$
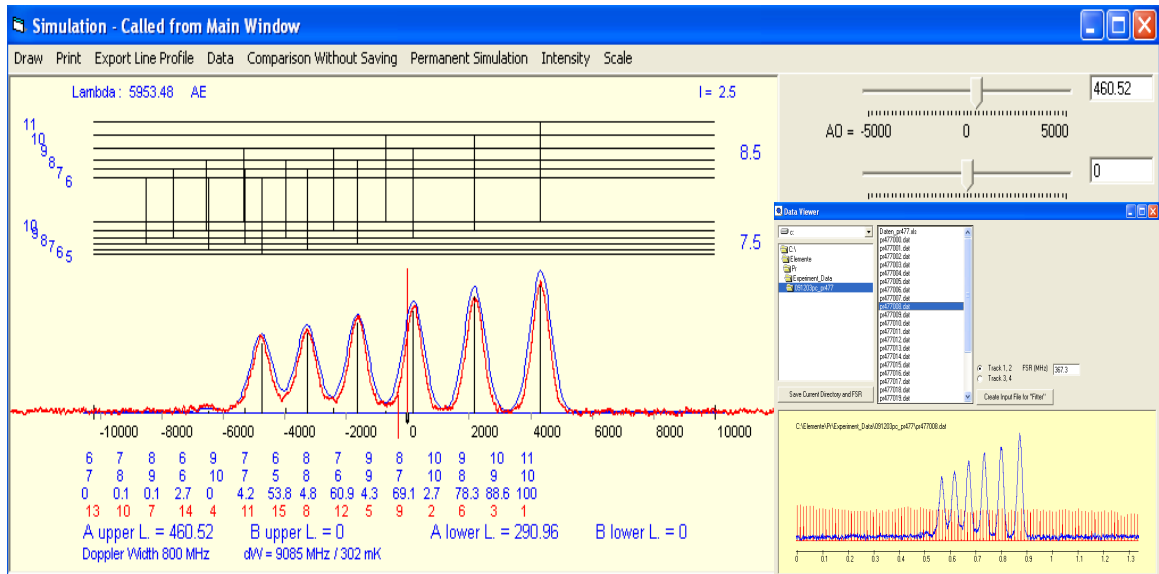
Figure 7.40: Comparison of the recorded hyperfine structure (Red curve) of the line 5953.48 Å with the predicted hyperfine structure (Blue curve).
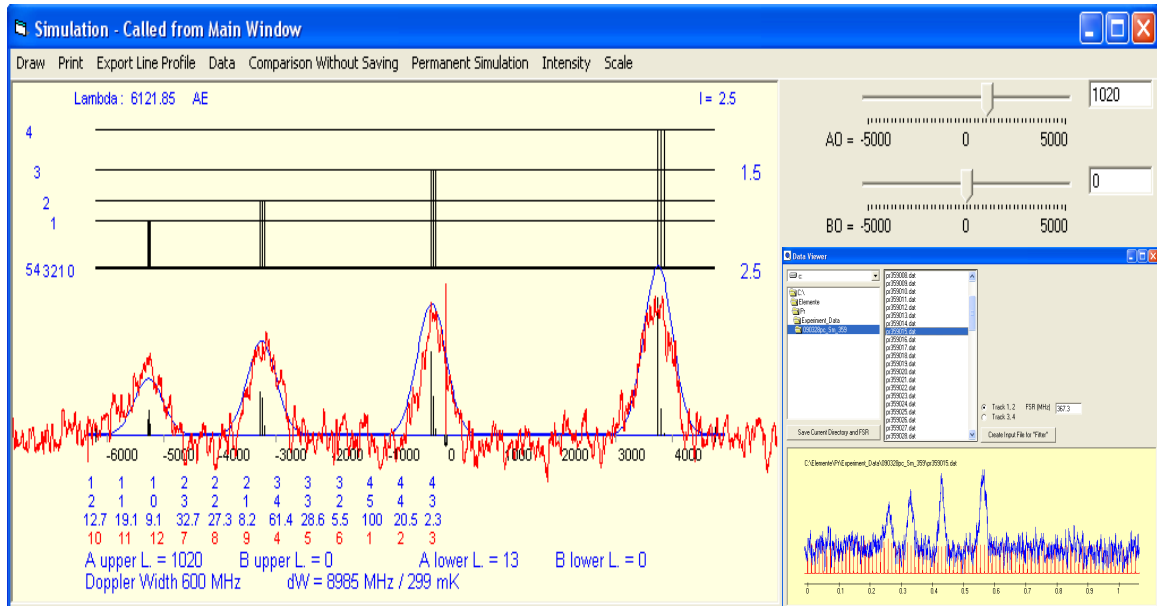

Figure 7.41: Comparison of the recorded hyperfine structure (Red curve) of the line 6546.12 Å with the predicted hyperfine structure (Blue curve).

105

Figure 7.42: Comparison of the recorded hyperfine structure (Red curve) of the line 6583.65 Å with the predicted hyperfine structure (Blue curve).

A set of three levels were discovered with a high angular momentum values. All the three levels were independently confirmed by excitation to or from already known upper and lower levels. The hyperfine interaction *A* constant and level energies were corrected. All the excited lines were then classified. The energy level diagram is shown in Figure 7.43.

Figure 7.43: Energy level diagram for the set of newly discovered levels

7.1.5 Doublet Hyperfine Structure: Excitation from a Pair of Lower Levels to a New Upper Level

Continuing the systematic investigations of the spectrum of praseodymium, the FT-spectrum in the vicinity of 5594.56 $\mathring{A}$ was investigated. More than one line appears to be in a close proximity with each other with their hyperfine components mixed together, see Figure 7.44. The signal-to-noise ratio is not good with a relative intensity of 8. Although the classification program shows a number of suggestions but due to the mixed appearance of hyperfine structure components, the lines in this segment of FT-spectrum could not be explained without laser excitation. Laser excitation was performed by tuning the laser frequency to each hyperfine component in FT-spectrum and searching for fluorescence lines.
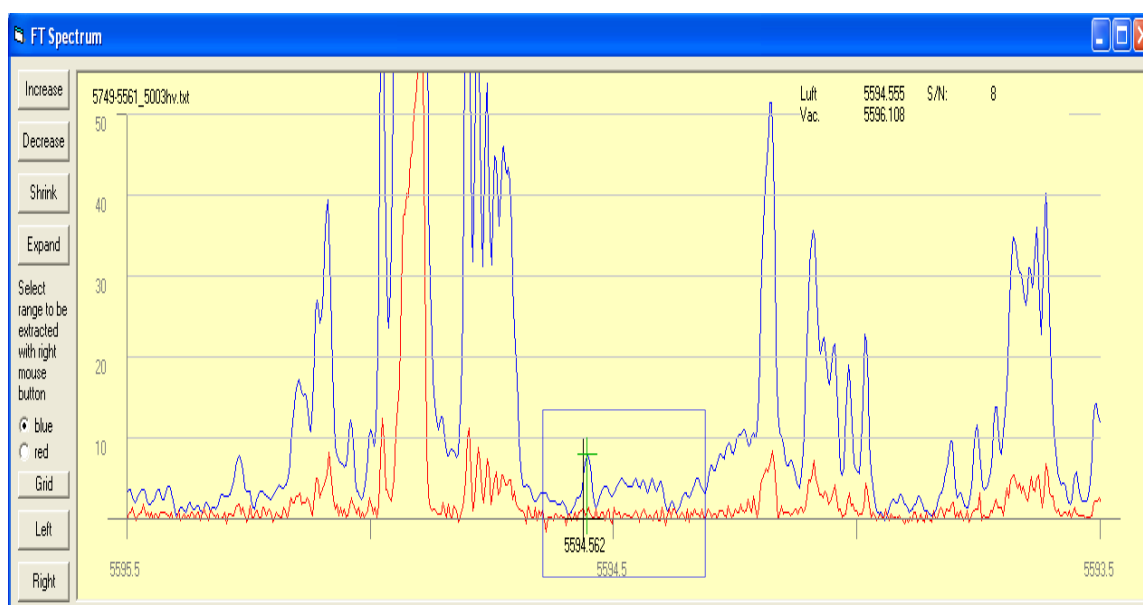
Figure 7.44: FT-spectrum for the line 5594.56 $\mathring{A}$

Initially laser excitation wavelength was set to 5594.56 Å and fluorescence lines were searched by tuning the monochromator. LIF signal was observed on 4716 $\mathring{A}$, 4827 $\mathring{A}$, 5823 $\mathring{A}$ with best signal-to-noise ratio at 4827 $\mathring{A}$. LIF spectrum was then recorded by scanning the laser wavelength starting from 5594.73 $\mathring{A}$ down to a 45 GHz length. The recorded LIF spectrum (Figure 7.43) shows two groups of hyperfine structure components with an approximate center-of-gravity separation of 0.700 cm^{-1}. The appearance of two hyperfine structures in a single scan can be attributed to an excitation or fluorescence blend situation due to the fact that praseodymium has high line density. To clarify the observed behavior, LIF spectrum was recorded on all observed fluorescence lines. Interestingly, the same two groups or doublet was recorded on all other observed fluorescence lines. In both groups intensity ratios of the diagonal hyperfine components are in agreement with the intensity rule for a normal hyperfine structure pattern. The first group of hyperfine components at lower frequency with an approximate center-of-gravity wavelength 5594.56 $\mathring{A}$ gives an impression of a narrow peak structure with closely lying diagonal components. The off-diagonal components appear on one side and are not well separated from diagonal components. The second group of hyperfine structure components at higher frequency with an approximate center-of-gravity wavelength 5594.36 $\mathring{A}$ shows a hyperfine structure with six diagonal hyperfine components, the last two of which are very close to each other. Comparatively faster decrease in spacing between diagonal hyperfine structure

components is observed. The off-diagonal components appear only on the high frequency side.
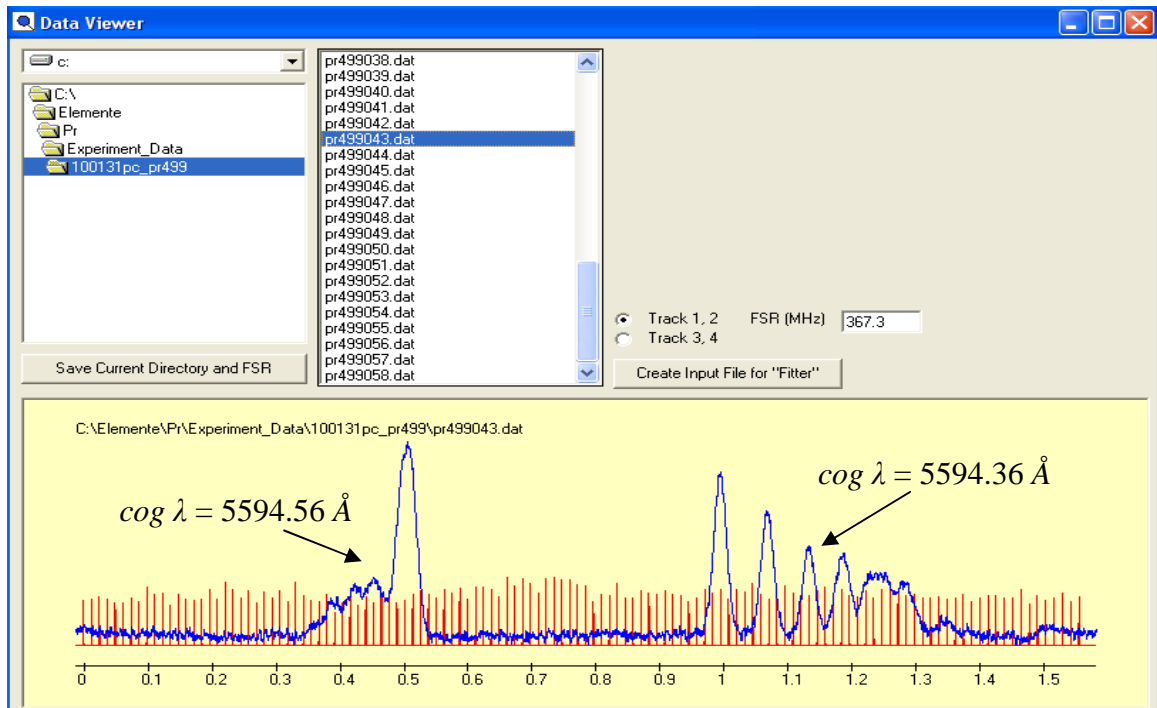
Figure 7.45: Recorded hyperfine structures of the lines 5594.56 Å and 5594.36 Å

Since the same two groups appear on all observed fluorescence lines so a model is proposed (Figure 7.46) in which two lower levels are excited to a single upper level in a single scan range of laser.
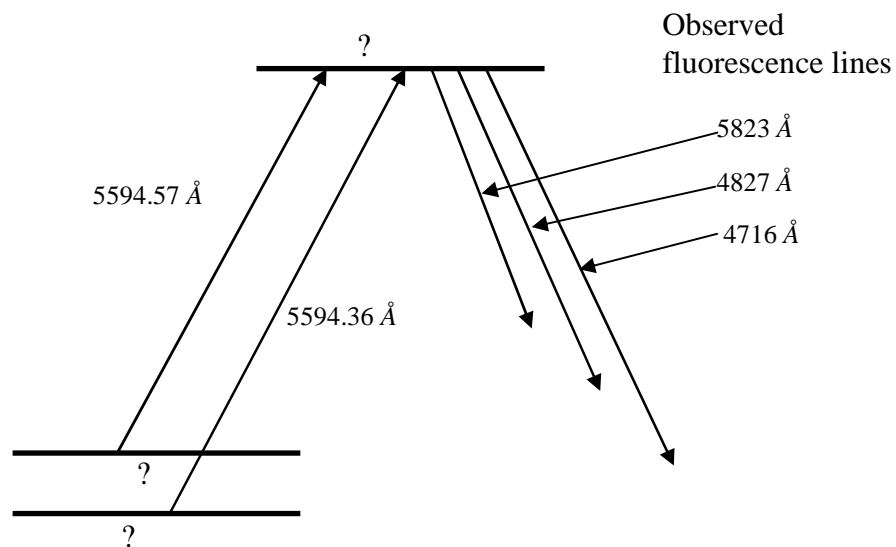
Figure 7.46: Suggested model scheme for the combining levels

Since the intensity ratios of the hyperfine components in the recorded structure follow the normal intensity ratios for hyperfine pattern, the recorded structure is fitted by using a multiline fitting procedure in the Fitter program. A best fit situation with a quality factor $Q = 11$ (Figure 7.47) was obtained for $\Delta J = -1$ for hyperfine structure at lower frequency with

center-of-gravity excitation wavelength 5594.562 Å and *ΔJ* = +1 for the hyperfine structure at higher frequency with center-of-gravity excitation wavelength 5594.36 Å. As a result of fitting process, the *A*- and *J*-values for the upper level i.e. A_o = 647 MHz, J_o = 5/2, turn out to be same for the hyperfine structure of both lines but for lower levels in both cases the values were different i.e. for the hyperfine structure of the line at 5594.562 Å the interaction constant A_u = 905 MHz and J_u = 3/2 and for the hyperfine structure of the line at 5594.36 Å the interaction constant A_u = 892 MHz and J_u = 7/2. The same *A*-values for the upper levels and different *A*-values for the lower levels of the two hyperfine structures of the lines give an indication to a first approximation that two different lower levels are excited to a single upper level as initially suggested in the proposed model.
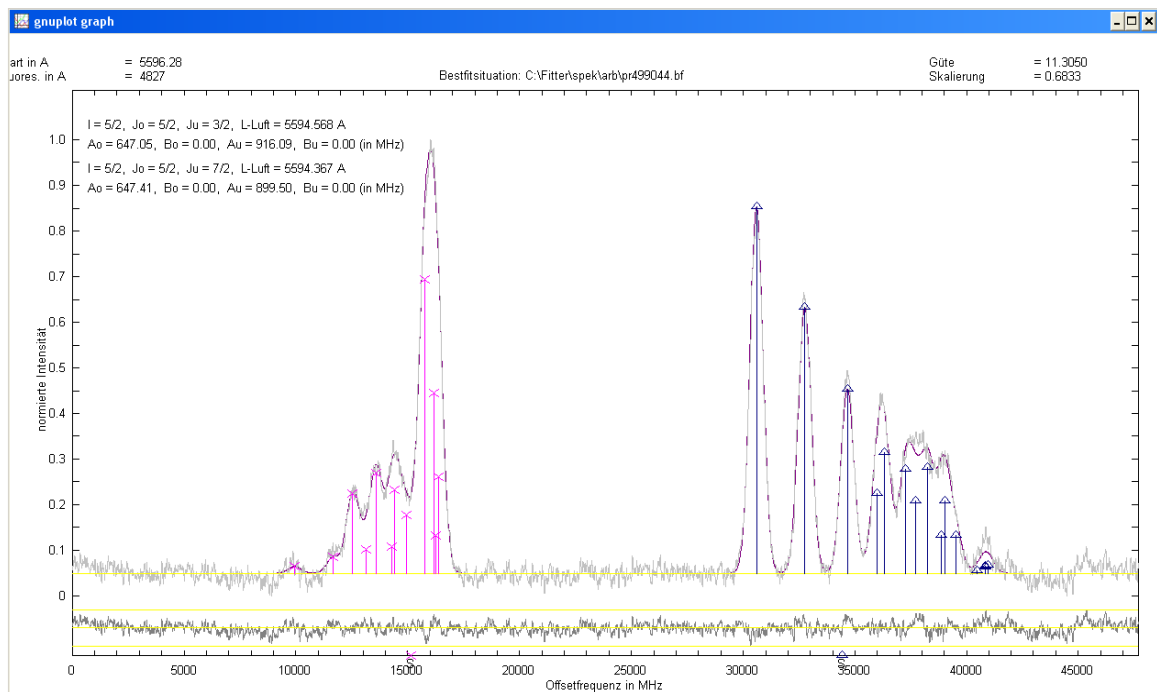
Figure 7.47: Multiline fitting for two Pr I lines 5594.562 Å and 5594.36 Å

Now with an initial assumption that an unknown upper level is involved in the excitation of both lines, the two lower levels were searched in the data base of known levels using fitted *A*-values of lower levels [A_u (5594.562 Å) = 905 MHz and A_u (5594.36 Å) = 892 MHz] and corresponding *J*-values [J_o = 5/2, J_u = 3/2, J_o = 5/2, J_u = 7/2]. The search for lower levels was done successively for both lines using the searching routine in the classification program. First the line at 5594.562 Å was inserted in the classification program and a known lower level is searched. Number of suggestions was computed for the line and an even parity lower level was found, this lower level combines with a possible new odd parity upper level which explained all the observed fluorescence lines, (Figure 7.48). The spectroscopic parameters for the lower level are **13033.280 *cm*$^{-1}$**, **even parity**, J_u = **3/2** and A_u = **905(4) MHz**. Next the line at 5594.36 Å is inserted and a known lower level is searched at this line. Again from among the listed suggestions, a known even parity lower level was found combining with an odd parity upper level with approximately the same energy. This new odd parity upper level explained the same observed fluorescence lines (Figure 7.49). The spectroscopic parameters for the lower level in this case are **13032.634 *cm*$^{-1}$**, **even parity**, J_u = **7/2** and A_u = **892.6 MHz**.
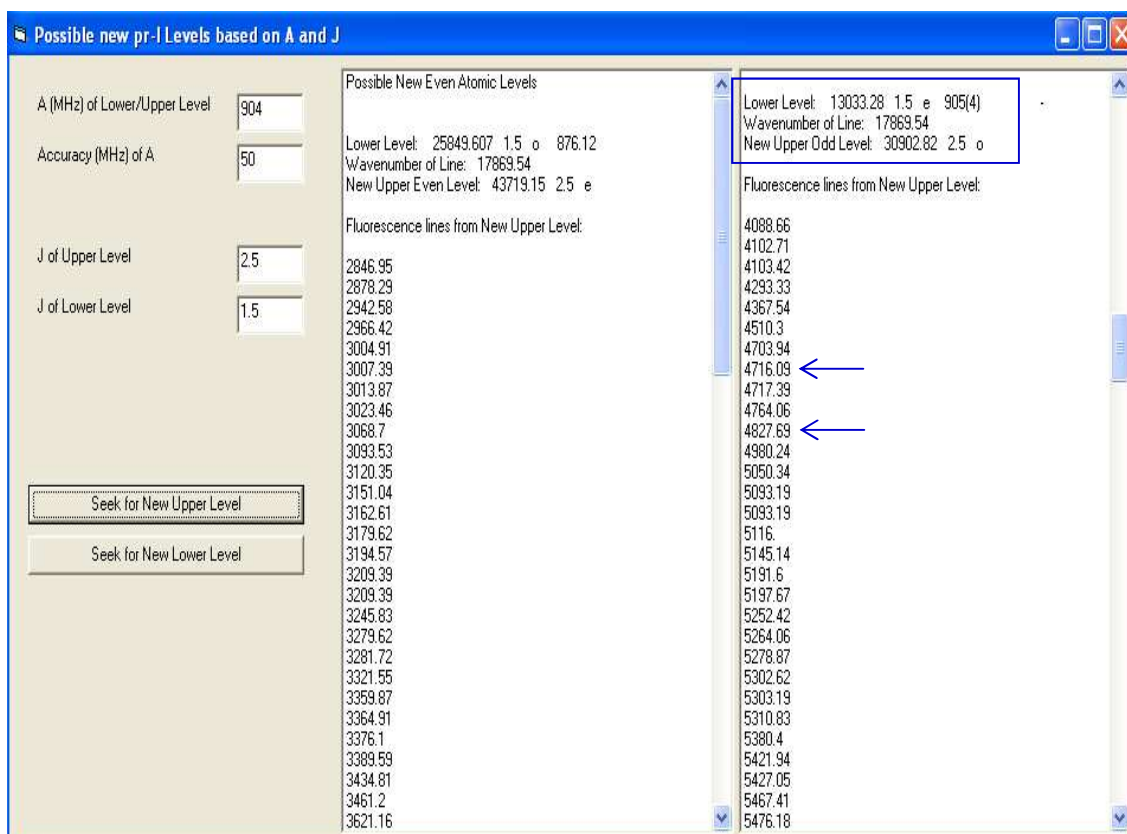
Figure 7.48: Possible suggestions for the line 5594.56 Å, a possible new odd parity upper level 30902.82 cm^{-1}
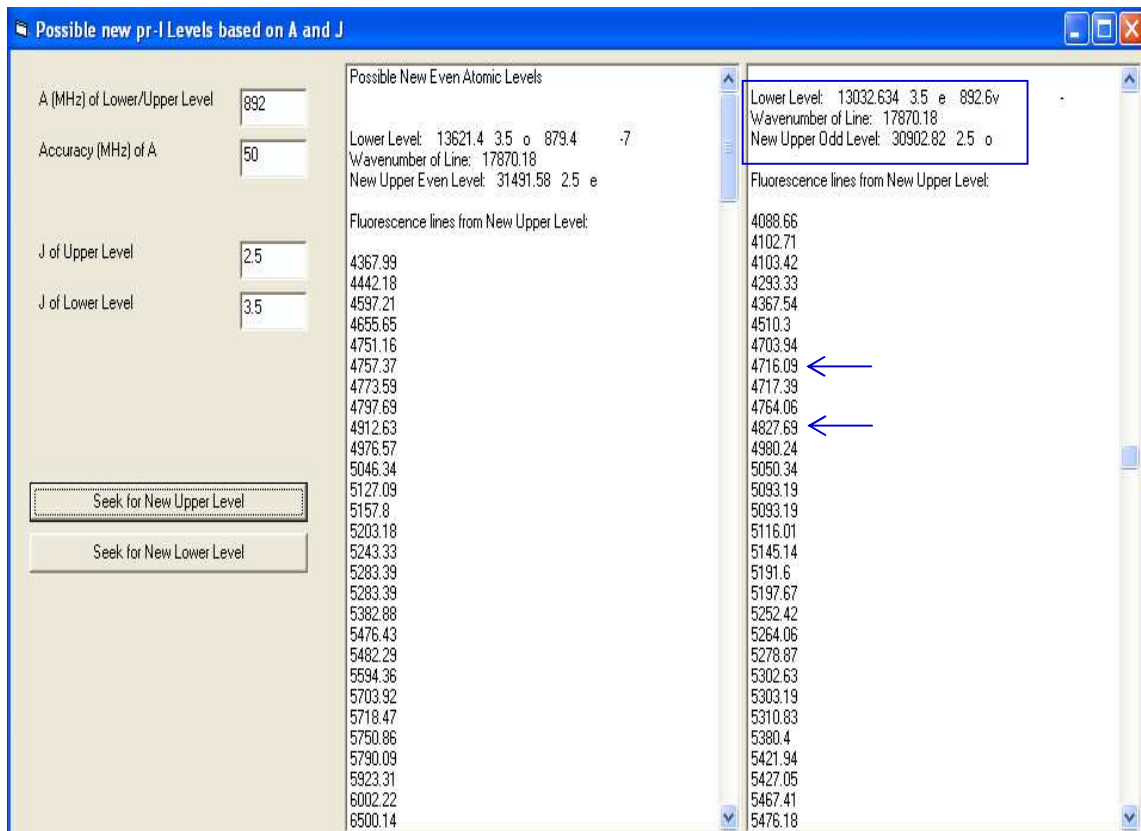
Figure 7.49: Possible suggestions for the line 5594.36 Å, a possible new odd parity upper level 30902.82 cm^{-1}

The recorded hyperfine pattern was fitted again using multiline fit procedure but this time keeping fix the *A*-values of the known lower levels at both lines. A best fit situation was obtained with the same quality factor $Q = 11$. The *A*-value obtained for the upper level is $A_o = 639$ MHz, the center-of-gravity wavenumber and wavelength of the recorded hyperfine structure at lower frequency are 17869.538 cm^{-1}, 5594.562 $\overset{\circ}{A}$ and for hyperfine structure at higher frequency are 17870.183 cm^{-1}, 5594.36 $\overset{\circ}{A}$.

The energy of the upper level at both lines was separately determined by using the respective center-of-gravity wavenumbers of the lines and the energy of the corresponding lower levels, at both lines i.e. 5594.562 $\overset{\circ}{A}$ and 5594.36 $\overset{\circ}{A}$, the energy of upper level determined is 30902.82 cm^{-1}. Corresponding to the lower level, the parity of upper level is taken to be odd, total electronic angular momentum $J_o = 5/2$ and magnetic hyperfine interaction constant $A_o = 647$ MHz. The fit gives us the possibility to determine more accurately the energy difference of the two lower levels, since they combine with the same upper level. From the multiline fit of the recorded structure (Figure 7.47) the estimated difference of the cg. is 19200 MHz $\triangleq$ 0.640 cm^{-1} which is in close agreement with the wave number difference of the two lower levels involved in the excitation of lines.

In order to confirm the existence and energy of the newly found upper level more than one laser excitation from a different lower level was performed. At one of the observed fluorescence lines i.e. 5823 $\overset{\circ}{A}$, the newly found upper level was excited from another known lower level. This line also exists in the transition list of the upper level. The hyperfine structure profile of the line at 5823.34 $\overset{\circ}{A}$ predicted by the classification program does not appear in FT-spectrum (Figure 7.50) so possibly a blend of more than one lines exist in FT -spectrum.

Laser excitation was performed by tuning the laser frequency at 5823.34 $\overset{\circ}{A}$ and setting the monochromator transmission wavelength to previously observed strongest line i.e. 4827 $\overset{\circ}{A}$. LIF signal was observed not only on 4827 $\overset{\circ}{A}$ but also on 4716 $\overset{\circ}{A}$ and 5594 $\overset{\circ}{A}$. LIF spectrum was then recorded on all observed fluorescence lines by scanning the laser frequency.
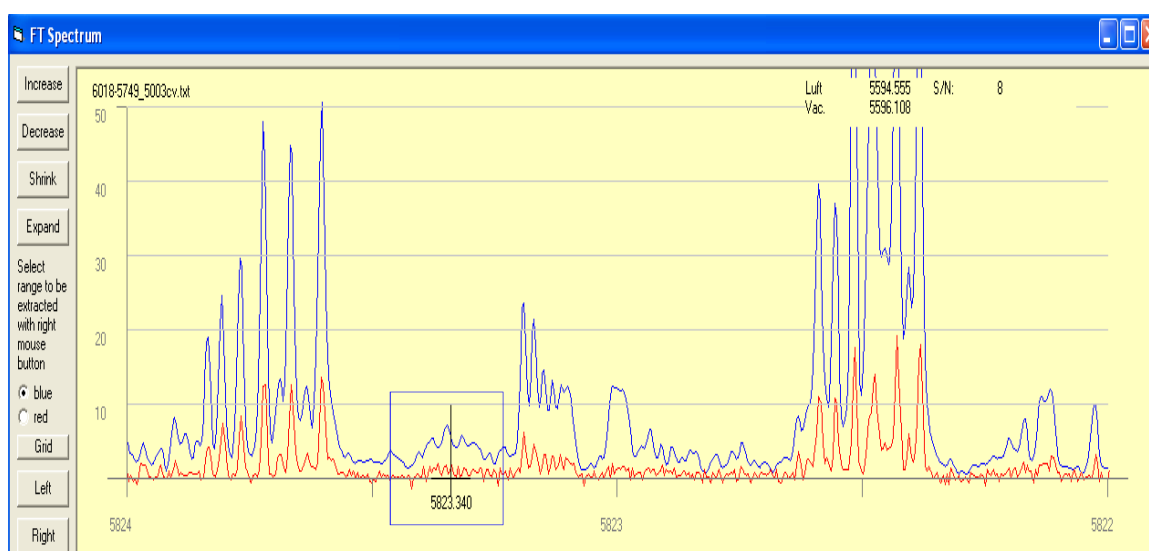
Figure 7.50: FT-spectrum for the line 5823.34 $\overset{\circ}{A}$

The recorded hyperfine structure of the line is in good agreement with the hyperfine pattern of the line predicted by classification program (Figure 7.51). This confirms the existence of the upper level and the level scheme adopted earlier in the first excitation. The

upper level energy and the value of A constant was corrected which gives **30902.82(3) cm^{-1}, odd parity, J_o = 5/2 and A_o = 636(6) MHz.**
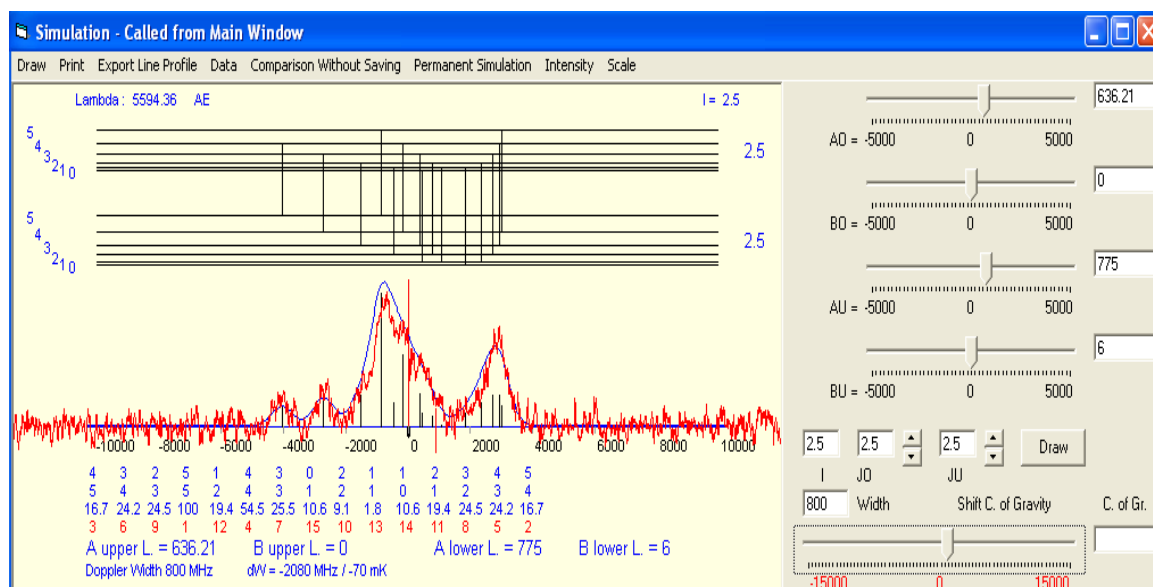
Figure 7.51: Comparison of the recorded hyperfine structure of the line 5823.34 Å (Red curve) with the predicted hyperfine pattern of line (Blue curve).

The two closely spaced lower set of levels are not always excited simultaneously but only dipole allowed transitions occur from both lower levels to a single upper level. This similar behavior was also observed in the investigation of lines at 5764.39 Å and at 5764.17 Å in which the two levels were excited to a known upper level in a single scan range of laser (Figure 7.52).
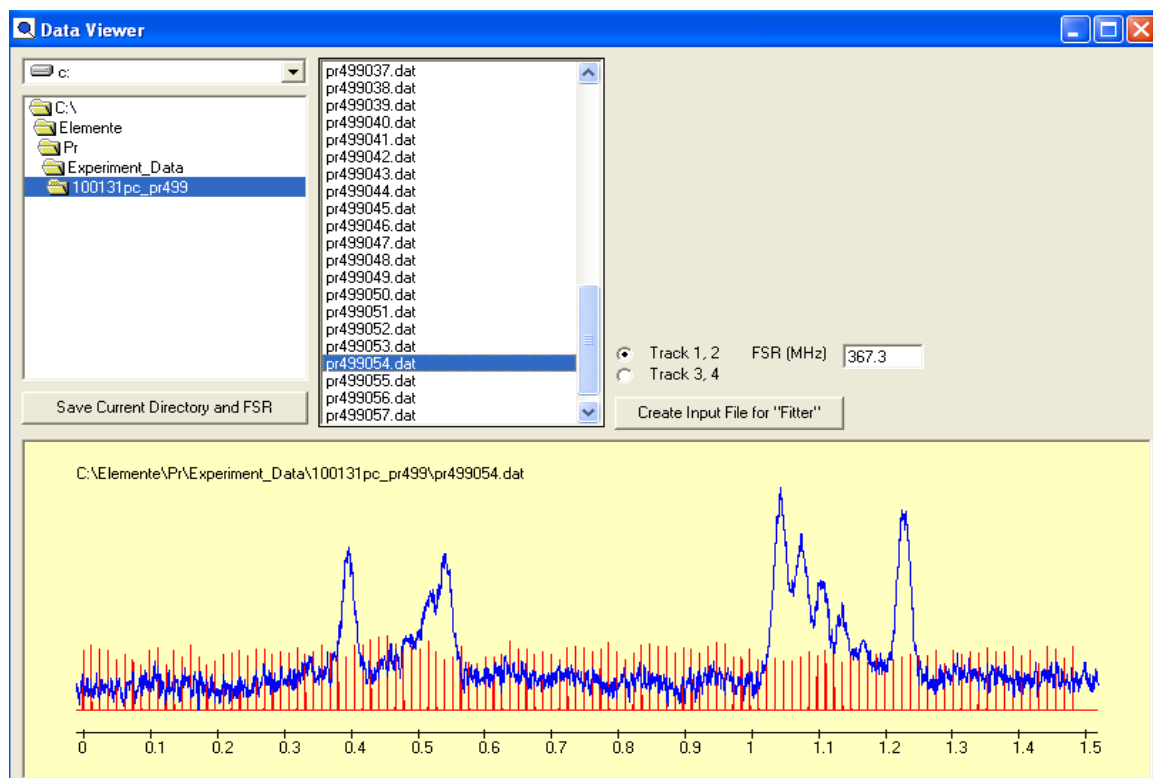
Figure 7.52: Recorded LIF spectrum of the lines 5764.39 Å and 5764.17 Å

Furthermore despite of the fact that the two lower levels are in a close proximity with each other, the intensity distribution of hyperfine components for both structure show a normal behavior. This is contrary to an investigation conducted in our group [74] where three closely lying lower levels simultaneously excite a single upper level. The recorded hyperfine structure profile in this case show transitions from all three lower levels but the intensity distribution of hyperfine components appears disturbed.

7.1.6 Discovery of a New Pr-I Level with a Low Angular Momentum Value i.e. J = 1/2

In order to systematically classify the spectral lines in FT-spectrum, the spectral region in the neighborhood of 5756.53 Å was experimentally investigated. A trace of FT-spectrum showing the region of investigation is shown in Figure 7.53.
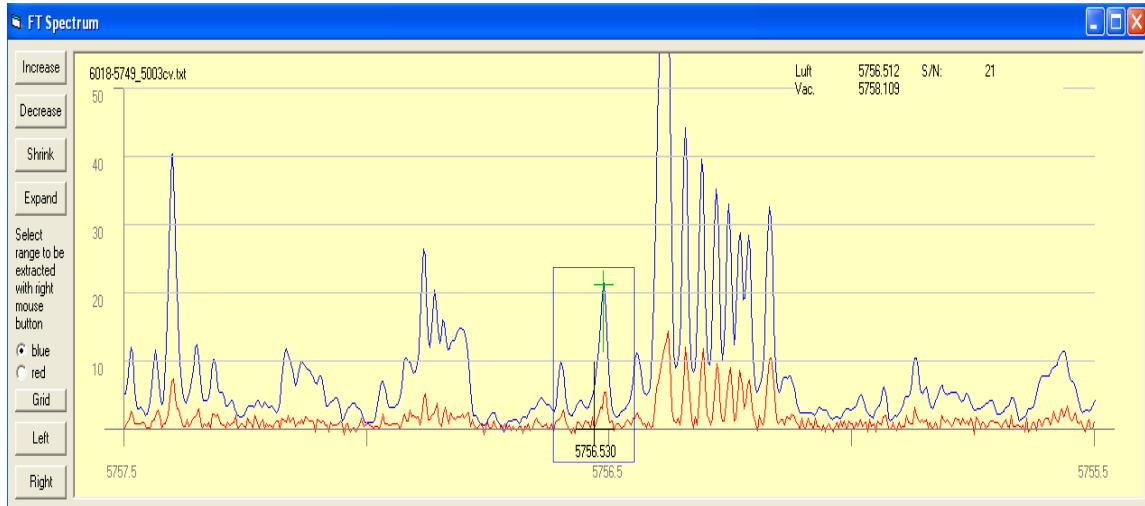
Figure 7.53: FT-spectrum for the region around 5756.53 Å

Initially the laser wavelength is set to 5756.53 Å and fluorescence lines were searched. LIF signal was observed on fluorescence lines at wavelengths 4067 Å, 4151 Å, 4189 Å, 4388 Å, 4635 Å, 4695 Å, 4823 Å, 5129 Å, 5141 Å, 5202 Å, 5251 Å, 5351 Å, 5395 Å and 5448 Å. Two different hyperfine structures were recorded at these fluorescence wavelengths i.e. one hyperfine structure was recorded at 5141 Å, 5251 Å and 5448Å and the other on 4067 Å, 4151 Å, 4189 Å, 4388 Å, 4635 Å, 4695 Å, 4823 Å, 5129 Å, 5202 Å, 5351 Å, 5395 Å. The hyperfine structure (Figure 7.54) at center-of-gravity wavelength 5756.52 Å was identified as a transition between known levels i.e. $30399.423^o_{9/2} \, cm^{-1}$ - $13032.634^e_{7/2} \, cm^{-1}$ The line was then classified.
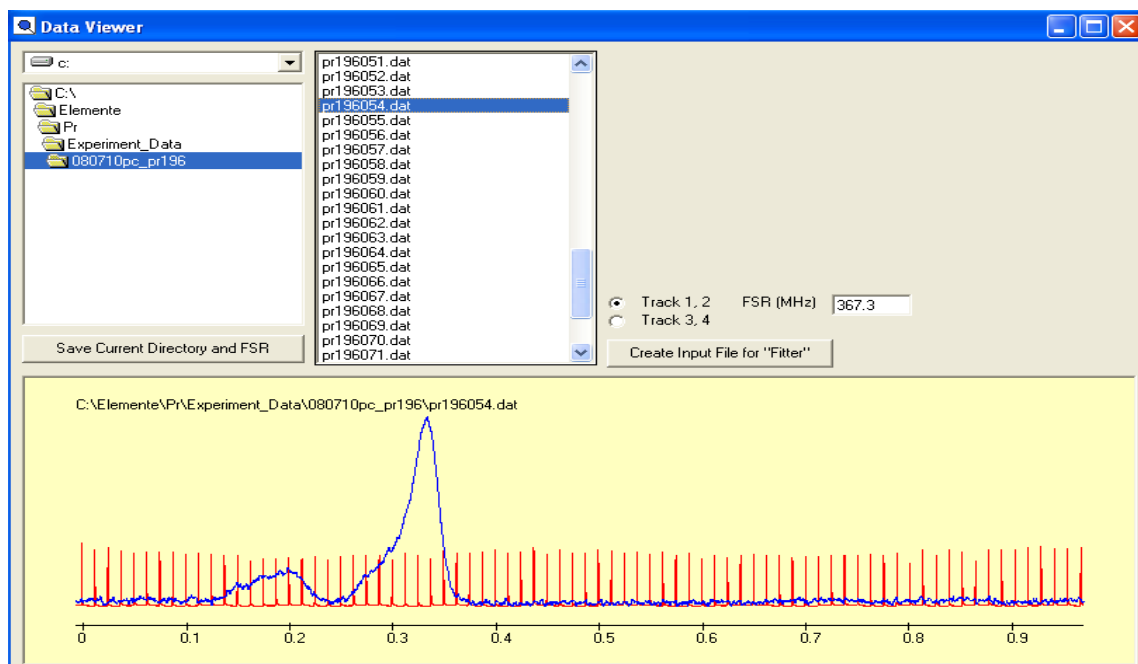
Figure 7.54: FT-spectrum for the Line 5756.52 Å

114

The recorded structure of the line at fluorescence wavelengths 5141 Å, 5251 Å and 5448Å reveal (Figure 7.55) a smaller number of hyperfine components suggesting that the combining levels have small angular momentum values. The recorded hyperfine structure at fluorescence lines 5141 Å, 5251 Å and 5448 Å is not visible in FT-spectrum and is completely masked by the hyperfine structure components of the other line involving levels with angular momentum $J_{upper} = 9/2$ and $J_{lower} = 7/2$. In order to ascertain the shape of recorded structure and to filter out any blend situation (convolution of more than one line) which is common in praseodymium, entrance and exit slit sizes of the monochromator is reduced and the hf structure of the line is again recorded. No change was observed and same hyperfine structure pattern was recorded on all fluorescence lines.
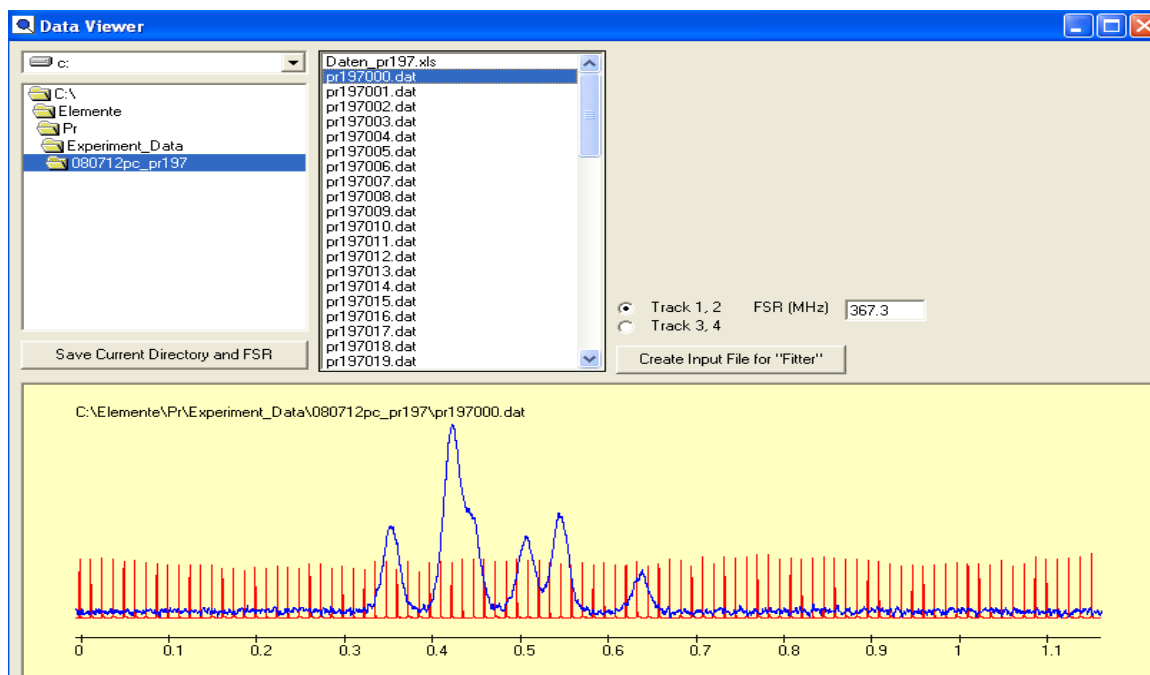
Figure 7.55: FT-spectrum for the line 5756.53 Å

To evaluate J and A values of the involved lower and upper levels, the recorded structure is fitted by using Fitter program. Table 7.3 gives the A and B values determined by the Fitter program for different pair of J values of the combining lower and upper levels.

Table 7.3: Possible A and B values for different pairs of J values of the combining levels. The quality (inverse proportional to the error squares sum) of the fit result indicates the best pair of J values.

Upper Level J_{up}	Lower level J_{lo}	Quality of fit	Upper level		Lower level	
			A_{up} (MHz)	B_{up} (MHz)	A_{lo} (MHz)	B_{lo} (MHz)
1/2	3/2	7.97	1881.82	0.00	910.21	3.24
1	2	2.65	1668.74	-52.40	799.03	4.24
1.5	2.5	1.81	1549.10	-646.54	745.27	-534.66

The highest quality of fit is obtained for $J_o = 1/2$ and $J_u = 3/2$. $J_o = 1/2$ implies $L = 0$ i.e. S-orbit for which $B = 0$. Assuming an unknown upper level is involved in the excited

transition, a known lower level is searched using *J*, *A* and *B* values in the database of known levels. A level with energy 13033.280 cm^{-1}, *J* = 3/2, even parity and *A* = 905(4) MHz was found. The recorded structure is again fitted taking *J* and *A* values of the known lower level. This gives a best fit with A_o = 1881.82 MHz of the upper level, the best fit situation is shown in Figure 7.56. The energy of the upper level is determined by adding the center-of-gravity wavenumber of the recorded structure. A newly discovered fine structure level with parameters **30400.04 cm^{-1}, J_o = 1/2, odd parity** and A_o = **1881.82 MHz** is obtained. This level is then introduced into the classification program which generates a transition list.
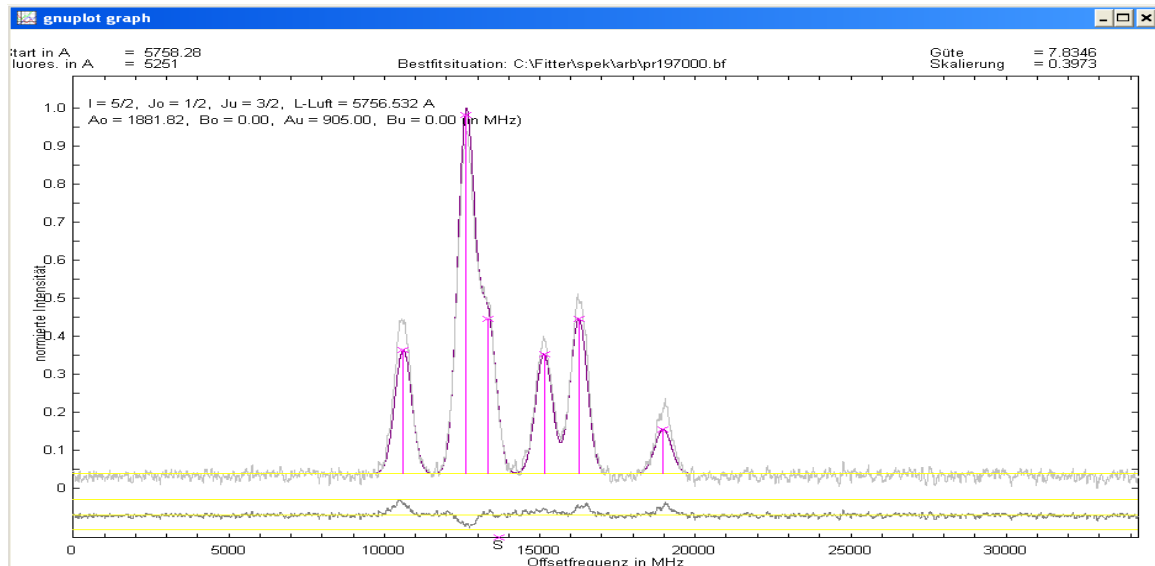
Figure 7.56: Best fit situation of the recorded hyperfine structure of the line 5756.53 Å

The correct assignment of the energy of the newly calculated upper level is only ensured if it explains all the observed fluorescence lines. A laser excitation at 5141.703 Å, which is one of the observed fluorescence line, is performed. The recorded hf structure of the line at 5141.703 Å is in full agreement with the predicted hf structure pattern of the excited line, see Figure 7.57.
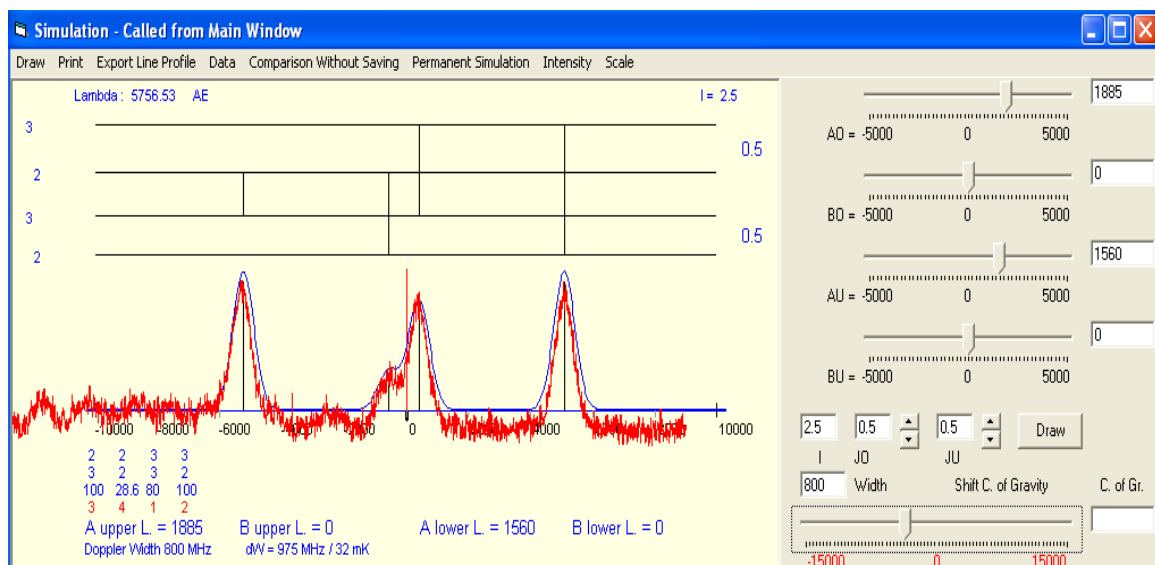
Figure 7.57: Comparison of the recorded hyperfine structure of the line 5141.703 Å (Red curve) with the predicted hyperfine structure of the line (Blue Curve)

116

The lines at 5141.703 Å and 5251.114 Å have suitable SNR (4 and 15, respectively) to determine finally the level energy to be 30400.042(30) cm^{-1}. The observed fluorescence line at 5448.506 Å appears in a blend situation and its hf structure is not visible, and the line was classified on the basis of observed fluorescence wavelength.

Thus the following lines are then classified:

5756.529 Å (wavelength calculated from level energies): $30400.042^{o}_{1/2}$ - $13033.280^{e}_{3/2}$

5448.506 Å (wavelength calculated from level energies): $30400.042^{o}_{1/2}$ – $12051.488^{e}_{3/2}$

5251.114 Å (wavelength from FT): $30400.042^{o}_{1/2}$ – $11361.746^{e}_{3/2}$

5141.703 Å (wavelength from FT): $30400.042^{o}_{1/2}$ – $10956.651^{e}_{1/2}$

For the A constant the average of all recordings at both excitation wavelengths were determined, this gives A = 1890(10) MHz.

The energy of the upper level is correct and its existence is beyond all doubts. A level scheme for the involved levels is shown in Figure 7.58.
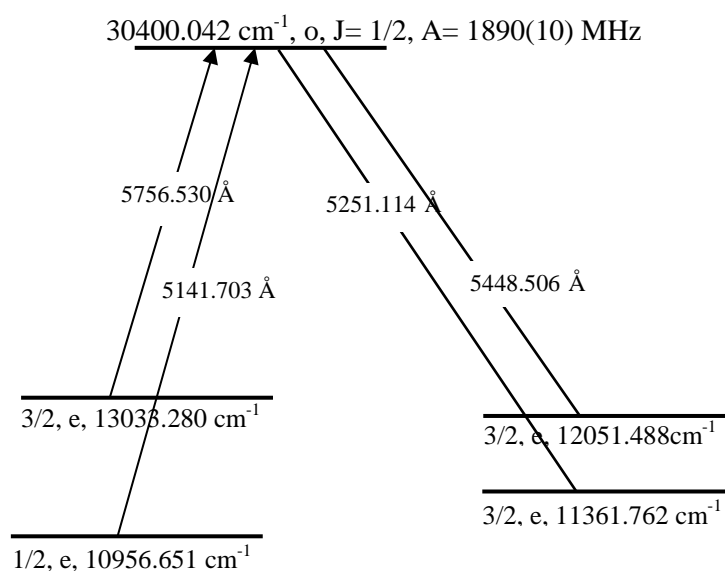
Figure 7.58: Level scheme for the excitation of 30400.042(20) *cm^{-1}*

7.1.7 Discovery of Pr-I Level $29341.96^{\circ}_{1/2}$

The hyperfine structure profile appearing in FT-spectrum at 5854.17 Å cannot be explained by any of the listed suggestions of the line in classification program (Figure 7.59). Therefore laser excitation was performed in order to investigate the line.
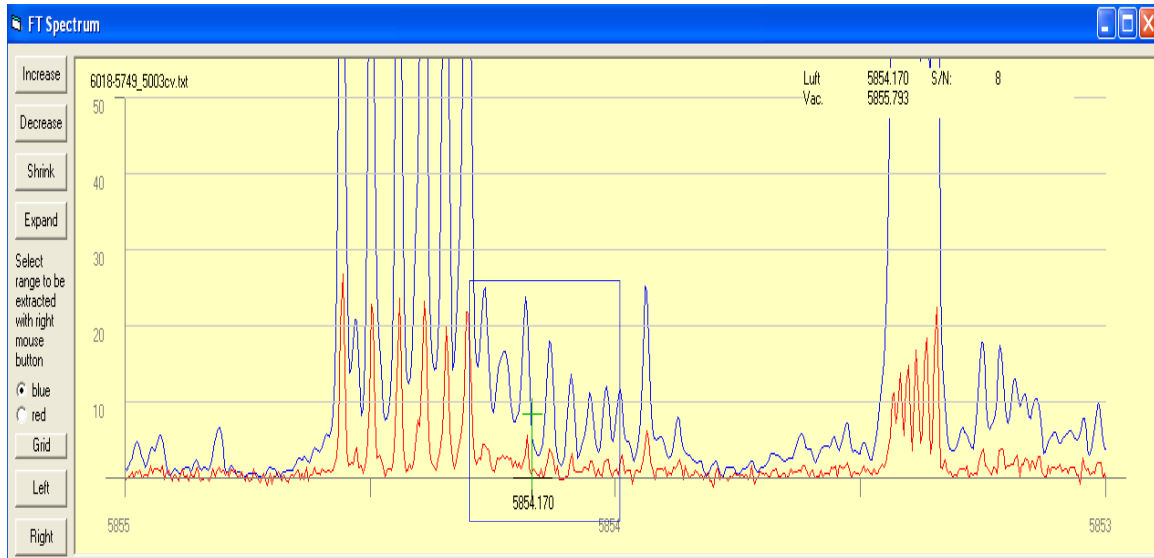
Figure 7.59: FT-spectrum for the line 5854.17 Å

The laser wavelength is set 5854.17 Å and fluorescence lines were searched by tuning the transmission wavelength of the monochromator. LIF signals were observed on 5560 Å, 5720 Å, 5781 Å. LIF spectrum was then recorded on all observed fluorescence wavelengths showing a hyperfine structure with small number of hyperfine components (Figure 7.60).
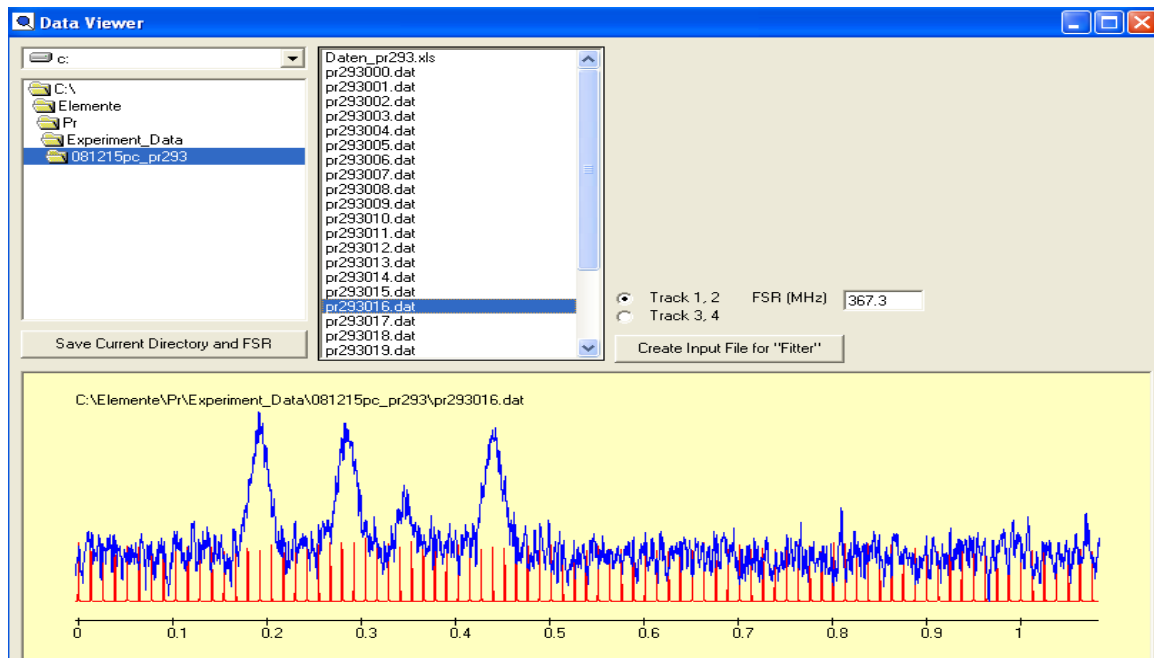
Figure 7.60: Hyperfine structure of the line 5854.17 Å

Using simulation program a hyperfine structure profile is simulated showing a nice agreement with recorded structure at $J = 1/2$ for the combining levels and $A_o = 900$ MHz and $A_u = 1530$ MHz. For $J < I$, the statistical weight of a fine structure level is given by $2J$

118

+ 1 which means that a fine structure level splits into 2 hyperfine structure levels. This gives two diagonal and two off-diagonal hyperfine components. It is important to note here that middle two components i.e. $F_o = 3$ to $F_u = 3$ and $F_o = 2$ to $F_u = 2$ are the diagonal components and the other two i.e. $F_o = 2$ to $F_u = 3$ and $F_o = 3$ to $F_u = 2$ are off diagonal components. This shows that the intensity rule is different for a transition with combining levels $J < I$.
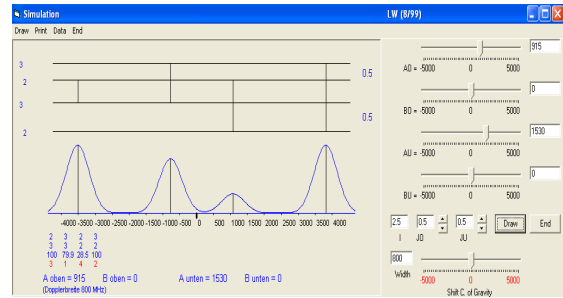
Figure 7.61: Simulation of the recorded line profile

The recorded hyperfine structure is then fitted taking J- and A-values from the simulation program. The best fitted values $J_o = 1/2$, $J_u = 1/2$, $A_o = 911$ MHz and $A_u = 1543$ MHz are obtained with a quality factor $Q = 2.4$ (Figure 7.62).
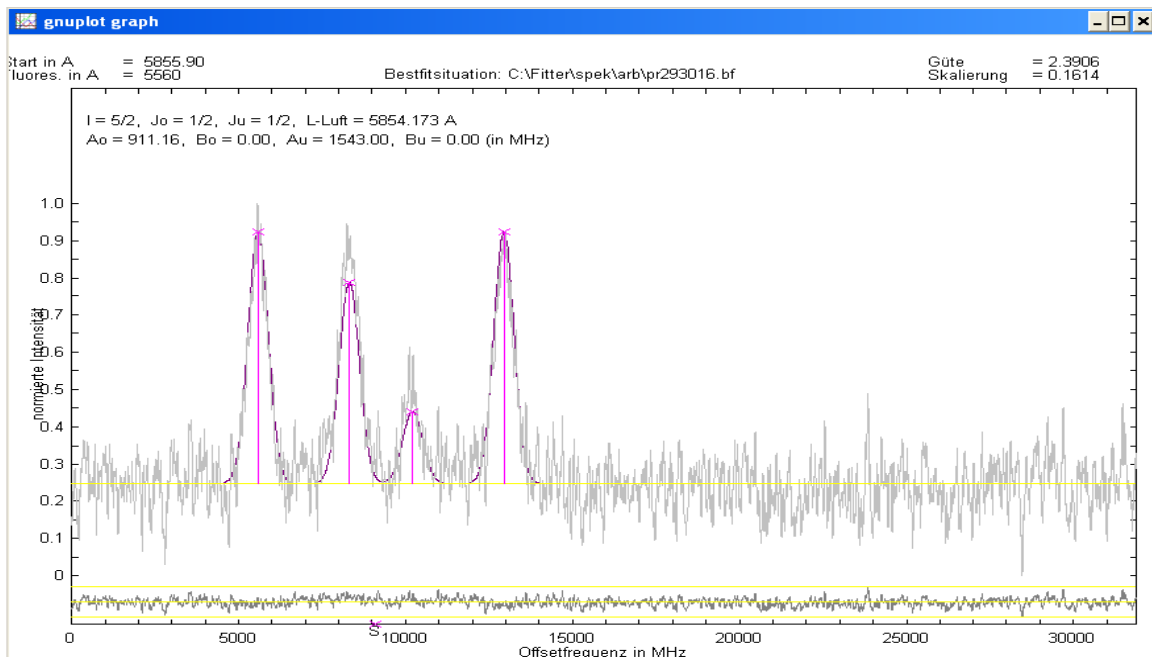
Figure 7.62: Best fit situation of the hyperfine structure of line 5854.17 $\mathring{A}$

In a similar manner assuming one of the combining levels are known, say, the lower level of the excited transition is known, a possible new upper level was found which explained all the observed fluorescence lines. The known lower level has the parameters **12264.864 cm^{-1}, even parity, $J_u = 1/2$ and $A_u = 1534$ MHz**. The energy of the possible new upper level was determined by the center-of-gravity wave number of the line and the energy of the lower level. This gives the new upper level **29341.96 cm^{-1}, odd parity, $J_o = 1/2$ and $A_o = 915.26$ MHz.** The newly determined level is then introduced in the database of known levels and is loaded in the classification program which generates a transition list from this level.

Usually the correct assignment of energy of a new level is only guaranteed if the transition list of the upper level explains all the observed fluorescence lines and their hyperfine structure predicted by the classification program is in agreement with the hyperfine structure of these lines in FT-spectrum.

In case of lines involving levels with low angular momentum values ($J = 1/2$ or $3/2$),

119

usually the hyperfine components are overlapped by the hyperfine structure components of the nearby lines involving levels with angular momentum values J > 3/2. This is common in praseodymium which has high line density. This is one of the reasons that lines involving levels with low angular momentum values are most times not visible in FT spectrum and laser excitation must be performed in order to confirm their energy and existence.

Two of the observed fluorescence lines i.e. at 5720 Å, 5781 Å lie in the emission spectrum of Rhodamine 6G, further the line at 5735.44 Å also exist in the transition list of the newly found upper level so laser excitations were performed at lines 5735.44 Å and 5781.93 Å. At both lines, a LIF signal was seen on the previously observed fluorescence line at 5560 Å. The detection of LIF signal is not possible at or near 5854.17 Å due to laser stray light. The recorded LIF spectrum at lines 5735.44 Å and 5781.93 Å are in full agreement with the predicted hyperfine structure of lines by the classification program both in terms of shape and hyperfine component positions (Figure 7.63 & 7.64).
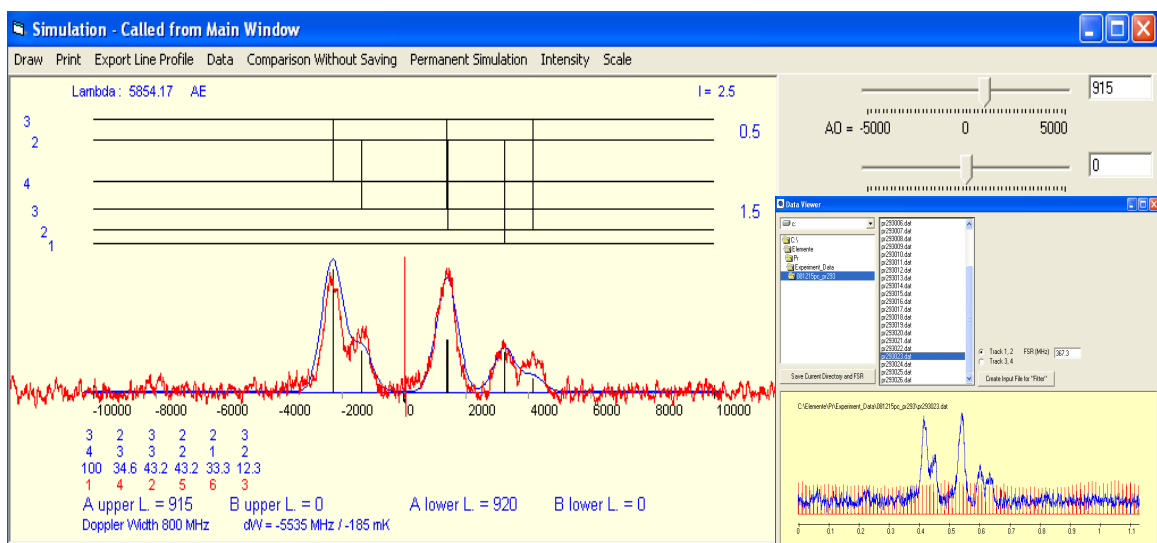
Figure 7.63: Comparison of the recorded hyperfine structure (red curve) of the line 5735.44 Å with the predicted hyperfine structure pattern (blue curve).
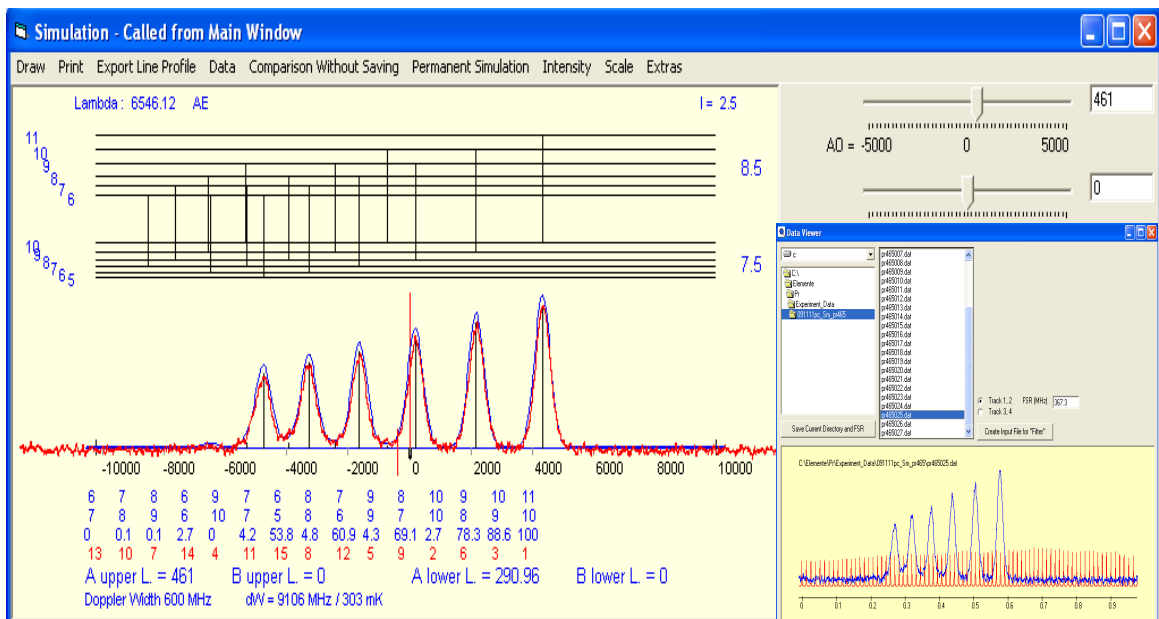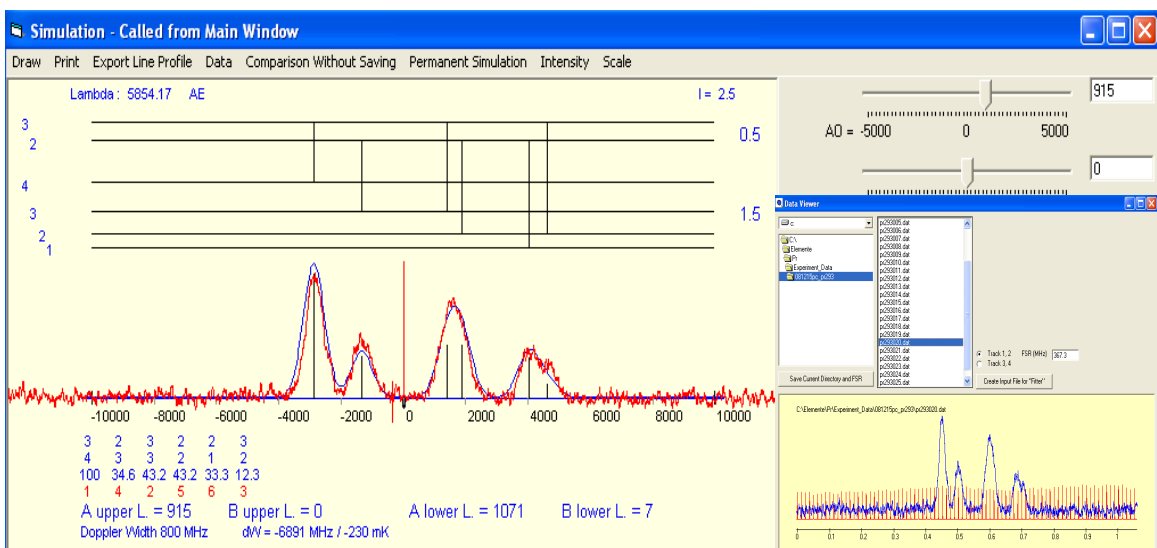

Figure 7.64: Comparison of the recorded hyperfine structure (red curve) of the line 5781.93 Å with predicted hyperfine structure pattern (blue curve).

This confirms the existence of the newly discovered upper level. The level energy was then corrected and the lines were then classified as transitions between

$$29341.96^o_{1/2} - 12264.864^e_{1/2}$$

$$29341.96^o_{1/2} - 11911.350^e_{3/2}$$

$$29341.96^o_{1/2} - 12051.488^e_{3/2}$$

It should be noted that at each of the excited line, the hyperfine structure of the line is not visible in FT-spectrum and appears in a blend of lines. In each case, the hyperfine components of the line are overlapped by the hyperfine components of the neighboring lines involving levels with large angular momentum values.

7.1.8 Discovery of New Pr-I Level at Line 5636.940 Å

A very prominent line in FT-spectrum at 5636.940 Å was investigated using laser excitation. The line has a very good signal-to-noise ratio with a relative intensity of 140 and has clearly visible hyperfine components, see Figure 7.65. The suggestions listed for the line in the classification program were examined but none of the suggestion coincides with the hyperfine structure profile given in FT-spectrum.
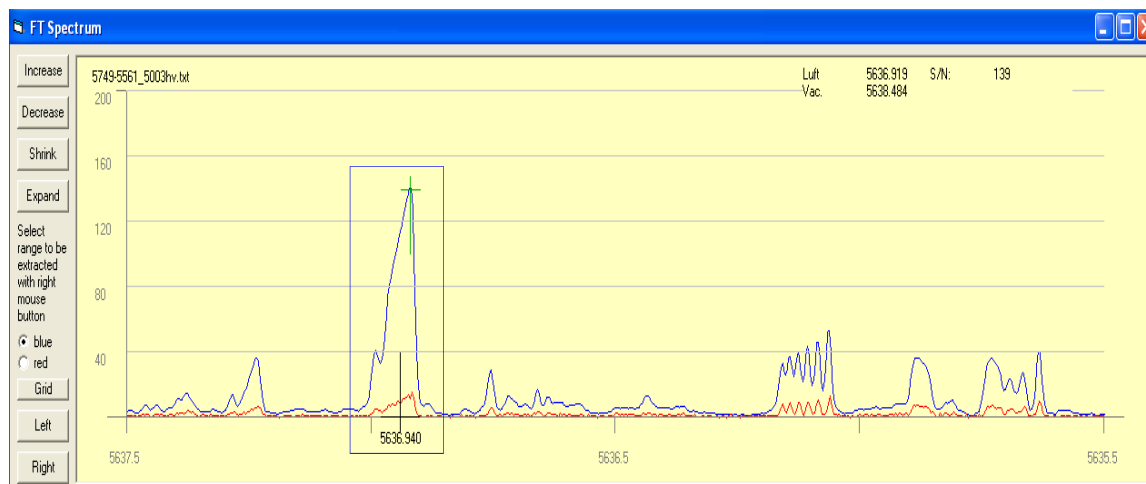
Figure 7.65: FT-spectrum of the line 5636.940 Å

Laser excitation was performed by tuning the laser wavelength to the highest hyperfine component which in this case is 5636.92 Å. A single fluorescence line at 5228 Å was observed in the transmission range of the monochromator from 3000 Å to 7000 Å. This can happen if the upper level has a few number of decay channels or has a very low transition probability for other lines. It could also happen that the upper excited level is a low lying level, excited either from the ground level or from a very low lying level.

In this case two decay channels are apparent, one to the same lower level from where it is excited and the second is the fluorescence lower level. In any case hyperfine structure of the line is recorded by scanning the laser frequency across the hyperfine components of the line. As expected the recorded LIF spectrum has good signal-to-noise ratio with the same hyperfine structure pattern as displayed in FT-spectrum (Figure 7.66).
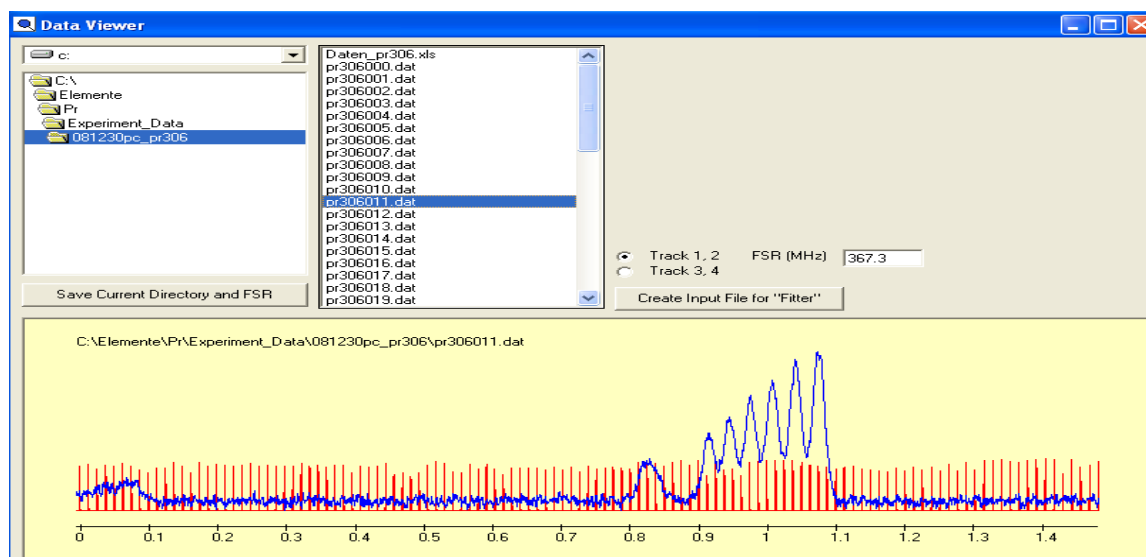
Figure 7.66: Recorded hyperfine structure of the line 5636.940 Å

The recorded structure was then fitted and a best fit situation was obtained for $J_o = 13/2$, $J_u = 11/2$, $A_o = 762$ MHz and $A_u = 733$ MHz with quality factor $Q = 8$ (Figure 7.67). The center-of-gravity wavelength obtained from fitter program is 5636.940 Å. Inserting the center-of-gravity wavelength in the classification program, a known lower level is initially searched in the database of known levels. This is done by giving the J-values of the lower and upper levels and the A-value of the lower level to the searching routine. A number of suggestions for the possible new upper levels with their fluorescence lines were displayed. But none of the suggestion neither of even parity nor of odd parity could explain the only observed fluorescence line at 5228 Å. Once again fitting procedure was revised with different values of angular momentum (including ionic values) for lower and upper levels but in each case the quality of fit was not good.
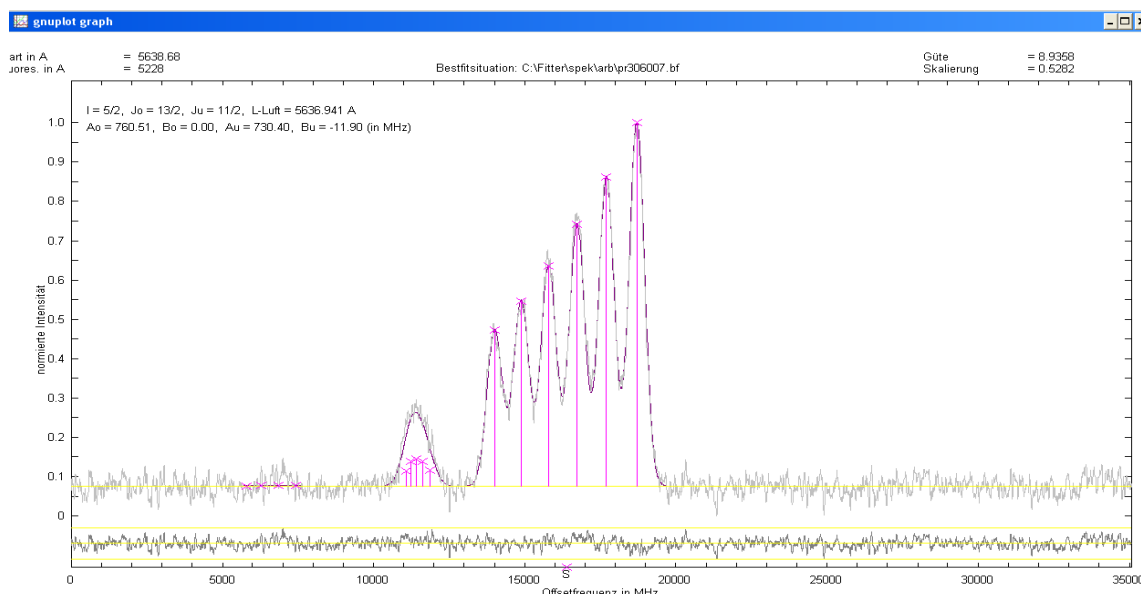
Figure 7.67: Best fit situation of the recorded hyperfine structure of line 5636.940 Å

As a next step assuming an unknown lower level, a known upper level was searched in the database of known levels using fitted J values of the combining levels and A-value of the upper level. This gives again number of suggestions for possible unknown lower level combining with known upper level. Again none of the listed suggestions could explain the only observed fluorescence wavelength.

It can then be concluded that possibly both the lower and upper combining levels at the excited line 5636.940 Å are still unknown and yet to be discovered. In situations like this another method is used which require fluorescence information for the identification of the lower combining level at the fluorescence line. For the method to work successfully, atleast three fluorescence lines with exact measure of their wavelength must have been observed experimentally with known lower combining levels. But in this case only single fluorescence line at 5228 Å was detected which means that the method is not applicable. In any case the exact value of the fluorescence wavelength was determined. This was done by using a second lock-in amplifier in our experimental setup. Modulated fluorescence light from hollow cathode lamp is given to the monochromator and the LIF signal together with the emission spectrum of the hollow cathode in the desired spectral range is recorded. Exact value of the fluorescence wavelength is determined using a computer program called "Comparison" which turns out to be 5227.967 Å. This program takes as input the recorded file and the FT-spectrum file of the desired spectral range, see Figure 7.68.

123
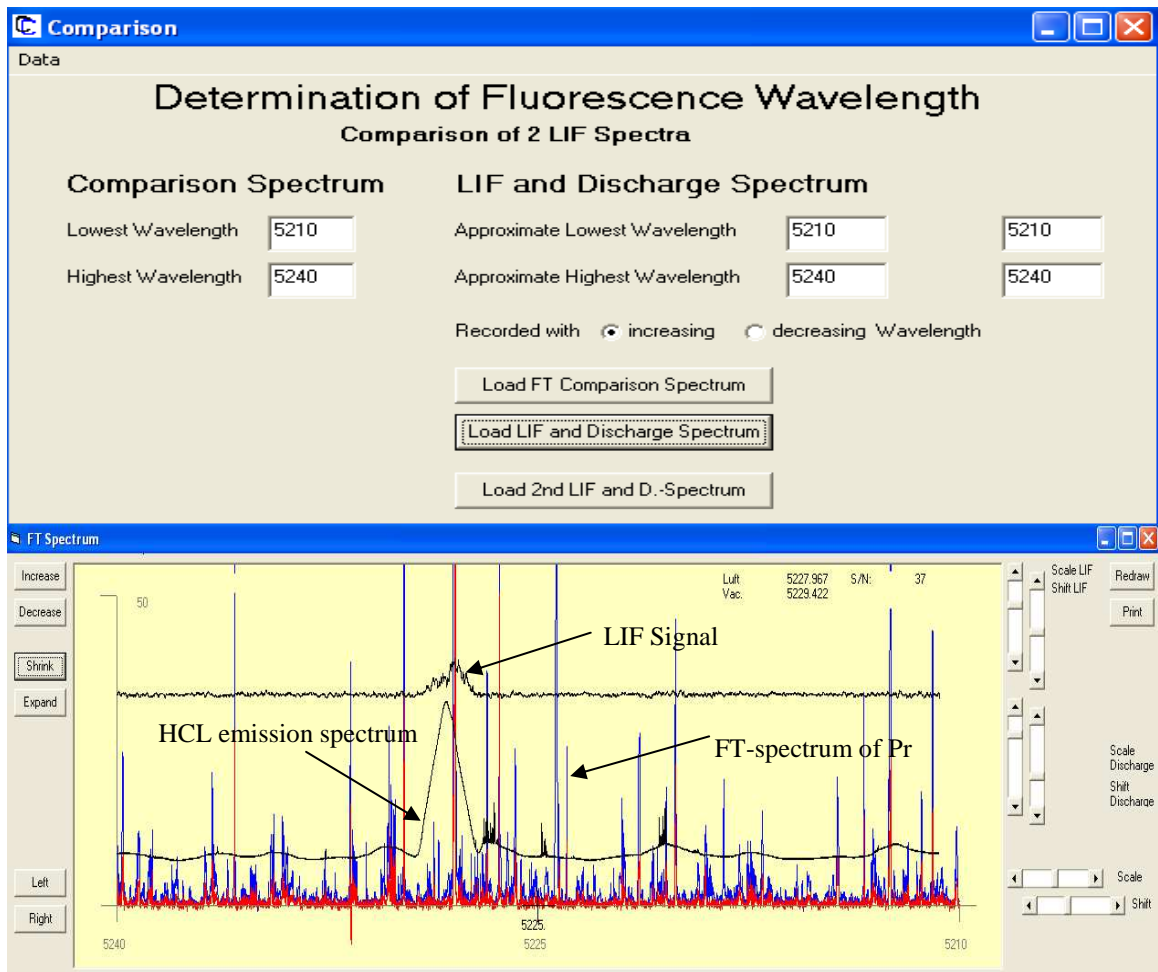
Figure 7.68: Exact measure of fluorescence wavelength 5227.967 Å

The line at 5227.968 Å was inserted in the classification program which displays number of suggestions for the line. A classified line at slightly different center-of-gravity wavelength i.e. 5227.968 Å with a transition from ground to a known low lying upper level $19122.567^e_{11/2}$ was seen in FT-spectrum. The line has a very good signal-to-noise ratio with a relative intensity of 5171 (Figure 7.69).
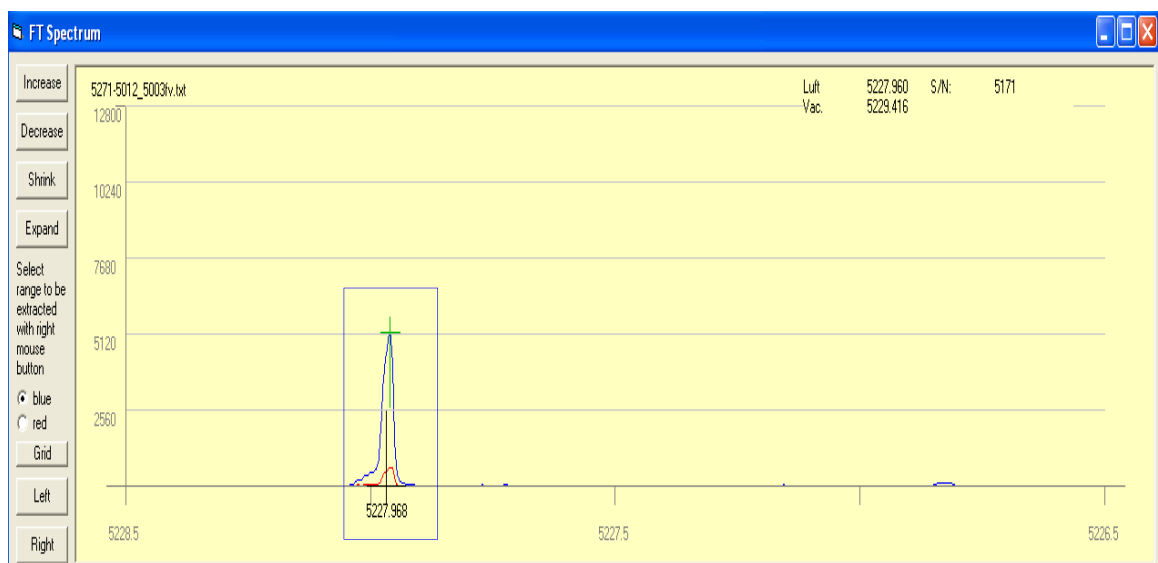
Figure 7.69: Spectral line in FT spectrum at 5227.968 Å

124

Furthermore the predicted hyperfine structure of the line by the classification program is in extremely good agreement with the hyperfine structure profile seen in FT-spectrum. Assuming an unknown lower level is involved in the excitation of line at 5636.940 Å, the recorded hyperfine structure of the line was again fitted but now taking J-values in accordance with the J-value of the assumed known upper level i.e. $19122.567^{e}_{11/2}$. For fitting, the hyperfine interaction A constant of the known upper level was taken as fixed and letting free the hyperfine interaction A constant of the assumed unknown lower level. The fit of the recorded structure gave a very poor result for the pair of J-values and A-values of upper and lower levels. This indicates that the upper level involved in the excitation of line at 5636.940 Å is not 19122.567 cm^{-1} and again one could say that both the combining levels may not be known till now.

There could now be two possible models (i) both the combining levels at 5636.940 Å are unknown and the lower level at the fluorescence line 5227 Å is also unknown or (ii) lower combining level at the excited line 5636.940 Å is known and the observed fluorescence signal at 5227 Å is an indirect fluorescence i.e. not originating from the excited upper level but in the hollow cathode glow region, collisional coupling had occurred between the excited unknown upper level at the line 5636.940 Å and $19122.567^{e}_{11/2}$. This results in the excitation of level 19122.567 cm^{-1} which then decay via fluorescence line at 5227 Å. So might be a low lying unknown upper level with energy comparable to the energy of 19122.567 cm^{-1} is involved.

For the first model to be true requires more fluorescence lines possibly in the infrared region. Since our monochromator works best in the region from 3000 Å to 7000 Å and so fluorescence lines in IR were not observed. If such fluorescence lines exist one can then investigate those lines to solve the problem. As far as second model is concerned one could inspect the list of possible suggestions for new upper level at the line 5636.940 Å based on A-value of the lower combining level and J-values of both combining levels and look for a level with low energy and having hyperfine A constant of lower known level to be nearly of same value as determined by the fitting process, see Figure 7.70.
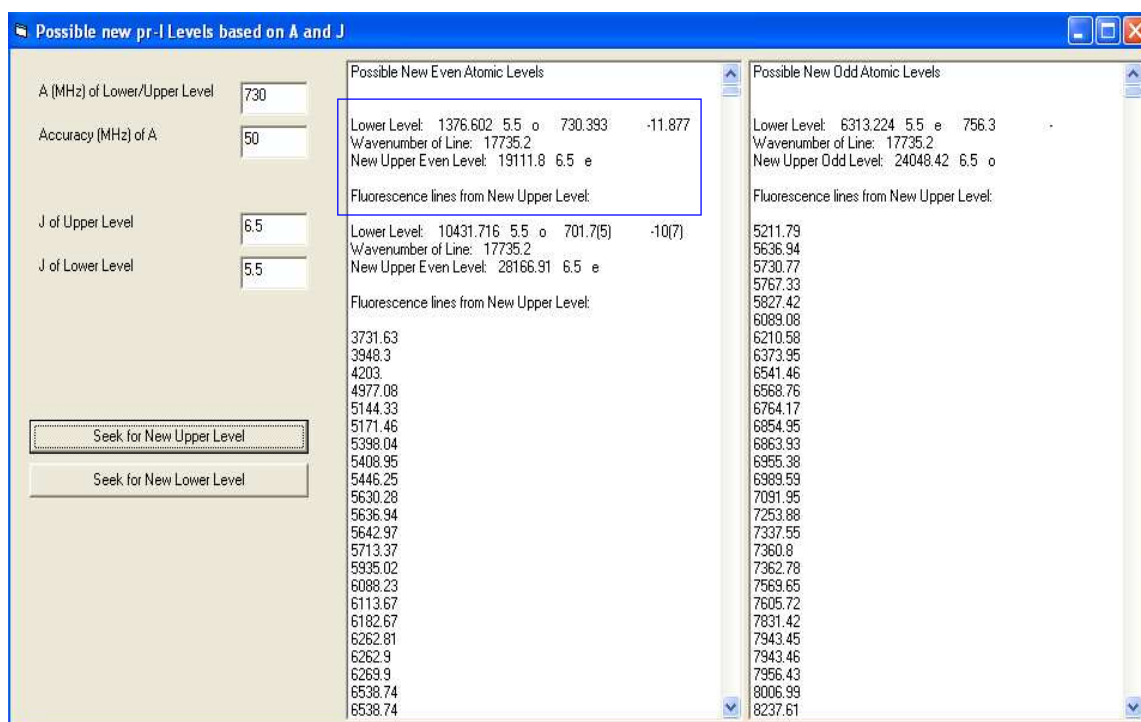
Figure 7.70: Possible suggestions for the line 5636.940 Å

The first even parity suggestion has exactly the same hyperfine interaction constant as determined by the fitting process of the experimentally recorded file. The suggestion show a known lower level i.e. **1376.602 cm^{-1}, odd parity, $J_u = 11/2$** and A_u = **730.393 MHz, B_u = -11.877 MHz.** The possible new upper combining level determined using this lower level and center-of-gravity wave number is **19111.80 cm^{-1}, even parity, $J_u = 13/2$, A_u = 761.83 MHz.** The level was introduced in the database of known levels and is uploaded in the classification program. The transition list generated by the classification program does not explain the single observed fluorescence line 5227 Å but at the line 6146.447 Å the hyperfine structure calculated by classification program appears to have some coincidence with the hyperfine structure profile shown in FT-spectrum. Laser excitation at the line 6146.447 Å was performed and an LIF signal was observed at 5227 Å. The recorded hyperfine structure of the line at 6146.447 Å is in excellent agreement with the predicted hyperfine structure by the classification program both in terms of hyperfine pattern and wave number (Figure 7.71). This confirms the existence of the newly found upper level first excited at the line 5636.940 Å. The center-of-gravity wavelength determined by the fitting process is 6146.447 Å. The energy of the newly found level was then corrected and the excited lines were then classified.
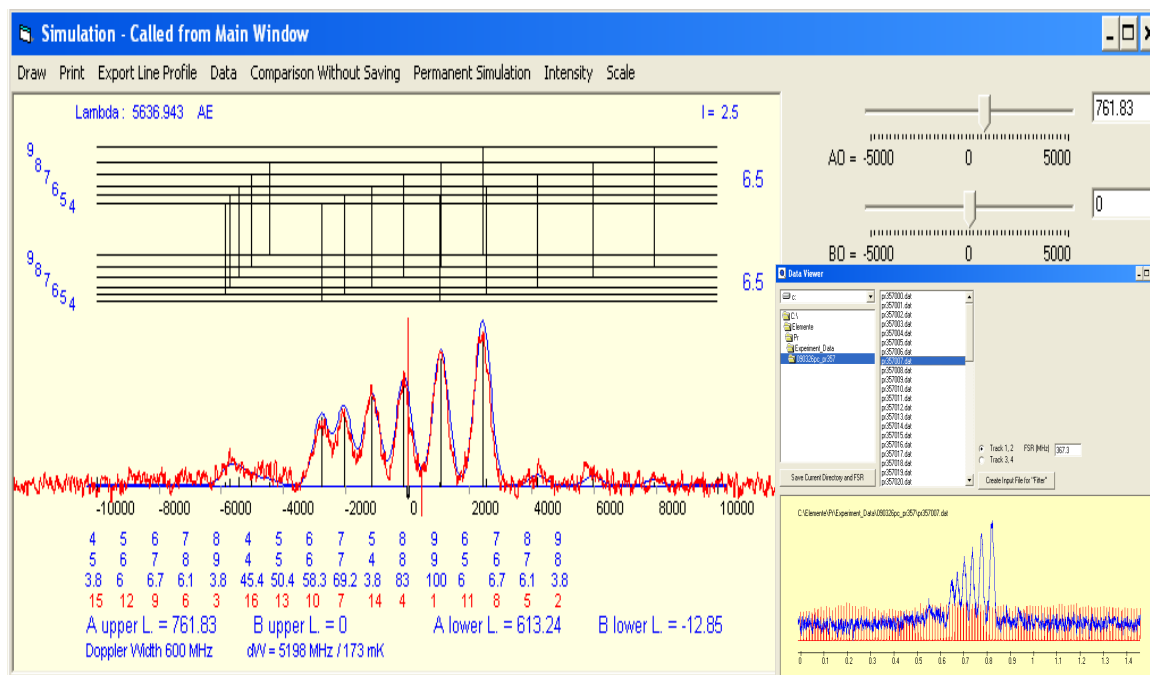
Figure 7.71: Comparison of the recorded hyperfine structure (Red curve) of the line 6146.447 Å with the predicted hyperfine structure (Blue curve).

It can now be said beyond doubt that the single fluorescence line observed at 5227 Å is an indirect fluorescence line occurred as a result of collisional coupling between newly found upper level with energy **19111.800 cm^{-1}** and known level with energy **19122.567 cm^{-1}** as depicted in Figure 7.72. The observed fluorescence line originates from the known upper level **19122.567 cm^{-1}**.

126
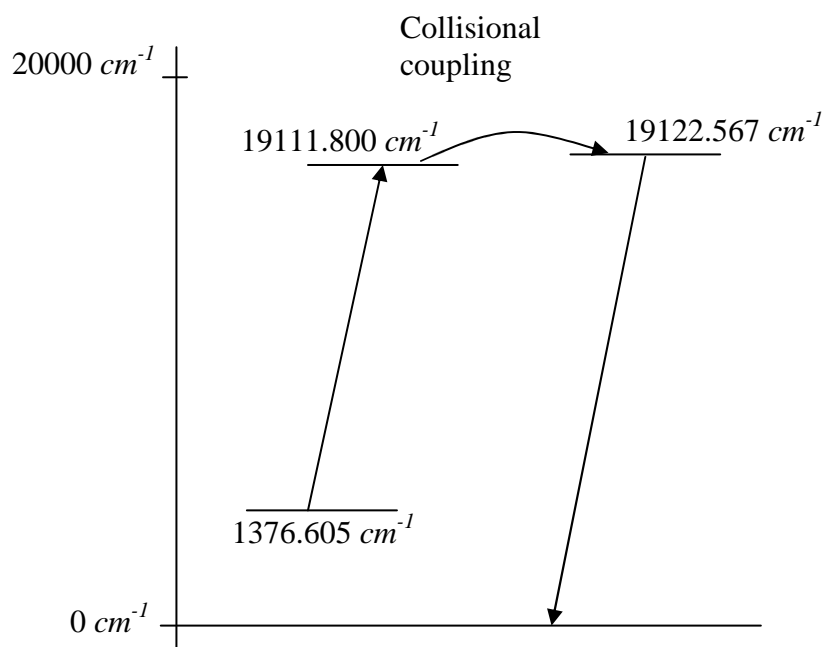
Figure 7.72: Level scheme showing collisionally coupled upper levels

7.1.9 Discovery of a New Pr-I Level at Line 4660.92 Å using FT-Spectrum

The line at 4660.916 Å in FT-spectrum show clearly resolved hyperfine components with a good signal-to-noise ratio and has a relative intensity of 192 (Figure 7.73). None of the suggestions listed in the classification program match hyperfine structure profile in FT spectrum.
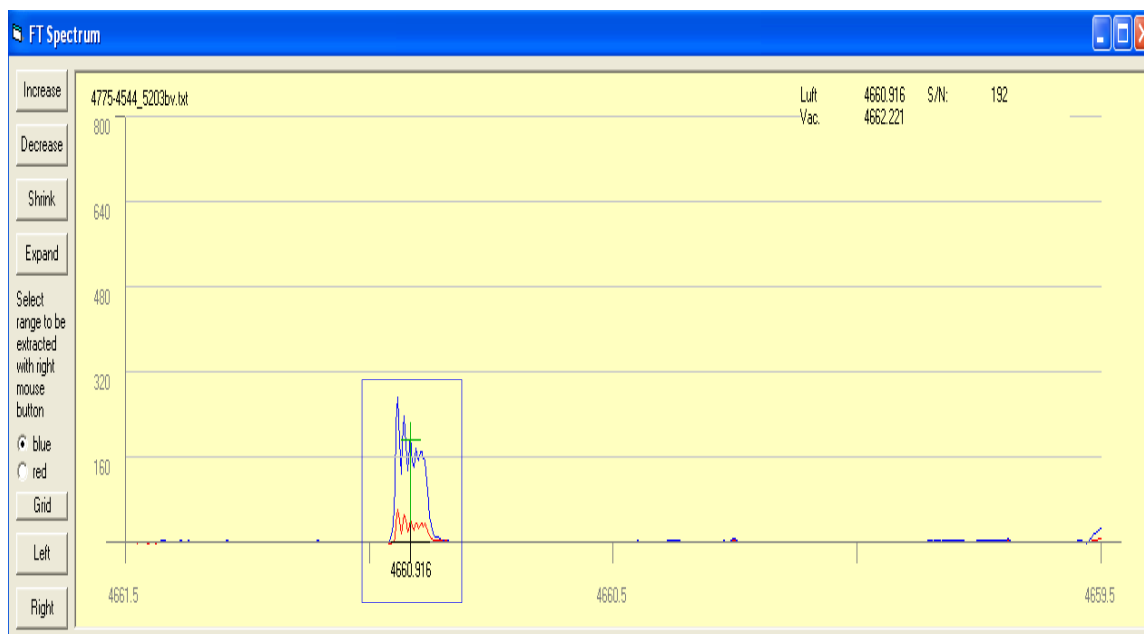
Figure 7.73: FT-spectrum for the line 4660.916 Å

This motivated the investigation of the spectral line by extracting the line profile from FT-spectrum and fitting it to a mathematical function using fitter program. Provided the hyperfine components of a line in FT-spectrum are clearly resolved, this method of investigation could give a reasonable estimate of the spectroscopic parameters of the levels involved in the formation of the line even if the line is not experimentally investigated. The disadvantage in this approach of investigation is the unavailability of fluorescence information which is very important in the identification of the involved levels. This can be avoided by using a search routine in classification program based on the A- and J-values which generate possible number of suggestions and depending on the reliability and authenticity of the estimated spectroscopic fitted parameters of the combining levels, one of the suggestion can be selected.

The line profile comprising the hyperfine components of the line at 4660.916 Å is extracted from the FT-spectrum. This gives a set of data points which is stored in the form of a data file. A program converts the data file in to linearized data file in a format acceptable to the fitter program. Best fit situation with theoretical coupling between intensities of all components was obtained for spectroscopic values $J_o = 9/2$, $J_u = 11/2$, $A_o = 564$ MHz and $A_u = 728$ MHz with a quality factor $Q = 38$ (Figure 7.74). Assuming an unknown upper level is involved in the formation of the line a known lower level is search in the database of known levels. Taking A-value of the assumed known lower level and J-values of the both upper and lower levels the searching routine gives a number of suggestions for possible new upper levels with their fluorescence lines (Figure 7.75). In the absence of the fluorescence information, the key to a reliable identification of the combining levels is to look for the known lower level with A-value nearly the same as determined by the fitter program. In case more than one suggestion has nearly the same A-value then from all such

128

suggestion the possible (new) upper levels are selected and introduced in the database of known levels. For each possible upper level classification program generates a transition list.
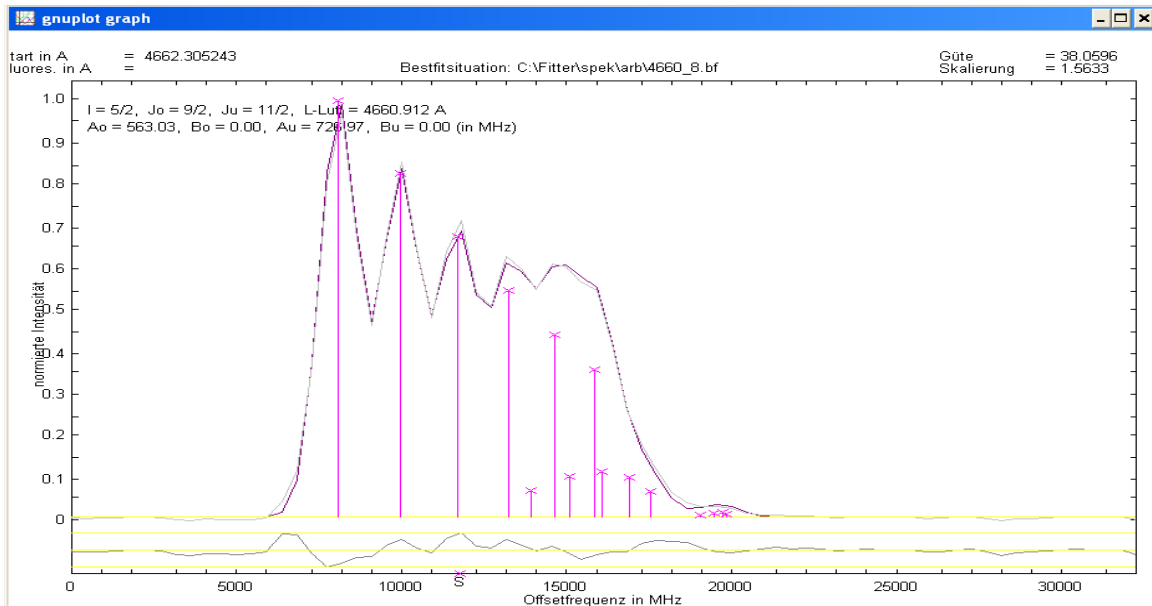
Figure 7.74: Fitted line profile from FT-spectrum of the line 4660.916 $\mathring{A}$
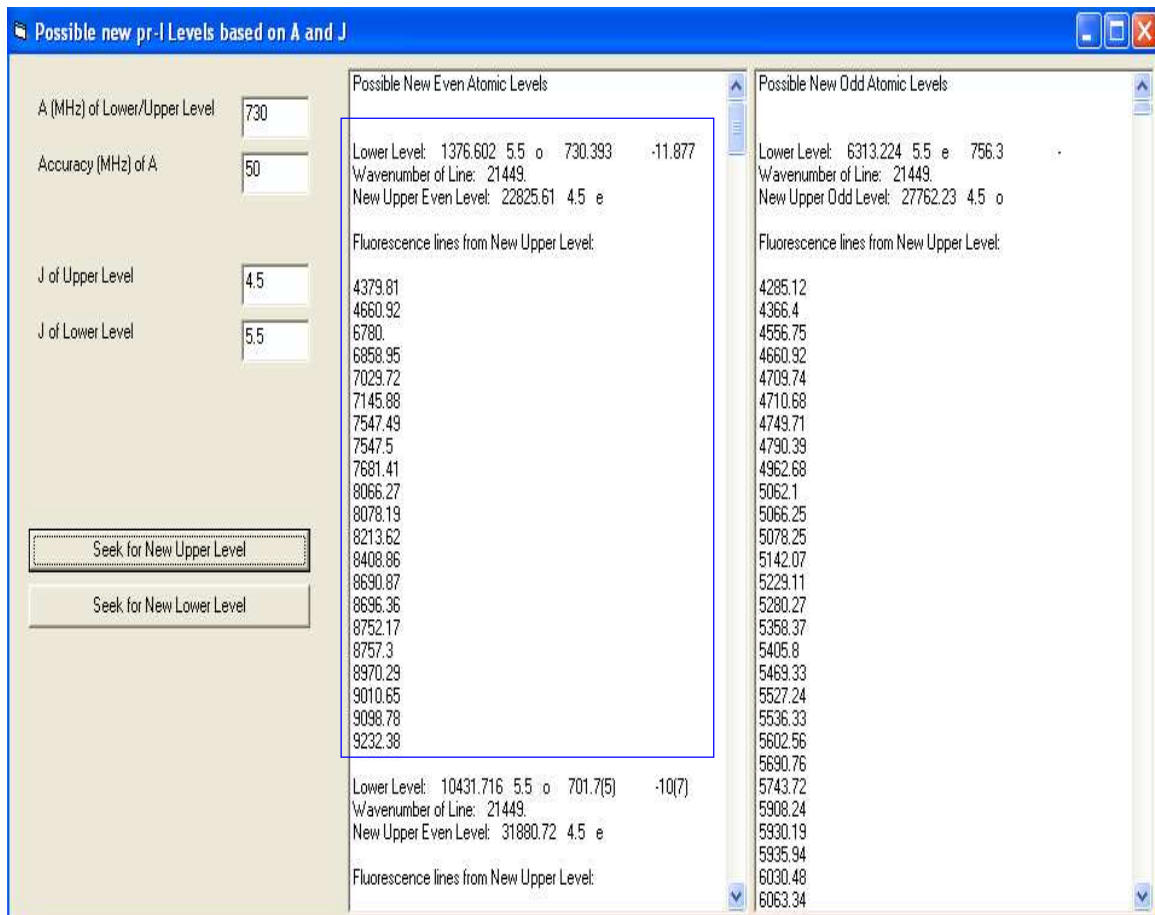
Figure 7.75: Possible suggestions for the line 4660.916 $\mathring{A}$

Those suggestions in which none of the fluorescence lines could be explained from the FT spectrum are rejected. There is a certain margin of error in this process because it might happen that the involved upper level has a low emission probability although this is not true in this case. The first even suggestion has a lower level with parameters **1376.602 cm^{-1}, odd parity, $J_u = 11/2$** and **$A_u = 730.393$ MHz, $B_u = -11.877$ MHz**. The A-value of this lower level is almost the same as the fitted A-value. Assuming this as a known lower level involved in the formation the line at 4660.92 $\mathring{A}$, the line profile from FT-spectrum was again fitted keeping fix the A and B values of the lower combining level. The possible new upper level with parameters **22825.61 cm^{-1}, even parity, $J_o = 9/2$** and **$A_o = 566.83$ MHz** is obtained. This newly found upper level is introduced in the database of known levels and is reloaded in the classification program which generates a transition list. At two lines i.e. 4379.81 $\mathring{A}$ and 7145.88 $\mathring{A}$ the predicted hyperfine structure of lines are partly in agreement with the hyperfine structure profile of the respective lines in FT-spectrum.

In order to confirm the existence of this upper level laser excitation is performed at 7145.88 $\mathring{A}$. A strong LIF signal was observed on 4660 $\mathring{A}$. The hyperfine structure of the line is then recorded by scanning the laser frequency across a certain range. The recorded hyperfine structure of the line at 7145.88 $\mathring{A}$ is in excellent agreement with the hyperfine structure of the line predicted by classification program (Figure 7.76).
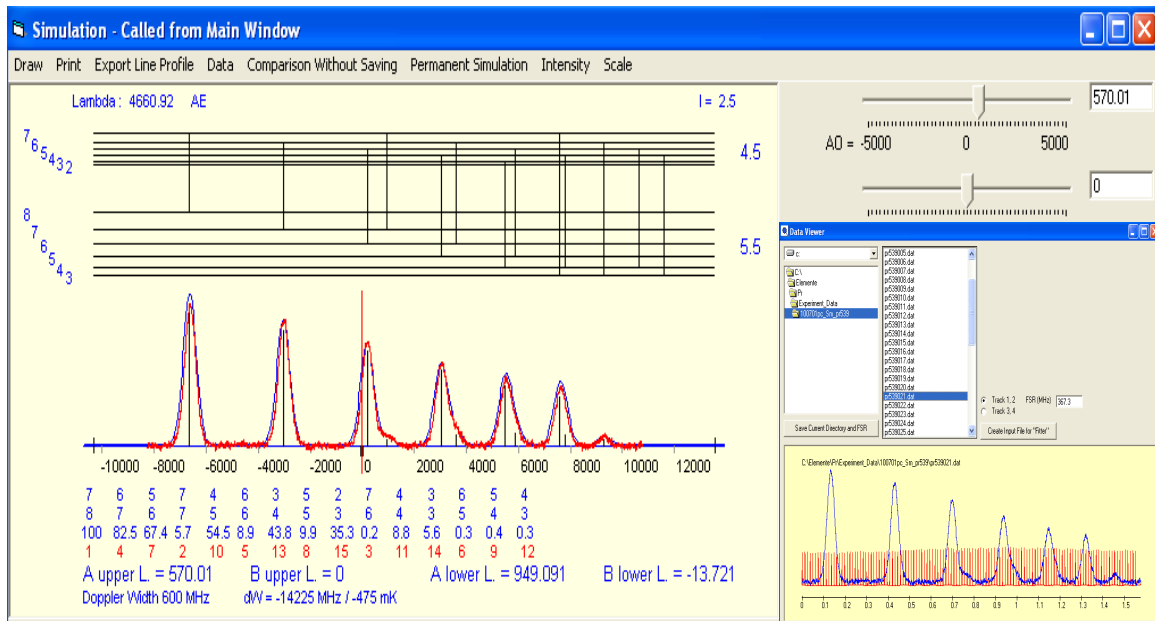
Figure 7.76: Comparison of the recorded hyperfine structure (Red curve) of the line 7145.88 $\mathring{A}$ with the predicted hyperfine structure (Blue curve).

This confirmed the existence of the upper level. In order to have a good estimate of the hyperfine interaction A constant of the new upper level, the recorded hyperfine structure of the line at 7145.88 $\mathring{A}$ is fitted using fitter program. The best fit situation with a quality factor $Q = 14$ was obtained. The corrected energy of the new upper level together with best fit values are **22825.611 cm^{-1}, even parity, $J_o = 9/2$** and **$A_o = 570(5)$ MHz.** The lines 4660.916 $\mathring{A}$ and 7145.88 $\mathring{A}$ were then classified.

7.1.10 Discovery of a New Pr-II Level at Line 4328.42 Å

During the systematic investigation of the spectrum of praseodymium, a number of singly ionized praseodymium levels were also discovered. One such example is presented in this section. Due to discharge conditions inside the hollow cathode lamp, the population of singly ionized Pr ions is not very large and amounts to only 10 % of plasma. This may be the reason that in most cases the ionic lines are not visible in FT-spectrum. One such line in FT-spectrum at 4328.42 Å with a very weak signal-to-noise ratio and having a relative intensity of only 1 is shown in Figure 7.77. Since the hyperfine components of the line are not visible in FT-spectrum, an optogalvanic signal was first recorded to have some idea about the hyperfine component positions of the investigated line.
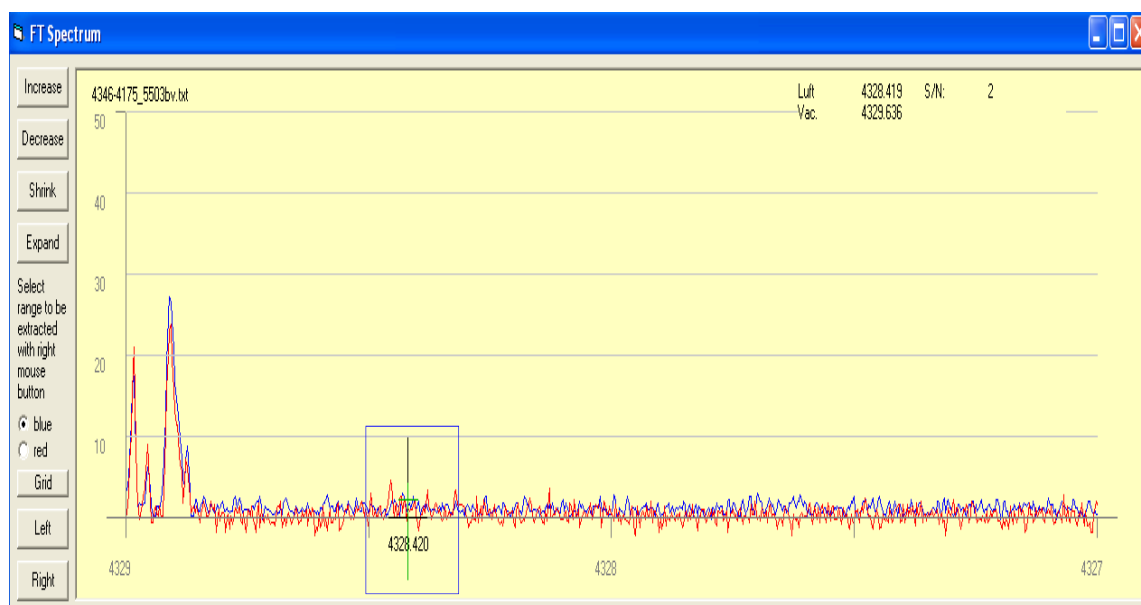
Figure 7.77: FT-spectrum for the line 4328.42 Å

Laser excitation wavelength was set to 4328.42 Å which is the strongest hyperfine component position obtained from the optogalvanic scan. LIF signal was observed on a number of fluorescence line i.e. 3820 Å, 3912 Å, 4156 Å, 4517 Å. Hyperfine structure was then recorded by scanning the laser frequency across a certain range and setting successively the transmission wavelength of the monochromator to all the observed fluorescence wavelengths. On all observed fluorescence lines, same hyperfine structure was recorded with best signal-to-noise ratio at 3820 Å (see Figure 7.78). The recorded hyperfine structure was then linearized and fitted using the Fitter program. Table 7.5 gives the A and B values determined by the Fitter program for different pair of J values of the combining lower and upper levels. The highest quality of fit with $Q = 26$ was obtained for an ionic transition i.e. between $J_o = 3$ and $J_u = 3$. Assuming an unknown upper level is involved in the excited transition, a known lower level is searched in the database of known levels. A number of suggestions for a possible new upper level are displayed with their calculated fluorescence lines. One of the odd parity suggestions for a possible upper level explained all the observed fluorescence lines. The known lower connecting level was discovered by Furmann et. al.[35] with level parameters **10289.48 cm^{-1}, J_u = 3, even parity and A_u = 2114 MHz.** The energy of the possible new upper level was determined using the center-of-gravity excitation wave number and the energy of the lower level. The recorded hyperfine structure was again fitted but now keeping fix the J and A values of the

known lower level. A best fit was obtained with $A_o = 1348.21$ MHz of the upper level see Figure 7.79.
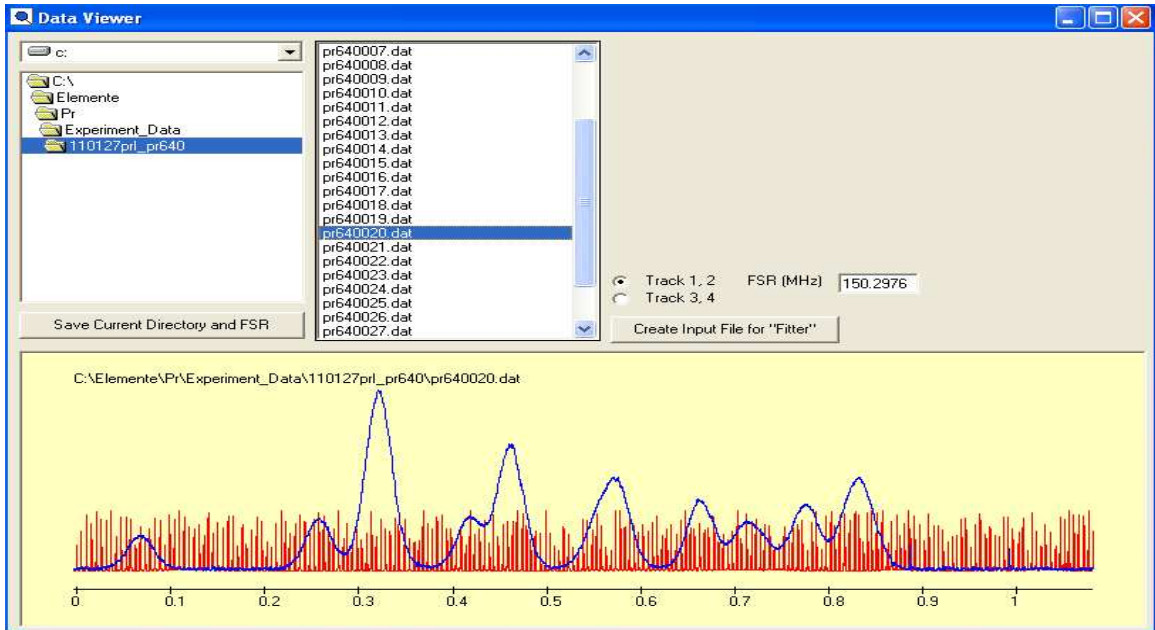
Figure 7.78: Recorded hyperfine structure of the line 4328.42 $\mathring{A}$

Table 7.5: For different pair of *J* values the possible *A* and *B* values of the combining levels are obtained. Quality of fit indicates the best pair of *J* values.

Upper Level J_o	Lower level J_u	Quality of fit	Upper level		Lower level	
			A (MHz)	B(MHz)	A(MHz)	B(MHz)
7/2	7/2	5.25	1197.18	0.00	1880.59	0.00
3	3	26	1352.98	0.00	2123.02	0.00
5/2	5/2	3.26	1547.33	0.00	2416.23	0.00
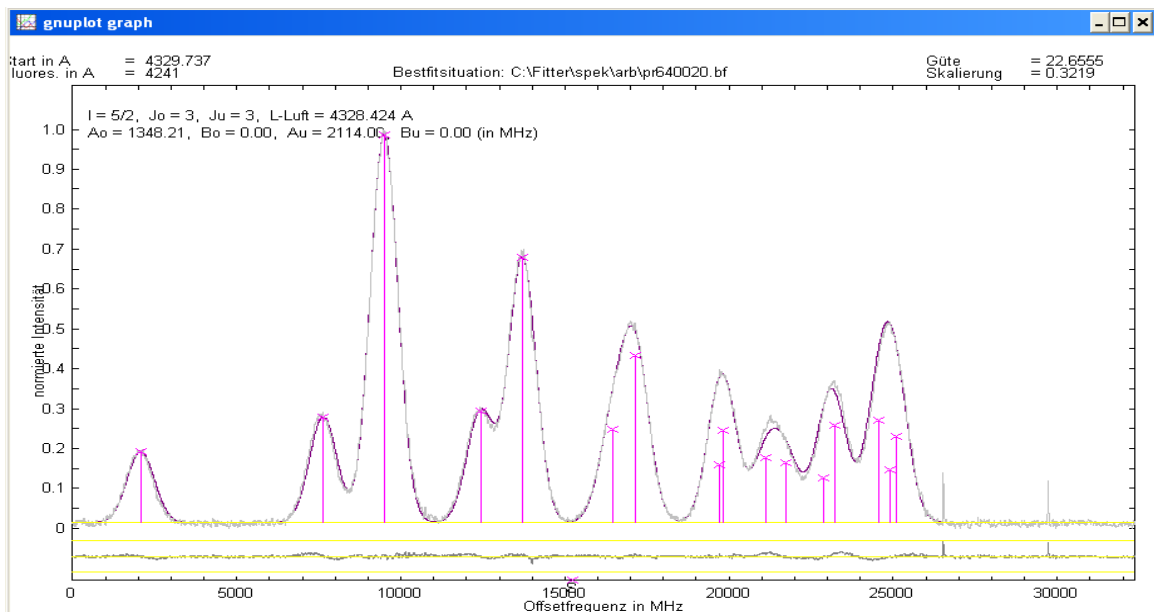
Figure 7.79: Best fit situation of the line 4328.42 $\mathring{A}$

132

The spectroscopic parameters of the newly found upper level are **33386.2 *cm^{-1}*, odd parity, *J_o* = 3 and *A_o* = 1348 MHz**. The level is introduced in the database of known levels and is then uploaded in the classification program. Besides the observed fluorescence lines, the hyperfine structure of the line at 4241.249 *Å* in FT-spectrum sufficiently explains the hyperfine structure predicted by the classification program. In any case for the confirmation of the energy of the newly found ionic upper level a second laser excitation from some other known lower level needs to be performed. A line at 4361.81 *Å* is selected which is present in the transition list of the newly found upper level. Although at this position FT-spectrum the line is not visible but in any case laser excitation was performed for this line and a hyperfine structure with good signal-to-noise ratio was recorded. The recorded hyperfine structure was in agreement with the hyperfine structure of the line predicted by classification program (Figure 7.80).
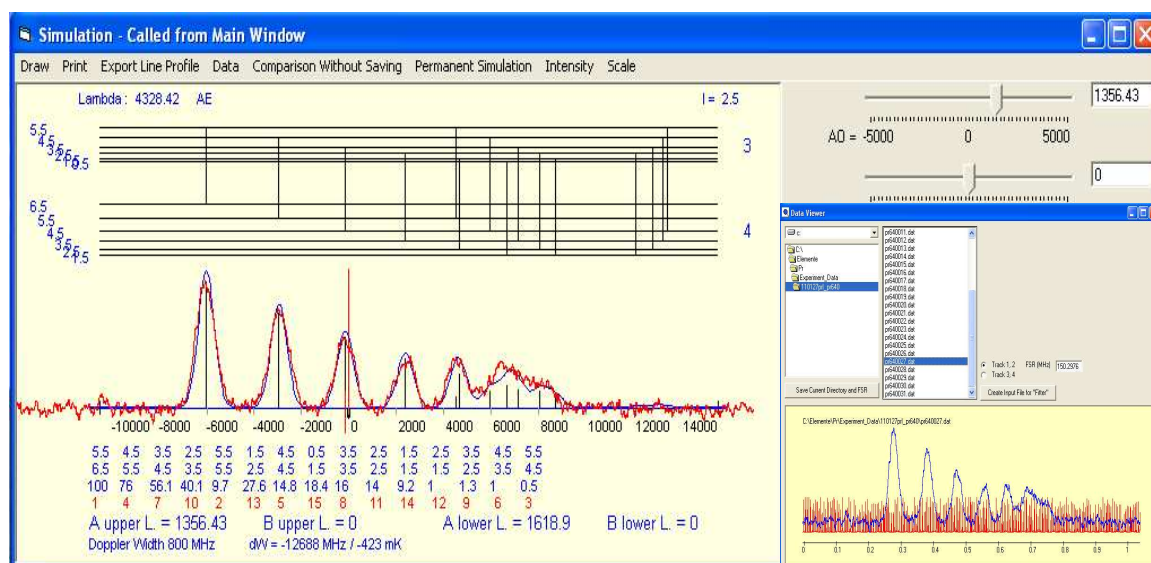
Figure 7.80: Comparison of the recorded hyperfine structure (Red curve) of the line 4361.81 *Å* with the predicted hyperfine structure (Blue curve).

The energy of the newly found upper level and its hyperfine interaction *A* constant was then corrected. The corrected spectroscopic parameters are 33386.215 *cm^{-1}*, odd parity, *J_o* = 3 and *A_o* = 1352(5) MHz. Both the excited lines were then classified.

7.2 Tables

Table 7.4 lists the data of new atomic levels sorted according to J value and energy. Column 1 gives the angular momentum J, in column 2 energy values are given in cm^{-1}, in column 3 values of hyperfine structure constant A (in MHz) are given for the newly discovered levels. Column 4 presents the wavelength of the excitation lines in Å (in air) and column 5 lists the observed fluorescence lines in Å (in air). In all cases B value is very small and is neglected. In most cases the existence of a level is checked by one or two further laser excitations, from other known lower levels. In some cases a newly discovered level is confirmed by analyzing up to now unclassified lines in the FT spectrum, the wavelength of such lines is given in brackets in column 4. This happens in cases where the wavelengths for further laser excitations do not lie in the available spectral range of our laser dyes.

The energies of the newly discovered levels are calculated using the center-of-gravity wave number of the excited lines and the energies of the already known levels involved in the transitions. Therefore the energy accuracy of newly discovered levels not only depend on the energy accuracy of the already known level in the excited transition but also on whether or not the excitation and fluorescence lines appear in FT spectrum with good signal-to-noise ratio (SNR). Since the FT spectrum is only roughly intensity calibrated, the given SNR is only an indication for the line intensity. In cases where a line is excited and neither excitation nor fluorescence lines appear in the FT spectrum with good SNR, then the accuracy of the determined level is limited by the reading accuracy of our lambda meter (±0.01 Å). This limits the accuracy of the calculated level to ±0.05 cm^{-1}.

Table 7.5 contains a list of spectral lines investigated by laser excitation in the discovery/confirmation of the newly found levels. Column 1 gives the center-of-gravity excitation wavelengths in Å (in air), column 2 gives the SNR of the line observed in FT spectrum. The designation 'nl' means a new line not appearing in published wavelength tables. The accuracy in center-of-gravity wavelength for lines with SNR > 3 is better than 0.003 Å. The SNR of a line which does not appear in FT spectrum but nevertheless was successfully observed with LIF method is set as '<1'. For lines appearing in a blend situation in which the SNR cannot be estimated from the FT spectrum, SNR is indicated by '-'. In such cases the center-of-gravity wavelength listed in column 1 is calculated from the level energies and has an estimated uncertainty of 0.01 Å. Columns 3 and 5 gives the J and columns 4 and 6 give the energies for the even and odd levels, respectively, explaining the line.

Table 7.6 lists spectral lines classified by observed fluorescence and has the same structure as table 7.5 except that column 1 gives the observed fluorescence wavelength in Å (in air).

Table 7.7 lists additional lines in which the new levels are involved, classified by means of their hyperfine patterns and wave numbers.

Table 7.8 lists the newly discovered lower levels combining with already known levels.

Table 7.9 list new levels of Pr I found by the analysis of hyperfine patterns in the FT spectrum.

Table 7.10 lists the newly found ionic levels.

Table 7.4: Up to now unknown Pr I energy levels discovered within this work

J	Energy (cm⁻¹)	A (MHz)	$\lambda_{ex.}$ (Å, air)	$\lambda_{fl.}$ (Å, air)
Even Parity				
3/2	27983.773(10)	723(5)	5935.823, 6297.509	5481.402, 6252.794
3/2	28067.892(20)	588(5)	5906.33, 6264.314,	5906.33
3/2	28986.540(20)	637(4)	5923.35, 5882.885,	5602.27
3/2	29234.227(10)	1038(4)	5837.68, 5798.372,	5525.571
5/2	22959.928(10)	1231(5)	7154.439	[1]4640, (8650.457)
5/2	27251.230(10)	335(6)	7143.366, 7334.830,	5473.50, 6308.113, 6676.713,
5/2	27471.606(10)	755(4)	6121.994, 6458.657	5408.24, 5639.78, 5944.52, 6579.870
5/2	27573.343(20)	747(3)	5908.776, 6084.088,	6416.478, 6536.10, 7165.483, (7370.361)
5/2	28055.421(10)	887(3)	5745.08, 6003.473,	5242.66, 6269.21, 6926.166, 7117.40
5/2	28890.950(15)	765(4)	5916.17, 6259.369	5022.587, 5481.87, 5957.086
5/2	29216.845(20)	522(3)	5901.932, 6134.198	4941.673, 5327.06, 5530.88, 5612.06
5/2	30454.610(15)	755(3)	5938.992, 6079.050	4827.405, 5022.27
5/2	31158.848(20)	767(5)	5814.30, 6124.573	4668.641
5/2	31245.375(20)	586(3)	5785.19, 5800.15,	4807.417
5/2	32050.34(5)	594(4)	4334.56, 5807.40	4628.25
7/2	22486.816(20)	948.34	7022.178	4445.802, (8448.802)
7/2	26121.378(15)	805(5)	5594.030,6792.357	5594.030, 6792.357
7/2	27123.623(15)	684(3)	6070.12, 6255.292,	3685.774, 5296.965, 6494.68, (7209.096), (7273.985)
7/2	27231.854(15)	773(2)	7153.27, 7217.149	5266.763, 6213, 6449.336
7/2	27381.794(15)	662(3)	6256.568, 6387.550, 6545.725	5976.44, 5668.50, (7968.417)
7/2	27679.200(20)	654(5)	5802.49, 6045.15	5145.50, 5574.49,

J	Energy (cm^{-1})	A (MHz)	$\lambda_{ex.}$ (Å, air)	$\lambda_{fl.}$ (Å, air)
				6991.366
7/2	27998.766(20)	520(4)	6145.299, 6586.785	6145.299, 6586.785
7/2	28311.416(20)	624(5)	6147.799, 6453.839	5337.09, 5384.67, 5753.877, 5912.58, 6029.42, 6495.04, 6683.82, (7550.905)
7/2	28375.220(20)	863(4)	5890.35, 6123.771	5366.227
7/2	28822.147(20)	693(5)	7186.228, 7270.444,	5240.51, 5441.51, 5502.63, 5589.570, 5654.36, (7865.265)
7/2	28865.800(25)	740(2)	6269.24, 6230.842	6444.941, 5834.35
7/2	29308.235(20)	713(2)	5870.260, 6099.994	5870.260, 6099.994
7/2	29327.656(20)	827(3)	5681.214, 5863.573	5062.435,5786.20, (5805.996)
7/2	29499.235(25)	882(2)	5748.71, 7467.49	5060.878
7/2	29583.69(3)	990(4)	5776.82, 5999.16	5776.82, 5999.16
7/2	29674.025(25)	1005(3)	5746.82, 6125.763,	5473.63, 5672.48, 5746.82, 5932.02, 5966.82, 6846.30
7/2	30654.508(20)	599(3)	5869.291, 5778.59, 6551.97	4781.251, 5173.255, 5373.53, 5605.88, 6006.045
7/2	30920.300(25)	420(5)	6101.124, 6439.79	4684.62, 4884.761, 5103.06
7/2	31079.962(25)	498(3)	5841.10, 6071.44	4649.834, 4845.964
7/2	31292.93(3)	620(4)	5657.25, 5769.31	4604.226, 4796.448
7/2	31355.053(25)	696(3)	5943.423, 6051.829	3188.36, 4992.28, 5393.99, 5422.74, 5637.43
7/2	31531.30(5)	619(4)	6195.93, 5987.94	317053, 5691.02, 5881.793
7/2	31593.97(5)	641(4)	6050.73, 6171.956	5670.79, 4575.66
7/2	31664.74(5)	732(4)	6145.11, 5940.46	4916.248
7/2	31817.13(5)	752(2)	5887.15, 5599.90	4529.40, 4678.77, 4879.68
7/2	32248.10(4)	599(3)	5820.30, 5643.78	4779.144
9/2	22825.611(20)	570(5)	7145.88	4660.915, 4379.813
9/2	22996.562(20)	779(5)	7059.610	4624.060

J	Energy (cm^{-1})	A (MHz)	$\lambda_{ex.}$ (Å, air)	$\lambda_{fl.}$ (Å, air)
9/2	24606.934(10)	777(2)	6111.977, 7052.620	4303.506
9/2	25744.156(10)	823(2)	5659.740, 5912.451	3883.276, 5912.451, (6751.467)
9/2	26231.182(10)	645(3)	6327.578, 6705.624	6327.578, 6894.405, (8762.130)
9/2	27109.741(15)	783(3)	6075.244, 6181.40, 6500.543	3687.661, 5253.579 ,5300.862, 6181.40, 6500.543, (7631.188)
9/2	27251.615(15)	741(3)	5943.69, 6023.313,	5261.283, 6276.05, 6307.96, 6441.122, 6576.41, 6643.862
9/2	27282.000(15)	750(3)	5647.454, 6630.474	5419.539, 6266.953, 6428.537
9/2	27913.895(15)	496(3)	6025.531, 5888.603	3767.21, 5240.04, 6363.744
9/2	28042.800(25)	796(4)	6809.044, 6251.06	6251.05, 5979.08
9/2	28375.291(25)	739(3)	6006.28, 5890.33	5571.478, 5890.33
9/2	28605.413(15)	615(3)	5811.530, 5784.439, 5658.13	5658.13
9/2	28840.315(15)	768(2)	6009.385, 6262.898	5190.530, 5706.87, (7131.339)
9/2	29123.494(15)	733(3)	5641.621, 6132.350	3432.67, 4927.62, 5412.84, 5348.46, 5496.953,
9/2	29370.862(15)	758(2)	5823.66, 6076.770	3404.758, 3571.141, 5051.384, 5278.599, 5541.34, 5563.95, 6040.687, 6076, 6347.67, 6871.28
9/2	29600.360(20)	659(4)	6409.279, 6502.639	4993.48, 6502.639, 6635.64
9/2	29624.447(20)	549(3)	5984.527, 6399.395	4987.48, 5462.36, 6399.395, 6492.36, 6625.05
9/2	29682.07(3)	995(2)	7366.87, 5669.89	5198.20, 5929.19, 5949.178

137

J	Energy (cm^{-1})	A (MHz)	$\lambda_{ex.}$ (Å, air)	$\lambda_{fl.}$ (Å, air)
9/2	29865.350(20)	740(3)	5660.602, 6054.777	5149.13, 5281.51, 5391.40, 5414.93, 5512.76, 5884.990, 5899.45
9/2	30144.181(20)	923(2)	5803.95, 5595.593	(3316.437), 4861.43, 5076.223
9/2	31368.505(15)	526(2)	5759.010, 5938.674	4588.26, 4779.12, 4988.93, 5390.07, 5551.547, 6008.07
9/2	31721.60(5)	574(4)	6123.70, 5644.20	4901.54, 5442.87, 5523.27
9/2	32247.808(20)	592(2)	5820.397, 5706.514	4410.27, 5258.59, 5643.872
11/2	23654.406(10)	613(2)	6419.18, 6489.916	6489.916, (6700.129), (7156.112), (8615.006)
11/2	23865.973(15)	752(2)	6997.854, 7049.349	4445.297
11/2	25357.817(10)	669(3)	6050.701, 6336.190, 6697.82	3942.441, 4168.755, (8346.322)
11/2	25855.320(10)	683(2)	5838.861, 5873.834	3866.580,(6481.778), (6879.053),(7077.868), (7085.725)
11/2	26222.282(15)	590(3)	5749.862, 6007.065, 6044.970	4023.706, 4276.771, 6540.284, (7140.794), (7131.724)
11/2	26467.248(15)	857(2)	5669.98, 7326.027	3984.422, 5956.74
11/2	26937.739(15)	720(5)	5794.30, 7359.74, 7363.24	3711.208, 5491.678
11/2	27888.407(20)	570(4)	5726.871, 6193.275	3770.83, 6374.11, (7800.123)
11/2	27985.186(15)	618(2)	5688.50, 5695.298	3572.299, 5462.66, 6156.364
11/2	28323.602(20)	570(2)	5880.320, 6208.876	6202.021, 6448.764, 6678.37, (6681.265)
11/2	28485.173(20)	702(3)	5966.89, 6082.804	3687.821, 5288.038, 5537.568, 5696.909, 6147.196, 6405.410, 6599.140

J	Energy (cm^{-1})	A (MHz)	$\lambda_{ex.}$ (Å, air)	$\lambda_{fl.}$ (Å, air)
11/2	28522.075(20)	734(3)	5953.78, 6133.279	5277.736, 6390.30
11/2	28680.018(20)	919(2)	5903.75, 6011.536	5037.74, 5234.09, 6525.82
11/2	28818.13(4)	498(4)	5714.11, 5850.62, 5962.02	3469.043, 3643.07, 5196.52, 5437.29
11/2	29323.690(20)	656(4)	5682.494, 6078.823, 6253.032	3409.235, 5291.782,
11/2	29565.016(20)	603(2)	6423.831, 6640.565	5002.311
11/2	29993.26(5)	800(3)	5625.53, 5841.01	3493.47, 5354.56, 5474.15,
11/2	30645.242(30)	473(2)	5775.611,6006.89	5783.846, 5175.74, 5426.45
11/2	30869.567(25)	577(3)	6120.065, 6193.79	4886.50, 5114.42, 5707.64
11/2	30968.412(25)	447(3)	5892.48, 5971.282	3378.343, 5090.56, 5200.901, 5269.653, 5508.91, 5675.61
11/2	31083.29(4)	620(2)	5638.83, 6041.03	3216.23, 3365.279, 5170.000, 5060.960, 5930.585, 6353.15
11/2	31222.52(5)	596(7)	5803.37, 6297.43	5200.01, 5025.54, 5433.84, 6169.445
11/2	31332.402(25)	628(2)	5844.22, 6761.49	3337.29, 4595.870, 4997.932, 5104.245, 5555.084
11/2	31591.14(3)	515(4)	5681.79, 6051.767	5481.81, 5326.141, 5342.262
11/2	31641.39(4)	587(8)	5835.687, 5665.61	3303.219, 4531.50, 5024.97
13/2	19111.800(10)	760(2)	5636.940, 6146.447	[2]5228
13/2	22592.830(15)	500(5)	6888.745	5062, (5489.434), (8384.228)
13/2	24722.464(15)	703(2)	4914.712, 6252.560	4570.00, (7113.696)
13/2	27020.835(15)	632(3)	6026.379, 6368.318, 6747.350,	3898.408, 4135.493, 4415.767, 5754.13, 6755.464, (7305.278)
13/2	27150.550(15)	536(2)	5711.488, 6065.693, 6688.793	3878.79, 4113.422, 5428.225, 6696.766

J	Energy (cm^{-1})	A (MHz)	$\lambda_{ex.}$ (Å, air)	$\lambda_{fl.}$ (Å, air)
13/2	27340.868(15)	557(2)	5662.00, 5996.449,	5650.054, 6438.937, (6612.468)
13/2	27519.089(15)	487(3)	5933.025, 6172.411	3824.103, 4051.976, 5593.71, (6365.865), (7048.643)
13/2	27626.232(15)	443(3)	6836.085, 6489.97, 7007.878,	6131.846, 6295.526, (8922.973)
13/2	27821.680(25)	644(5)	6745.932	5828.36, 6218.985, 6408.65
13/2	28315.140(20)	687(2)	6528.545, 6674.05,	6528.545
13/2	28351.711(15)	633(3)	5870.615, 6020.478	3706.067, 5122.49, (5344.713), 5355.506, 6198.058, 6512.989
13/2	28840.756(20)	667(3)	6015.660, 6262.729, 6458.064	5501.503, 5848.24, 6311.89
13/2	29523.411(20)	622(2)	5623.659, 5772.366, 6185.298, 6264.76	3747.529, 5039.114, 5236.42, 5302.309, 6438.418,
13/2	29909.117(20)	535(3)	5652.29, 5869.87, 7412.60	3503.770, 5525.015
13/2	30013.473(25)	580(4)	5834.121, 6078.089	3491.00, 5619.14, 6003.273, 6241.43
13/2	30371.975(20)	613(3)	5876.76, 6191.866	(3447.838), (3631.995), 5008.312, 5387.207, 6107.159, 6302.73
13/2	30722.337(20)	679(4)	5826.961, 6266.756, 6502.304	3586.34, 4927.01, 5338.91, 5602.365
13/2	30896.129(20)	526(4)	5915.451, 6219.288	3386.616, 5239.223, 5353.54, 5548.33, 6296.26
13/2	30953.27(4)	791(3)	5749.58, 5674.647, 5976.692	3380.073, 5223.58, 5273.87, 5569.10, 5895.52,
13/2	31049.456(20)	438(2)	5717.94, 6044.55	3369.116, 5197.461, 5247.22, 5309.94, 6160.530
13/2	31238.225(30)	1023(3)	5656.87, 5800.225,	3723.34, 5656.87

J	Energy (cm^{-1})	A (MHz)	$\lambda_{ex.}$ (Å, air)	$\lambda_{fl.}$ (Å, air)
13/2	31333.26(5)	576(3)	5766.30, 6054.65, 6253.81	5453.65, 5554.83
13/2	31535.09(5)	509(3)	5702.014, 5775.789, 5872.13, 6195.54,	3314.86, 3486.74, 3681.65, 5069.47, 5116.817, 5394.26, 5962.96, 6052.69,
13/2	31693.804(25)	498(5)	5892.86, 6058.29	(3297.508), 5075.586
13/2	32302.560(25)	571(3)	5688.738, 5701.939, 5783.94	3393.941, 5896.28
13/2	32384.45(5)	590(5)	5662.351, 5975.56	4903.64, 5157.87, 5505.620,
13/2	32726.84(4)	565(3)	[a]5701.10, [a]5701.31, [a]5701.37, 6050.93	5337.28, 5403.72, 5554.632
13/2	33015.19(5)	570(2)	5867.70, 6025.00	5657.46, 5758.45, 5949.14
15/2	24987.630(15)	716(2)	6150.557, 6516.764	4515.26, 4851.468, (6532.670), 6858.285, (7550.048), (7589.206)
15/2	26191.727(15)	478(2)	6334.990, 6440.366	4282.37, 5726.351, 6042.485, 6920.710
15/2	27904.945(20)	570(2)	5714.60, 5817.565, 6186.936	4249.803, 6193.793, 6213.21, 6708.241, (6835.934), (7187.606), (8628.120)
15/2	28252.321(15)	403(3)	5702.284, 6063.298	3935.030, 6236.487, (7414.819)
15/2	28474.736(15)	437(2)	5614.592, 5630.850	5982.597, 6579.583, 6705.396, (8223.709)
15/2	28661.560(15)	550(2)	5910.190, 5916.448,	3872.645, 5572.214, 5477.684 , (8009.741), (8417.492), (8474.743)
15/2	28791.510(15)	437(2)	5871.296, 6565.889	5532.144, (7609.835)
15/2	29287.637(25)	510(3)	7092.05, 7092.47, 7005.999	3780.946, 5705.063, (6358.696)
15/2	29620.381(20)	525(4)	6139.106, 6616.234	5746.098, 5275.178, 6015.78, 6226.910, 6542.61

J	Energy (cm^{-1})	A (MHz)	$\lambda_{ex.}$ (Å, air)	$\lambda_{fl.}$ (Å, air)
15/2	30577.00(5)	628(5)	7360.88, 5798.48	6222.30
15/2	30959.764(25)	573(5)	6077.508, [a]6399.981, [a]6340.26, [a]6340.33	5747.42, 6242.05, 6271.13, 6424.668, 6531.782
15/2	31270.29(5)	579(2)	5964.898, 5787.32, 6625.04	(3517.205), 5248.38, 5557.14, 5574.32, 6123.328, 6298.97
15/2	31536.710(30)	619(2)	5699.421, 6052.100	3484.54, 5492.73, 5562.907, 5871.57
15/2	31887.920(20)	563(4)	5900.125, 5840.05, 6063.021, 6044.092	3442.400, 3634.422, 5293.48, 5372.677, 5697.16, 5752.1, 6158.326, 6374.62, 6420.91
15/2	32383.385(25)	574(2)	5732.499, 5868.310	(3517.114), 5886.15, 5975.935, 6179.38, 6410.22
15/2	33808.50(4)	480(6)	5679.13, 6197.13	5506.819, 5415.298, 5430.487
15/2	34000.50(50)	462(2)	5807.04, 6124.242,	3375.19, 5084.97, 5359.55, 6157.77
17/2	29552.460(20)	515(2)	5636.109, 6019.90	3971.641, (6843.378)
17/2	31055.361(20)	568(4)	5716.01, 5980.927, 6138.608	5195.86, 5520.31, 6205.019
17/2	32925.14(4)	562(2)	5704.20, 6193.94	5506.41, 5559.785
17/2	33114.40(4)	422(2)	5643.260, 6208.778	3479.283, 5501.874
17/2	33264.21(4)	544(4)	6066.498, 6151.543	3461.236, 5002.66, 5414.331, 5851.804, 6096.18
17/2	33997.515(30)	477(3)	5879.995, 6170.063, 6125.364	(3375.533), 4825.58, 5207.51, 6447.86,
19/2	27999.623(15)	505(2)	7318.926, 6640.853	6214.669, 6791.964, 6157.67
19/2	33534.065(30)	544(2)	6646.53, 6304.38	5208.54, 6044.767
19/2	34225.35(5)	478(2)	6041.031, 5802.241	5027.47, 5146.44, 5184.87, 6354.49
19/2	34580.89(5)	475(2)	5913.97, 5684.93	5053.93, 6214.050

J	Energy (cm^{-1})	A (MHz)	$\lambda_{ex.}$ (Å, air)	$\lambda_{fl.}$ (Å, air)
21/2	32243.14 (5)	385 (5)	7415.509, 5731.270	7415.509, 5731.270
Odd Parity				
1/2	27453.746(20)	781(7)	7016.879, 7546.55	5615.227
1/2	27599.95(3)	2039(6)	6006.76, 6353.48, 6429.72	5569.489
1/2	29341.96(3)	915(7)	5735.44, 5781.93, 5854.17	5560.13, 5720.195
1/2	30400.042(20)	1890(10)	5141.703, 5756.53	5251.114, 5448.51
3/2	25947.350(10)	929(8)	5809.035, 6854.190	6157.164
3/2	25986.120(10)	727(4)	5795.98, 6719.285	5117.771
3/2	27383.021(20)	571(4)	5656.96, 6039.18	5361.743
3/2	28323.695(15)	522(3)	5714.46, 6074.09, 6399.23	4570.798
3/2	29350.190(15)	584(4)	5779.18, 6135.45	5090.336, 5397.74, 5557.586, 5646.92
3/2	29499.10(3)	260(5)	4337.685, 5729.86	5354.69
3/2	29750.67(3)	1112(4)	5657.08, 5717.34, 6216.99	4757.60, 4988.61, 5319.36
3/2	29944.814(15)	1375(5)	5654.555, 6352.081	4940.745, 5379.75
3/2	30000.532(20)	1000(15)	5700.92, 5848.56, 6121.87	4927.177, 5363.671, 5446.82
3/2	30166.356(20)	1106(4)	5842.79, 6170.56	4872.79, 4887.23, 5476.43, 5518.794
3/2	30371.08(3)	535(4)	5657.75, 6052.04	4838.81, 5115.76, 5402.094, 5415.69, 5457.12, 5521.43
3/2	30706.200(20)	1077(6)	5712.74, 5890.81	4747.86, 4761.57, 5061.99, 5101.010, 5168.005, 5306.01
3/2	30778.71(3)	1063(5)	5768.51, 6111.26	4109.52, 4745.18, 5225.28, 5285.67, 5463.860
3/2	31260.067(25)	618(5)	5704.63, 5742.98, 6029.61	4029.78, 4438.76, 5263.022, 5386.74
3/2	33248.19(3)	860(8)	4236.42, 4459.23,	4567.76, 4716.39, 4988.16

J	Energy (cm⁻¹)	A (MHz)	λ_ex. (Å, air)	λ_fl. (Å, air)
5/2	22863.048(10)	502(4)	6732.167	[1]4640, (6091.698), (8504.428), (9246.821),
5/2	24388.693(10)	1116(5)	5960.932, 6810.994	5573.558, 5599.708, (6782.978), (9110.822)
5/2	24675.173(10)	485(4)	5860.82, 6272.728, 6680.601	5511.269
5/2	25191.854(10)	925(4)	5688.51, 5819.526, 6075.756, 6432.445	5334.682, 6457.639, 6545.41, (7183.152)
5/2	25859.364(20)	1033(5)	7145.95	5151.197
5/2	27613.57(3)	548(6)	6349.76, 5739.33, 6537.74	4999.573
5/2	27897.591(15)	1287(5)	5647.248, 6045.80, 6237.24,	4661.616, 5027.640, 5217.742
5/2	28106.771(15)	664(8)	5939.23, 6391.111	4879.23, 4975.300
5/2	28219.904(20)	781(4)	5969.39, 6040.218,	5462.45
5/2	28292.560(20)	1070(3)	5874.387, 6165.82	4594.939, 5440.851
5/2	28351.325(20)	470(3)	5797.64, 7491.60,	4565.031
5/2	28617.067(10)	1184(3)	5709.646, 5764.47	5028.902, 5270.821
5/2	29404.602(15)	962(6)	5636.746, 5770.078	4355.54, 4588.573, 5074.76, 5514.07
5/2	29726.88(3)	763(4)	5046.88, 5791.29,	4295.234, 4993.08, 5118.35, 5290.15, 5369.31
5/2	29851.062(20)	922(7)	4272.44, 5801.11	5255.610, 5333.74, 5616.551
5/2	30000.493(20)	708(8)	5700.94, 5848.58, 6121.88	4978.12, 5291.55, 5338.61, 5578.225
5/2	30568.035(20)	735(3)	5758.20, 5828.51	4355.961, 4791.77, 5181.57, 5289.75, 5527.508
5/2	30868.400(20)	1115(10)	5738.81, 5812.94	4725.07, 5125.032
5/2	30902.82(3)	636(6)	5594.36, 5594.562 5823.34, 6419.14	4827.69
5/2	33205.09 (5)	533(3)	5627.26, 5681.53	4085.89, 4254.06
7/2	20012.862(15)	1133(5)	7045.286	[3]4976, (8793.404),

J	Energy (cm⁻¹)	A (MHz)	$\lambda_{ex.}$ (Å, air)	$\lambda_{fl.}$ (Å, air)
				(9903.501)
7/2	21975.458(10)	344(3)	6440.004, 5698.62	6189.254, (7498.891), (7551.988), (8604.437), (9588.908)
7/2	22451.973(15)	1125(4)	6248.204, 7240.105, 7490.283	⁴4743, (5547.926), (7289.586) (7976.244), (8156.221), (8265.447), (8943.890), (9169.796), (9637.438)
7/2	23293.356(15)	759(3)	5722.36, 5936.052 5965.723,	5300.434,(8256.077), (8457.236), (8751.047), (9834.368)
7/2	23628.220(10)	560(3)	5820.324, 5848.847, 6408.919,	5207.970, (7810.871), (7984.691), (8033.905), (8033.635),(8655.932) (9789.258)
7/2	24443.790(10)	1046(2)	7016.088, 7496.383,	5582.478, (7591.178), (8357.456), (8477.849), (9091.907)
7/2	25350.082(15)	1074(3)	5984.12, 6478.297	4779.268, 5290.019, 5313.57 (7057.366), (7307.241), (7872.786)
7/2	25788.548(15)	138(6)	5624.172, 5831.080	5501.713, 5007.20, 5192.56, 5863.14, 6215.714
7/2	26915.490(15)	1122(3)	5613.118, 5808.71, 6547.336	4446.504, 4739.674, 4905.42, 5288.863, (7853.831)
7/2	27852.358(15)	868(4)	5661.72, 7469.521	4268.629, (4671.468), (5043.218)
7/2	27890.013(15)	877(5)	5649.664, 6504.25	4261.77, 4530.358, 4663.263, 4681.55, 4931.41, 503.57, 5219.81
7/2	28565.989(15)	1077(6)	6536.973, 6319.40	4142.404, 4395.704, 4520.717, 4864.13, 5018.135

J	Energy (cm^{-1})	A (MHz)	$\lambda_{ex.}$ (Å, air)	$\lambda_{fl.}$ (Å, air)
7/2	28757.902 (15)	950(4)	5688.81, 5718.04	4358.92, 4822.90, 4891.56, 4970.255, 5086.89, 5432.93
7/2	29233.565(15)	780(3)	5684.359, 6123.31, 6547.53	4388.244, 4714.71, 4855.43, 4966.682, 5119.209, 5250.971
7/2	29450.41(3)	783(6)	5622.22, 5939.19, 5949.52,	3995.96, 4231.161, 4346.871, 4826.57, 5062.992, 5192.837
7/2	29651.540(20)	967(3)	5913.605, 5685.61	5413.517, 5181.300, 5011.938
7/2	29728.713(20)	867(5)	5842.57, 6458.45	4294.895, 4310.407, 4762.579, 4847.439, 4992.62
7/2	29827.87(3)	845(3)	5763.37, 5852.56	5262.02, 4824.242
7/2	30183.72(4)	600(4)	5659.66, 5700.74, 5702.23	4212.55, 4661.53, 5042.225, 5261.88, 5286.88, 5458.66
7/2	30709.41(4)	698(2)	5615.68, 5935.81	4121.256, 5217.81, 5365.97
7/2	30818.62(4)	797(3)	5620.843, 5802.79	4386.78, 5167.53, 5326.40, 5404.892, 5502.95
7/2	31478.935(20)	731(6)	5676.45, 5802.38	5273.007, 5308.651, 5382.988
7/2	32010.763(25)	804(5)	5649.740, 5796.68, 5841.88	4364.49, 4740.17, 4821.06, 5012.99, 5164.07, 5267.757, 5385.64, 5510.06
7/2	32077.74(4)	651(6)	6111.89, 6328.71	3616.19, 3901.192, 4351.77, 4909.13, 4998.83, 5214.85, 5356.99, 5431.04, 5856.26
9/2	21063.222(15)	1093(2)	6967.185, 7055.071, 7435.22	6011.20, (8171.588)
9/2	22395.493(15)	724(4)	7269.896, 7369.16	5703.289, 6216.346, 6303.498, (8194.017),

J	Energy (cm⁻¹)	A (MHz)	λ_ex. (Å, air)	λ_fl. (Å, air)
				(8304.292), (8917.363), (8996.381), (9839.580)
9/2	22524.055(10)	1129(2)	6706.579, 6252.773	6252 .773, (7542.062), (7666.289), (8603.474), (8816.190), (8893.417), (9045.943), (9109.571), (9247.454), (9449.344)
9/2	23008.838(10)	1227(2)	6673.919, 6666.715,	5381.616, 5510.442, (7275.959), (8525.734), (8850.571), (9035.326), (9278.867), (9531.064)
9/2	23934.491(10)	785(3)	5673.386, 5745.890 6126.862	5242.94, 5673.386, 5745.890, 6618.31, (7672.215), (8337.793), (9846.492)
9/2	24196.152(10)	714(4)	5058.313, 5660.757 6177.590	5058.313, 5171.962, 5441.178, 6297.108, 6428.128, (8561.896), (9273.537)
9/2	24485.172(10)	1105(3)	6069.198, 6570.02	4985.41, 5095.768, 5569.608, (8453.073), (9176.124), (9511.740), (9339.919), (9699.660)
9/2	24830.361(10)	940(4)	5807.98, 5944.622	4901.040, 5259.627, 5398.903, 6055.21, (6176.266), (8476.085)
9/2	26035.395(10)	877(2)	5962.563, 6121.76	4946.052, 4722.595, 4627.654, 5069.024, 5174.218, 5427.976, (7819.677)
9/2	26748.510(15)	912(5)	5865.622, 6423.26	4568.687, 4990.040, 5034.96, 5340.614, 5424.938
9/2	27292.757(20)	768(2)	5684.117, 5613.504	4656.39, 4858.07, 5360.746
9/2	27659.987(15)	927(2)	5966.37, 6411.85	4303.982, 4385.986, 4683.240, 4987.99,

J	Energy (cm^{-1})	A (MHz)	$\lambda_{ex.}$ (Å, air)	$\lambda_{fl.}$ (Å, air)
				5257.221, 5567.857
9/2	27980.556(15)	768(3)	5987.19, 6871.86, 7418.838	4245.390, 4512, 4661.788, 474.793, 4909
9/2	28328.419(15)	889(9)	5862.04, 6537.250	4441.044, 4541.044, 4626.285, 4827.008, 4996.562, 5368.08
9/2	29040.590(20)	620(4)	5598.743, 5690.53	4062.510, 4305.85, 4513.885, 4758.01, 5014.761, 5056.285, 5111.82, 5162.37, 5304.74, 5351.73
9/2	29518.913(20)	900(3)	6193.338, 5960.368	4652.102, 4218.928, 5173.43, 5352.55, 5452.68
9/2	30372.918(15)	830(3)	5962.35, 6550.292	(4193.916), 4700.61, 5234.50, 5139.28, 5599.68, 5643.53
9/2	30576.811(20)	766(6)	5699.31, 5984.74	4789.75, 4655.97, 5155.219, 5179.21, 5254.166
9/2	31234.656(25)	665(8)	5670.90, 5615.73	3934.071, 4077.072, 4517.560, 4788, 4902.212, 4917.315
9/2	31500.25(5)	787(4)	5803.11, 6410.40	3693.34, 3893.38, 4033.38, 4496.85, 5189.14, 5581.95
9/2	31604.60(4)	742(2)	5846.50, 6195.97	3738.920, 4917.38
9/2	31693.821(15)	733(5)	5816.14, 5738.62	3973.715, 4152.277, 4874.445, 4898, 5089.105
9/2	31955.363(15)	757(3)	5860.85, 5740.11	3825.57, 3932.829, 4178.361, 4448.76, 4493.00, 4899.21, 5069.39, 5351.04, 5392.35, 5704.123
9/2	32343.24(5)	654(3)	5698.84, 5908.75, 5811.23	4108.96, 4218.32, 4410.22, 4513.72, 4835.54, 4900.82, 4971.60, 5068.16, 5385.88
9/2	32631.71(3)	687(5)	5664.08, 5706.11,	3798.53, 3996.588,

J	Energy (cm⁻¹)	A (MHz)	$\lambda_{ex.}$ (Å, air)	$\lambda_{fl.}$ (Å, air)
			5809.68	4587.91, 5288.35
9/2	33958.36(3)	718(3)	5822.75, 6086.89	3385.86, 3436.40, 3553.22, 3616.242, 3693.703, 3795.30, 3949.18, 4566.97, 4827.78, 5244.95
11/2	21926.369(10)	882(3)	5714.613, 6992.918	5714.613, (7898.193), (8022.233),(8640.942), (8691.213), (9634.268)
11/2	23042.780(10)	891(4)	7033.518, 7362.643	5371.801, 5500.152, 5805.63, (6122.530), (7172.779), (7824.854), (8430.534), (9500.322), (9620.895), (9709.175)
11/2	24816.383(10)	744(2)	5927.775, 5955.302, 6060.343	4904.40, 5402.980, 5522.655,(6363.059), (6602.604), (8643.863), (8660.299)
11/2	25009.019(10)	983(3)	5860.83, 5990.391, 6439.24	5347.309, 5464.505, (7709.545)
11/2	25746.884(10)	784(2)	5617.818, 5845.29, 6544.17	4690.294, 4787.849, 5017.675, 5144.278, 5222.310, 5252.653, 5909.289
11/2	26848.512(15)	590(5)	5634.305, 5686.773	4459.79, 4547.902, 4965.254, 5395.657, 5290.319
11/2	27944.838(15)	654(4)	5964.78, 6537.026	4519.130, 4921.168, 5352.94, 5415.225
11/2	28713.780(25)	694(2)	5618.50, 6023.98, 6224.08	4192.172, 4462.92, 4521.53, 4544.26, 4581.49, 5027.59, 5098.342, 5419.347, 5465.91
11/2	28895.833(15)	643(2)	5763.34, 5897.504	4086.550, 4332.863, 4426.94, 4506.97, 4773.186, 4791.017, 5051.441, 5093.57, 6154.321, 6389.980

J	Energy (cm^{-1})	A (MHz)	$\lambda_{ex.}$ (Å, air)	$\lambda_{fl.}$ (Å, air)
11/2	29089.508(20)	595(5)	5830.88, 5890.61	4658.66, 5099.060, 5149.360
11/2	29354.638(15)	908(4)	5614.83, 5839.495, 5985.273	4011.32, 4415.63, 4450.78, 4687.94, 4977.226, 5262.27
11/2	29775.190(20)	802(3)	5699.49, 5838.27	4514.415, 4836.54, 4922.13, 5297.618, 5377.51, 5406.15
11/2	30320.091(20)	730(5)	5688.64, 6025.11	3861.719, 3927.61, 4215.287, 4406.00, 4469.265, 4484.89, 4985.25, 5024.624, 5036.44, 5148.94,
11/2	31129.206(20)	435(6)	5591.744, 5801.77	4028.52, 4313.24, 4539.19, 4573.18, 4618.56, 4828.27, 5037.31, 5210.96, 5525.31
11/2	31319.42(5)	593(4)	5801.59, 7422.950	3718.18, 3779.23, 4044.85, 4618.84, 5060.17, 5099.01, 5185.88, 5223.40
11/2	31396.143(25)	667(3)	5079.13, 5704.92, 5775.875, 6024.08	3707.605, 3909.228, 3985.645 4032.33, 5037.26, 5217.34
11/2	31449.773(25)	606(7)	5758.03, 6039.87	3700.245, 3760.70, 3901.045, 4041.62, 4254.40, 4507.09, 4551.16, 4754.66, 5023.68, 5318.18, 5899.91
11/2	31677.187(30)	807(3)	5599.21, 5958.01	3669.358, 3866.73, 3941.486, 4504.526, 5111.28
11/2	32444.655(30)	697(2)	5654.423, 5777.18	3868.71, 4353.961, 4390.582, 4918.29, 5052.61, 5180.42, 5208.52, 5258.32, 5367.99, 5390.28
11/2	32588.71(4)	507(5)	5620.20, 6465.07	3606.189, 3550.57, 3847.26, 4070.606,

J	Energy (cm^{-1})	A (MHz)	λ$_{ex.}$ (Å, air)	λ$_{fl.}$ (Å, air)
				4257.08, 4510.34, 4610.26, 4788.97, 4842.55, 4883.68
11/2	33149.53(5)	613(3)	5753.14, 5939.05	3766.98, 4408.9, 4997.87, 5056.11
11/2	33857.14(5)	533(2)	5699.46, 5701.29, 5833.79	3397.51, 3629.53, 4562.24, 4611.89, 5119.19, 5306.31, 5408.33
13/2	25443.665(15)	491(2)	5715.20, 5994.217	5225.814, 5306.358, 5389.124, 5612.150, 6655.946, 6675.071, (7577.605), (7909.719)
13/2	25765.460(15)	582(3)	5902.808, 6140.074	4783.593, 5217.246, 5297.23, 5512.568, 5612.568, (6132.88), (6232.154), (7284.603), (7325.375)
13/2	26810.061(15)	860(3)	5699.239, 5763.547, 5769.892,	4877.439, 4947.529, 5301.107, (5212.333) (5419.676), (5540.310), (6100.929)
13/2	27139.468(15)	776(3)	5662.24, 5747.48, 7264.132, 7413.66 7535.314,	5124.323, (5440.982), 5459.858, 5594.186
13/2	27500.400(25)	883(2)	5608.43, 5800.91	4416.914, 5548.813
13/2	28731.611(20)	578(4)	5822.890, 6017.51	4189.04, 4459.37, 4908.36, 5007.100, 5588.10
13/2	29123.747(15)	868(4)	4910.653, 6298.229	4721.319, 4721.803, 5085.23, 5140.295
13/2	30011.992(15)	686(4)	4915.783, 5628.602, 5888.937	4270.768, 5063.04, 5115.847, 5586.931, 5623.567
13/2	30135.234(20)	587(6)	5720.274, 5846.49, 6597.21	4591.91, 4640.860, (5071.747), 5082.844,
13/2	31377.435(20)	568(2)	5664.164, 5912.93	4053.47, 4083.6, 4267.540, 4521.84, 4735.46, 4781.727, 5190.825,

J	Energy (cm⁻¹)	A (MHz)	λ_ex. (Å, air)	λ_fl. (Å, air)
				5573.08,
13/2	31754.678(25)	753(5)	4388.66, 7219.86	3718.05, 5071.37, 5372.51, 5458.293, 5523.29
13/2	31906.825(25)	561(2)	5888.73, 5952.38	4511.075, 4663.635, 5081.90 , (5906.671)
13/2	32283.572(20)	724(2)	5623.21, 5808.863	3849.45, 4108.611, 4179.48, 4573.30, 4806.35, 4990.359, 5252.60, 5429.94
13/2	32498.59(5)	653(8)	5707.12, 5837.35	4757.14, 5076.24
13/2	32906.84(4)	545(3)	5617.88, 5658.16,	3759.23, 3800.73, 4823.345, 5312.22
13/2	32909.62(4)	256(5)	5716.13, 5833.68, 6961.32,	3758.840
13/2	32966.30(4)	656(2)	5916.78, 6004.40,	3996.476, 4063.50, 4130.94, 4257.24, 4305.25, 4443.993, 4653.57, 4777.72, 4958.48, 5119.62, 5196.377, 5363.874, 5437.14, 5503.38, 5682.17
15/2	24685.348(15)	349(2)	5861.684, 6125.212	5528.900, (5974.210)
15/2	25370.585(15)	814(2)	5739.179, 5635.27	5327.022, 6737.304, (6707.801), (7198.917), (7619.816), (7912.995), (8378.818), (9053.560)
15/2	25853.590(15)	885(2)	6413.79, 5716.07	5193.359, 5485.908
15/2	26430.800(15)	560(3)	5659.258, 5991.595, 6184.761	5042.168, 5317.480, (5409.904), 6245.480, (7336.711), (8188.073), (8435.496)
15/2	28577.388(15)	780(2)	5841.379, 6123.177	4549.60, 4846.879, 5046.077, 5315.657, 5506.978, 5520.06, (6963.749), (7742.845)
15/2	29886.515(15)	657(2)	6381.80, 5626.38	4557.607, 4963.576, 5147.943, 5165.301,

J	Energy (cm⁻¹)	A (MHz)	$\lambda_{ex.}$ (Å, air)	$\lambda_{fl.}$ (Å, air)
				5426.307, 5501.394
15/2	30283.462(25)	524(3)	6011.96, 6150.34	4867.643, 5045.752, 5317.66,
15/2	32502.962(20)	618(6)	5688.947, 5835.858	3860.003, 4019.314, 4550.174, 4936.297, 5373.38, 5468.43, 5500.62
15/2	34031.358(30)	520(2)	5744.06, 5782.57	3833.263, 3894.88, 4694.68, 5073.92
15/2	34678.30(5)	543(2)	5641.133, 5821.10	3740.47, 4121.75, 5961.21
15/2	34785.20(5)	479(3)	5961.87, 6094.05	3842.15, 3783.75, 3992.51, 4880.90, 4997.53, 5406.58, 5228.82
15/2	34926.79(5)	448(2)	5801.66, 5911.95	3706.02, 4783.79, 5035.49, 5190.39, 5240.65, 5280.59, 5365.51, 5402.56
17/2	28224.462(15)	888(2)	7326.637, 5629.774,	5417.315 , (7960.439)
17/2	28694.480(15)	432(2)	5808.608, 5698.68, 6079.576	6291.519
17/2	28951.616(15)	596(3)	5985.973, 6191.330, 7524.748	5211.948, 5408.309, 5427.471, (6786.832), (8725.714)
17/2	29373.942(15)	785(2)	5661.073, 5838.334	(5093.196), 5099.665, 5287.503, 5588.002
17/2	29471.666(15)	438(2)	5998.147, 5629.92	5067.964, 5260.315, 5278.341, 6590.663
17/2	30546.666(15)	638(2)	5634.717, 5613.25	4506.740, 4589.847, 5308.545
17/2	31125.712(15)	680(4)	5913.967, 6531.40	4392.09, 4681.34, 5005.04, 5150.188, 5296.485, 5456.628
17/2	31397.849(20)	591(2)	5820.268, 5944.20	4617.116, 5566.742
17/2	33475.43(5)	634(3)	5941.95, 6255.68	4212.878, (5390.631), 5214.336
19/2	30260.968(20)	539(2)	5704.764, 5681.470	5231.533, 6158.868
19/2	34473.61(3)	580(5)	5638.334, 6015.84	5315

J	Energy (cm^{-1})	A (MHz)	$\lambda_{ex.}$ (Å, air)	$\lambda_{fl.}$ (Å, air)
21/2	26826.517(20)	341(5)	7059.326, 7573.761	(5861.328), 6377.79, 7095.327
21/2	26994.346(25)	359(5)	6976.646, 7478.673	6976.646, 7478.673
21/2	31825.917(25)	385(5)	6255.842	5217.443, 5493.207

[1-4]Indirect positive fluorescence due to collisional transfer of population from upper excited level to 22924.39$^e_{9/2}$ or/ and 22921.344$^e_{9/2}$ which decay via fluorescence channel 4640 Å to 1376.602$^o_{11/2}$

19122.567$^e_{11/2}$ which decay via fluorescence channel 5228 Å to Ground$^o_{9/2}$

20089.29$^e_{11/2}$ which decay via fluorescence channel 4976 Å to Ground$^o_{9/2}$

22451.755$^e_{9/2}$ which decay via fluorescence channel 4743 Å to 1376.602$^o_{11/2}$

[a]Excited from level triplet [74]

Table 7.5: Lines classified via laser excitation. For hf patterns not visible in the FT spectrum or masked in blend situations (SNR <1 or -) the calculated cg wavelength is given (number of figures after decimal point depending on energy accuracy, see table 7.4).

λ_{air} (Å)	SNR	Even Levels		Odd Levels	
		J	Energy (cm^{-1})	J	Energy (cm^{-1})
4236.42	nl <1	3/2	9649.970	3/2	33248.19
4272.44	nl -	5/2	6451.808	5/2	29851.062
4334.56	nl -	5/2	32050.34	3/2	8986.443
4337.685	nl 3	5/2	6451.808	3/2	29499.10
4348.66	nl 1	15/2	8765.541	13/2	31754.678
4459.23	nl <1	5/2	10829.070	3/2	33248.19
4910.653	36	15/2	8765.541	13/2	29123.747
4914.712	160	13/2	24722.464	15/2	4381.072
4915.783	20	11/2	9675.029	13/2	30011.992
5046.88	nl -	7/2	9918.190	5/2	29726.88
5058.313	108	9/2	4432.225	9/2	24196.152
5079.13	nl -	9/2	11713.236	11/2	31396.143
5141.703	nl 4	1/2	10956.651	1/2	30400.042
5591.744	nl 14	11/2	13250.662	11/2	31129.206
5594.030	nl 22	7/2	26121.378	9/2	8250.143
5594.36	nl -	7/2	13032.634	5/2	30902.82
5594.562	nl 8	3/2	13033.280	5/2	30902.82
5595.593	nl 11	9/2	30144.181	7/2	12277.935
5598.743	18	9/2	11184.396	9/2	29040.590
5599.21	nl -	9/2	13822.494	11/2	31677.187
5599.90	nl -	7/2	31817.13	5/2	13964.630
5608.43	nl -	11/2	9675.029	13/2	27500.400
5613.25	nl -	17/2	12736.621	17/2	30546.666
5613.504	nl 22	11/2	9483.518	9/2	27292.757
5614.592	nl 15	15/2	28474.736	15/2	10668.95
5614.83	nl -	9/2	11549.602	11/2	29354.638
5615.68	nl -	5/2	12907.057	7/2	30709.41
5615.73	nl -	9/2	13432.468	9/2	31234.656
5617.818	90	13/2	7951.323	11/2	25746.884
5617.88	nl -	11/2	15111.485	13/2	32906.84
5618.50	nl -	9/2	10920.365	11/2	28713.780
5620.20	nl -	11/2	14800.680	11/2	32588.71
5620.843	nl 8	7/2	13032.634	7/2	30818.62

λ_{air} (Å)	SNR	Even Levels		Odd Levels	
		J	Energy (cm⁻¹)	J	Energy (cm⁻¹)
5622.22	nl -	7/2	11668.794	7/2	29450.41
5623.21	nl -	11/2	14505.065	13/2	32283.572
5623.659	45	13/2	29523.411	13/2	11746.328
5624.172	75	7/2	8013.089	7/2	25788.548
5625.53	nl -	11/2	29993.26	13/2	12222.095
5626.38	nl -	13/2	12118.039	15/2	29886.515
5628.602	nl 15	15/2	12250.519	13/2	30011.992
5629.774	60	15/2	10466.689	17/2	28224.462
5629.92	nl -	17/2	11714.352	17/2	29471.666
5630.850	nl 16	15/2	28474.736	17/2	10720.359
5634.305	40	9/2	9105.020	11/2	26848.512
5634.717	95	15/2	12804.468	17/2	30546.666
5635.270	94	13/2	7630.132	15/2	25370.585
5636.109	52	17/2	29552.460	15/2	11814.647
5636.746	29	7/2	11668.794	5/2	29404.602
5636.940	140	13/2	19111.800	11/2	1376.602
5638.333	nl 15	17/2	16742.797	19/2	34473.61
5638.83	nl -	11/2	31083.29	9/2	13354.046
5641.133	nl 6	15/2	16956.282	15/2	34678.30
5641.621	31	9/2	29123.494	7/2	11403.011
5643.260	31	17/2	33114.40	15/2	15399.063
5643.78	nl -	7/2	32248.10	9/2	14534.393
5644.20	nl -	9/2	31721.60	7/2	14009.225
5647.248	nl 12	7/2	10194.768	5/2	27897.591
5647.454	nl 16	9/2	27282.000	9/2	9579.832
5649.665	nl 20	7/2	10194.768	7/2	27890.013
5649.740	nl 9	5/2	14315.745	7/2	32010.763
5652.29	nl -	13/2	29909.117	13/2	12222.095
5627. 26	nl -	7/2	15439.372	5/2	33205.09
5654.423	nl 10	9/2	14764.288	11/2	32444.655
5654.555	nl 7	1/2	12264.864	3/2	29944.814
5656.87	nl -	13/2	31238.225	15/2	13565.490
5656.96	nl -	5/2	9710.600	3/2	27383.021
5657.08	nl <1	5/2	12078.621	3/2	29750.67
5657.25	nl -	7/2	31292.93	7/2	13621.400
5657.75	nl -	3/2	12701.121	3/2	30371.08

λ_air (Å)	SNR	Even Levels		Odd Levels	
		J	Energy (cm⁻¹)	J	Energy (cm⁻¹)
5658.13	nl -	9/2	28605.413	9/2	10936.650
5658.16	nl -	11/2	15238.143	13/2	32906.84
5659.257	nl 24	15/2	8765.541	15/2	26430.800
5659.570	nl 15	9/2	25744.156	11/2	8080.404
5659.66	nl -	9/2	12519.707	7/2	30183.72
5660.602	nl 12	9/2	29865.350	11/2	12204.285
5660.757	27	7/2	6535.572	9/2	24196.152
5661.073	nl 16	17/2	11714.352	17/2	29373.942
5661.72	nl -	7/2	10194.768	7/2	27852.358
5662.01	nl -	13/2	27340.868	13/2	9684.184
5662.24	nl -	11/2	9483.518	13/2	27139.468
5662.351	8	13/2	32384.45	11/2	14728.846
5664.08	nl -	11/2	14981.500	9/2	32631.71
5664.164	nl 7	11/2	13727.482	13/2	31377.435
5665.61	nl -	11/2	31641.39	13/2	13995.931
5669.89	-	9/2	29682.09	9/2	12049.940
5669.98	-	11/2	26467.248	11/2	8835.383
5670.79	nl -	7/2	31593.97	5/2	13964.630
5673.386	118	11/2	6313.224	9/2	23934.491
5674.64	nl -	13/2	30953.27	13/2	13335.870
5676.45	nl -	7/2	13867.177	7/2	31478.935
5679.13	nl -	15/2	33808.50	13/2	16205.044
5681.214	nl 7	7/2	29327.656	9/2	11730.668
5681.470	nl 10	21/2	12664.774	19/2	30260.968
5681.53	nl -	5/2	15609.10	5/2	33205.09
5681.79	nl -	11/2	31591.140	13/2	13995.931
5682.494	nl 24	11/2	29323.690	9/2	11730.668
5684.117	41	7/2	9704.744	9/2	27292.757
5684.359	nl 10	5/2	11646.312	7/2	29233.565
5684.93	nl -	19/2	34580.89	17/2	16995.410
5685.61	nl -	9/2	12068.17	7/2	29651.540
5686.773	nl 14	11/2	9268.726	11/2	26848.512
5688.51	nl -	7/2	7617.440	5/2	25191.854
5688.64	nl -	9/2	12746.067	11/2	30320.091
5688.738	nl 8	13/2	32302.560	11/2	14728.846
5688.81	nl -	9/2	11184.396	7/2	28757.902

λ_{air} (Å)	SNR	Even Levels		Odd Levels	
		J	Energy (cm⁻¹)	J	Energy (cm⁻¹)
5688.947	nl 14	15/2	14929.926	15/2	32502.962
5688.947	nl 14	15/2	14929.926	15/2	32502.962
5690.53	-	7/2	11472.410	9/2	29040.590
5698.62	nl -	9/2	4432.225	7/2	21975.458
5698.68	nl -	19/2	11151.433	17/2	28694.480
5698.84	nl -	11/2	14800.68	9/2	32343.24
5699.239	nl 17	11/2	9268.726	13/2	26810.061
5699.31	nl -	11/2	13035.697	9/2	30576.811
5699.421	nl 24	15/2	31536.710	13/2	13995.931
5699.46	nl -	11/2	16316.469	11/2	33857.14
5699.49	nl -	11/2	12234.616	11/2	29775.190
5700.74	nl -	5/2	12646.996	7/2	30183.72
5700.92	nl -	3/2	12464.369	3/2	30000.532
5700.94	nl -	3/2	12464.369	5/2	30000.493
5701.10	nl -	13/2	32726.84	13/2	15191.218
5701.29	nl -	9/2	16322.122	11/2	33857.14
5701.31	nl -	13/2	32726.84	13/2	15191.891
5701.37	nl -	13/2	32726.84	15/2	15192.075
5701.939	nl 7	13/2	32302.560	15/2	14769.532
5702.014	25	13/2	31535.09	11/2	14002.294
5702.23	-	9/2	12651.589	7/2	30183.72
5702.284	25	15/2	28252.321	17/2	10720.359
5704.123	nl 11	7/2	14429.047	9/2	31955.363
5704.20	nl -	17/2	32925.14	15/2	15399.063
5704.63	nl -	5/2	13735.298	3/2	31260.067
5704.764	nl 20	17/2	12736.621	19/2	30260.968
5704.92	nl -	11/2	13872.266	11/2	31396.143
5706.11	nl -	11/2	15111.485	9/2	32631.71
5706.514	nl 7	9/2	32247.808	11/2	14728.846
5707.12	nl -	11/2	14981.500	13/2	32498.59
5709.646	nl 3	5/2	11107.696	5/2	28617.067
5712.74	nl -	3/2	13206.325	3/2	30706.200
5714.46	nl -	5/2	10829.070	3/2	28323.695
5714.60	-	15/2	27904.945	13/2	10410.745
5714.613	175	9/2	4432.225	11/2	21926.369
5715.20	nl -	13/2	7951.323	13/2	25443.665

λ_air (Å)	SNR	Even Levels		Odd Levels	
		J	Energy (cm⁻¹)	J	Energy (cm⁻¹)
5716.01	nl -	17/2	31055.361	15/2	13565.490
5716.07	nl -	15/2	8363.901	15/2	25853.590
5716.13	nl -	13/2	15420.118	13/2	32909.62
5717.34	nl <1	1/2	12264.864	3/2	29750.67
5717.94	-	13/2	31049.456	15/2	13565.490
5718.04	nl -	7/2	11274.229	7/2	28757.902
5720.274	nl 9	11/2	12658.401	13/2	30135.234
5722.36	nl -	9/2	5822.890	7/2	23293.356
5726.871	nl 8	11/2	27888.407	11/2	10431.716
5729.86	nl -	3/2	12051.488	3/2	29499.10
5731.270	80	21/2	32243.14	19/2	14799.842
5732.499	nl 12	15/2	32383.385	17/2	14943.825
5735.44	nl -	3/2	11911.350	1/2	29341.96
5738.622	nl 10	9/2	14272.877	9/2	31693.821
5738.81	nl -	5/2	13448.016	5/2	30868.400
5739.179	nl 12	13/2	7951.323	15/2	25370.585
5739.33	nl -	7/2	10194.768	5/2	27613.57
5740.11	nl -	7/2	14538.930	9/2	31955.363
5742.98	nl <1	1/2	13852.32	3/2	31260.067
5744.06	nl -	13/2	16626.878	15/2	34031.358
5745.08	nl -	5/2	28055.421	7/2	10654.053
5745.890	50	11/2	6313.224	9/2	23934.491
5746.82	nl -	7/2	29674.025	7/2	12277.935
5747.48	nl -	15/2	9745.376	13/2	27139.468
5748.71	nl -	7/2	29499.235	5/2	12108.867
5749.58	nl 6	13/2	30953.27	15/2	13565.490
5749.862	nl 12	11/2	26222.282	11/2	8835.383
5753.14	-	13/2	15772.545	11/2	33149.53
5756.53	nl -	3/2	13033.280	1/2	30400.042
5758.03	nl -	13/2	14087.545	11/2	31449.773
5758.20	nl -	3/2	13206.325	5/2	30568.035
5759.010	nl 13	9/2	31368.505	7/2	14009.225
5763.34	nl -	9/2	11549.602	11/2	28895.833
5763.37	nl -	5/2	12481.714	7/2	29827.87
5763.547	nl 6	13/2	9464.440	13/2	26810.061
5764.47	nl -	7/2	11274.229	5/2	28617.067

λ_air (Å)	SNR	Even Levels		Odd Levels	
		J	Energy (cm⁻¹)	J	Energy (cm⁻¹)
5766.30	nl -	13/2	31333.26	13/2	13995.931
5768.51	nl -	5/2	13448.016	3/2	30778.71
5769.31	nl -	7/2	31292.93	5/2	13964.630
5769.892	nl 7	11/2	9483.518	13/2	26810.061
5770.078	nl 5	5/2	12078.621	5/2	29404.602
5772.366	30	13/2	29523.411	11/2	12204.285
5775.611	nl 5	11/2	30645.242	13/2	13335.870
5775.789	nl 10	13/2	31535.09	11/2	14226.210
5775.875	nl 10	13/2	14087.545	11/2	31396.143
5776.82	nl -	7/2	29583.69	7/2	12277.935
5777.18	nl -	9/2	15139.967	11/2	32444.655
5778.59	nl <1	7/2	30654.508	9/2	13354.046
5779.18	nl -	3/2	12051.488	3/2	29350.190
5781.93	nl -	3/2	12051.488	1/2	29341.96
5782.57	nl -	17/2	16742.797	15/2	34031.358
5783.846	nl 16	11/2	30645.242	11/2	13360.502
5783.94	nl -	13/2	32302.560	13/2	15018.088
5784.439	16	9/2	28605.413	11/2	11322.443
5785.19	nl -	5/2	31245.375	5/2	13964.63
5787.32	nl -	15/2	31270.29	13/2	13995.931
5791.29	nl -	3/2	12464.369	5/2	29726.88
5794.30	nl -	11/2	26937.739	13/2	9684.184
5795.98	nl -	5/2	8737.556	3/2	25986.120
5796.68	nl -	9/2	14764.288	7/2	32010.763
5797.64	nl -	5/2	11107.696	5/2	28351.325
5798.372	nl 22	3/2	29234.227	3/2	11992.788
5798.48	nl -	15/2	30577.00	13/2	13335.870
5800.15	nl -	5/2	31245.375	7/2	14009.225
5800.225	nl 10	13/2	31238.225	11/2	14002.294
5800.91	nl -	13/2	10266.501	13/2	27500.400
5801.11	nl -	7/2	12617.767	5/2	29851.062
5801.59	nl -	13/2	14087.545	11/2	31319.42
5801.66	nl -	17/2	17695.093	15/2	34926.79
5801.77	nl -	13/2	13897.874	11/2	31129.206
5802.241	nl 13	19/2	34225.35	17/2	16995.410
5802.38	nl -	7/2	14249.395	7/2	31478.935

λ_air (Å)	SNR	Even Levels		Odd Levels	
		J	Energy (cm⁻¹)	J	Energy (cm⁻¹)
5802.49	-	7/2	27679.200	7/2	10449.997
5802.79	nl -	7/2	13590.315	7/2	30818.62
5803.11	nl -	9/2	14272.877	9/2	31500.25
5803.37	nl -	11/2	31222.52	13/2	13995.931
5803.95	nl -	9/2	30144.181	7/2	12919.316
5807.04	nl -	15/2	34000.50	15/2	16784.800
5807.40	nl -	5/2	32050.34	5/2	14835.699
5807.98	nl -	7/2	7617.440	9/2	24830.361
5808.609	nl 31	15/2	11483.427	17/2	28694.480
5808.863	nl 9	13/2	15073.268	13/2	32283.572
5809.035	nl 4	5/2	8737.556	3/2	25947.350
5809.68	nl -	9/2	15423.841	9/2	32631.71
5811.23	nl -	9/2	15139.967	9/2	32343.24
5811.530	10	9/2	28605.413	7/2	11403.011
5812.94	nl -	5/2	13670.175	5/2	30868.400
5814.30	nl -	5/2	31158.848	5/2	13964.63
5816.14	nl -	11/2	14505.065	9/2	31693.821
5817.556	nl 30	15/2	27904.945	17/2	10720.359
5819.526	nl 4	7/2	8013.089	5/2	25191.854
5820.268	nl 7	15/2	14221.272	17/2	31397.849
5820.30	nl -	7/2	32248.10	9/2	15071.618
5820.324	nl 55	5/2	6451.808	7/2	23628.220
5820.397	nl 21	9/2	32247.808	9/2	15071.618
5822.75	nl -	7/2	16789.096	9/2	33958.36
5822.890	nl 5	13/2	11562.762	13/2	28731.611
5823.34	nl -	5/2	13735.298	5/2	30902.82
5823.66	nl -	9/2	29370.862	11/2	12204.285
5826.961	nl 16	13/2	30722.337	15/2	13565.490
5828.51	nl -	7/2	13415.739	5/2	30568.035
5830.88	nl -	11/2	11944.207	11/2	29089.508
5831.080	nl 11	9/2	8643.824	7/2	25788.548
5833.68	nl	13/2	15772.545	13/2	32909.62
5833.79	nl -	9/2	16720.373	11/2	33857.14
5834.121	nl 16	13/2	30013.473	11/2	12877.682
5835.687	nl 8	11/2	31641.39	13/2	14510.22
5835.858	nl 5	13/2	15372.271	15/2	32502.962

λ_air (Å)	SNR	Even Levels		Odd Levels	
		J	Energy (cm⁻¹)	J	Energy (cm⁻¹)
5835.858	nl 5	13/2	15372.271	15/2	32502.962
5837.35	nl -	13/2	15372.271	13/2	32498.59
5837.68	nl -	3/2	29234.227	5/2	12108.867
5838.27	nl -	9/2	12651.589	11/2	29775.190
5838.334	nl 10	15/2	12250.519	17/2	29373.942
5838.861	nl 7	11/2	25855.320	13/2	8733.440
5839.495	nl 6	11/2	12234.616	11/2	29354.638
5840.05	nl -	15/2	31887.920	15/2	14769.532
5841.01	nl -	11/2	29993.26	11/2	12877.682
5841.10	nl -	7/2	31079.962	5/2	13964.630
5841.379	28	13/2	11462.895	15/2	28577.388
5841.88	nl -	9/2	14897.721	7/2	32010.763
5842.57	nl -	7/2	12617.701	7/2	29728.713
5842.79	nl -	1/2	13055.995	3/2	30166.356
5844.22	nl -	11/2	31332.402	11/2	14226.210
5845.29	nl -	9/2	8643.824	11/2	25746.884
5846.49	nl -	11/2	13035.697	13/2	30135.234
5846.49	-	11/2	14505.065	9/2	31604.603
5848.56	nl -	5/2	12907.057	3/2	30000.532
5848.58	nl -	5/2	12907.057	5/2	30000.493
5848.847	nl 35	7/2	6535.572	7/2	23628.220
5852.56	nl -	9/2	12746.067	7/2	29827.87
5854.17	nl -	1/2	12264.864	1/2	29341.96
5860.82	nl -	7/2	7617.440	5/2	24675.173
5860.83	nl -	13/2	7951.323	11/2	25009.019
5862.04	nl -	7/2	11274.229	9/2	28328.419
5863.573	nl 15	7/2	29327.656	7/2	12277.935
5865.622	nl 9	7/2	9704.744	9/2	26748.510
5867.70	-	13/2	33015.19	11/2	15977.45
5868.310	nl 12	15/2	32383.385	13/2	15347.425
5869.292	24	7/2	30654.508	7/2	13621.400
5869.87	nl -	13/2	29909.117	11/2	12877.682
5870.260	20	7/2	29308.235	7/2	12277.935
5870.615	100	13/2	28351.711	11/2	11322.443
5871.296	nl 35	15/2	28791.510	17/2	11764.216
5872.13	nl -	13/2	31535.09	13/2	14510.22

λ_{air} (Å)	SNR	Even Levels		Odd Levels	
		J	Energy (cm^{-1})	J	Energy (cm^{-1})
5873.834	nl 30	11/2	25855.320	11/2	8835.383
5874.387	nl 4	7/2	11274.229	5/2	28292.560
5879.995	15	17/2	33997.515	17/2	16995.410
5880.320	nl 10	11/2	28323.602	11/2	11322.443
5881.603	18	9/2	27913.895	9/2	10936.650
5882.885	24	3/2	28986.540	3/2	11992.788
5887.15	nl -	7/2	31817.13	5/2	14835.699
5888.73	-	15/2	14929.926	13/2	31906.825
5888.937	18	11/2	13035.697	13/2	30011.992
5890.33	-	9/2	28375.291	7/2	11403.011
5890.35	nl -	7/2	28375.220	7/2	11403.011
5890.61	-	13/2	12118.054	11/2	29089.508
5890.81	nl <1	5/2	13735.298	3/2	30706.200
5892.47	-	11/2	30968.412	11/2	14002.294
5892.87	-	13/2	31693.804	11/2	14728.846
5897.504	nl 8	11/2	11944.207	11/2	28895.833
5900.125	4	15/2	31887.920	17/2	14943.825
5901.932	18	5/2	29216.845	7/2	12277.935
5902.808	33	11/2	8829.063	13/2	25765.460
5903.75	-	11/2	28680.018	13/2	11746.328
5906.33	nl -	3/2	28067.892	5/2	11141.576
5908.75	nl -	9/2	15423.884	9/2	32343.24
5908.776	27	5/2	27573.343	7/2	10654.053
5910.190	14	15/2	28661.560	13/2	11746.328
5911.95	nl -	13/2	18016.597	15/2	34926.79
5912.451	45	9/2	25744.156	11/2	8835.383
5912.93	nl -	13/2	14470.042	13/2	31377.435
5913.605	nl 2	9/2	12746.067	7/2	29651.540
5913.967	35	15/2	14221.272	17/2	31125.712
5913.97	nl -	19/2	34580.89	17/2	17676.472
5915.451	nl 12	13/2	30896.129	13/2	13995.931
5916.17	-	5/2	28890.950	3/2	11992.788
5916.448	22	15/2	28661.560	17/2	11764.216
5916.78	nl -	13/2	16069.885	13/2	32966.30
5923.35	nl -	3/2	28986.540	5/2	12108.867
5927.775	17	13/2	7951.323	11/2	24816.383

λ_air (Å)	SNR	Even Levels		Odd Levels	
		J	Energy (cm⁻¹)	J	Energy (cm⁻¹)
5933.025	42	13/2	27519.089	15/2	10668.95
5935.81	nl -	7/2	13867.177	7/2	30709.41
5935.823	22	3/2	27983.773	5/2	11141.576
5936.052	nl 50	5/2	6451.808	7/2	23293.356
5938.674	nl 8	9/2	31368.505	9/2	14534.393
5938.992	11	5/2	30454.610	7/2	13621.400
5939.05	nl -	11/2	16316.469	11/2	33149.53
5939.17	nl -	7/2	12617.701	7/2	29450.41
5939.23	nl -	7/2	11274.229	5/2	28106.771
5940.46	nl -	7/2	31664.74	5/2	14835.699
5941.95	nl -	15/2	16650.602	17/2	33475.43
5943.69	nl -	9/2	27251.615	11/2	10431.716
5944.20	nl -	15/2	14579.390	17/2	31397.849
5944.622	132	7/2	8013.089	9/2	24830.361
5949.52	-	5/2	12646.996	7/2	29450.41
5952.38	nl -	11/2	15111.485	13/2	31906.825
5955.302	120	9/2	8029.275	11/2	24816.383
5958.01	nl -	9/2	14897.721	11/2	31677.187
5960.368	nl 6	9/2	12746.067	9/2	29518.913
5960.932	110	7/2	7617.440	5/2	24388.693
5961.21	nl -	15/2	17907.816	15/2	34678.30
5961.87	nl -	13/2	18016.597	15/2	34785.20
5962.36	nl -	9/2	13605.667	9/2	30372.918
5962.563	14	11/2	9268.726	9/2	26035.395
5964.78	-	9/2	11184.396	11/2	27944.838
5964.905	17	15/2	31270.29	13/2	14510.22
5965.723	11	7/2	6535.572	7/2	23293.356
5966.37	nl -	11/2	10904.034	9/2	27659.987
5966.89	nl -	11/2	28485.173	9/2	11730.668
5969.39	nl -	7/2	11472.410	5/2	28219.904
5971.282	4	11/2	30968.412	11/2	14226.210
5975.56	-	13/2	32384.45	13/2	15654.235
5976.692	nl 55	13/2	30953.27	11/2	14226.210
5980.927	nl 10	17/2	31055.361	17/2	14340.175
5984.12	-	9/2	8643.824	7/2	25350.082
5984.527	nl 4	9/2	29624.447	7/2	12919.316

λ_air (Å)	SNR	Even Levels		Odd Levels	
		J	Energy (cm⁻¹)	J	Energy (cm⁻¹)
5984.74	-	11/2	13872.266	9/2	30576.811
5985.273	10	9/2	12651.589	11/2	29354.638
5985.973	nl 27	15/2	12250.519	17/2	28951.616
5987.19	nl -	11/2	11282.865	9/2	27980.556
5987.94	nl -	7/2	31531.30	5/2	14835.699
5990.391	11	9/2	8320.240	11/2	25009.019
5991.595	120	15/2	9745.376	15/2	26430.800
5994.217	30	15/2	8765.541	13/2	25443.665
5996.449	28	13/2	27340.868	15/2	10668.95
5998.147	20	15/2	12804.468	17/2	29471.666
5999.16	nl -	7/2	29583.69	7/2	12919.316
6003.473	14	5/2	28055.421	7/2	11403.011
6004.40	-	11/2	16316.469	13/2	32966.30
6006.28	-	9/2	28375.291	9/2	11730.668
6006.76	nl -	1/2	10956.651	1/2	27599.95
6006.89	nl -	11/2	30645.242	11/2	14002.294
6007.065	9	11/2	26222.282	9/2	9579.832
6009.385	nl 6	9/2	28840.315	11/2	12204.285
6011.536	58	11/2	28680.018	9/2	12049.940
6011.96	-	13/2	13654.555	15/2	30283.462
6015.666	21	13/2	28840.756	13/2	12222.095
6015.84	-	17/2	17855.428	19/2	34473.61
6017.51	-	13/2	12118.039	13/2	28731.611
6019.90	nl -	17/2	29552.460	19/2	12945.474
6020.478	nl 25	13/2	28351.711	13/2	11746.328
6023.313	110	9/2	27251.615	7/2	10654.053
6023.98	nl -	13/2	12118.054	11/2	28713.780
6024.08	nl -	11/2	14800.680	11/2	31396.143
6025.00	nl -	13/2	33015.19	11/2	16422.282
6025.11	nl -	11/2	13727.482	11/2	30320.091
6025.531	19	9/2	27913.895	11/2	11322.443
6026.379	70	13/2	27020.835	11/2	10431.716
6029.61	nl -	1/2	14679.85	3/2	31260.067
6039.18	nl -	5/2	10829.070	3/2	27383.021
6039.87	nl -	9/2	14897.721	11/2	31449.773
6040.218	10	7/2	11668.794	5/2	28219.904

λ_air (Å)	SNR	Even Levels		Odd Levels	
		J	Energy (cm⁻¹)	J	Energy (cm⁻¹)
6041.03	nl -	11/2	31083.29	9/2	14534.393
6041.031	nl 38	19/2	34225.35	17/2	17676.472
6044.092	9	15/2	31887.920	13/2	15347.425
6044.55	nl -	13/2	31049.456	13/2	14510.22
6044.970	43	11/2	26222.282	13/2	9684.184
6045.14	nl -	7/2	27679.200	5/2	11141.576
6045.80	nl -	3/2	11361.762	5/2	27897.591
6050.701	25	11/2	25357.817	11/2	8835.383
6050.73	-	7/2	31593.97	9/2	15071.618
6050.93	nl -	13/2	32726.84	13/2	16205.044
6051.767	13	11/2	31591.140	9/2	15071.618
6052.04	nl -	1/2	13852.32	3/2	30371.08
6052.099	11	15/2	31536.710	13/2	15018.088
6054.64	-	13/2	31333.26	11/2	14821.565
6054.777	16	9/2	29865.350	9/2	13354.046
6060.343	44	9/2	8320.240	11/2	24816.383
6063.021	nl 10	15/2	31887.920	15/2	15399.063
6063.298	14	15/2	28252.321	17/2	11764.216
6066.498	nl 5	17/2	33264.21	15/2	16784.800
6069.198	19	7/2	8013.089	9/2	24485.172
6070.12	nl -	7/2	27123.623	7/2	10654.053
6071.44	nl -	7/2	31079.962	7/2	14613.96
6074.09	nl -	1/2	11864.887	3/2	28323.695
6075.244	134	9/2	27109.741	7/2	10654.053
6075.756	nl 7	5/2	8737.556	5/2	25191.854
6076.770	nl 26	9/2	29370.862	7/2	12919.316
6077.508	nl 25	15/2	30959.764	13/2	14510.22
6078.089	9	13/2	30013.473	15/2	13565.490
6078.823	nl 12	11/2	29323.690	11/2	12877.682
6079.050	nl 12	5/2	30454.610	7/2	14009.225
6079.576	80	15/2	12250.519	17/2	28694.480
6082.804	32	11/2	28485.173	9/2	12049.940
6084.088	13	5/2	27573.343	5/2	11141.576
6086.89	nl -	9/2	17534.157	9/2	33958.36
6094.05	nl -	17/2	18380.302	15/2	34785.20
6096.18	-	17/2	33264.21	15/2	16865.034

λ_air (Å)	SNR	Even Levels		Odd Levels	
		J	Energy (cm⁻¹)	J	Energy (cm⁻¹)
6099.995	9	7/2	29308.235	7/2	12919.316
6101.124	nl 6	7/2	30920.300	9/2	14534.393
6111.26	nl -	3/2	14420.00	3/2	30778.71
6111.89	nl -	5/2	15720.838	7/2	32077.74
6111.977	64	9/2	24606.934	9/2	8250.143
6120.065	nl 9	11/2	30869.567	9/2	14534.393
6121.76	-	7/2	9704.744	9/2	26035.395
6121.87	nl <1	5/2	13670.175	3/2	30000.532
6121.88	nl <1	5/2	13670.175	5/2	30000.493
6121.994	32	5/2	27471.606	5/2	11141.576
6123.177	nl 9	15/2	12250.519	15/2	28577.388
6123.31	nl -	5/2	12907.057	7/2	29233.565
6123.70	-	9/2	31721.60	9/2	15396.135
6123.771	nl 19	7/2	28375.220	9/2	12049.940
6124.242	7	15/2	34000.50	17/2	17676.472
6124.573	nl 3	5/2	31158.848	5/2	14835.699
6125.364	10	17/2	33997.515	17/2	17676.472
6125.763	16	7/2	29674.025	9/2	13354.046
6126.862	27	7/2	7617.440	9/2	23934.491
6132.350	nl 5	9/2	29123.494	9/2	12821.043
6134.198	4	5/2	29216.845	7/2	12919.316
6135.45	nl -	1/2	13055.995	3/2	29350.190
6138.608	24	17/2	31055.361	15/2	14769.532
6139.106	nl 20	15/2	29620.381	13/2	13335.870
6140.074	100	11/2	9483.518	13/2	25765.460
6145.11	nl -	7/2	31664.74	9/2	15396.135
6145.299	nl 8	7/2	27998.766	9/2	11730.668
6146.447	25	13/2	19111.800	13/2	2846.741
6147.798	8	7/2	28311.416	9/2	12049.940
6150.34	nl -	17/2	14028.707	15/2	30283.462
6150.557	78	15/2	24987.630	13/2	8733.44
6151.543	nl 4	17/2	33264.21	15/2	17012.626
6165.82	nl -	5/2	12078.621	5/2	28292.560
6170.063	12	17/2	33997.515	15/2	17794.708
6170.56	nl -	5/2	13964.855	3/2	30166.356
6171.956	nl 6	7/2	31593.97	9/2	15396.135

λ_air (Å)	SNR	Even Levels		Odd Levels	
		J	Energy (cm⁻¹)	J	Energy (cm⁻¹)
6172.411	48	13/2	27519.089	11/2	11322.443
6177.590	130	7/2	8013.089	9/2	24196.152
6181.40	nl -	9/2	27109.741	9/2	10936.650
6184.761	22	13/2	10266.501	15/2	26430.800
6185.298	30	13/2	29523.411	11/2	13360.502
6186.936	nl 6	15/2	27904.945	13/2	11746.328
6191.330	70	15/2	12804.468	17/2	28951.616
6193.275	23	11/2	27888.407	13/2	11746.328
6193.34	nl -	11/2	13376.992	9/2	29518.913
6193.79	nl -	11/2	30869.567	11/2	14728.846
6193.94	nl -	17/2	32925.14	15/2	16784.800
6195.54	-	13/2	31535.09	15/2	15398.916
6195.93	nl -	7/2	31531.30	9/2	15396.135
6195.97	nl -	11/2	15469.547	9/2	31604.603
6197.13	nl -	15/2	33808.50	17/2	17676.472
6208.778	14	17/2	33114.40	15/2	17012.626
6208.876	5	11/2	28323.602	13/2	12222.095
6216.99	nl <1	5/2	13670.175	3/2	29750.67
6219.288	35	13/2	30896.129	11/2	14821.565
6224.08	nl -	9/2	12651.589	11/2	28713.780
6230.842	nl 13	7/2	28865.800	9/2	12821.043
6237.24	nl <1	7/2	11869.290	5/2	27897.591
6248.203	nl 70	5/2	6451.808	7/2	22451.973
6252.560	9	13/2	24722.464	13/2	8733.440
6252.773	82	7/2	6535.572	9/2	22524.055
6253.032	nl 11	11/2	29323.690	13/2	13335.870
6253.81	nl -	13/2	31333.26	13/2	15347.425
6255.292	nl 21	7/2	27123.623	5/2	11141.576
6255.68	nl -	17/2	17494.383	17/2	33475.43
6255.842	50	19/2	15845.280	21/2	31825.917
6256.568	30	7/2	27381.794	7/2	11403.011
6259.369	7	5/2	28890.950	7/2	12919.316
6262.729	23	13/2	28840.756	11/2	12877.682
6262.898	11	9/2	28840.315	11/2	12877.67
6264.314	10	3/2	28067.892	5/2	12108.867
6264.75	-	13/2	29523.411	15/2	13565.490

λ_air (Å)	SNR	Even Levels		Odd Levels	
		J	Energy (cm⁻¹)	J	Energy (cm⁻¹)
6266.756	14	13/2	30722.337	15/2	14769.532
6269.24	nl -	7/2	28865.800	7/2	12919.316
6272.728	nl 5	5/2	8737.556	5/2	24675.173
6297.43	nl -	11/2	31222.52	13/2	15347.425
6297.509	nl 10	3/2	27983.773	5/2	12108.867
6298.229	9	11/2	13250.662	13/2	29123.747
6304.38	nl -	19/2	33534.065	17/2	17676.472
6319.40	nl <1	9/2	12746.067	7/2	28565.989
6327.579	nl 30	9/2	26231.182	11/2	10431.716
6328.71	nl -	5/2	16281.125	7/2	32077.74
6334.990	33	15/2	26191.727	13/2	10410.745
6336.190	19	11/2	25357.817	9/2	9579.832
6339.981	18	15/2	30959.764	13/2	15191.218
6340.26	nl -	15/2	30959.764	13/2	15191.891
6340.33	nl -	15/2	30959.764	15/2	15192.075
6349.76	nl -	7/2	11869.290	5/2	27613.57
6352.081	nl 3	3/2	14206.294	3/2	29944.814
6353.48	nl -	1/2	11864.887	1/2	27599.95
6368.318	nl 50	13/2	27020.835	11/2	11322.443
6381.792	12	15/2	14221.272	15/2	29886.515
6387.550	6	7/2	27381.794	9/2	11730.668
6391.111	nl 4	3/2	12464.369	5/2	28106.771
6399.23	nl -	3/2	12701.121	3/2	28323.695
6399.395	15	9/2	29624.447	11/2	14002.294
6408.919	36	9/2	8029.275	7/2	23628.220
6409.279	12	9/2	29600.360	11/2	14002.294
6410.40	nl -	11/2	15904.915	9/2	31500.25
6411.85	nl -	9/2	12068.17	9/2	27659.987
6413.793	25	13/2	10266.501	15/2	25853.590
6419.14	nl -	5/2	15328.721	5/2	30902.82
6419.18	-	11/2	23654.406	11/2	8080.404
6423.26	nl -	9/2	11184.396	9/2	26748.510
6423.831	-	11/2	29565.016	11/2	14002.294
6429.72	nl <1	3/2	12051.488	1/2	27599.95
6432.445	nl 10	3/2	9649.970	5/2	25191.854
6439.24	-	11/2	9483.518	11/2	25009.019

λ_air (Å)	SNR	Even Levels		Odd Levels	
		J	Energy (cm^{-1})	J	Energy (cm^{-1})
6439.79	nl -	7/2	30920.300	9/2	15396.135
6440.004	nl 28	5/2	6451.808	7/2	21975.458
6440.366	54	15/2	26191.727	15/2	10668.95
6444.941	25	7/2	28865.800	9/2	13354.046
6453.838	19	7/2	28311.416	9/2	12821.043
6458.064	20	13/2	28840.756	11/2	13360.502
6458.45	nl -	7/2	14249.395	7/2	29728.713
6458.657	9	5/2	27471.606	3/2	11992.788
6465.07	nl -	9/2	17125.257	11/2	32588.71
6478.297	15	7/2	9918.190	7/2	25350.082
6489.916	80	11/2	23654.406	9/2	8250.143
6489.97	nl -	13/2	27626.232	13/2	12222.095
6500.543	7	9/2	27109.741	9/2	11730.668
6502.304	6	13/2	30722.337	13/2	15347.425
6502.639	nl 10	9/2	29600.360	11/2	14226.210
6504.25	nl -	9/2	12519.707	7/2	27890.013
6516.764	36	15/2	24987.630	15/2	9646.83
6528.545	11	13/2	28315.140	15/2	13002.023
6531.40	<1	15/2	15819.276	17/2	31125.712
6536.97	nl -	9/2	13272.613	7/2	28565.989
6537.026	nl 4	9/2	12651.589	11/2	27944.838
6537.250	nl 4	11/2	13035.697	9/2	28328.419
6537.74	nl -	7/2	12321.991	5/2	27613.57
6544.17	-	13/2	10470.329	11/2	25746.884
6545.725	nl 8	7/2	27381.794	5/2	12108.867
6547.53	nl -	5/2	13964.855	7/2	29233.565
6550.292	nl 5	7/2	15110.642	9/2	30372.918
6551.97	nl -	7/2	30654.508	9/2	15396.135
6565.889	nl 8	15/2	28791.510	15/2	13565.490
6570.02	nl -	11/2	9268.726	9/2	24485.172
6586.785	8	7/2	27998.766	9/2	12821.043
6597.21	nl -	11/2	14981.500	13/2	30135.234
6616.235	nl 10	15/2	29620.381	15/2	14510.22
6625.04	nl -	15/2	31270.29	15/2	16180.200
6630.474	11	9/2	27282.000	11/2	12204.285
6640.565	nl 4	11/2	29565.016	13/2	14510.22

λ_air (Å)	SNR	Even Levels		Odd Levels	
		J	Energy (cm⁻¹)	J	Energy (cm⁻¹)
6640.853	8	19/2	27999.623	19/2	12945.474
6646.533	10	19/2	33534.065	17/2	18492.78
6666.715		7/2	8013.089	9/2	23008.838
6673.919	41	9/2	8029.275	9/2	23008.838
6674.05	nl -	13/2	28315.140	13/2	13335.870
6680.601	5	5/2	9710.600	5/2	24675.173
6697.824	40	11/2	25357.817	11/2	10431.716
6705.023	nl 10	9/2	26231.182	11/2	11322.443
6706.579	21	7/2	7617.440	9/2	22524.055
6719.285	10	5/2	11107.696	3/2	25986.120
6732.167	19	7/2	8013.089	5/2	22863.048
6747.350	35	13/2	27020.835	11/2	12204.285
6761.49	nl -	11/2	31332.402	11/2	16546.840
6792.357	nl 17	7/2	26121.378	7/2	11403.011
6809.044	nl 7	9/2	28042.800	11/2	13360.502
6810.994	18	5/2	9710.600	5/2	24388.693
6836.09	nl -	13/2	27626.232	15/2	13002.023
6854.190	13	3/2	11361.762	3/2	25947.350
6871.86	nl -	9/2	13432.468	9/2	27980.556
6888.745	28	13/2	22592.830	11/2	8080.404
6961.32	nl	15/2	18548.497	13/2	32909.62
6967.185	nl 7	11/2	6714.184	9/2	21063.222
6976.646	90	21/2	12665.074	21/2	26994.656
6992.918	nl 28	13/2	7630.132	11/2	21926.369
6997.854	22	11/2	23865.975	9/2	9579.832
7005.999	nl 6	15/2	29287.637	13/2	15018.088
7007.878	6	13/2	27626.232	11/2	13360.502
7016.088	nl 8	7/2	10194.768	7/2	24443.790
7016.879	4	3/2	13206.325	1/2	27453.746
7022.178	55	7/2	22486.816	9/2	8250.143
7033.518	20	11/2	8829.063	11/2	23042.780
7045.286	nl 10	9/2	5822.890	7/2	20012.862
7049.349	nl 6	11/2	23865.975	13/2	9684.184
7052.620	nl 7	9/2	24606.934	11/2	10431.716
7055.071	15	11/2	6892.934	9/2	21063.222
7059.060	76	9/2	22996.562	11/2	8835.383

λ_air (Å)	SNR	Even Levels		Odd Levels	
		J	Energy (cm⁻¹)	J	Energy (cm⁻¹)
7059.326	24	21/2	12664.774	19/2	26826.517
7092.051	nl -	15/2	29287.637	13/2	15191.218
7092.470	nl -	15/2	29287.637	15/2	15192.075
7143.366	nl 8	5/2	27251.230	5/2	13256.082
7145.88	nl -	9/2	22825.611	11/2	8835.383
7145.96	nl -	7/2	11869.290	5/2	25859.364
7153.27	nl -	7/2	27231.854	5/2	13256.082
7154.439	nl 7	5/2	22959.928	3/2	8986.443
7186.228	nl 8	7/2	28822.147	9/2	14910.476
7217.149	nl 4	7/2	27231.854	9/2	13379.788
7219.86	nl <1	15/2	17907.816	13/2	31754.678
7264.132	nl 5	11/2	13376.992	13/2	27139.468
7269.896	nl 45	9/2	8643.824	9/2	22395.393
7270.444	14	7/2	28822.147	9/2	15071.618
7289.586	nl 5	5/2	8737.556	7/2	22451.973
7318.925	24	19/2	27999.623	17/2	14340.175
7326.027	nl 9	11/2	26467.248	9/2	12821.043
7326.637	nl 4	15/2	14579.390	17/2	28224.462
7334.830	10	5/2	27251.230	7/2	13621.400
7359.74	nl <1	11/2	26937.739	9/2	13354.046
7360.88	nl 3	15/2	30577.00	17/2	16995.410
7362.643	nl 22	13/2	9464.440	11/2	23042.780
7363.24	nl <1	11/2	26937.739	11/2	13360.502
7366.87	nl -	9/2	29682.09	7/2	16111.549
7369.16	nl -	11/2	8829.063	9/2	22395.393
7412.60	nl -	13/2	29909.117	11/2	16422.282
7413.66	nl -	13/2	13654.555	13/2	27139.468
7415.509	nl 4	21/2	32243.14	19/2	18761.608
7418.838	nl 7	11/2	14505.065	9/2	27980.556
7422.950	nl 3	13/2	17851.395	11/2	31319.42
7435.22	nl -	7/2	7617.440	9/2	21063.222
7442.26	nl -	11/2	13376.992	13/2	26810.061
7467.49	nl -	7/2	29499.235	7/2	16111.549
7469.521	nl 3	9/2	14468.303	7/2	27852.358
7478.673	52	19/2	13626.687	21/2	26994.361
7490.283	6	9/2	9105.020	7/2	22451.973

λ_{air} (Å)	SNR	Even Levels		Odd Levels	
		J	Energy (cm⁻¹)	J	Energy (cm⁻¹)
7491.60	nl -	5/2	15006.728	5/2	28351.325
7496.383	nl 6	5/2	11107.696	7/2	24443.790
7520.75	nl -	13/2	27519.089	11/2	14226.210
7524.748	nl 3	17/2	15665.829	17/2	28951.616
7535.314	nl 4	11/2	13872.266	13/2	27139.468
7546.55	nl -	3/2	14206.294	1/2	27453.746
7573.761	78	19/2	13626.672	19/2	26826.517

Table 7.6: Lines classified via laser-induced fluorescence

λ_{air} (Å)	SNR	Even Levels		Odd Levels	
		J	Energy (cm⁻¹)	J	Energy (cm⁻¹)
3170.53	nl -	7/2	31531.30	9/2	0.000
3216.23	nl <1	11/2	31083.29	9/2	0.000
3303.219	nl 3	11/2	31641.39	11/2	1376.602
3316.437	nl 4	9/2	30144.181	9/2	0.000
3337.29	-	11/2	31332.402	11/2	1376.602
3365.279	nl 8	11/2	31083.29	11/2	1376.602
3375.19	nl -	15/2	34000.50	15/2	4381.072
3375.533	nl 7	17/2	33997.515	15/2	4381.072
3378.343	nl 3	11/2	30968.412	11/2	1376.602
3385.86	<1	9/2	4432.225	9/2	33958.36
3397.51	nl <1	9/2	4432.225	11/2	33857.14
3403.758	nl 6	9/2	29370.862	9/2	0.000
3409.235	nl 7	11/2	29323.690	9/2	0.000
3432.67	nl <1	9/2	29123.494	9/2	0.000
3436.40	nl <1	11/2	4866.515	9/2	33958.36
3442.400	nl 15	15/2	31887.920	13/2	2846.741
3461.236	nl 12	17/2	33264.21	15/2	4381.072
3479.283	nl 17	17/2	33114.40	15/2	4381.072
3484.54	nl <1	15/2	31536.710	13/2	2846.741
3493.47	nl <1	11/2	29993.26	11/2	1376.602
3550.57	nl <1	9/2	4432.225	11/2	32588.71
3553.22	nl -	9/2	5822.890	9/2	33958.36
3571.141	nl 3	9/2	29370.862	11/2	1376.602
3606.189	nl 5	11/2	4866.515	11/2	32588.71
3616.19	nl <1	9/2	4432.225	7/2	32077.74
3616.242	nl 7	11/2	6313.224	9/2	33958.36
3629.53	nl <1	11/2	6313.224	11/2	33857.14
3634.422	nl 8	15/2	31887.920	15/2	4381.072
3669.358	nl 9	9/2	4432.225	11/2	31677.187
3685.774	nl 3	7/2	27123.623	9/2	0.000
3687.661	nl 14	9/2	27109.741	9/2	0.000
3687.821	nl 6	11/2	28485.173	11/2	1376.602
3693.34	nl -	9/2	4432.225	9/2	31500.25
3693.703	nl 4	11/2	6892.934	9/2	33958.36
3700.245	nl 8	9/2	4432.225	11/2	31449.773

λ_air (Å)	SNR	Even Levels		Odd Levels	
		J	Energy (cm⁻¹)	J	Energy (cm⁻¹)
3706.02	nl -	13/2	7951.323	15/2	34926.79
3707.605	9	9/2	4432.225	11/2	31396.143
3711.208	nl 30	11/2	26937.739	9/2	0.000
3718.18	nl -	9/2	4432.225	11/2	31319.42
3738.920	nl 4	11/2	4866.515	9/2	31604.603
3740.47	nl <1	13/2	7951.323	15/2	34678.30
3760.70	nl <1	11/2	4866.515	11/2	31449.773
3765.98	-	13/2	6603.591	11/2	33149.53
3767.21	<1	9/2	27913.895	11/2	1376.602
3770.83	nl <1	11/2	27888.407	11/2	1376.602
3779.23	nl <1	11/2	4866.515	11/2	31319.42
3780.946	nl 8	15/2	29287.637	13/2	2846.741
3783.75	nl -	15/2	8363.901	15/2	34785.20
3795.30	nl -	7/2	7617.440	9/2	33958.36
3798.53	nl <1	11/2	6313.224	9/2	32631.71
3825.571	nl <1	9/2	5822.890	9/2	31955.363
3833.263	nl 14	13/2	7951.323	15/2	34031.358
3842.16	nl -	15/2	8765.541	15/2	34785.20
3847.26	nl <1	13/2	6603.591	11/2	32588.71
3860.003	nl 31	13/2	6603.591	15/2	32502.962
3861.719	nl 5	9/2	4432.225	11/2	30320.091
3866.580	nl 8	11/2	25855.320	9/2	0.000
3866.73	nl <1	9/2	5822.890	11/2	31677.187
3868.71	nl <1	13/2	6603.591	11/2	32444.655
3870.69	nl -	9/2	8029.275	11/2	33857.14
3872.646	nl 17	15/2	28661.560	13/2	2846.741
3883.276	nl 10	9/2	25744.156	9/2	0.000
3893.38	nl -	9/2	5822.890	9/2	31500.25
3894.88	<1	15/2	8363.901	15/2	34031.358
3901.045	nl 4	9/2	5822.890	11/2	31449.773
3901.192	nl 4	5/2	6451.808	7/2	32077.74
3909.228	nl 7	9/2	5822.890	11/2	31396.143
3927.61	nl <1	11/2	4866.515	11/2	30320.091
3932.829	nl 5	7/2	6535.572	9/2	31955.363
3934.071	nl 3	9/2	5822.890	9/2	31234.656
3935.029	nl 8	15/2	28252.321	13/2	2846.741

λ_{air} (Å)	SNR	Even Levels		Odd Levels	
		J	Energy (cm⁻¹)	J	Energy (cm⁻¹)
3941.486	nl 3	11/2	6313.224	11/2	31677.187
3942.441	nl 8	11/2	25357.817	9/2	0.000
3949.18	nl <1	9/2	8643.824	9/2	33958.36
3971.64	nl -	17/2	29552.460	15/2	4381.072
3973.715	nl 5	7/2	6535.572	9/2	31693.821
3984.422	nl 7	11/2	26467.248	11/2	1376.602
3985.645	nl 6	11/2	6313.224	11/2	31396.143
3992.51	nl -	15/2	9745.376	15/2	34785.20
3995.96	nl -	9/2	4432.225	7/2	29450.41
3996.558	nl 6	7/2	7617.440	9/2	32631.71
4011.32	nl <1	9/2	4432.225	11/2	29354.638
4019.314	nl 4	13/2	7630.132	15/2	32502.962
4023.706	nl 13	11/2	26222.282	11/2	1376.602
4028.52	nl <1	11/2	6313.224	11/2	31129.206
4029.78	nl -	5/2	6451.808	3/2	31260.067
4032.33	nl <1	13/2	6603.591	11/2	31396.143
4033.38	nl -	11/2	6714.184	9/2	31500.25
4041.62	nl <1	11/2	6714.184	11/2	31449.773
4044.85	nl -	13/2	6603.591	11/2	31319.42
4062.510	nl 8	9/2	4432.225	9/2	29040.590
4070.606	nl 3	9/2	8029.275	11/2	32588.71
4077.072	nl 3	11/2	6714.184	9/2	31234.656
4085.89	nl -	5/2	8737.556	5/2	33205.09
4086.550	nl 8	9/2	4432.225	11/2	28895.833
4108.97	nl <1	7/2	8013.089	9/2	32343.24
4109.52	nl <1	5/2	6451.808	3/2	30778.71
4121.256	nl 9	5/2	6451.808	7/2	30709.41
4121.76	nl <1	13/2	10423.654	15/2	34678.30
4142.404	nl 47	9/2	4432.225	7/2	28565.989
4152.277	nl 16	7/2	7617.440	9/2	31693.821
4168.755	nl 11	11/2	25357.817	11/2	1376.602
4178.361	nl 4	9/2	8029.275	9/2	31955.363
4192.172	nl 5	11/2	4866.515	11/2	28713.780
4193.916	nl 6	7/2	6535.572	9/2	30372.918
4212.55	nl <1	5/2	6451.808	7/2	30183.72
4212.878	nl 4	15/2	9745.376	17/2	33475.43

λ_air (Å)	SNR	Even Levels		Odd Levels	
		J	Energy (cm⁻¹)	J	Energy (cm⁻¹)
4215.287	nl 5	13/2	6603.591	11/2	30320.091
4218.32	nl <1	9/2	8643.824	9/2	32343.24
4218.928	nl 3	9/2	5822.890	9/2	29518.913
4231.161	nl 7	9/2	5822.890	7/2	29450.41
4245.390	nl 9	9/2	4432.225	9/2	27980.556
4249.803	nl 5	15/2	27904.945	15/2	4381.072
4254.06	nl -	7/2	9704.744	5/2	33205.09
4254.40	nl -	13/2	7951.323	11/2	31449.773
4257.08	nl <1	9/2	9105.020	11/2	32588.71
4261.78	nl -	9/2	4432.225	7/2	27890.013
4268.629	nl 12	9/2	4432.225	7/2	27852.358
4276.771	nl 8	11/2	26222.282	13/2	2846.741
4282.37	nl -	15/2	26191.727	13/2	2846.741
4294.895	nl 3	5/2	6451.808	7/2	29728.713
4295.234	nl 2	5/2	6451.808	5/2	29726.88
4303.506	nl 41	9/2	24606.934	11/2	1376.602
4303.982	nl 11	9/2	4432.225	9/2	27659.987
4305.85	nl -	9/2	5822.890	9/2	29040.590
4310.407	nl 10	7/2	6535.572	7/2	29728.713
4313.24	nl <1	13/2	7951.323	11/2	31129.206
4332.862	nl 10	9/2	5822.890	11/2	28895.833
4346.871	nl 3	5/2	6451.808	7/2	29450.41
4351.77	nl -	9/2	9105.020	7/2	32077.74
4353.961	nl 6	11/2	9483.518	11/2	32444.655
4355.54	nl <1	5/2	6451.808	5/2	29404.602
4355.961	nl 2	7/2	7617.440	5/2	30568.035
4358.920	nl 5	9/2	5822.890	7/2	28757.902
4364.49	nl -	9/2	9105.020	7/2	32010.763
4379.813	nl 5	9/2	22825.611	9/2	0.000
4385.986	nl 11	11/2	4866.515	9/2	27659.987
4386.78	nl -	9/2	8029.275	7/2	30818.62
4388.244	nl 7	5/2	6451.808	7/2	29233.565
4390.582	nl 7	11/2	9675.029	11/2	32444.655
4392.09	nl -	15/2	8363.901	17/2	31125.712
4395.703	nl 10	9/2	5822.890	7/2	28565.989
4406.00	nl -	13/2	7630.132	11/2	30320.091

λ_air (Å)	SNR	Even Levels		Odd Levels	
		J	Energy (cm⁻¹)	J	Energy (cm⁻¹)
4408.09	nl <1	13/2	10470.329	11/2	33149.53
4410.22	nl -	11/2	9675.029	9/2	32343.24
4410.27	nl -	9/2	32247.808	9/2	9579.832
4415.63	nl <1	11/2	6714.184	11/2	29354.638
4426.94	-	11/2	6313.224	11/2	28895.833
4438.76	nl <1	5/2	8737.556	3/2	31260.067
4445.297	nl 45	11/2	23865.973	11/2	1376.602
4445.802	nl 9	7/2	22486.816	9/2	0.000
4448.76	nl -	11/2	9483.518	9/2	31955.363
4450.77	nl <1	11/2	6892.934	11/2	29354.638
4459.79	nl <1	9/2	4432.225	11/2	26848.512
4462.92	nl -	11/2	6313.224	11/2	28713.780
4469.265	nl 5	13/2	7951.323	11/2	30320.091
4484.89	nl -	9/2	8029.275	11/2	30320.091
4493.00	nl <1	7/2	9704.744	9/2	31955.363
4496.855	nl <1	11/2	9268.726	9/2	31500.25
4504.526	nl 6	11/2	9483.518	11/2	31677.187
4506.740	nl 7	15/2	8363.901	17/2	30546.666
4506.97	nl -	11/2	6714.184	11/2	28895.833
4507.09	nl <1	11/2	9268.726	11/2	31449.773
4510.34	nl <1	13/2	10423.654	11/2	32588.71
4511.84	nl -	9/2	5822.890	9/2	27980.556
4513.72	nl <1	7/2	10194.768	9/2	32343.24
4513.884	nl 5	11/2	6892.934	9/2	29040.590
4514.414	nl 4	13/2	7630.132	11/2	29775.190
4515.26	nl -	15/2	24987.630	13/2	2846.741
4517.560	nl 6	9/2	9105.020	9/2	31234.656
4519.130	nl 18	9/2	5822.890	11/2	27944.838
4520.717	nl 5	5/2	6451.808	7/2	28565.989
4521.53	nl <1	13/2	6603.591	11/2	28713.780
4529.40	nl <1	7/2	31817.13	5/2	9745.334
4530.358	nl 8	9/2	5822.890	7/2	27890.013
4531.50	nl -	11/2	31641.39	9/2	9579.832
4539.19	nl <1	9/2	9105.020	11/2	31129.206
4541.044	nl 52	11/2	6313.224	9/2	28328.419
4544.26	nl <1	11/2	6714.184	11/2	28713.780

λ_air (Å)	SNR	Even Levels		Odd Levels	
		J	Energy (cm⁻¹)	J	Energy (cm⁻¹)
4547.902	nl 2	11/2	4866.515	11/2	26848.512
4549.60	nl <1	13/2	6603.591	15/2	28577.388
4550.174	nl 5	17/2	10531.951	15/2	32502.962
4551.16	nl -	11/2	9483.518	11/2	31449.773
4557.607	nl 4	13/2	7951.323	15/2	29886.515
4562.24	nl <1	11/2	11944.207	11/2	33857.14
4565.031	nl 10	5/2	6451.808	5/2	28351.325
4566.98	nl <1	9/2	12068.17	9/2	33958.36
4567.76	nl <1	3/2	11361.762	3/2	33248.19
4568.687	nl 9	11/2	4866.515	9/2	26748.510
4570.798	nl 24	5/2	6451.808	3/2	28323.695
4573.18	nl <1	11/2	9268.726	11/2	31129.206
4575.66	nl <1	7/2	31593.97	5/2	9745.334
4581.49	nl -	11/2	6892.949	11/2	28713.780
4587.91	nl -	11/2	10841.417	9/2	32631.71
4588.26	nl <1	9/2	31368.505	9/2	9579.832
4588.573	nl 4	7/2	7617.440	5/2	29404.602
4589.845	nl 8	15/2	8765.541	17/2	30546.666
4594.939	nl 3	7/2	6535.572	5/2	28292.560
4595.870	9	11/2	31332.402	9/2	9579.832
4604.226	nl 5	7/2	31292.93	9/2	9579.832
4610.26	nl <1	11/2	10904.034	11/2	32588.71
4611.89	nl <1	11/2	12180.13	11/2	33857.14
4617.116	nl 16	15/2	9745.376	17/2	31397.849
4618.56	nl <1	11/2	9483.518	11/2	31129.206
4618.84	nl -	11/2	9675.029	11/2	31319.42
4624.060	nl 94	9/2	22996.562	11/2	1376.602
4625.285	nl 11	11/2	6714.184	9/2	28328.419
4627.654	nl 19	9/2	4432.225	9/2	26035.395
4628.25	nl -	5/2	32050.34	7/2	10449.997
4649.833	4	7/2	31079.962	9/2	9579.832
4652.103	nl 3	9/2	8029.275	9/2	29518.913
4655.97	nl -	9/2	9105.020	9/2	30576.811
4656.39	nl -	9/2	5822.890	9/2	27292.757
4660.915	260	9/2	22825.611	11/2	1376.602
4661.53	nl <1	5/2	8737.556	7/2	30183.72

λ_{air} (Å)	SNR	Even Levels		Odd Levels	
		J	Energy (cm^{-1})	J	Energy (cm^{-1})
4661.616	nl 6	5/2	6451.808	5/2	27897.591
4661.788	nl 3	7/2	6535.572	9/2	27980.556
4663.26	nl <1	5/2	6451.808	7/2	27890.013
4668.641	8	5/2	31158.848	5/2	9745.334
4678.77	nl <1	7/2	31817.13	7/2	10449.997
4681.34	nl <1	17/2	9770.273	17/2	31125.712
4681.556	nl <1	7/2	6535.572	7/2	27890.013
4683.240	nl 22	11/2	6313.224	9/2	27659.987
4684.62	nl <1	7/2	30920.300	9/2	9579.832
4687.94	nl -	9/2	8029.275	11/2	29354.638
4690.294	60	9/2	4432.225	11/2	25746.884
4694.68	-	17/2	12736.621	15/2	34031.358
4700.61	nl -	9/2	9105.020	9/2	30372.918
4701.092	nl 1	13/2	7630.132	11/2	28895.833
4714.71	nl <1	9/2	8029.275	7/2	29233.565
4716.39	nl <1	3/2	12051.488	3/2	33248.19
4722.595	13	11/2	4866.515	9/2	26035.395
4725.07	nl <1	5/2	9710.600	5/2	30868.400
4740.17	nl -	9/2	10920.365	7/2	32010.763
4740.793	5	11/2	6892.934	9/2	27980.556
4745.18	nl <1	5/2	9710.600	3/2	30778.71
4747.86	nl <1	3/2	9649.970	3/2	30706.200
4754.66	nl -	13/2	10423.654	11/2	31449.773
4757.60	-	5/2	8737.556	3/2	29750.67
4758.01	nl -	9/2	8029.275	9/2	29040.590
4761.57	nl -	5/2	9710.600	3/2	30706.200
4762.579	nl 6	5/2	8737.556	7/2	29728.713
4773.186	4	13/2	7951.323	11/2	28895.833
4779.12	-	9/2	31368.505	7/2	10449.997
4779.144	40	7/2	32248.10	9/2	11329.696
4779.268	45	9/2	4432.225	7/2	25350.082
4781.251	nl 5	7/2	30654.508	5/2	9745.334
4783.79	nl <1	17/2	14028.707	15/2	34926.79
4787.849	8	11/2	4866.515	11/2	25746.884
4788.41	nl -	9/2	10356.737	9/2	31234.656
4788.97	nl <1	9/2	11713.236	11/2	32588.71

λ_{air} (Å)	SNR	Even Levels		Odd Levels	
		J	Energy (cm⁻¹)	J	Energy (cm⁻¹)
4789.75	nl <1	7/2	9704.744	9/2	30576.811
4791.017	10	9/2	8029.275	11/2	28895.833
4791.77	-	7/2	9704.744	5/2	30568.035
4796.448	10	7/2	31292.93	7/2	10449.997
4807.417	28	5/2	31245.375	7/2	10449.997
4815.039	4	13/2	7951.323	11/2	28713.780
4821.06	nl <1	7/2	11274.229	7/2	32010.763
4822.90	nl -	9/2	8029.275	7/2	28757.902
4824.242	6	9/2	9105.020	7/2	29827.87
4825.58	nl <1	17/2	33997.515	17/2	13280.404
4826.57	-	5/2	8737.556	7/2	29450.41
4827.008	nl 10	7/2	7617.440	9/2	28328.419
4827.405	nl 8	5/2	30454.610	5/2	9745.334
4827.69	-	7/2	10194.768	5/2	30902.82
4827.78	nl <1	11/2	13250.69	9/2	33958.36
4828.27	nl <1	13/2	10423.654	11/2	31129.206
4835.54	nl -	7/2	11668.794	9/2	32343.24
4836.54	-	9/2	9105.020	11/2	29775.190
4838.81	nl <1	5/2	9710.600	3/2	30371.08
4842.55	nl -	11/2	11944.207	11/2	32588.71
4845.964	50	7/2	31079.962	7/2	10449.997
4846.879	10	13/2	7951.323	15/2	28577.388
4847.440	5	9/2	9105.020	7/2	29728.713
4851.468	30	15/2	24987.630	15/2	4381.072
4855.43	nl <1	9/2	8643.824	7/2	29233.565
4858.07	nl -	11/2	6714.184	9/2	27292.757
4861.43	nl -	9/2	30144.181	9/2	9579.832
4864.13	nl <1	7/2	8013.089	7/2	28565.989
4867.643	nl 8	15/2	9745.376	15/2	30283.462
4872.79	nl <1	3/2	9649.970	3/2	30166.356
4879.23	nl -	7/2	7617.440	5/2	28106.771
4879.68	nl -	7/2	31817.13	9/2	11329.696
4880.90	nl -	17/2	14302.875	15/2	34785.20
4883.68	nl -	13/2	12118.054	11/2	32588.71
4883.761	17	7/2	30920.300	7/2	10449.997
4886.50	nl <1	11/2	30869.567	13/2	10410.745

λ_air (Å)	SNR	Even Levels		Odd Levels	
		J	Energy (cm⁻¹)	J	Energy (cm⁻¹)
4887.23	nl <1	5/2	9710.600	3/2	30166.356
4891.56	nl <1	9/2	8320.240	7/2	28757.902
4899.21	nl <1	9/2	11549.602	9/2	31955.363
4900.82	nl -	11/2	11944.207	9/2	32343.24
4901.040	40	9/2	4432.225	9/2	24830.361
4902.212	6	11/2	10841.405	9/2	31234.656
4902.543	nl 3	9/2	31721.60	9/2	11329.714
4904.40	nl -	9/2	4432.225	11/2	24816.383
4909.13	nl -	9/2	11713.236	7/2	32077.74
4909.469	nl <1	7/2	7617.440	9/2	27980.556
4916.247	nl 3	7/2	31664.74	9/2	11329.696
4917.315	6	11/2	10904.034	9/2	31234.656
4917.38	nl <1	7/2	11274.229	9/2	31604.603
4918.29	nl -	13/2	12118.054	11/2	32444.655
4921.168	5	13/2	7630.132	11/2	27944.838
4922.13	nl <1	13/2	9464.440	11/2	29775.190
4927.177	8	5/2	9710.600	3/2	30000.532
4927.62	nl <1	9/2	29123.494	11/2	8835.383
4931.40	-	7/2	7617.440	7/2	27890.013
4936.297	15	15/2	12250.519	15/2	32502.962
4940.745	nl 4	5/2	9710.600	3/2	29944.814
4941.673	6	5/2	29216.845	3/2	8986.443
4946.052	22	9/2	5822.890	9/2	26035.395
4963.576	8	15/2	9745.376	15/2	29886.515
4965.254	8	11/2	6714.184	11/2	26848.512
4966.682	4	9/2	9105.020	7/2	29233.565
4970.255	15	9/2	8643.824	7/2	28757.902
4971.60	nl -	11/2	12234.616	9/2	32343.24
4975.300	nl 10	7/2	8013.089	5/2	28106.771
4977.226	16	11/2	9268.726	11/2	29354.638
4978.12	nl <1	7/2	9918.190	5/2	30000.493
4985.25	nl <1	13/2	10266.501	11/2	30320.091
4985.41	nl -	9/2	4432.225	9/2	24485.172
4987.48	nl -	9/2	29624.447	9/2	9579.832
4987.99	nl -	7/2	7617.440	9/2	27659.987
4988.16	-	3/2	13206.325	3/2	33248.19

λ_air (Å)	SNR	Even Levels		Odd Levels	
		J	Energy (cm⁻¹)	J	Energy (cm⁻¹)
4988.61	-	5/2	9710.600	3/2	29750.67
4988.93	nl <1	9/2	31368.505	9/2	11329.714
4990.040	14	11/2	6714.184	9/2	26748.510
4992.62	nl -	7/2	9704.744	7/2	29728.713
4993.08	nl <1	7/2	9704.744	5/2	29726.88
4993.48	nl -	9/2	29600.360	9/2	9579.832
4996.562	5	9/2	8320.240	9/2	28328.419
4997.54	nl <1	15/2	14780.94	15/2	34785.20
4997.87	nl -	13/2	13146.584	11/2	33149.53
4997.932	nl 4	11/2	31332.402	9/2	11329.696
4998.83	nl -	5/2	12078.621	7/2	32077.74
4999.573	nl 3	7/2	7617.440	5/2	27613.57
5002.311	55	11/2	29565.016	9/2	9579.832
5002.66	nl -	17/2	33264.21	17/2	13280.404
5005.04	nl -	19/2	11151.433	17/2	31125.712
5007.20	nl -	9/2	5822.890	7/2	25788.548
5011.938	nl 3	7/2	9704.744	7/2	29651.540
5012.99	nl -	9/2	12068.17	7/2	32010.763
5014.761	32	9/2	9105.020	9/2	29040.590
5017.675	66	9/2	5822.890	11/2	25746.884
5018.136	70	9/2	8643.824	7/2	28565.989
5022.27	nl -	5/2	30454.610	3/2	10548.845
5022.587	78	5/2	28890.950	3/2	8986.443
5023.68	nl <1	9/2	11549.602	11/2	31449.773
5024.624	nl 5	13/2	10423.654	11/2	30320.091
5024.97	nl -	11/2	31641.39	13/2	11746.328
5025.54	nl -	11/2	31222.52	9/2	11329.696
5027.47	nl -	19/2	34225.35	17/2	14340.175
5027.59	nl -	11/2	8829.063	11/2	28713.780
5027.640	27	7/2	8013.089	5/2	27897.591
5028.902	nl 23	5/2	8737.556	5/2	28617.067
5033.66	nl -	9/2	8029.275	7/2	27890.013
5034.96	nl -	11/2	6892.934	9/2	26748.510
5035.49	nl -	13/2	15073.268	15/2	34926.79
5036.44	nl -	13/2	10470.329	11/2	30320.091
5037.26	nl -	9/2	11549.602	11/2	31396.143

λ_air (Å)	SNR	Even Levels		Odd Levels	
		J	Energy (cm⁻¹)	J	Energy (cm⁻¹)
5037.31	nl -	11/2	11282.865	11/2	31129.206
5037.74	nl -	11/2	28680.018	11/2	8835.383
5042.168	60	13/2	6603.591	15/2	26430.800
5042.225	nl 8	9/2	10356.737	7/2	30183.72
5045.752	68	13/2	10470.329	15/2	30283.462
5046.078	105	15/2	8765.541	15/2	28577.388
5051.384	nl 2	9/2	29370.862	9/2	9579.832
5051.441	30	9/2	9105.020	11/2	28895.833
5052.61	nl <1	11/2	12658.416	11/2	32444.655
5053.93	nl -	19/2	34580.89	19/2	14799.842
5056.11	nl 1	11/2	13376.992	11/2	33149.53
5056.282	19	11/2	9268.726	9/2	29040.590
5060.17	nl -	13/2	11562.762	11/2	31319.42
5060.880	nl 16	7/2	29499.246	5/2	9745.334
5060.960	45	11/2	31083.29	9/2	11329.696
5061.824	6	7/2	31079.962	9/2	11329.696
5061.99	nl -	1/2	10956.651	3/2	30706.200
5062.435	9	7/2	29327.656	9/2	9579.832
5062.992	nl 30	7/2	9704.744	7/2	29450.41
5067.964	28	15/2	9745.376	17/2	29471.666
5068.16	nl -	7/2	12617.701	9/2	32343.24
5069.024	60	11/2	6313.224	9/2	26035.395
5069.39	nl -	11/2	12234.616	9/2	31955.363
5073.92	nl -	13/2	14328.241	15/2	34031.358
5074.76	nl -	7/2	9704.744	5/2	29404.602
5076.223	23	9/2	30144.181	7/2	10449.997
5084.97	nl -	15/2	34000.50	17/2	14340.175
5086.89	nl -	9/2	9105.020	7/2	28757.902
5089.105	15	7/2	12049.480	9/2	31693.821
5090.336	24	5/2	9710.600	3/2	29350.190
5090.56	nl -	11/2	30968.412	9/2	11329.696
5093.57	nl -	11/2	9268.726	11/2	28895.833
5095.768	58	11/2	4866.515	9/2	24485.172
5098.342	18	9/2	9105.020	11/2	28713.780
5099.01	-	9/2	11713.236	11/2	31319.42
5099.060	nl 22	11/2	9483.518	11/2	29089.508

λ_air (Å)	SNR	Even Levels		Odd Levels	
		J	Energy (cm⁻¹)	J	Energy (cm⁻¹)
5099.664	25	17/2	9770.273	17/2	29373.942
5101.010	nl 7	5/2	11107.696	3/2	30706.200
5103.06	nl -	7/2	30920.300	9/2	11329.696
5104.245	nl 7	11/2	31332.402	13/2	11746.328
5111.28	nl -	13/2	12118.054	11/2	31677.187
5111.815	nl -	11/2	9483.518	9/2	29040.590
5114.42	nl -	11/2	30869.567	11/2	11322.443
5115.76	nl -	5/2	10829.070	3/2	30371.08
5117.771	38	5/2	6451.808	3/2	25986.120
5118.35	nl -	7/2	10194.768	5/2	29726.88
5119.19	nl -	13/2	14328.241	11/2	33857.14
5119.209	24	7/2	9704.744	7/2	29233.565
5125.032	nl 10	3/2	11361.762	5/2	30868.400
5139.28	nl -	9/2	10920.365	9/2	30372.918
5144.278	78	11/2	6313.224	11/2	25746.884
5145.50	nl -	7/2	27679.200	9/2	8250.143
5146.44	nl -	19/2	34225.35	19/2	14799.842
5147.943	nl 16	15/2	10466.689	15/2	29886.515
5148.94	-	11/2	10904.034	11/2	30320.091
5149.13	nl -	9/2	29865.350	7/2	10449.997
5149.360	16	11/2	9675.029	11/2	29089.508
5150.188	nl 4	17/2	11714.352	17/2	31125.712
5151.197	nl 28	5/2	6451.808	5/2	25859.364
5155.219	nl 15	9/2	11184.396	9/2	30576.811
5162.37	nl -	11/2	9675.029	9/2	29040.590
5164.07	nl -	9/2	12651.589	7/2	32010.763
5165.301	39	17/2	10531.951	15/2	29886.515
5167.53	nl -	7/2	11472.410	7/2	30818.62
5168.005	nl 7	3/2	11361.762	3/2	30706.200
5170.000	nl 9	11/2	31083.29	13/2	11746.328
5171.962	nl 18	11/2	4866.515	9/2	24196.152
5173.255	nl 25	7/2	30654.508	9/2	11329.696
5173.43	nl -	7/2	10194.768	9/2	29518.913
5174.218	nl 11	11/2	6714.184	9/2	26035.395
5175.74	nl -	11/2	30645.242	9/2	11329.696
5179.21	nl -	7/2	11274.229	9/2	30576.811

λ_air (Å)	SNR	Even Levels		Odd Levels	
		J	Energy (cm⁻¹)	J	Energy (cm⁻¹)
5180.42	nl -	13/2	13146.584	11/2	32444.655
5181.300	nl 4	9/2	10356.737	7/2	29651.540
5181.57	nl -	7/2	11274.229	5/2	30568.035
5184.87	nl -	19/2	34225.35	17/2	14943.825
5185.88	nl -	13/2	12041.655	11/2	31319.42
5189.14	nl <1	11/2	12234.616	9/2	31500.25
5190.39	nl -	17/2	15665.796	15/2	34926.79
5190.530	53	9/2	28840.315	9/2	9579.832
5191.837	nl 4	7/2	10194.768	7/2	29450.41
5192.56	nl -	7/2	6535.572	7/2	25788.548
5193.360	48	13/2	6603.591	15/2	25853.590
5195.86	nl <1	17/2	31055.361	15/2	11814.647
5198.20	nl -	9/2	29682.07	7/2	10449.997
5200.01	-	11/2	31222.52	11/2	11997.137
5200.901	17	11/2	30968.412	13/2	11746.328
5207.51	nl -	17/2	33997.515	19/2	14799.842
5207.969	nl 13	9/2	4432.225	7/2	23628.220
5208.51	nl -	11/2	13250.662	11/2	32444.655
5208.54	nl -	19/2	33534.065	17/2	14340.175
5210.96	-	11/2	11944.207	11/2	31129.206
5211.948	nl 13	17/2	9770.273	17/2	28951.616
5212.79	nl -	7/2	12321.991	9/2	31500.25
5214.337	60	17/2	14302.875	17/2	33475.43
5214.85	nl <1	5/2	12907.057	7/2	32077.74
5217.34	nl -	11/2	12234.616	11/2	31396.143
5217.443	30	21/2	12664.774	21/2	31825.917
5217.742	nl 13	5/2	8737.556	5/2	27897.591
5217.81	nl -	9/2	11549.602	7/2	30709.41
5219.81	nl -	5/2	8737.556	7/2	27890.013
5222.310	nl 17	13/2	6603.591	11/2	25746.884
5223.40	-	11/2	12180.13	11/2	31319.42
5225.28	nl -	5/2	11646.312	3/2	30778.71
5228.83	nl -	17/2	15665.796	15/2	34785.20
5231.533	28	19/2	11151.433	19/2	30260.968
5234.09	nl -	11/2	28680.018	9/2	9579.832
5234.50	nl -	7/2	11274.229	9/2	30372.918

λ_air (Å)	SNR	Even Levels		Odd Levels	
		J	Energy (cm⁻¹)	J	Energy (cm⁻¹)
5240.04	nl <1	9/2	27913.895	11/2	8835.383
5240.51	nl -	7/2	28822.147	5/2	9745.334
5240.65	nl -	13/2	15850.485	15/2	34926.79
5242.66	nl -	5/2	28055.421	3/2	8986.443
5242.94	nl -	11/2	4866.515	9/2	23934.491
5244.95	nl -	9/2	14897.721	9/2	33958.36
5248.38	nl -	15/2	31270.29	13/2	12222.095
5250.970	nl 10	7/2	10194.768	7/2	29233.565
5251.114	nl 13	3/2	11361.762	1/2	30400.042
5252.653	nl 8	11/2	6714.184	11/2	25746.884
5253.579	nl 15	9/2	27109.741	11/2	8080.404
5254.166	nl 9	9/2	11549.602	9/2	30576.811
5255.610	17	5/2	10829.070	5/2	29851.062
5257.221	60	9/2	8643.824	9/2	27659.987
5258.59	nl -	9/2	32247.808	9/2	11329.714
5259.627	62	9/2	5822.890	9/2	24830.361
5260.315	nl 10	15/2	10466.689	17/2	29471.666
5261.283	18	9/2	27251.615	9/2	8250.143
5261.88	nl -	9/2	11184.396	7/2	30183.72
5262.02	nl -	5/2	10829.070	7/2	29827.87
5262.27	-	9/2	10356.737	11/2	29354.638
5263.022	17	1/2	12264.864	3/2	31260.067
5266.763	nl 14	7/2	27231.854	9/2	8250.143
5267.757	nl 15	7/2	13032.634	7/2	32010.763
5269.653	nl 4	11/2	30968.412	11/2	11997.137
5270.821	40	3/2	9649.970	5/2	28617.067
5273.007	nl 15	9/2	12519.707	7/2	31478.935
5275.178	nl 12	15/2	29620.381	15/2	10668.95
5278.442	24	17/2	10531.951	17/2	29471.666
5278.599	14	9/2	29370.862	11/2	10431.716
5280.59	nl -	15/2	15994.780	15/2	34926.79
5281.51	nl -	9/2	29865.350	9/2	10936.650
5285.67	nl -	1/2	11864.887	3/2	30778.71
5286.88	nl -	7/2	11274.229	7/2	30183.72
5287.504	25	15/2	10466.689	17/2	29373.942
5288.038	52	11/2	28485.173	9/2	9579.832

λ_air (Å)	SNR	Even Levels		Odd Levels	
		J	Energy (cm⁻¹)	J	Energy (cm⁻¹)
5288.35	nl -	11/2	13727.482	9/2	32631.71
5289.75	nl -	7/2	11668.794	5/2	30568.035
5290.019	35	5/2	6451.808	7/2	25350.082
5290.15	nl -	5/2	10829.070	5/2	29726.88
5290.319	nl 8	13/2	7951.323	11/2	26848.512
5291.55	nl -	5/2	11107.696	5/2	30000.493
5291.782	16	11/2	29323.690	11/2	10431.716
5293.48	nl -	15/2	31887.920	15/2	13002.023
5296.485	16	15/2	12250.519	17/2	31125.712
5296.965	nl 20	7/2	27123.623	9/2	8250.143
5297.618	nl 14	11/2	10904.034	11/2	29775.190
5300.434	60	9/2	4432.225	7/2	23293.356
5300.862	42	9/2	27109.741	9/2	8250.143
5304.74	nl -	7/2	10194.768	9/2	29040.590
5306.01	nl -	1/2	11864.887	3/2	30706.200
5306.31	nl -	9/2	15016.889	11/2	33857.14
5308.545	nl 12	17/2	11714.352	17/2	30546.666
5308.651	11	5/2	12646.996	7/2	31478.935
5312.230	nl 24	9/2	8029.275	11/2	26848.512
5313.57	nl -	7/2	6535.572	7/2	25350.082
5315.46	nl -	17/2	15665.796	19/2	34473.61
5315.657	nl 15	17/2	9770.273	15/2	28577.388
5317.480	35	13/2	7630.132	15/2	26430.800
5317.66	nl -	15/2	11483.427	15/2	30283.462
5318.18	nl -	9/2	12651.589	11/2	31449.773
5319.36	nl 3	1/2	10956.651	3/2	29750.67
5326.141	nl 10	11/2	31591.140	9/2	12821.043
5326.41	-	7/2	12049.480	7/2	30818.62
5327.022	nl 22	13/2	6603.591	15/2	25370.585
5327.06	nl -	5/2	29216.845	7/2	10449.997
5333.74	nl -	5/2	11107.696	5/2	29851.062
5334.682	80	5/2	6451.808	5/2	25191.854
5336.754	nl 6	9/2	10356.737	11/2	29089.508
5337.09	nl -	7/2	28311.416	9/2	9579.832
5338.61	nl -	7/2	11274.229	5/2	30000.493
5340.614	nl 28	9/2	8029.275	9/2	26748.510

λ_air (Å)	SNR	Even Levels		Odd Levels	
		J	Energy (cm⁻¹)	J	Energy (cm⁻¹)
5342.262	nl 4	11/2	31591.140	11/2	12877.682
5347.309	nl 28	11/2	6313.224	11/2	25009.019
5348.46	nl -	9/2	29123.494	11/2	10431.716
5350.73	nl -	9/2	10356.737	9/2	29040.590
5351.04	nl -	9/2	13272.613	9/2	31955.363
5352.55	nl -	11/2	10841.417	9/2	29518.913
5352.94	nl -	11/2	9268.726	11/2	27944.838
5354.46	nl -	11/2	29993.26	11/2	11322.443
5354.69	nl -	5/2	10829.070	3/2	29499.10
5356.99	nl -	7/2	13415.739	7/2	32077.74
5359.55	nl -	15/2	34000.50	13/2	15347.425
5360.746	68	9/2	8643.824	9/2	27292.757
5361.743	nl 15	5/2	8737.556	3/2	27383.021
5363.671	nl 8	3/2	11361.762	3/2	30000.532
5365.51	nl -	15/2	16294.40	15/2	34926.79
5365.97	nl -	5/2	12078.621	7/2	30709.41
5366.227	nl 16	7/2	28375.220	5/2	9745.334
5368.018	nl 20	7/2	9704.744	9/2	28328.419
5369.31	nl -	5/2	11107.696	5/2	29726.88
5371.801	92	9/2	4432.225	11/2	23042.780
5372.678	nl 10	15/2	31887.920	17/2	13280.404
5373.38	nl -	13/2	13897.874	15/2	32502.962
5373.53	nl -	7/2	30654.508	9/2	12049.940
5377.51	nl -	9/2	11184.396	11/2	29775.190
5379.75	nl -	3/2	11361.762	3/2	29944.814
5381.616	nl 106	9/2	4432.225	9/2	23008.838
5382.988	nl 9	5/2	12907.057	7/2	31478.935
5384.67	nl -	7/2	28311.416	5/2	9745.334
5385.64	nl -	5/2	13448.016	7/2	32010.763
5385.88	nl -	7/2	13781.35	9/2	32343.24
5386.74	-	3/2	12701.121	3/2	31260.067
5390.07	nl -	9/2	31368.505	9/2	12821.043
5391.40	-	9/2	29865.350	11/2	11322.443
5392.35	nl -	7/2	13415.739	9/2	31955.363
5395.657	nl 24	9/2	8320.240	11/2	26848.512
5397.74	nl -	5/2	10829.070	3/2	29350.190

λ_air (Å)	SNR	Even Levels		Odd Levels	
		J	Energy (cm⁻¹)	J	Energy (cm⁻¹)
5398.903	88	11/2	6313.224	9/2	24830.361
5402.094	nl 15	1/2	11864.887	3/2	30371.08
5402.56	nl -	13/2	16422.190	15/2	34926.79
5402.980	158	11/2	6313.224	11/2	24816.383
5404.892	19	7/2	12321.991	7/2	30818.62
5406.15	nl -	11/2	11282.865	11/2	29775.190
5406.59	nl -	15/2	16294.40	15/2	34785.20
5408.24	nl -	5/2	27471.606	3/2	8986.443
5408.309	nl 12	15/2	10466.689	17/2	28951.616
5408.33	nl -	13/2	15372.271	11/2	33857.14
5412.84	nl -	9/2	29123.494	7/2	10654.053
5413.517	nl 10	9/2	11184.396	7/2	29651.540
5414.331	nl 15	17/2	33264.21	19/2	14799.842
5414.93	nl -	9/2	29865.350	7/2	11403.011
5415.225	nl 20	11/2	9483.518	11/2	27944.838
5415.298	10	15/2	33808.50	13/2	15347.425
5415.69	-	3/2	11911.350	3/2	30371.08
5417.316	85	17/2	9770.273	17/2	28224.462
5419.347	nl 8	13/2	10266.501	11/2	28713.780
5419.539	nl -	9/2	27282.000	11/2	8835.383
5424.938	nl 10	9/2	8320.240	9/2	26748.510
5426.307	42	13/2	11462.895	15/2	29886.515
5426.45	nl -	11/2	30645.242	13/2	12222.095
5427.471	80	17/2	10531.951	17/2	28951.616
5427.976	28	7/2	7617.440	9/2	26035.395
5430.487	nl 2	15/2	33808.50	15/2	15399.063
5431.04	nl -	5/2	13670.175	7/2	32077.74
5432.84	nl -	11/2	31222.52	9/2	12821.043
5432.93	nl -	9/2	10356.737	7/2	28757.902
5440.851	nl 20	7/2	9918.190	5/2	28292.560
5441.178	28	9/2	5822.890	9/2	24196.152
5441.51	-	7/2	28822.147	7/2	10449.997
5442.87	nl -	9/2	31721.60	9/2	13354.046
5446.82	-	5/2	11646.312	3/2	30000.532
5448.51	-	3/2	12051.488	1/2	30400.042
5452.68	nl -	9/2	11184.396	9/2	29518.913

λ_air (Å)	SNR	Even Levels		Odd Levels	
		J	Energy (cm^-1)	J	Energy (cm^-1)
5456.628	110	15/2	12804.468	17/2	31125.712
5457.12	nl -	3/2	12051.488	3/2	30371.08
5458.66	nl -	7/2	11869.290	7/2	30183.72
5462.45	nl -	7/2	9918.190	5/2	28219.904
5463.860	nl 6	5/2	12481.714	3/2	30778.71
5464.505	30	11/2	6714.184	11/2	25009.019
5465.91	nl -	13/2	10423.654	11/2	28713.780
5468.43	nl -	15/2	14221.272	15/2	32502.962
5473.50	nl -	5/2	27251.230	3/2	8986.443
5473.63	nl -	7/2	29674.025	9/2	11409.7
5474.15	nl -	11/2	29993.26	9/2	11730.668
5476.43	-	3/2	11911.350	3/2	30166.356
5477.684	42	15/2	28661.560	13/2	10410.745
5481.402	nl 13	3/2	27983.773	5/2	9745.334
5481.81	nl -	11/2	31591.140	9/2	13354.046
5481.87	nl -	5/2	28890.950	7/2	10654.053
5485.908	82	13/2	7630.132	15/2	25853.590
5491.679	95	11/2	26937.739	13/2	8733.440
5492.73	nl -	15/2	31536.710	13/2	13335.870
5493.207	nl 15	19/2	13626.672	21/2	31825.917
5496.953	24	9/2	29123.494	9/2	10936.650
5500.152	170	11/2	4866.515	11/2	23042.780
5500.62	nl -	13/2	14328.241	15/2	32502.962
5501.394	nl 10	17/2	11714.352	15/2	29886.515
5501.713	nl 40	7/2	7617.440	7/2	25788.548
5501.875	15	17/2	33114.40	17/2	14943.825
5502.63	nl -	7/2	28822.147	7/2	10654.053
5502.95	nl -	9/2	12651.589	7/2	30818.62
5506.41	nl -	17/2	32925.14	15/2	14769.532
5506.819	50	15/2	33808.50	13/2	15654.235
5506.978	11	13/2	10423.654	15/2	28577.388
5508.91	nl -	11/2	30968.412	9/2	12821.043
5510.06	nl -	7/2	13867.177	7/2	32010.763
5510.442	nl 21	11/2	4866.515	9/2	23008.838
5511.269	94	7/2	6535.572	5/2	24675.173
5512.76	nl -	9/2	29865.350	9/2	11730.668

λ_air (Å)	SNR	Even Levels		Odd Levels	
		J	Energy (cm⁻¹)	J	Energy (cm⁻¹)
5514.07	nl -	7/2	11274.229	5/2	29404.602
5518.794	nl 14	3/2	12051.488	3/2	30166.356
5520.06	nl -	15/2	10466.689	15/2	28577.388
5520.31	nl -	17/2	31055.361	19/2	12945.474
5521.43	nl -	1/2	12264.864	3/2	30371.08
5522.655	120	11/2	6714.184	11/2	24816.383
5523.27	nl -	9/2	31721.60	7/2	13621.400
5525.31	nl -	11/2	13035.697	11/2	31129.206
5525.571	nl 21	3/2	29234.227	5/2	11141.576
5527.508	nl 7	5/2	12481.714	5/2	30568.035
5530.88	nl -	5/2	29216.845	5/2	11141.576
5532.144	nl 20	15/2	28791.510	17/2	10720.359
5537.568	nl 26	11/2	28485.173	11/2	10431.716
5541.34	nl -	9/2	29370.862	9/2	11329.714
5551.547	nl 5	9/2	31368.505	11/2	13360.502
5555.083	25	11/2	31332.402	13/2	13335.870
5557.14	nl -	15/2	31270.29	17/2	13280.404
5557.586	nl 13	3/2	11361.762	3/2	29350.190
5559.785	nl 5	17/2	32925.14	17/2	14943.825
5560.13	nl -	3/2	11361.762	1/2	29341.96
5562.907	18	15/2	31536.710	15/2	13565.490
5563.95	nl -	9/2	29370.862	7/2	11403.011
5566.742	nl 18	15/2	13439.008	17/2	31397.849
5567.857	nl 20	7/2	9704.744	9/2	27659.987
5569.489	nl 16	3/2	9649.970	1/2	27599.95
5569.608	nl 33	7/2	6535.572	9/2	24485.172
5571.478	33	9/2	28375.291	11/2	10431.716
5572.214	nl 30	15/2	28661.560	17/2	10720.359
5573.558	nl 40	5/2	6451.808	5/2	24388.693
5574.32	nl -	15/2	31270.29	13/2	13335.870
5574.49	nl -	7/2	27679.200	5/2	9745.334
5578.225	nl 10	5/2	12078.621	5/2	30000.493
5581.95	nl -	7/2	13590.350	9/2	31500.25
5582.478	104	7/2	6535.572	7/2	24443.790
5588.002	80	15/2	11483.427	17/2	29373.942
5589.570	nl 24	7/2	28822.147	9/2	10936.650

λ_air (Å)	SNR	Even Levels		Odd Levels	
		J	Energy (cm⁻¹)	J	Energy (cm⁻¹)
5599.68	nl -	9/2	12519.707	9/2	30372.918
5599.708	nl 46	7/2	6535.572	5/2	24388.693
5602.27	nl -	3/2	28986.540	5/2	11141.576
5605.88	nl -	7/2	30654.508	9/2	12821.043
5612.06	nl -	5/2	29216.845	7/2	11403.011
5615.227	nl 13	3/2	9649.970	1/2	27453.746
5616.551	nl 7	3/2	12051.488	5/2	29851.062
5639.78	nl -	5/2	27471.606	5/2	9745.334
5643.53	-	11/2	12658.416	9/2	30372.918
5643.872	nl 5	9/2	32247.808	9/2	14534.393
5646.92	nl -	5/2	11646.312	3/2	29350.190
5654.36	nl -	7/2	28822.147	5/2	11141.576
5668.50	nl -	7/2	27381.794	5/2	9745.334
5670.90	nl -	9/2	13605.667	9/2	31234.656
5672.48	nl -	7/2	29674.025	9/2	12049.940
5675.61	nl -	11/2	30968.412	9/2	13354.046
5691.02	nl -	7/2	31531.30	5/2	13964.630
5696.909	nl 10	11/2	28485.173	9/2	10936.650
5697.16	nl -	15/2	31887.920	17/2	14340.175
5703.289	nl 7	11/2	4866.515	9/2	22395.393
5705.063	nl 9	15/2	29287.637	17/2	11764.216
5706.87	nl -	9/2	28840.315	11/2	11322.443
5707.64	nl -	11/2	30869.567	9/2	13354.046
5720.195	nl 8	1/2	11864.887	1/2	29341.96
5726.351	nl 22	15/2	26191.727	13/2	8733.44
5746.098	nl 22	15/2	29620.381	13/2	12222.095
5747.42	nl -	15/2	30959.764	15/2	13565.490
5752.91	nl -	15/2	31887.920	13/2	14510.22
5753.877	nl 10	7/2	28311.416	9/2	10936.650
5786.20	nl -	7/2	29327.656	9/2	12049.940
5805.63	nl -	9/2	5822.890	11/2	23042.780
5834.35	nl -	7/2	28865.800	9/2	11730.668
5851.804	nl 5	17/2	33264.21	15/2	16180.200
5863.14	nl -	5/2	8737.556	7/2	25788.548
5871.57	nl -	15/2	31536.710	13/2	14510.22
5881.793	nl 3	7/2	31531.30	9/2	14534.393

λ_air (Å)	SNR	Even Levels		Odd Levels	
		J	Energy (cm⁻¹)	J	Energy (cm⁻¹)
5884.990	9	9/2	29865.350	11/2	12877.682
5886.15	nl -	15/2	32383.385	15/2	15399.063
5899.45	nl -	9/2	29865.350	7/2	12919.316
5899.91	nl -	11/2	14505.065	11/2	31449.773
5909.289	23	11/2	8829.063	11/2	25746.884
5929.19	nl -	9/2	29682.07	9/2	12821.043
5930.585	nl 7	11/2	31083.29	11/2	14226.210
5932.02	-	7/2	29674.025	9/2	12821.043
5944.52	-	5/2	27471.606	7/2	10654.053
5949.178	5	9/2	29682.07	11/2	12877.682
5956.74	nl -	11/2	26467.248	13/2	9684.184
5957.086	8	5/2	28890.950	5/2	12108.867
5966.82	nl -	7/2	29674.025	7/2	12919.316
5975.935	nl 6	15/2	32383.385	13/2	15654.235
5976.44	-	7/2	27381.794	7/2	10654.053
5979.08	nl -	9/2	28042.800	11/2	11322.443
5982.597	60	15/2	28474.736	17/2	11764.216
6006.045	nl 4	7/2	30654.508	7/2	14009.225
6008.07	-	9/2	31368.505	11/2	14728.846
6011.20	-	9/2	4432.225	9/2	21063.222
6015.78	nl -	15/2	29620.381	15/2	13002.023
6029.42	nl -	7/2	28311.416	9/2	11730.668
6040.687	-	9/2	29370.862	9/2	12821.043
6042.485	115	15/2	26191.727	15/2	9646.83
6044.767	26	19/2	33534.065	17/2	16995.410
6055.21	nl -	9/2	8320.240	9/2	24830.361
6123.328	nl 8	15/2	31270.29	17/2	14943.825
6147.196	16	11/2	28485.173	13/2	12222.095
6154.321	25	9/2	12651.589	11/2	28895.833
6157.164	nl 12	5/2	9710.600	3/2	25947.350
6157.67	nl -	19/2	27999.623	17/2	11764.216
6157.77	nl -	15/2	34000.50	13/2	17765.348
6158.326	26	15/2	31887.920	13/2	15654.235
6158.868	70	17/2	14028.707	19/2	30260.968
6169.445	nl 3	11/2	31222.52	13/2	15018.088
6179.39	-	15/2	32383.385	13/2	16205.044

λ_air (Å)	SNR	Even Levels		Odd Levels	
		J	Energy (cm⁻¹)	J	Energy (cm⁻¹)
6189.254	10	9/2	5822.890	7/2	21975.458
6193.793	35	15/2	27904.945	17/2	11764.216
6202.021	15	11/2	28323.602	11/2	12204.285
6205.019	17	17/2	31055.361	17/2	14943.825
6213.21	nl -	7/2	27231.854	5/2	11141.587
6213.21	nl -	15/2	27904.945	15/2	11814.647
6214.050	nl 20	19/2	34580.89	17/2	18492.78
6214.669	nl 20	19/2	27999.623	19/2	11913.115
6215.714	nl 15	7/2	9704.744	7/2	25788.548
6216.346	nl 10	11/2	6313.224	9/2	22395.393
6222.30	nl -	15/2	30577.00	13/2	14510.22
6226.910	nl 6	15/2	29620.381	15/2	13565.490
6236.487	nl 10	15/2	28252.321	13/2	12222.095
6242.05	nl -	15/2	30959.764	17/2	14943.825
6245.480	35	13/2	10423.654	15/2	26430.800
6251.06	nl -	9/2	28042.800	9/2	12049.940
6251.794	nl 5	3/2	27983.773	3/2	11992.788
6266.953	4	9/2	27282.000	9/2	11329.696
6269.21	-	5/2	28055.421	5/2	12108.867
6271.13	-	15/2	30959.764	13/2	15018.088
6276.05	nl -	9/2	27251.615	11/2	11322.443
6291.519	23	15/2	12804.468	17/2	28694.480
6297.108	17	9/2	8320.240	9/2	24196.152
6298.97	nl -	15/2	31270.29	15/2	15399.063
6303.498	nl 21	7/2	6535.572	9/2	22395.393
6307.96	nl -	9/2	27251.615	7/2	11403.011
6308.113	10	5/2	27251.230	7/2	11403.011
6347.67	nl -	9/2	29370.862	7/2	13621.400
6353.15	nl -	11/2	31083.29	13/2	15347.425
6354.481	5	19/2	34225.35	17/2	18492.78
6363.744	22	9/2	27913.895	11/2	12204.285
6374.11	nl -	11/2	27888.407	11/2	12204.285
6374.62	-	15/2	31887.920	13/2	16205.044
6377.79	nl -	19/2	11151.433	19/2	26826.517
6389.980	nl 6	11/2	13250.662	11/2	28895.833
6405.410	3	11/2	28485.173	11/2	12877.682

λair (Å)	SNR	Even Levels		Odd Levels	
		J	Energy (cm⁻¹)	J	Energy (cm⁻¹)
6410.22	nl -	15/2	32383.385	15/2	16787.601
6416.478	nl 6	5/2	27573.343	3/2	11992.788
6420.91	nl -	15/2	31887.920	13/2	16318.118
6424.668	nl 8	15/2	30959.764	15/2	15399.063
6428.128	21	9/2	8643.824	9/2	24196.152
6428.537	7	9/2	27282.000	9/2	11730.668
6441.122	nl 10	9/2	27251.615	9/2	11730.668
6447.86	nl -	17/2	33997.515	17/2	18492.78
6448.764	nl 13	11/2	28323.602	9/2	12821.043
6449.336	nl 9	7/2	27231.854	9/2	11730.668
6457.639	nl 6	5/2	9710.600	5/2	25191.854
6492.46	-	9/2	29624.447	11/2	14226.210
6494.68	nl -	7/2	27123.623	9/2	11730.668
6495.04	nl -	7/2	28311.416	7/2	12919.316
6525.82	nl -	11/2	28680.018	11/2	13360.502
6531.782	14	15/2	30959.764	13/2	15654.235
6536.10	-	5/2	27573.343	7/2	12277.935
6540.285	nl 15	11/2	26222.282	9/2	10936.650
6542.61	nl -	15/2	29620.381	17/2	14340.175
6545.41	nl -	7/2	9918.190	5/2	25191.854
6576.41	nl -	9/2	27251.615	9/2	12049.940
6579.583	17	15/2	28474.736	17/2	13280.404
6579.870	nl 13	5/2	27471.606	7/2	12277.935
6590.663	nl 6	17/2	14302.875	17/2	29471.666
6599.140	10	11/2	28485.173	13/2	13335.870
6618.31	nl -	11/2	8829.063	9/2	23934.491
6625.05	-	9/2	29624.447	9/2	14534.393
6635.64	nl -	9/2	29600.360	9/2	14534.393
6643.862	12	9/2	27251.615	11/2	12204.285
6676.713	nl 7	5/2	27251.230	7/2	12277.935
6678.37	nl -	11/2	28323.602	9/2	13354.046
6683.82	nl -	7/2	28311.416	9/2	13354.046
6705.396	29	15/2	28474.736	15/2	13565.490
6708.241	38	15/2	27904.945	15/2	13002.023
6791.964	14	19/2	27999.623	17/2	13280.404
6846.30	-	7/2	29674.025	9/2	15071.618

λ_{air} (Å)	SNR	Even Levels		Odd Levels	
		J	Energy (cm^{-1})	J	Energy (cm^{-1})
6858.285	nl 5	15/2	24987.630	13/2	10410.745
6871.28	nl -	9/2	29370.862	11/2	14821.551
6894.405	nl 29	9/2	26231.182	9/2	11730.668
6920.710	28	15/2	26191.727	13/2	11746.328
6926.166	18	5/2	28055.421	7/2	13621.400
6991.366	18	7/2	27679.200	9/2	13379.788
7095.327	nl 4	17/2	12736.621	19/2	26826.517
7117.40	nl -	5/2	28055.421	7/2	14009.225
7165.483	8	5/2	27573.343	7/2	13621.400

Table 7.6: Lines classified by means of their hyperfine patterns and wave numbers, appearing in the FT spectrum, involving new levels given in the table7.4

λair (Å)	SNR	Even Levels		Odd Levels	
		J	Energy (cm^{-1})	J	Energy (cm^{-1})
3517.205	nl 11	15/2	31270.29	13/2	2846.741
3570.114	nl 9	15/2	32383.385	15/2	4381.072
4671.467	8	5/2	6451.808	7/2	27852.358
5043.218	38	9/2	8029.275	7/2	27852.358
5093.196	13	15/2	9745.376	17/2	29373.942
5212.333	nl 16	13/2	7630.132	13/2	26810.061
5344.713	nl 6	13/2	28351.711	15/2	9646.83
5357.215	25	17/2	12736.621	17/2	31397.849
5390.632	12	15/2	14929.886	17/2	33475.43
5409.904	nl 15	13/2	7951.323	15/2	26430.800
5419.676	36	15/2	8363.901	13/2	26810.061
5440.982	nl 40	15/2	8765.541	13/2	27139.468
5489.434	nl 22	13/2	22592.830	15/2	4381.072
5540.310	nl 11	15/2	8765.541	13/2	26810.061
5547.926	nl 34	9/2	4432.225	7/2	22451.973
5805.996	6	7/2	29327.656	5/2	12108.867
5861.328	nl 7	17/2	9770.273	19/2	26826.517
5906.671	11	11/2	14981.500	13/2	31906.825
6091.698	10	5/2	6451.808	5/2	22863.048
6100.929	12	13/2	10423.654	13/2	26810.061
6122.530	nl 8	11/2	6714.184	11/2	23042.780
6132.888	11	13/2	9464.440	13/2	25765.460
6176.266	nl 8	9/2	8643.824	9/2	24830.361
6213.154	nl 52	11/2	9675.029	13/2	25765.460
6358.696	nl 6	15/2	29287.637	15/2	13565.490
6363.059	6	9/2	9105.020	11/2	24816.383
6365.865	13	13/2	27519.089	15/2	11814.647
6481.778	48	11/2	25855.320	11/2	10431.716
6532.670	15	15/2	24987.630	13/2	9684.184
6602.604	10	11/2	9675.029	11/2	24816.383
6612.534	12	13/2	27340.889	13/2	12222.095
6681.265	4	11/2	28323.602	11/2	13360.502
6700.129	nl 5	11/2	23654.406	13/2	8733.440
6707.802	3	15/2	10466.689	15/2	25370.585

λair (Å)	SNR	Even Levels		Odd Levels	
		J	Energy (cm⁻¹)	J	Energy (cm⁻¹)
6737.304	22	17/2	10531.951	15/2	25370.585
6751.467	21	9/2	25744.156	9/2	10936.650
6782.978	20	3/2	9649.970	5/2	24388.693
6786.832	nl 7	15/2	14221.272	17/2	28951.616
6835.934	20	15/2	27904.945	17/2	13280.404
6843.378	5	17/2	29552.460	17/2	14943.825
6879.052	22	11/2	25855.320	11/2	11322.443
6963.749	9	15/2	14221.272	15/2	28577.388
7048.643	7	13/2	27519.089	13/2	13335.870
7057.366	nl 6	9/2	11184.396	7/2	25350.082
7077.868	nl 7	11/2	25855.320	9/2	11730.668
7085.725	9	11/2	25855.320	13/2	11746.328
7113.696	9	13/2	24722.464	15/2	10668.95
7131.339	nl 6	9/2	28840.315	11/2	14821.565
7131.724	nl 5	11/2	26222.282	11/2	12204.285
7140.794	nl 5	11/2	26222.282	13/2	12222.095
7156.112	18	11/2	23654.406	13/2	9684.184
7172.779	11	9/2	9105.020	11/2	23042.780
7183.152	nl 4	7/2	11274.229	5/2	25191.854
7187.606	3	15/2	27904.945	13/2	13995.931
7198.917	12	15/2	11483.427	15/2	25370.585
7209.095	8	7/2	27123.623	5/2	13256.082
7240.105	45	9/2	8643.824	7/2	22451.973
7273.985	10	7/2	27123.623	9/2	13379.788
7275.959	nl 8	11/2	9268.726	9/2	23008.838
7284.603	nl 9	13/2	12041.655	13/2	25765.460
7305.278	nl 5	13/2	27020.835	13/2	13335.870
7307.241	nl 3	7/2	11668.794	7/2	25350.082
7325.375	nl 15	13/2	12118.039	13/2	25765.460
7336.711	10	15/2	12804.468	15/2	26430.800
7370.361	nl 6	5/2	27573.343	7/2	14009.225
7414.819	nl 4	15/2	28252.321	15/2	14769.532
7498.891	nl 17	9/2	8643.824	7/2	21975.458
7542.062	15	11/2	9268.726	9/2	22524.055
7550.048	12	15/2	24987.630	13/2	11746.328
7550.905	nl 8	7/2	28311.416	9/2	15071.618

λair (Å)	SNR	Even Levels		Odd Levels	
		J	Energy (cm⁻¹)	J	Energy (cm⁻¹)
7551.988	nl 11	5/2	8737.556	7/2	21975.458
7562.373	9	5/2	28055.421	5/2	14835.699
7577.607	4	15/2	12250.519	13/2	25443.665
7589.206	13	15/2	24987.630	15/2	11814.647
7590.434	nl 5	7/2	12617.701	7/2	25788.548
7591.178	nl 6	7/2	11274.229	7/2	24443.790
7609.835	10	15/2	28791.510	13/2	15654.235
7619.816	10	15/2	12250.519	15/2	25370.585
7631.186	3	9/2	27109.741	7/2	14009.225
7666.289	nl 3	11/2	9483.518	9/2	22524.055
7672.215	3	11/2	10904.034	9/2	23934.491
7690.755	15	11/2	14981.500	9/2	27980.556
7709.545	nl 5	13/2	12041.655	11/2	25009.019
7742.845	nl 10	17/2	15665.796	15/2	28577.388
7800.123	nl 6	11/2	27888.407	9/2	15071.618
7810.871	nl 3	5/2	10829.070	7/2	23628.220
7819.677	5	11/2	13250.662	9/2	26035.395
7824.854	6	13/2	10266.501	11/2	23042.780
7865.266	nl 6	7/2	28822.147	7/2	16111.549
7872.786	nl 12	9/2	12651.589	7/2	25350.082
7898.193	13	11/2	9268.726	11/2	21926.369
7909.719	12	7.5	12804.468	13/2	25443.665
7912.995	35	17/2	12736.621	15/2	25370.585
7960.439	35	17/2	15665.796	17/2	28224.462
7968.417	nl 3	7/2	27381.794	5/2	14835.699
7976.244	nl 8	7/2	9918.190	7/2	22451.973
7984.691	nl 6	5/2	11107.696	7/2	23628.221
8009.741	nl 2	15/2	28661.560	15/2	16180.200
8022.233	nl 7	13/2	9464.440	11/2	21926.369
8023.198	nl7	9/2	27282.000	11/2	14821.565
8033.904	nl 2	9/2	11184.396	7/2	23628.220
8081.917	nl 5	11/2	13376.992	11/2	25746.884
8156.221	nl 8	7/2	10194.768	7/2	22451.973
8171.576	nl 8	11/2	8829.063	9/2	21063.22
8188.073	4	15/2	14221.272	15/2	26430.800
8194.017	nl 10	7/2	10194.768	9/2	22395.393

λair (Å)	SNR	Even Levels		Odd Levels	
		J	Energy (cm⁻¹)	J	Energy (cm⁻¹)
8223.709	4	15/2	28474.736	13/2	16318.118
8256.077	12	9/2	11184.396	7/2	23293.356
8265.447	24	9/2	10356.737	7/2	22451.973
8304.292	nl 7	9/2	10356.737	9/2	22395.393
8337.793	7	11/2	11944.207	9/2	23934.491
8346.322	nl 4	11/2	25357.817	9/2	13379.788
8357.456	8	5/2	12481.714	7/2	24443.790
8378.819	15	15/2	13439.008	15/2	25370.585
8384.228	9	13/2	22592.830	15/2	10668.95
8417.491	nl 3	15/2	28661.560	15/2	16784.800
8430.534	nl 5	9/2	11184.396	11/2	23042.780
8435.496	nl 3	15/2	14579.390	15/2	26430.800
8448.802	nl 4	7/2	22486.816	7/2	10654.053
8453.073	nl 7	11/2	12658.416	9/2	24485.172
8457.236	8	7/2	11472.410	7/2	23293.356
8474.743	nl 2	15/2	28661.560	15/2	16865.034
8476.085	nl 5	11/2	13035.697	9/2	24830.361
8477.849	nl 5	9/2	12651.589	7/2	24443.790
8504.428	nl 6	5/2	11107.696	5/2	22863.048
8525.734	58	11/2	11282.865	9/2	23008.838
8561.896	11	9/2	12519.707	9/2	24196.152
8603.474	nl 12	11/2	10904.034	9/2	22524.055
8604.434	nl 7	9/2	10356.737	7/2	21975.458
8615.006	nl 6	11/2	23654.406	9/2	12049.940
8628.120	nl 8	15/2	27904.945	13/2	16318.118
8640.942	nl 3	9/2	10356.737	11/2	21926.369
8643.863	nl 2	11/2	13250.662	11/2	24816.383
8650.457	nl 6	5/2	22959.928	7/2	11403.011
8655.932	9	5/2	12078.621	7/2	23628.220
8660.299	nl 7	9/2	13272.613	11/2	24816.383
8691.213	15	13/2	10423.654	11/2	21926.369
8725.714	nl 6	17/2	17494.383	17/2	28951.616
8751.047	nl 3	7/2	11869.290	7/2	23293.356
8762.130	22	9/2	26231.182	11/2	14821.565
8793.405	10	9/2	8643.824	7/2	20012.862
8816.190	nl 10	9/2	11184.396	9/2	22524.055

λair (Å)	SNR	Even Levels		Odd Levels	
		J	Energy (cm⁻¹)	J	Energy (cm⁻¹)
8850.571	15	9/2	11713.236	9/2	23008.838
8893.417	14	11/2	11282.865	9/2	22524.055
8917.363	nl 7	9/2	11184.396	9/2	22395.393
8922.972	nl 8	13/2	27626.232	11/2	16422.282
8943.890	34	7/2	11274.229	7/2	22451.973
8996.381	nl 21	11/2	11282.865	9/2	22395.393
8997.500	nl 7	13/2	13897.874	11/2	25009.019
9035.326	50	11/2	11944.207	9/2	23008.838
9045.943	nl 3	7/2	11472.410	9/2	22524.055
9053.560	nl 4	13/2	14328.241	15/2	25370.585
9091.907	9	5/2	13448.016	7/2	24443.790
9109.571	20	9/2	11549.602	9/2	22524.055
9110.822	nl 12	7/2	13415.739	5/2	24388.693
9169.796	19	9/2	11549.602	7/2	22451.973
9176.124	27	11/2	12658.416	9/2	24485.172
9246.821	13	3/2	12051.488	5/2	22863.048
9247.454	15	9/2	11713.236	9/2	22524.055
9273.537	13	7/2	13415.739	9/2	24196.152
9278.867	31	11/2	12234.616	9/2	23008.838
9339.919	5	7/2	13781.374	9/2	24485.172
9449.344	27	11/2	11944.207	9/2	22524.055
9500.322	7	9/2	12519.707	11/2	23042.780
9504.224	9	7/2	13415.739	9/2	23934.491
9511.740	16	9/2	13974.732	9/2	24485.172
9531.064	8	9/2	12519.707	9/2	23008.838
9588.908	13	9/2	11549.602	7/2	21975.458
9620.895	6	9/2	12651.589	11/2	23042.780
9632.786	6	13/2	19111.800	13/2	8733.440
9634.268	nl 17	9/2	11549.602	11/2	21926.369
9637.438	24	5/2	12078.621	7/2	22451.973
9699.660	nl 7	11/2	14178.365	9/2	24485.172
9709.175	14	9/2	12746.067	11/2	23042.780
9789.259	9	7/2	13415.739	7/2	23628.220
9834.368	nl 5	5/2	13127.722	7/2	23293.356
9846.492	7	7/2	13781.374	9/2	23934.491
9903.501	55	7/2	9918.190	7/2	20012.862

Table 7.8: Newly discovered Pr I levels of even and odd parity combining with known upper levels

| New lower level | | | $\lambda_{ex.}$ (Å, air) | $\lambda_{fl.}$ (Å, air) | File No. |
Energy(cm^{-1})	J	A (MHz)			Comments
Even Configuration					
14429.047	7/2	912(3)	5704.12	3825, 3933, 4178, 4448, 4492, 4759, 5069, 5180, 5350, 5392, 6539	pr511001 (31955.363 cm^{-1})
			5667.41	5251, 5099, 4993, 4088, 3917	pr511023 (32068.921 cm^{-1})
Odd Configuration					
15396.075	9/2	719(8)	5995.55	4820, 5701 , 5881	pr317027 (32070.498 cm^{-1})
			6145.27	4916, 5904	pr356032 (31664.301 cm^{-1})
			6551.96	4781, 5173, 5373, 5605, 5778, 5869, 6006	pr434041 (30654.52 cm^{-1})
			5714.24	4784, 4635, 5437 5593	pr244038 (32891.402 cm^{-1})
17518.420	9/2	847(4)	7449.321	4880, 5685, 5773, 5905, 5982, 6094, 6167	pr568029 (30938.740 cm^{-1})
			7566.65	4727, 4930, 5755, 6172	pr631018 (30730.786 cm^{-1})
16180.200	15/2	883.26	5851.80	3460, 5001, 5414, 5851, 6096, 6153	pr348053 (33264.21 cm^{-1})
			6625.03	5248, 5558, 5574, 5965, 6124, 6298,	pr440042 (31270.281 cm^{-1})
16784.800	15/2	297(5)	5925.18	3416, 5175, 5301, 6303	pr330087 (33657.265 cm^{-1})
			5807.00	3375, 5083, 5359, 6156	pr471024 (34000.50 cm^{-1})
			6193.94	5505, 5559, 5704	pr374038 (32925.14 cm^{-1})

New lower level			$\lambda_{ex.}$ (Å, air)	$\lambda_{fl.}$ (Å, air)	File No. Comments
Energy(cm^{-1})	J	A (MHz)			
16865.034	15/2	291(4)	6096.18	3460, 5001, 5414, 5851, 6096, 6151	pr366081 (33264.21 cm^{-1})
			5953.48	5301, 3416, 5175, 6303	pr477008 (33657.265 cm^{-1})
			6546.12	5207, 5756, 5974, 6512	pr465025 (32137.040 cm^{-1})
			7340.31	3434, 5354	pr637003 (30484.724 cm^{-1})
17012.626	15/2	494(6)	6006.28	5301, 3416, 5175, 6303	pr330048 (33657.265 cm^{-1})
			6151.40	3460, 5001, 5414, 5851, 6096, 6151	pr366089 (33264.21 cm^{-1})
			6208.78	3479, 5501	pr371024 (33114.40 cm^{-1})
18492.78	17/2	104(4)	6166.51	5870	pr387002 (34704.94 cm^{-1})
			6214.04	5054, 5684, 5914	pr362078 (34580.89 cm^{-1})

Table 7.9: New levels of Pr I found by the analysis of hyperfine patterns in the FT spectrum

J	Energy (cm^{-1})	A (MHz)	Lines which can be explained (Å, air)
Even Parity			
7/2	21487.127(15)	820(10)	(7592.721), (7419.626), (9703.503), (9788.856)
9/2	19042.997(15)	711(10)	(9119.426), (9262.825), (9793.869)
9/2	21159.184(15)	703(10)	(4724.758), (5053.543), (8112.149)
Odd Parity			
7/2	21722.562(15)	691(10)	(6546.654), (7292.217), (7459.340), (8469.107), (9921.608)
9/2	20622.833(15)	635(10)	(7928.195), (7938.3385), (8476.724), (9738.130)
19/2	24751.739(15)	1010(10)	(7668.138), (8271.098), (8320.561), (8986.242)
19/2	25487.571(15)	392(10)	(7364.750), (8189.66), (8968.242), (9353.958), (9481.693)

Table 7.10: Up to now unknown Pr II energy levels discovered within this work

New energy level			Excitation Wavelength λ_{air} / Å	Fluorescence Channels λ_{air} / Å
Energy / cm^{-1}	J	A/ MHz		
Even parity				
32776.99(4)	2	1464(7)	4473.84 4405.12	4473.84, 4405.12
33473.73(5)	3	998 (10)	4399.325 4273.91	4273.91, 4498.98
Odd parity				
33386.21(5)	3	1352(5)	4361.81 4328.40	3821.806, 3912.21, 4156.75, 4517.81
33850.96(5)	3	938(4)	4275.12 4385.45	3755.09, 3842.328, 4243.02, 4343.88

8 Conclusion

An experimental investigation of the hyperfine structure of a large number of spectral lines of the praseodymium atoms has been carried out using laser spectroscopy in a hollow cathode discharge lamp. The investigated spectral region lie in the range 4200 Å -7500 Å. The main emphasis was directed to the discovery of fine structure levels using the hyperfine structure of the investigated spectral line. Excitation wavelengths are extracted from a high resolution Fourier transform spectrum of praseodymium. The levels were discovered by analysis of the recorded hyperfine patterns of the investigated transitions. A total of 313 levels of Pr I were discovered, out of which 148 are even parity and 165 are odd parity energy levels. With the help of these newly discovered levels 652 spectral lines were classified directly by laser excitation and 836 spectral lines were classified as fluorescence lines. In addition to this, 178 lines in the FT spectrum were also classified by their hyperfine structures and wave numbers involving these newly discovered levels. 4 new levels of singly ionised praseodymium were also discovered during the course of this dissertation.

The electronic angular momentum J values of the newly discovered levels range from 1/2 to 21/2 for neutral praseodymium. Most of these newly found levels have angular momentum values lying in the mid range and only few levels were discovered with angular momentum values J = 1/2 and J = 21/2. Lines with combining levels having J ≤ 5/2 are very rarely visible in the FT spectrum. In most cases, the hyperfine structure of these lines is completely or partially masked by the hyperfine structure of nearby lying lines involving levels with high angular momenta. Nevertheless, carefully done laser spectroscopic investigations made it possible to find 54 up to now unknown levels with small J: 4 levels having J = 1/2, 19 levels having J = 3/2, and 31 levels having J = 5/2. On the higher side i.e. for large J value, also a small number of levels were found. About 54 levels were experimentally discovered i.e. 29 levels having J = 15/2, 15 levels having J = 17/2, 6 having J = 19/2 and 4 levels having J = 21/2. This is consistent with the theoretical predictions that only a small number of LS terms is possible for small and large J values.

Apart from the applications in other branches of physics, the hyperfine structure investigations presented in this dissertation will be helpful for further theoretical analysis and understanding of the atomic structure of praseodymium.

9 Bibliography

9.1 Literature Consulted

- H. E. White, "Introduction to Atomic Spectra", McGraw Hill (1934)
- H. G. Kuhn, "Atomic Spectra" Longmans, Green & CO. LTD. (1969)
- I. I. Sobel'man, "An Introduction to the Theory of Atomic Spectra", Pergamon Press (1972)
- R.D. Cowan, "The Theory of Atomic Structure and Spectra", University of California Press, (1981)
- I. I. Sobel'man, L. A. Vanshtein, E. A. Yukov, "Excitation of atoms and broadenings of spectral lines", Springer (1981)
- W. Demtröder, "Laser Spectroscopy", Springer (1982)
- G. K. Woodgate, "Elementary Atomic Structure", Second Edition Oxford Science Publications (2000)
- S. Svanberg, "Atomic and Molecular Spectroscopy", Springer (2004)

9.2 References:

1. R. M. Macfarlane, D. P. Burum, R. M. Shelby, *Phys Rev Lett* **49**, 636 (1982).
2. K. D. Böklen, T. Bossert, W. Foerster, H. H. Fuchs, G. Nachtsheim, *Springer-Verlag* **274**, 195 (1975).
3. H. E. White, *Phys Rev* **34**, 1397 (Dec, 1929).
4. P. Brix, *Phys Rev* **89**, 1245 (1953).
5. H. Lew, *Phys Rev* **91**, 619 (1953).
6. J. M. Baker, B. Bleaney, *Proceedings of the Physical Society of London Section A* **68**, 936 (1955).
7. K. Murakawa, *J. Phys. Soc. Jpn.* **15**, 2306 (1960).
8. R. D. Amado, *Phys Rev* **127**, 261 (1962).
9. R. Zalubas, Borchard.Br, *Journal of the Optical Society of America* **63**, 102 (1973).
10. J. Sugar, J. Reader, *J Chem Phys* **59**, 2083 (1973).
11. A. Ginibre, *Physica Scripta* **23**, 260 (1981).
12. W. J. Childs, L. S. Goodman, *Phys Rev A* **24**, 1342 (1981).
13. K. T. Cheng, W. J. Childs, *Phys Rev A* **31**, 2775 (1985).
14. M. N. Reddy, G. N. Rao, *Physica B & C* **150**, 457 (Jun, 1988).
15. A. Ginibre, *Atomic Data and Nuclear Data Tables* **44**, 1 (Jan, 1990).
16. A. Ginibre, *Physica Scripta* **39**, 694 (Jun, 1989).
17. A. Ginibre, *Physica Scripta* **39**, 710 (Jun, 1989).
18. A. Ginibre, Emery, Thèse Université de Paris-Sud, Centre d'Orsay (1988).

19. T. Kuwamoto *et al.*, *J. Phys. Soc. Jpn.* **65**, 3180 (Oct, 1996).

20. A. Krzykowski, B. Furmann, D. Stefanska, A. Jarosz, A. Kajoch, *Optics Communications* **140**, 216 (Aug 1, 1997).

21. J. Ruczkowski, E. Stachowska, M. Elantkowska, G. H. Guthohrlein, J. Dembczynski, *Physica Scripta* **68**, 133 (Aug, 2003).

22. M. Song *et al.*, *The European Physical Journal D - Atomic, Molecular, Optical and Plasma Physics* **2**, 115 (1998).

23. B. Furmann, A. Krzykowski, D. Stefanska, J. Dembezynski, *Physica Scripta* **74**, 658 (Dec, 2006).

24. S. Oppel, G. H. Guthohorlein, W. Kaenders, J. von Zanthier, *Applied Physics B-Lasers and Optics* **101**, 33 (Oct, 2010).

25. B. Gamper, et al., *Journal of Physics B: Atomic, Molecular and Optical Physics* **44**, 045003 (2011).

26. N. Rosen, G. R. Harrison, J. R. McNally, *Phys Rev* **60**, 722 (Nov, 1941).

27. H. Iimura *et al.*, *J. Phys. Soc. Jpn.* **59**, 4208 (1990).

28. M. K. Kim, R. Kachru, *Physical Review B* **44**, 9826 (1991).

29. H. Iimura, Y. Nakahara, S. Ichikawa, M. Kubota, T. Horiguchi, *Physical Review C* **50**, 661 (1994).

30. L. Maosheng *et al.*, *Phys Rev A* **62**, 052504 (2000).

31. M. Li *et al.*, *Hyperfine Interactions* **128**, 417 (2000).

32. S. Ivarsson, U. Litzen, G. M. Wahlgren, *Physica Scripta* **64**, 455 (Nov, 2001).

33. B. Furmann, D. Stefańska, E. Stachowska, J. Ruczkowski, J. Dembczyński, *The European Physical Journal D - Atomic, Molecular, Optical and Plasma Physics* **17**, 275 (2001).

34. M. Hong-Liang, *Chin. Phys.* **11**, 905 (2002).

35. B. Furmann, D. Stefanska, J. Dembczynski, E. Stachowska, *Physica Scripta* **72**, 300 (Oct, 2005).

36. H. N. Russell, F. A. Saunders, *Astrophys. J.* **61**, p.38 (1925).

37. A. R. Edmonds, *Angular Momenta and Quantum Mechanics* (Princeton University Press, Princeton, New Jersey, 1960).

38. B. R. Judd, *Operator Techniques in Atomic Spectroscopy.* (McGraw-Hill Book Company, Inc., New York, 1963).

39. H. C. Burger, H. B. Dorgelo, *Zeitschrift für Physik A Hadrons and Nuclei* **23**, 258 (1924).

40. L. S. Ornstein, H. C. Burger, *Zeitschrift für Physik A Hadrons and Nuclei* **24**, 41 (1924).

41. M. Göppert-Mayer, *Ann Phys-Berlin* **9**, 273 (May, 1931).

42. T. W. Hansch, I. S. Shahin, A. L. Schawlow, *Phys Rev Lett* **27**, 707 (1971).

43. M. D. Levenson, A. L. Schawlow, *Phys Rev A* **6**, 10 (1972).

44.   C. Borde, *Cr Acad Sci B Phys* **271**, 371 (1970).

45.   D. A. Jackson, H. Kuhn, *Proc. Roy. Soc.* **A154**, 679 (1936).

46.   S. Ezekiel, R. Weiss, *Phys Rev Lett* **20**, 91 (1968).

47.   P. F. Liao, G. C. Bjorklund, *Phys Rev Lett* **36**, 584 (1976).

48.   C. Wieman, T. W. Hänsch, *Phys Rev Lett* **36**, 1170 (1976).

49.   R. Frisch, *Zeitschrift für Physik A Hadrons and Nuclei* **86**, 42 (1933).

50.   A. Ashkin, *Phys Rev Lett* **25**, 1321 (1970).

51.   P. Jacquinot, S. Liberman, J. L. Picqué, J. Pinard, *Optics Communications* **8**, 163 (1973).

52.   I. I. Rabi, J. R. Zacharias, S. Millman, P. Kusch, *Phys Rev* **53**, 318 (Feb, 1938).

53.   I. I. Rabi, *Phys Rev* **87**, 379 (1952).

54.   R. Marrus, D. Mccolm, *Phys Rev Lett* **15**, 813 (1965).

55.   F. M. Penning, *Physica* **8**, 137 (1928).

56.   R. B. Green, R. A. Keller, G. G. Luther, P. K. Schenck, J. C. Travis, *Appl Phys Lett* **29**, 727 (1976).

57.   D. S. King, P. K. Schenck, K. C. Smyth, J. C. Travis, *Appl. Opt.* **16**, 2617 (1977).

58.   T. Caesar, J. Heully, L., *J. Phys. Colloques* **44**, C7 (1983).

59.   J.-P. Grandin, X. Husson, *Journal of Physics B: Atomic and Molecular Physics* **14**, 433 (1981).

60.   M. Skolnick, *Ieee J Quantum Elect* **6**, 139 (1970).

61.   W. H. Thomason, D. C. Elbers, *Rev Sci Instrum* **46**, 409 (1975).

62.   F. Paschen, R. Ritschl, *Ann Phys-Berlin* **410**, 867 (1933).

63.   H. Schüler, *Z Phys* **59**, 149 (1930).

64.   H. Schüler, *Zeitschrift für Physik A Hadrons and Nuclei* **35**, 323 (1926).

65.   D. Feldmann, *Optics Communications* **29**, 67 (1979).

66.   K. Miyazaki, H. Scheingraber, C. R. Vidal, *Phys Rev A* **28**, 2229 (1983).

67.   H. O. Behrens, G. H. Guthöhrlein, *Journal De Physique* **44**, 149 (1983).

68.   H. O. Behrens, G. H. Guthöhrlein, A. Kasper, *Journal De Physique* **44**, 239 (1983).

69.   E. R. Peck, K. Reeder, *J. Opt. Soc. Am.* **62**, 958 (1972).

70.   L. Windholz, G. H. Guthöhrlein, *Physica Scripta* **T105**, 55 (2003).

71.   W. Ritz, *Astrophys. J.* **28**, 237 (1908).

72.   T.Quiering, Universität der Bundeswehr (1984).

73.   G. H. Guthöhrlein. (Helmut-Schmidt-Universität, Universität der Bundeswehr, Holstenhofweg 85, D-22043 Hamburg, Germany, 2005).

74.   I. A. Siddiqui, PhD Thesis, Institute of Experimental Physics TU Graz (2010).